VAAL UNIVERSITY OF TECHNOLOGY

Inspiring thought. Shaping talent.

Hybrid light photocatalysis of aromatic wastes in a fluidized bed reactor

Thesis submitted in fulfilment of the requirements for the degree

Doctor of Philosophy: Chemical Engineering

In the Faculty of Engineering and Technology

John Willis Juma Pesa Akach

(M.Tech. Chemical Engineering)

Student number: 211050563

Supervisor: Prof. Ochieng Aoyi

Co-Supervisor: Prof. John Kabuba Tshilenge

(1 August 2022)

Declaration

I, John Willis Juma Pesa Akach, declare that the material in this thesis is my work, except where it is stated otherwise. This work has not been submitted to another university for any other degree.

Signed  ……..

Name: J.W.J.P. Akach

Student number: 211050563

Date: 1 August 2022

Place: Vanderbijlpark

Acknowledgement

Firstly, I thank God for giving me the strength and determination to see this work through and for enabling my success in innumerable ways. I would also like to thank my supervisors Prof. Ochieng Aoyi and Prof. John Kabuba Tshilenge for their support and guidance throughout the duration of this work. My gratitude also goes to the Vaal University of Technology for supporting me through Hubs and Spokes bursary and the provision of the laboratory and equipment for the experiments. Finally, I would like to thank my mum and late dad, siblings and friends for their logistical and emotional support during the course of this work. Special thanks to my wife, Javelah, for encouraging me and cheering me on.

List of publications

Journal articles

Akach, J. and Ochieng, A., 2018. Monte Carlo simulation of the light distribution in an annular slurry bubble column photocatalytic reactor. *Chemical Engineering Research and Design, 129,* 248-258.

This journal article is based on chapter 4 of the thesis. John Akach carried out the experiments, wrote the manuscript draft and corresponded with the journal editor.

Akach, J., Kabuba, J. and Ochieng, A., 2020. Simulation of the light distribution in a solar photocatalytic bubble column reactor using the Monte Carlo method. *Industrial & Engineering Chemistry Research, 59*(40), 17708-17719.

This journal article is based on chapter 5 of the thesis. John Akach carried out the experiments, wrote the manuscript draft and corresponded with the journal editor.

Book chapters

Akach, J., Kabuba, J. and Ochieng, A., 2022. Modelling and simulation of photocatalytic reactors for wastewater treatment. In *Photoreactors in Advanced Oxidation Processes: The Future of Wastewater Treatment*, 279 – 306. Wiley (Accepted for publication: In proof)

This book chapter is based on Chapter 2 of the thesis. John Akach wrote the manuscript draft.

Conference Proceedings

Akach, J., Nyembe, N., Ochieng, A., 2018. Numerical simulation of the hydrodynamics in a bubble column reactor: influence of turbulence models, *11th South African Conference on Computational and Applied Mechanics (SACAM 2018),* Vanderbijlpark, South Africa, 17th - 19th September 2018.

This conference proceeding is based on Chapter 3 of the thesis. John Akach carried out the experiments, wrote the manuscript and corresponded with the conference organizers.

Abstract

The use of solar photocatalysis for the treatment of aromatic chemicals like phenol in wastewater has attracted significant attention due to the low cost of sunlight. However, sunlight is unreliable since its intensity fluctuates during the day. This drawback can be addressed by supplementing sunlight with artificial UV lamps when the solar intensity reduces. In this work, such a hybrid solar/UV lamp reactor, internally illuminated by the UV lamp and externally by sunlight, was designed. Phenol was used as the model pollutant and the nanophase Aeroxide P25 TiO_2 was employed as the photocatalyst and fluidized by compressed air. The catalyst and bubble distribution in the reactor was analysed using computational fluid dynamics (CFD) while the Monte Carlo (MC) method was used to model the light distribution and reaction kinetics. Finally, a lamp controller was designed to specify the required UV lamp output as a function of the solar intensity.

The CFD simulation using ANSYS CFX 17 showed that a fairly homogeneous distribution of the catalyst was achieved in the reactor. Consequently, accurate simulations of the light distribution could be achieved without considering the hydrodynamics. The MC models revealed that bubbles did not significantly influence light absorption at the optimum catalyst loading. This showed that air was a good medium for fluidization as it could provide good mixing and oxygen electron acceptor without negatively affecting light absorption. The forward scattering behaviour of the P25 TiO_2 and the increase in light attenuation with catalyst loading was confirmed in this work. The optimum catalyst loading in the different reactor configurations was 0.15 g/L (tubular solar), 0.2 g/L (annular solar), 0.4 g/L (annular UV lamp), and 0.4 g/L (hybrid light). This resulted in experimental reaction rates of 0.337 $mgL^{-1}min^{-1}$ (tubular solar), 0.584 $mgL^{-1}min^{-1}$ (annular UV lamp), and 0.93 $mgL^{-1}min^{-1}$ (hybrid light).

An analysis of the local volumetric rate of energy absorption (LVREA) and reaction rate profiles along the radial coordinate showed a non-uniformity which worsened with an increase in catalyst loading. The reaction order with respect to the volumetric rate of energy absorption (VREA) indicated that solar illumination resulted in a higher electron-hole recombination as compared to UV illumination. This, combined with the higher intensity of the UV lamp, resulted in a higher reaction rate under UV light as compared to sunlight, demonstrating that the UV lamp could be used to supplement sunlight. For a typical sunny day, a lamp controller was designed that could adjust the UV lamp output as a function of the solar intensity to maintain the reaction rate at a reference level while ensuring less energy consumption than an ON/OFF lamp controller. This work demonstrated the feasibility of hybrid solar/UV lamp

photocatalysis reactor which could maintain the advantages of solar photocatalysis while mitigating its drawbacks.

Table of contents

List of Figures

List of Tables

List of abbreviations

Acronyms

2D	two dimensional
3D	three dimensional
AMG	algebraic multigrid solver
CFD	computational fluid dynamics
CPC	compound parabolic concentrator
DAD	diode array detector
EADI	energy absorption distribution index
EEO	electrical energy per order
GHI	global horizontal irradiance
GNI	global normal irradiance
GPS	global positioning system
GTI	global tilt irradiance
HDKR	Hay, Davies, Klucher and Reindl
HPLC	high performance liquid chromatography
KTGF	kinetic theory of granular flow
LDA	laser doppler anemometer
LRR	local reaction rate
LVREA	local volumetric rate of energy absorption
NRMSE	normalized root mean square error
PISO	pressure implicit split operator
QUICK	quadratic upstream interpolation for convective kinematics
RANS	Reynolds-averaged Navier-Stokes
RNG	Re-normalization group
RRDI	reaction rate distribution index
RSD	relative standard deviation
RSM	Reynolds Stress Model
RTE	radiation transport equation
SIMPLE	semi-implicit method for pressure linked equations
TDMA	tri-diagonal matrix algorithm
TiO_2	titanium dioxide
TRR	total refracted radiation

UV	ultraviolet
VREA	volumetric rate of energy absorption

Nomenclature

C_i	interfacial force coefficient
E_i	experimental data points
g_0	radial distribution function
G_0	extra-terrestrial irradiance on a horizontal plane (moles m^{-2} s^{-1})
G_T	global tilt irradiance (moles m^{-2} s^{-1})
G_{be}	horizontal beam irradiance (moles m^{-2} s^{-1})
G_d	horizontal diffuse irradiance (moles m^{-2} s^{-1})
$G_{i,N}$	incident solar irradiance, normal to the reactor (moles m^{-2} s^{-1})
$G_{sc,UV}$	UV solar constant (moles m^{-2} s^{-1})
I_{UV}	percentage lamp output
M_i	model data points
$R_{1\ldots16}$	random number (-)
k_{app}	apparent first order rate constant
$k_{d,N}$	normal diffuse fraction (-)
k_d	horizontal diffuse fraction (-)
k_{int}	intrinsic rate constant
k_t	clearness index (-)
g	Henyey Greenstein phase function asymmetry factor (-)
h	reactor height (m)
k	turbulent kinetic energy (m^2 s^{-2})
Re	Reynolds number
C	substrate concentration
Eo	Eötvös number
G	global horizontal irradiance (moles m^{-2} s^{-1})
I	specific intensity of a ray of light (Einstein m^{-2} s^{-1} sr^{-1})
N	number of data points
P	pressure (Pa)
P_0	average power consumption (kW)
V	reactor volume (m^3)

d	diameter (m)
e	coefficient of restitution
g	acceleration due to gravity (m s^{-2})
l	photon path length (m)
n	number (-)
r	radius/radial location (m)
s	coordinate along direction Ω (m)
t	time
x, y, z	cartesian coordinates (m)
y	distance (m)
$\boldsymbol{F}$	interfacial forces (N)
$\boldsymbol{n}$	unit normal
$\boldsymbol{u}$	velocity (m s^{-1})

Greek

α_i	volume fraction
ε_g	global gas holdup (-)
θ_s	granular temperature (m^2 s^{-2})
ρ_G	ground reflectance (-)
ε	turbulent dissipation rate
Ω, Ω'	solid angle (steradian)
$p(\Omega' \rightarrow \Omega)$	scattering phase function (-)
α	reaction order
β	reactor tilt angle (rad)
γ	dissipation of granular energy (kg m^{-3} s^{-1})
θ	zenith angle (rad)
κ	absorption coefficient (m^{-1})
μ	viscosity (Pa s)
ρ	density (kg m^{-3})
σ	scattering coefficient (m^{-1})
τ	stress tensor
φ	angular location (rad)
ϕ	azimuth angle (rad)

Subscripts

max	maximum
BIT	bubble induced turbulence
D	drag force
D	for day of the year
I	molecular
L	lift force
TD	turbulent dispersion force
UV	related to UV photons
WL	wall lubrication force
b	related to bubble
c	related to catalyst
col	collision
eff	effective
g	gas
k	fluid phase
kin	kinetic
l	liquid
n	for new coordinates
o	for old coordinates
s	associated with solar or sunlight
s	solid
sc	associated with scattering
sol	related to solar photons
t	turbulence
w	related to reactor wall
λ	indicates wavelength dependence

Chapter 1

1 Introduction

1.1 Background

Rapid industrialization has resulted in an increase in the amount and variety of aromatic compounds in wastewater streams. Aromatic chemicals like phenol are toxic to humans and aquatic life and must be removed from wastewater. However, such chemicals are not easily eliminated in conventional wastewater treatment plants due to their biorecalcitrant nature (Ahmed et al., 2010). As a result, a concerted research effort has been targeted towards the development of alternative methods for their removal. In this respect, TiO_2 photocatalysis has emerged as one of the best alternative wastewater treatment methods for aromatic chemicals. In photocatalysis, TiO_2 in aqueous medium is activated by UV light which generates reactive species on the surface of the catalyst. These reactive species then attack and break down the aromatic chemicals into simpler and less toxic chemicals (Gaya and Abdullah, 2008).

Photocatalysis has been widely investigated; however, its commercialisation has been limited. This has been attributed to the high cost of running the ultraviolet (UV) lamps for catalyst activation. One popular way of reducing the high energy cost of photocatalysis has been the utilization of sunlight as the light source (Malato et al., 2009). However, solar energy is unreliable since the solar intensity varies with time of day, season of the year and cloud cover. This drawback can be addressed by employing a hybrid lighting system in which UV lamps are used to supplement sunlight when the solar intensity reduces. The resulting hybrid solar/UV lamp reactor would provide reliable illumination at the lowest cost.

Photocatalysis is normally carried out in specialised reactors which bring together catalysts, pollutants, light and oxygen. One of the best reactors for photocatalysis has been the fluidized bed reactor due to its high mass transfer characteristics and good light utilization (Braham and Harris, 2009). In such a reactor, the gas-liquid-solid hydrodynamics are complicated by turbulence, and this is compounded by the participation of light photons in the reaction. To design, optimise and scale up such a reactor for hybrid light photocatalysis, a rigorous analysis of the hydrodynamics and light distribution needs to be carried out (Boyjoo et al., 2013a). This can be done using computational fluid dynamics (CFD) and Monte Carlo simulation for the analysis of hydrodynamics and light distribution, respectively. In order to ensure the accuracy of the simulation models, validation has to be carried out by comparing simulated and

experimental measurements.

1.2 Purpose of the study

The purpose of this study was to remove aromatic wastes from wastewater using hybrid light photocatalysis. To this end, a hybrid solar/UV lamp fluidized bed reactor was designed and constructed. The gas-liquid-solid hydrodynamics in the reactor was simulated using CFD technique. The light distribution in the reactor under UV lamp, solar and hybrid light illumination was also modelled and validated using Monte Carlo simulation. Finally, the Monte Carlo light distribution model was used to design a lamp controller for adjusting the lamp intensity as a function of the solar intensity.

1.3 Significance of the study

This study attempts to address some of the problems which hinder the commercialisation of photocatalysis such as high energy cost. The high energy cost was addressed using a novel hybrid solar/UV lamp reactor in which the UV light was used to compensate for any reduction in the solar intensity. In order to design and optimise the hybrid light reactor, the hydrodynamics and light distribution in the reactor was modelled using CFD technique and Monte Carlo simulation, respectively. The use of Monte Carlo simulation was particularly novel since this technique has never been used to model a photocatalytic reactor with bubbles or a hybrid solar/UV lamp reactor. This study reports the first explicit validation of the Monte Carlo model in a solar illuminated reactor. Also, for the first time, the Monte Carlo light distribution model was used to design a lamp controller which could be used for hybrid light photocatalysis.

1.4 Problem statement

Aromatic chemicals in wastewater streams are toxic to humans and aquatic life and have to be removed from wastewater before being discharged into water streams. One of the most effective methods of eliminating these biorecalcitrant wastes is photocatalysis. However, conventional photocatalysis is too costly for commercial application due to the high energy requirement of the UV lamps. The high cost of UV light can be reduced by replacing the UV lamps with sunlight. This approach presents another problem since solar energy is unreliable as it fluctuates during the day and with seasons. To address both issues, a hybrid solar/UV lamp illumination system was developed to ensure a regular supply of light at a lower cost. In order

to develop the best possible reactor configuration, the hybrid light system was coupled with a fluidized bed reactor which is known for its high mass transfer properties and good light utilization. To optimise the hybrid light fluidized bed reactor, the hydrodynamics and light distribution was modelled using CFD and Monte Carlo simulation, respectively. Moreover, the Monte Carlo light distribution model was used to design a lamp controller which could be used to adjust the lamp intensity as a function of the solar intensity.

1.5 Objectives

The aim of this work was to design and model a hybrid solar/UV lamp illuminated fluidized bed reactor for the photocatalysis of aromatic wastes.

The specific objectives were to:

a) Analyse the fluidized bed reactor hydrodynamics using CFD technique.
b) Predict the light distribution in a UV lamp and solar illuminated reactor using Monte Carlo simulation.
c) Evaluate the local reaction rate profiles in a hybrid solar/UV lamp illuminated reactor.
d) Design the lamp controller for the hybrid solar/UV lamp illuminated reactor.

1.6 Structure of the thesis

This thesis is divided into eight chapters. Chapter one covers the introduction of the study which includes the background, problem statement and the objectives of the study. A general literature review is contained in chapter two. Chapter three contains the simulation of the reactor hydrodynamics using computational fluid dynamics. Monte Carlo simulation of the light distribution in the reactor under UV lamp illumination alone and solar illumination alone is covered in chapter four and five, respectively. Chapter six contains the simulation of the local reaction rate in the hybrid solar/UV lamp illuminated reactor while chapter seven addresses the design of the lamp controller. Finally, chapter eight covers the conclusion and recommendations.

References

Ahmed, S., Rasul, M.G., Martens, W.N., Brown, R. and Hashib, M.A., 2010. Heterogeneous photocatalytic degradation of phenols in wastewater: A review on current status and developments. *Desalination*, *261*(1–2), 3-18.

Boyjoo, Y., Ang, M. and Pareek, V., 2013a. Some aspects of photocatalytic reactor modeling using computational fluid dynamics. *Chemical Engineering Science*, *101*, 764-784.

Braham, R. J. and Harris, A. T., 2009. Review of major design and scale-up considerations for solar photocatalytic reactors, *Industrial & Engineering Chemistry Research*, *48*(19), 8890-8905.

Gaya, U. I. and Abdullah, A. H., 2008. Heterogeneous photocatalytic degradation of organic contaminants over titanium dioxide: A review of fundamentals, progress and problems, *Journal of Photochemistry and Photobiology C: Photochemistry Reviews*, *9*(1), 1-12.

Malato, S., Fernández-Ibáñez, P., Maldonado, M., Blanco, J. and Gernjak, W., 2009. Decontamination and disinfection of water by solar photocatalysis: Recent overview and trends, *Catalysis Today*, *147*(1), 1-59.

Chapter 2

2 Literature review

2.1 Aromatic wastes

Aromatic compounds are a large group of organic chemicals characterised by the presence of the benzene ring. The benzene ring makes these compounds very stable and therefore persistent in the environment. Many aromatic compounds are also mutagenic and carcinogenic (Cao et al., 2009). Aromatics are found in diverse applications such as textiles, petrochemical industries, household chemicals, and pesticides. One of the most common aromatics is phenol from which most of the other aromatics are derived (Figure 2.1). Phenol is a hygroscopic crystalline solid at room temperature and pressure with a sweet pungent odour. In water, it has a limited solubility of 9.3 g/100 mL of water. It is mainly used to manufacture phenolic resins, epoxy resins, nylons, polyesters and intermediates for a variety of chemicals such as paints, fertilizers, textiles, surfactants and pharmaceuticals (Busca et al., 2008).

Phenol is ubiquitous in industrial wastewater of petrochemical, paint, resin, coal and pesticide industries (Grabowska et al., 2012). Its concentration in wastewater can range from 2.8 mg/L in petrochemical wastewater to 6.8 g/L in highly polluted coal processing wastewaters (Busca et al., 2008). Phenol has been found to be toxic, mutagenic and biorecalcitrant (Ahmed et al., 2010). In humans, phenol can enter the body through the skin, mouth and nose where it irritates the skin, eyes and respiratory tract. Its ingestion can damage the kidneys and livers with a lethal dose of 1 g for humans. In drinking water systems, phenol at low concentrations of 2 µg/L can react with chlorine resulting in the formation of chlorinated phenols which give the water an objectionable smell and taste (Al-Khalid and El-Naas, 2012). In water streams, phenol affects photosynthesis and has been found to be toxic to fish and other aquatic life (Saha et al., 1999). Therefore, the South African Department of Water Affairs has specified a discharge limit of 30 µg/L for phenol into water streams (Department of Water Affairs and Forestry, 1996).

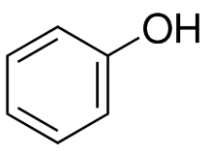

Figure 2.1: Structure of phenol

2.2 Treatment of aromatic wastes

Phenol is toxic to microorganisms; therefore, conventional biological treatment does not effectively remove it from wastewater. As a result, several alternative treatment methods have been investigated for phenol removal such as adsorption, wet air oxidation, and advanced oxidation processes like electrochemical oxidation, ozonation, photo-Fenton and photocatalysis (Busca et al., 2008; Ahmed et al., 2010; Mohammadi et al., 2014; Villegas et al., 2016).

2.2.1 Biological treatment

Some quantity of phenols can be removed by the activated sludge process; however, the process has been found to be very sensitive to fluctuating phenol loads (Mohammadi et al., 2014). Alternative biological treatment methods have been investigated using different types of bacteria, fungi and algae. Some of these species can use phenol as an energy and carbon source resulting in an enzymatic cleavage of the benzene ring (Pradeep et al., 2015). Most studies have used bacteria with fewer studies employing yeasts and algae. Phenol treatment under aerobic conditions has been preferred to anaerobic digestion due to the lower costs and faster growth of the aerobic species. Of the bacterial species which have been investigated for phenol treatment, the most promising has been *Pseudomonas putida* due to its high removal efficiency (Al-Khalid and El-Naas, 2012).

Despite this concerted research on the biological treatment of phenol, several drawbacks persist. Bacterial isolates are very specific on the type of phenol they can metabolize. Consequently, other chemicals including other phenolics, which often co-exist with phenol, have been observed to poison phenol-specific bacterial isolates (Busca et al., 2008). Also, bacteria have a very narrow optimum condition of pH (6 – 8) and temperature (25 – 35°C) and are inhibited by a high concentration of the target substrate (>1200 mg/L). Biological systems typically require a long residence time of several hours, and this increases the reactor size and capital cost of such systems. The use of bacteria also presents several environmental concerns since several of the bacterial species including *Pseudomonas putida*, have been observed to be infectious to fish (Al-Khalid and El-Naas, 2012). Moreover, aerobic systems result in a considerable sludge build up with associated disposal costs. These numerous challenges make biological treatment currently unfeasible for real phenolic industrial wastewater.

2.2.2 Adsorption

Adsorption has been used to remove phenol from wastewater due to its simplicity and low cost, especially with the inclusion of adsorbent regeneration (Issabayeva et al., 2017). Adsorbents can be classified as carbonaceous adsorbents such as commercial activated carbons and those derived from agricultural and industrial wastes; polymers and their modifications; and clays and their modifications (Issabayeva et al., 2017). Generally, the highest adsorption capacity (1000 mg/g) has been found in polymer-based adsorbents (Issabayeva et al., 2017). These adsorbents are also desirable due to their ease of regeneration which involves washing with low concentration of simple chemicals such as sodium hydroxide or methanol (Busca et al., 2008). Activated carbons exhibited an intermediate adsorption capacity (350 mg/g). However, carbonaceous adsorbents form very strong bonds with the substrates which require harsh chemicals or high temperature for regeneration. Thermal regeneration, in particular, destroys the structure of the adsorbent and contributes to air pollution (Busca et al., 2008). The lowest adsorption capacity was observed in natural clays (35 mg/g). Nevertheless, functionalization of the clays using surfactants significantly increased their adsorption capacity (333 mg/g) (Nafees and Waseem, 2014; Issabayeva et al., 2017). Adsorbents from wastes and clays are particularly attractive for use in developing nations due to their relatively low cost and the availability of raw materials (Lin and Juang, 2009). The major drawback of the adsorption of phenolics is the fact that this treatment method merely transfers the pollutant to another phase. Even after regeneration, the washed-off phenolics will have to be treated further. Moreover, adsorbents get spent after several cycles of reuse, and their disposal poses a very serious environmental challenge (Busca et al., 2008; Mohammadi et al., 2014).

2.2.3 Advanced oxidation techniques

To destroy phenol in short duration, advanced oxidation processes (AOPs) have been employed. These techniques rely on in-situ generation and the use of reactive species (H_2O_2, $O_2^{\bullet -}$, $^{\bullet}OH, O_3$) to destroy organic pollutants. AOPs include sonochemical degradation, electrochemical oxidation, ozonation, photo-Fenton and photocatalysis.

Sonochemical degradation

In the sonochemical process, the wastewater is subjected to high energy ultrasound. This creates cavitation bubbles or voids in the water in which water vapour and pollutants diffuse from the liquid. As the voids implode, a localized hotspot of high temperature (5000 K) and pressure (60 MPa) is created in which water and the pollutants are pyrolyzed (Oturan and Aaron, 2014). The pyrolysis disintegrates water into hydroxyl radicals which then react with

the pollutants within the bulk of the liquid (Kidak and Ince, 2006). The best conditions for phenol degradation is under high frequency (> 400 kHz) and low pH. Phenol degradation by sonochemical pyrolysis has been observed to be generally low. This has been attributed to the low volatility and hydrophobicity of phenol which reduces its diffusion into the cavitation bubble where it could be directly pyrolyzed. Instead, phenol is mainly degraded in the bulk liquid by means of the hydroxyl radicals (Chowdhury and Viraraghavan, 2009). The major disadvantage of sonochemical degradation is the high capital and operating cost of sonicators (Gogate, 2008; Miklos et al., 2018).

Ozonation

Ozone is a powerful oxidant which is effective in degrading several organic compounds (Liotta et al., 2009). It is generated from air or oxygen via electrical discharge. In the ozonation method, ozone gas is bubbled through the wastewater whereby it dissolves in the wastewater. This is a crucial step since ozonation is a liquid phase reaction (Wu et al., 2019). The rate of ozone gas-liquid transfer has been increased by two devices: turbulent injector and microbubble generator. The former method employs a venturi-type ejector in which ozone-laden gas is aspirated into a flowing wastewater stream at the venturi throat. This highly turbulent gas-liquid mixing at the venturi results in intimate contact and a high mass transfer (Chedeville et al., 2007). The alternative method involves the use of hydrodynamic cavitation or an air distributor with very small pores to generate ozone microbubbles. The high gas pressure inside the microbubbles results in a faster dissolution of ozone in the wastewater (Shangguan et al., 2018; Wu et al., 2019).

In water, ozone molecules self-decompose into oxygen. This process generates hydroxyl radicals in alkaline conditions (eq. 2.1) (Shangguan et al., 2018). The pollutants can then be directly attacked by ozone (eq. 2.2) or the hydroxyl radicals generated when ozone decomposes (eq. 2.3) (Charinpanitkul et al., 2010). The mechanism of ozone degradation depends on the solution pH. For example, phenol ionizes in alkaline media and the anion is more susceptible to direct attack by ozone. Therefore, phenol is degraded predominantly by direct attack of ozone which increases with an increase in pH (Wu et al., 2019). Direct attack by ozone opens the benzene ring and degrades the intermediate compounds to simpler organics such as carboxylic acids and aldehydes. However, the simpler organics are not susceptible to direct ozone attack which prevents complete mineralization of phenol by ozonation (Shangguan et al., 2018).

$$3O_3 + OH^- + H^+ \rightarrow 2\,^{\bullet}OH + 4O_2 \quad (2.1)$$

$$R - H + O_3 \rightarrow \text{Degradation products} \quad (2.2)$$

$$R - H + {}^{\bullet}OH \rightarrow \text{Degradation products} \quad (2.3)$$

Generally, ozone reacts slowly with aromatic compounds and is not able to mineralize them (Liotta et al., 2009). Moreover, ozone is costly to generate and it suffers from low solubility in water, especially at low concentrations in the gas phase (Mohammadi et al., 2014). Ozone solubility in water depends on the concentration of ozone in the gas since the ozone competes with the other gases for equilibrium solubility. This reduces the gas-liquid mass transfer and the amount of ozone in the liquid phase which is available for reaction.

Fenton/photo-Fenton

The Fenton reagent (H_2O_2 and Fe^{2+}) generates hydroxyl radicals and Fe^{3+} by the reaction between H_2O_2 and Fe^{2+} (eq. 2.4). The hydroxyl radicals can then attack and degrade pollutants such as phenol in solution. The Fenton reaction is normally carried out in acidic medium (pH 2.8 – 3), to prevent iron precipitation (Miklos et al., 2018). In the presence of excess peroxide, Fe^{3+} reacts with H_2O_2 to form Fe^{2+} (eq. 2.5 – 2.6). This regeneration of Fe^{2+} means that just a little of this ion is required and Fe^{2+}/ Fe^{3+} acts as a catalyst. The Fenton reaction has been observed to be much faster than the regeneration reaction. This can slow down the Fenton reaction due to inadequate Fe^{2+} ions. The regeneration process can be accelerated by UV irradiation in the photo-Fenton reaction in which Fe^{3+} are converted to Fe^{2+} with the generation of more hydroxyl radicals (eq. 2.7). To reduce costs associated with artificial light, the use of sunlight in the solar photo-Fenton process has been proposed with good results (Oturan and Aaron 2014). The Fenton process is highly reactive (Mohammadi et al., 2014) and has generally been observed to exhibit lower treatment costs as compared to other advanced oxidation processes (Durán et al., 2018b). However, the process suffers from high chemical costs related to acidification before the reaction and post-reaction neutralization as well as the need for a high quantity of hydrogen peroxide (Oturan and Aaron 2014).

$$Fe^{2+} + H_2O_2 \rightarrow Fe^{3+} + {}^{\bullet}OH + OH^- \quad (2.4)$$

$$Fe^{3+} + H_2O_2 \rightarrow Fe^{2+} + HO_2^{\bullet} + H^+ \quad (2.5)$$

$$Fe^{3+} + HO_2^{\bullet} \rightarrow Fe^{2+} + O_2 + H^+ \quad (2.6)$$

$$Fe^{3+} + H_2O \xrightarrow{hv} Fe^{2+} + {}^{\bullet}OH + H^+ \quad (2.7)$$

Photocatalysis

Photocatalysis is based on the use of a heterogenous semiconductor catalyst to degrade pollutants in the presence of light. The catalyst structure comprises of a filled valance band and an empty conduction band separated by a band gap (Figure 2.2). When the semiconductor is irradiated with light whose wavelength exceeds the band gap energy, electrons from the valence band move to the conduction band, leaving holes in the valence band. These electron-hole pairs can recombine or successfully migrate to the semiconductor surface where the electron is trapped by dissolved oxygen (eq. 2.8). The hole then reacts with water to form hydroxyl radicals (eq. 2.9). These radicals (eq. 2.10) together with the holes (eq. 2.11) attack the organic substrates, breaking them down into simpler molecules (Gaya and Abdullah, 2008). Oxidation by hydroxyl radicals is the main pathway of organic substrate breakdown by photocatalysis.

$$(O_2)_{ads} + e^- \rightarrow O_2^{\bullet -} \quad (2.8)$$

$$h^+ + H_2O \rightarrow {}^{\bullet}OH + H^+ \quad (2.9)$$

$$R - H + {}^{\bullet}OH \rightarrow R'^{\bullet} + H_2O \quad (2.10)$$

$$R + h^+ \rightarrow R^{+\bullet} \rightarrow \text{Degradation products} \quad (2.11)$$

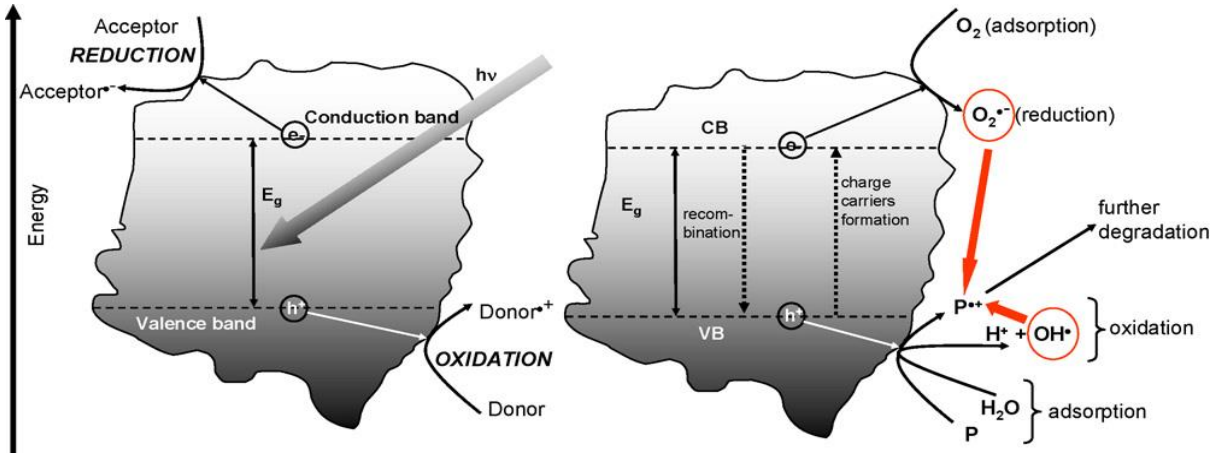

Figure 2.2: Process of photocatalysis (Malato et al., 2009)

Among the advanced oxidation processes, photocatalysis has emerged as one of the most promising methods of treating phenol (Ahmed et al., 2010). This is due to its relatively low cost, non-toxicity and its ability to degrade pollutants instead of merely transferring them to another phase (Malato et al., 2009). The process is also non-selective and proceeds under mild conditions of ambient temperature and pressure. Despite its success, several challenges have

limited the commercialization of photocatalysis. These include lack of reactive photocatalysts, low cost and reliable light sources, efficient reactors and tools for reactor design and scale up.

2.3 Photocatalysts

A high number of catalysts have been synthesized for application in photocatalysis. These include TiO_2 (Pelaez et al., 2012), ZnO (Pirhashemi et al., 2018), ZnS (Lee and Wu, 2017), CdS (Ayodhya and Veerabhadram, 2018), SnO_2 (Al-Hamdi et al., 2017), Ag_3PO_4 (Chen et al., 2015) and Bi-based catalysts ($BiVO_4$, Bi_2MoO_6, BiOCl) (Xu et al., 2020). The band gap of several catalysts is listed in **Table 2.1**. A good catalyst should possess a multiplicity of good properties for it to perform effectively in a wide range of different wastewaters. Several of these catalysts have serious drawbacks in respect to their application for photocatalysis. For example, ZnS, ZnO, CdS and Ag_3PO_4 undergo photo-corrosion in which their structure breaks down under light irradiation (Chen et al., 2015; Lee and Wu, 2017; Ayodhya and Veerabhadram, 2018; Pirhashemi et al., 2018). Additionally, ZnO dissolves in acidic and basic media. In this respect, TiO_2 has emerged as the most popular photocatalyst due to its balanced properties of high reactivity, chemical resistance, resistance to photo-corrosion, non-toxicity, commercial availability and low cost.

Table 2.1: Band gaps of different catalysts (Chen et al., 2015; Al-Hamdi et al., 2017; Lee and Wu, 2017; Sharma et al., 2019; Xu et al., 2020)

Catalyst	Band gap (eV)	Catalyst	Band gap (eV)
ZnS	3.7	WO_3	2.7
SnO_2	3.6	Bi_2MoO_6	2.6
$SrTiO_3$	3.4	Ag_3PO_4	2.4
BiOCl	3.2	$BiVO_4$	2.4
TiO_2	3.2	CdS	2.4
ZnO	3.2	CdSe	1.7

The semiconductor TiO_2 exists in three polymorphs: anatase, rutile and brookite with anatase being the most photocatalytically active. Several commercial TiO_2 brands are available with different compositions, sizes and surface areas (**Table 2.2**). Among these, Aeroxide P25 TiO_2 has been observed to be the most reactive (Dimitrakopoulou et al., 2012). This has been attributed to its composition of 80% anatase and 20% rutile which affords it a superior electron-hole separation as the rutile phase acts as a sink for electrons from the anatase phase (Pelaez et al., 2012). Therefore, Aeroxide P25 TiO_2 has essentially become the standard photocatalyst against which the performance of other catalysts is usually compared (Malato et al., 2009).

Despite its remarkable advantages, TiO_2 has its share of drawbacks: it has a large bandgap, low surface area and experiences a high electron-hole recombination. The large band gap of 3.2 eV means that TiO_2 can only be activated by UV light. This limits its use under less expensive light sources such as sunlight whose spectrum consists of 5% UV light and 46% visible light. The low surface area of TiO_2 (50 m^2/g) limits the rate of substrate adsorption which in turn slows down the rate of photocatalysis. High electron-hole recombination reduces the number of useful radicals generated by the catalyst per absorbed photon, and this decreases its quantum efficiency (Pelaez et al., 2012).

Table 2.2: Characteristics of several commercial TiO_2 catalysts (Dimitrakopoulou et al., 2012)

TiO_2 catalyst	Crystal form	BET surface area (m^2/g)	Particle size (nm)
Aeroxide P25	80% Anatase, 20% Rutile	50	21
Hombikat UV100	>99% Anatase	>250	5
Millennium PC100	>95% Anatase	80-100	15-25
Aldrich Anatase AA	>99% Anatase	190-290	15
Tronox AK1	>97% Anatase	90	20

A lot of research has been targeted towards improving the properties of TiO_2. One strategy that has been successfully employed is doping with noble metals, transition metals and non-metals. Doping with noble metals such as Au, Pd, Pt and Ag deposits small quantities of these metals on the surface of TiO_2. These deposits act as an electron trap which improves electron-hole separation (Rahimi et al., 2016). However, noble metals are costly and their use in doping considerably increases the cost of the catalyst (Chong et al., 2010). Doping with transition metals such as Fe, Co, Mn, W, Ni, Mo, V, Cr and Cu has also been carried out. These metals create impurity energy levels between the valence and conduction bands thus narrowing the catalyst band gap and affording visible light activity to the doped TiO_2 (Pelaez et al., 2012). Transition metal dopant sites has been observed to be a location for significant electron-hole recombination which decreases catalyst activity, possibly wiping the gains from a narrowed band gap. They have also been charged with blocking active sites on the surface of TiO_2 (Teh and Mohamed, 2011). Recently, non-metal doping has also been carried out using N, C, S and F. Some of these non-metals such as N can replace O in the TiO_2 lattice resulting in a narrowed band gap (Pelaez et al., 2012). Non-metal doping also inhibits anatase-rutile phase transformation at high temperature resulting in a smaller anatase crystal size and an increase in the TiO_2 surface area (Khaki et al., 2017). Unlike metals, non-metal dopant sites are less likely to be charge recombination sites (Rahimi et al., 2016). However, achieving the required amount of non-metal dopant into the TiO_2 crystal lattice has been a challenge due to the breakdown of the non-metal dopants during the annealing process (Teh and Mohamed, 2011).

A large majority of synthesized catalysts have been nano-sized, and this small size has been preferred due to their large surface area and high reaction rates. However, nano-catalysts suffer from several drawbacks such as increased agglomeration, reduced light transmission and challenging separation from wastewater (Chong et al., 2010; Shan et al., 2010). Inadequate post-separation of the catalyst result in catalyst loss and introduction of nanoparticles into receiving waters with potentially dangerous effects on aquatic life (Chong et al., 2010). To separate nano-catalysts from wastewater, various strategies have been used. These include rapid sedimentation by adjusting the solution pH to the zero point charge of the catalyst in order to induce spontaneous agglomeration (Malato et al., 2009). After sedimentation, the remaining suspended catalysts have been successfully removed by microfiltration (Chong et al., 2010). Membrane reactors have also been devised in which catalyst filtration is accomplished by a membrane in a continuous flow system (Molinari et al., 2017; Mozia, 2010). These separation techniques increase the cost of separation since they require long settling time with costly coagulants, filters and sedimentation tanks.

In order to reduce the cost of catalyst separation, various techniques have been investigated. One method has involved the immobilization of the catalyst on the reactor surface (Lin et al., 2012; Saran et al., 2016; Jafarikojour et al., 2018). This technique has also been applied in membrane reactors in which the catalyst is fixed on the surface of the filtration modules (Mozia, 2010). Catalyst particles have also been immobilized on inert supports such as glass, activated carbon, silica and polymers which are then fluidized in the reactor (Shan et al., 2010; Singh et al., 2013). Good supports should exhibit a strong bond with the catalyst, resist photodegradation and promote adsorption of the substrate (Singh et al., 2013). Immobilization on adsorbents is especially advantageous since the adsorbent would concentrate the substrate near the catalyst while the catalyst regenerates the adsorbent (Zhang et al., 2009). Catalysts have been supported on several adsorbents such as activated carbon, clays, zeolites and graphene-based materials (Yahya et al., 2018). Recently, immobilization on floating supports has also been advanced to increase light utilization and oxygen mass transfer (Nasir et al., 2020). Immobilized catalysts facilitate easy separation from the wastewater after the reaction. However, their larger size decreases their surface area resulting in a decreased reaction rate (Shan et al., 2010). An alternative strategy has been the introduction of nano-sized magnets into the catalyst matrix to form nano-composites (Gómez-Pastora et al., 2017). This results in a catalyst with a relatively high reactivity which can be easily separated from the wastewater using magnets.

2.4 Light sources

2.4.1 Mercury lamps

Traditionally, photocatalysis has been carried out using nanophase TiO_2 illuminated by mercury ultraviolet (UV) lamps. This is due to the fact that most commercial TiO_2 catalysts have a large band gap of about 3.0 eV and can only be activated by UV light. The most popular UV lamp for lab scale installations has been the low pressure black light and germicidal lamps (Apollo and Aoyi, 2016). These lamps are made of a small quantity of mercury and inert gas (argon) sealed in a glass envelope under low pressure (1 Pa). Filaments at both ends of the lamp are heated by an electric voltage which generates free electrons. As these electrons flow through the inert gas, they interact with mercury atoms generating UV photons with a wavelength of 254 nm. In germicidal lamps, the UV photons escape the lamp plasma through the fused quartz glass envelope as short-wave UVC light with a peak at 254 nm (Figure 2.3a) (Duran et al., 2010). Black light lamps, on the other hand, have a phosphor coating on the glass envelope which interacts with the UV photons generating long-wave UVA light with a peak at 365 nm (Figure 2.3c). Studies comparing the rate of photocatalysis under germicidal and blacklight lamps have shown that, in the presence of photolysis, a higher reaction rate was observed under germicidal lamp illumination (Joseph et al., 2016). However, in the absence of photolysis, blacklight illumination resulted in a higher reaction rate (Haranaka-Funai et al., 2017).

Low pressure lamps have a low wall temperature of 30 – 50 °C and a UVC efficiency of 30 – 40 % for a power input of 5 – 80 W (Schalk et al., 2005). In larger reactors, several low-pressure lamps are usually employed in order to increase the light output. When more power is required from a single lamp, medium pressure lamps are usually employed. These can have power ratings of 400 – 60,000 W. Medium pressure lamps have a high gas pressure (100 kPa) and high power input and they emit polychromatic light with several peaks between 200 and 400 nm (Figure 2.3a). These lamps maintain a very high wall temperature of 500 – 950 °C (Schalk et al., 2005). Therefore, a coolant liquid is usually circulated between the lamp sleeve and the wastewater in the reactors where they are employed (Al-Rasheed and Cardin, 2003). Furthermore, the lamps have a lower UVC efficiency (5 – 15%) and a shorter lifetime (< 5000 h) as compared to low pressure lamps (Schalk et al., 2005). The low-pressure lamps are cheaper, more efficient, long-lasting and require a simpler installation as compared to medium pressure variants. Nevertheless, all mercury lamps have disadvantages of fragility, mercury

toxicity and challenges in lamp disposal, long warm up time, unstable light output, high voltage requirement and relatively shorter lifetime (Natarajan et al., 2011).

2.4.2 Light emitting diodes (LEDs)

Recently, light emitting diodes (LEDs) have been applied for photocatalysis. These are *p*-*n* junction semiconductors which emit light when sufficient voltage is applied across the *p*-*n* junction. The voltage induces the movement of electrons from the *n*-type semiconductor to the *p*-type semiconductor where the electrons combine with positive charges. This lowers the energy level which results in the emission of the excess energy as light. The wavelength of the emitted light depends on the semiconductor material (Figure 2.3b) (Jo and Tayade, 2014). Gallium nitride (GaN) is used for UVA (365 nm) LEDs while longer wavelengths are achieved using indium gallium nitride (InGaN). The UVB and UVC wavelengths (< 365 nm) require materials made of aluminium indium gallium nitride (AlInGaN) and aluminium nitride (AlN) (Matafonova and Batoev, 2018).

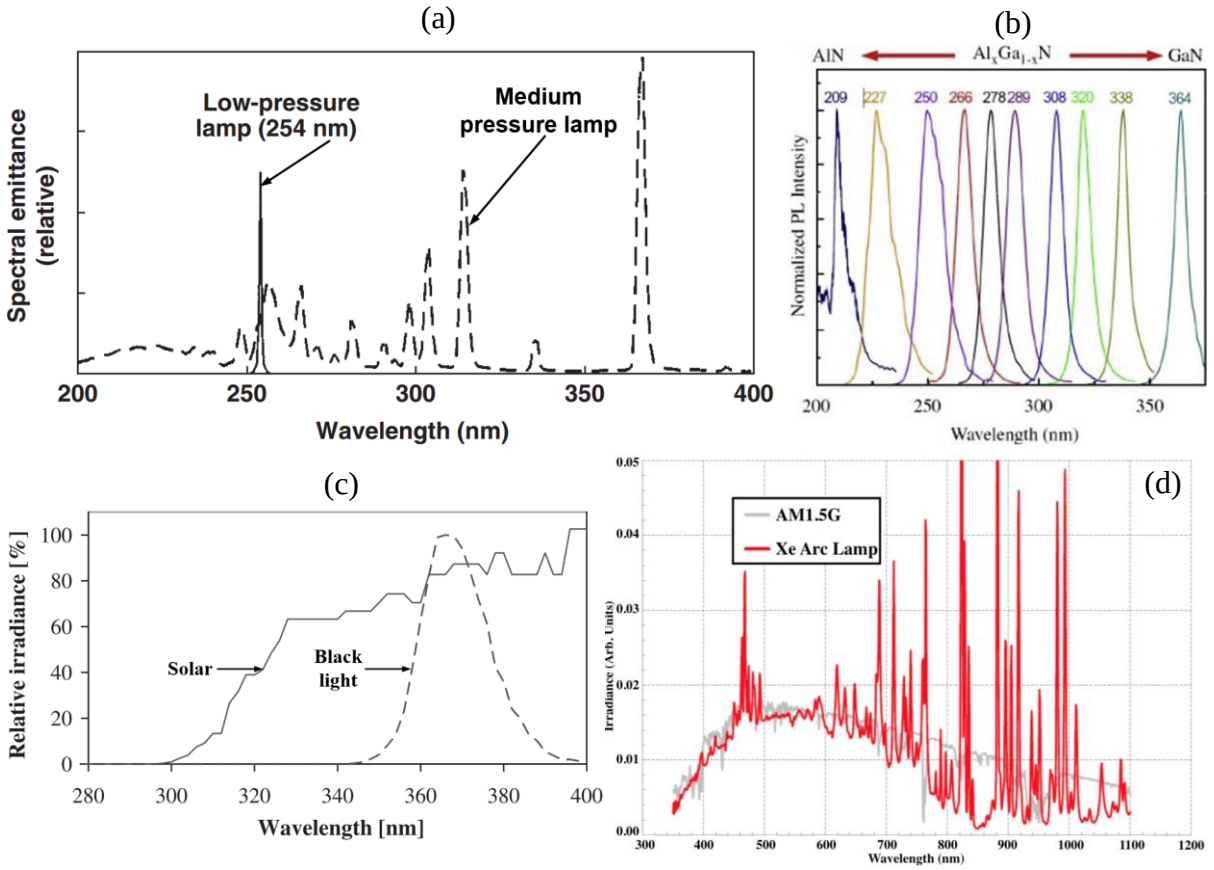

Figure 2.3: Spectra of different light sources: (a) Low and medium pressure lamps (Cutler and Zimmerman, 2011); (b) LEDs (Matafonova and Batoev, 2018); (c) Solar and black light UV lamp (Baransi et al., 2012); (d) solar and xenon arc lamp (Schembri, 2017).

Generally, LEDs have several advantages as photocatalysis light source. They are inherently safe since they do not contain mercury or gases under pressure. LEDs emit light at specific wavelengths, and this can be used to improve light utilization by selecting a combination of LEDs which match the absorption spectrum of the substrates/catalysts (Khademalrasool et al., 2016). The LED modules can be manufactured with a narrow directivity angle which is especially desirable for real wastewater applications as the light can penetrate the turbid wastewater more efficiently (Matafonova and Batoev, 2018). However, this results in a high light intensity in a single direction which has been observed to decrease the photonic efficiency. In comparative tests, low pressure lamps with their diffuse light output have demonstrated a higher photonic efficiency (Davididou et al., 2018). LEDs can be immediately turned on, a property which enables them to be illuminated periodically. This type of illumination has been observed to decrease electron-hole recombination, increase photonic efficiency, increase reaction rate and decrease the electrical energy per order (EEO) (Liang et al., 2017). UVA LEDs have been observed to be more energy efficient as compared to mercury UV lamps. For example, Dominguez et al. (2016) observed more than 12-fold reduction in the EEO while using LEDs as compared to a medium pressure mercury lamp. These LEDs also last longer (26,000 h) as compared to mercury lamps (12,000 h). They can be powered by low voltage (< 30 V_{DC}) from batteries or solar cells which enables them to be used in off-grid locations (Eskandarian et al., 2016).

The small size of LEDs also allows flexibility in application. They can be positioned outside the reactor and oriented such that they only illuminate the reactor. In this application, the unidirectional LED illumination has an advantage over mercury lamps which illuminate all directions resulting in photon loss (Tapia-Tlatelpa et al., 2020). The LEDs can also be installed inside the reactor and protected from the wastewater by a lamp sleeve (Dominguez et al., 2016). In this set up, the LED modules are usually distributed around a cylindrical support in order to approximate the emission from a low-pressure lamp. A novel application, which is only possible with LEDs, employed wirelessly powered autonomous LEDs which are fluidized in the reactor by the wastewater (Kuipers et al., 2015). Both external and internal LED illumination suffer from non-uniform illumination at the illuminated wall. It is often necessary to position the LEDs further away from the wall in order to achieve the kind of uniform wall illumination observed in mercury lamps (Khademalrasool et al., 2016). This requirement unnecessarily increases the reactor size.

The considerable research and development in LEDs has considerably increased their light

output and reduced their prices. This is especially true of visible LEDs which are now competitive with fluorescent lamps. However, their UV counterparts still suffer from low wall power efficiencies (< 21%) and higher prices (Matafonova and Batoev, 2018). High power LEDs which would be necessary to replace low pressure mercury lamps emit a lot of heat. Since the light output of LEDs decrease at high temperatures, they require active cooling to function properly (Khademalrasool et al., 2016). Moreover, commercial UV LED modules are still sold as discrete units which have to be assembled into useful arrays. The high capital cost of LEDs, cooling and assembly has been a barrier to widespread application of LEDs in photocatalysis.

2.4.3 Sunlight

The most significant cost of photocatalysis has been attributed to the electricity for running the lamps. In order to reduce these costs, sunlight has been proposed as an alternative source of light for photocatalysis (Malato et al., 2009). This is due to the fact that solar energy is free, renewable and about 5% of its spectrum consists of UV light which can activate TiO_2 catalyst (Figure 2.3c) (Malato et al., 2009). Several experimental studies have demonstrated that sunlight is competitive with artificial light in terms of photocatalytic kinetics and energy consumption. Kuo et al. (2008) found that the rate of photocatalysis under sunlight was similar to the rate under a similar intensity of UVC light. Under comparable conditions of absorbed light intensity, the rate of photocatalysis under sunlight has been observed to be higher than that under black light illumination (Sousa et al., 2013). The total capital and operational cost of photocatalysis has been demonstrated to be similar under solar and black light illumination (Haranaka-Funai et al., 2017). However, when electricity consumption was considered separately, Ljubas et al. (2015) reported more than a 60-fold increase in the cost of photocatalysis under lamp illumination as compared to solar illumination.

Despite these advantages, solar energy is unreliable since its intensity varies with time of day, cloud cover and season of the year and it is virtually unavailable at night (Natarajan et al., 2011). This has been found to significantly affect the rate of photocatalysis throughout the day (Portela et al., 2012; Ljubas et al., 2015). From an experimental point of view, the fluctuating solar intensity has presented a considerable challenge in kinetic studies. Some researchers have addressed this by employing the absorbed energy, instead of the time, in kinetic studies (Pereira et al., 2011). Others have used simulated sunlight from artificial light sources with a spectrum similar to that of the sun. These light sources include metal halide lamps (Shin et al., 2013), Osram Ultra Vitalux light bulb (Ljubas et al., 2015) and xenon lamps (Romero et al., 2014;

Ghosh et al., 2018). Xenon lamps have a spectrum that is very similar to that of sunlight (Figure 2.3d) and has been the basis of standardized full spectrum solar simulators such as the solarbox by CO.FO.ME.GRA (Romero et al., 2014) and SS1KW by Sciencetech (Ghosh et al., 2018). Studies comparing the rate of photocatalysis under natural and simulated solar have shown significant differences. These have been attributed to differences in the UV spectrum (Romero et al., 2014) and reactor geometry (Pereira et al., 2011) in the two setups. Despite these differences, solar simulators are still useful in establishing the effect of parameters that do not depend on light intensity such as catalyst type, substrate, pH and wastewater matrix on the rate of solar photocatalysis. They have also been used to investigate the toxicity of degradation products as well as to evaluate degradation pathways (Pereira et al., 2011; Ghosh et al., 2018).

From an industrial standpoint, the fluctuating solar intensity may prevent the wastewater treatment plant from achieving the discharge limit. This could potentially be addressed by adjusting the residence time of the wastewater in the reactor as a function of the solar intensity. However, this approach requires surge tanks to hold the wastewater during periods of increased residence time. An alternative approach would be to supplement sunlight with artificial light during periods of low solar intensity (Portela et al., 2012; Monteiro et al., 2015). This would result in a constant photocatalysis reaction rate and ensure that the plant achieves the discharge limit at a fixed residence time and wastewater flow rate.

2.4.4 Hybrid light

Several hybrid light systems have been reported in gas-phase reactors using black light lamps as the artificial light source (Portela et al., 2011; Portela et al., 2012; Monteiro et al., 2015). The first attempt at hybrid light operation was carried out by Portela et al. (2011) in which H_2S was photodegraded by sunlight during the day and UVA lamps at night. In a later article, they demonstrated a pilot scale solar/lamp reactor in which the UV lamp would be switched on when solar UV dropped below 20 W/m^2 (Portela et al., 2012). A few years later, Monteiro et al. (2015) investigated the feasibility of using sunlight during the day and UVA lamp at night for the photocatalysis of gas-phase *n*-decane. All these previous studies were carried out in gas phase reactors.

A few reactors with both artificial and solar illumination have been reported for wastewater treatment. Orozco et al. (2009) designed a hybrid light reactor made of an acrylic box which was internally irradiated by 6 black light lamps and illuminated by sunlight through a transparent glass at the top of the reactor. Chekir et al. (2017) reported a system in which one

reactor, illuminated by a blacklight (UVA) lamp, was connected in series to another reactor which was illuminated by sunlight. Durán et al. (2018a) designed a reactor with partially submerged rotating drum made of transparent quartz coated with a catalyst. The drum was internally irradiated by UVC lamps and externally illuminated by sunlight. The reactors by Chekir et al. (2017) and Durán et al. (2018a) employed supported catalysts which were fixed on the walls of the reactor. The aim of these studies was to increase the reaction rate by combining the two illumination sources, not to replace sunlight with UV light during low solar intensity. In fact, in the hybrid system by Chekir et al. (2017), the rate of reaction under UV light was 10 times lower than that under solar illumination. As a result, the UV light could not effectively replace the sunlight at night.

The choice of artificial light for hybrid light photocatalysis is important as this has a significant influence on the degradation mechanism. Catalyst and substrate light absorption depend strongly on the light spectrum (Li Puma et al., 2010; Joseph et al., 2016). Therefore, different light sources might yield radically different reaction mechanisms. For example, germicidal lamps degrade phenol via photolysis while sunlight requires photocatalysis in order to achieve a similar photodegradation. Photolysis and photocatalysis might even result in different degradation products with different toxicity. Such an outcome should be minimized as much as possible. This can be achieved by using an artificial light which matches the solar spectrum. Xenon lamps, which match the full spectrum of sunlight would be ideal. However, they are seldom used for this purpose due to their high cost, high voltage requirements and large sizes which necessitates external illumination (Ghosh et al., 2018). Moreover, full spectrum lamps emit a lot of light in the visible and infra-red spectrum which cannot activate the catalyst. This significantly reduces their efficiencies and increases their heat output. In practice, hybrid light systems have employed black light lamps as the artificial light source (Portela et al., 2011; Portela et al., 2012; Monteiro et al., 2015). Although their spectrum does not match the full solar spectrum, it lies within the solar UV spectrum (Figure 2.3c). Moreover, the black light low pressure lamp has other advantages such as low cost, high efficiency, small package and low heat output.

2.5 Photocatalytic reactors

Photocatalytic reactors bring together catalysts, substrates and photons. A wide variety of reactors have been proposed for photocatalysis. These can generally be categorized into thin film plate reactors, rotating disk reactors, photocatalytic membrane reactors, tubular slurry reactors and fluidized bed reactors.

2.5.1 Thin film plate reactors

In these reactors, wastewater flows over a catalyst that is supported onto a surface. This forms a thin film of wastewater over the catalyst which ensures a high mass transfer of species between the two phases (Braham and Harris, 2009). Several configurations of this type of reactor have been proposed with various surface areas and flow regimes. The classic inclined plate reactor (Figure 2.4a) is a flat plate, inclined at a certain angle, over which wastewater flows in a laminar flow regime (Saran et al., 2016). In a corrugated plate reactor, the catalyst is immobilized onto corrugated surfaces (Jiao et al., 2019). This increases the surface area of the catalyst and also improves photon utilization since scattered light can be absorbed on the sides of the grooves (Donaldson and Zhang, 2012). The step reactor (Figure 2.4b) consists of several steps on which wastewater flows (Stephan and Dominique, 2011). This results in a waterfall effect which creates turbulent flow and an increase in the mass transfer of air into the wastewater (Zeghioud et al., 2016).

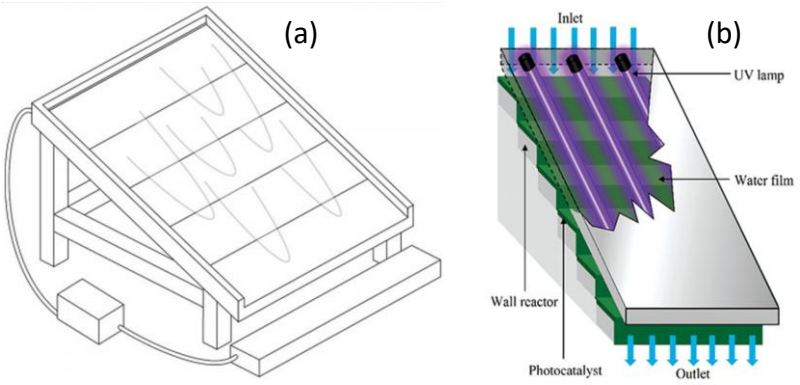

Figure 2.4: (a) Inclined plate reactor (Braham and Harris, 2009); (b) step reactor (Zeghioud et al., 2016)

The various types of the inclined plate reactors can be illuminated by either artificial light or sunlight (Senthilnathan and Philip, 2012). They can also be covered or exposed to the atmosphere. Covering the reactor prevents evaporation of volatile organics and shields the reactor from environmental contamination. However, the cover increases the reactor cost and decreases light penetration. The major advantage of inclined plate reactors is their lower capital and operation costs due to their use of supported catalysts which do not need downstream separation. However, maintaining a thin film in the reactors requires low flow rates, and this significantly reduces the quantity of wastewater that can be treated in such reactors (Braham and Harris, 2009).

2.5.2 Rotating disk/drum reactor.

In the rotating disk reactor, also referred to as the spinning disk reactor, a vertically oriented disk coated with supported catalyst is partially submerged in wastewater. The side of the disk above the wastewater is exposed to artificial light or sunlight (Figure 2.5a). As the disk rotates, it mixes the wastewater and a thin film of the wastewater is retained on the surface of the disk above the wastewater where photocatalysis takes place (Zhang et al., 2011). In some applications, the surface area of the disk has been increased through corrugation (Li et al., 2015). The rotating disk reactor can also be oriented horizontally (Figure 2.5b). In this orientation, wastewater from below the disk surface is pumped to the centre of a spinning disk from where it spreads across the disk surface by the action of centrifugal forces (Boiarkina et al., 2013). A variation of this is the impinging stream reactor in which wastewater falls on the rotating disk from above (Jafarikojour et al., 2018). The horizontal disk reactor experiences a desirable turbulent flow regime on the surface of the disk as well as total illumination of the disk as compared to the vertically oriented disk reactor (Braham and Harris, 2009). Rotating disk reactors can be scaled up by increasing the diameter (Van Gerven et al., 2007) or the number of the disks (Lin et al., 2012).

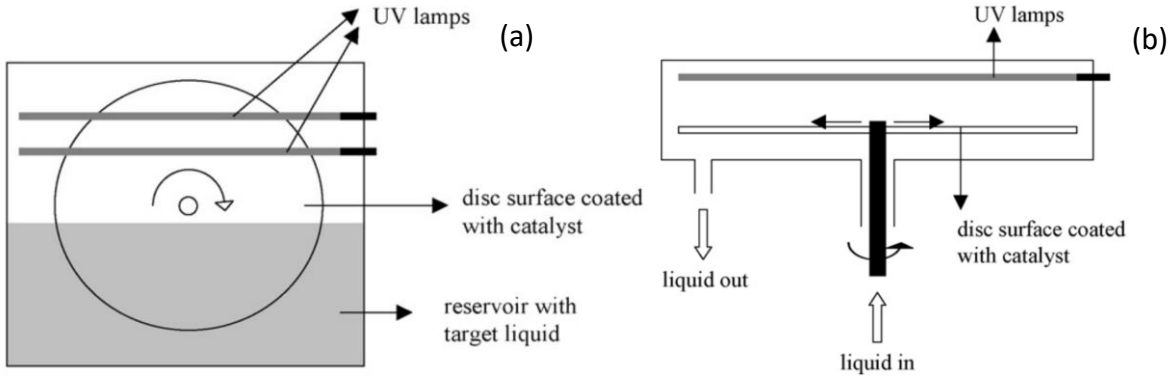

Figure 2.5: (a)Vertical rotating disk reactor; (b) Horizontal rotating disk reactor (Van Gerven et al., 2007)

In a rotating drum reactor, the catalyst is supported on the cylindrical surface of a partially submerged drum. These reactors can be externally illuminated by sunlight or by lamps located above the reactors. Internal illumination with UVC lamps has also been reported using a transparent quartz drum (Durán et al., 2018a). The surface area of the rotating drum has been increased using corrugations and fins (Ho et al., 2010). All rotating disk/drum reactors experience high mass transfer rates and periodical illumination resulting in high photonic

efficiencies. However, these reactors are mechanically complex and costly to scale up (Van Gerven et al., 2007; Braham and Harris, 2009).

2.5.3 Photocatalytic membrane reactors (PMR)

The major feature of these reactors is a membrane which allows water to pass through while blocking the catalyst and the substrate to be degraded. In this way, the membrane concentrates the substrate in the reactor thus increasing its residence time while also retaining the catalyst within the reactor (Zeghioud et al., 2016). This facilitates a high reaction rate and continuous flow operation for the dilute waste streams commonly treated by photocatalysis. Moreover, by retaining the degradation products in the reactor, the PMR ensures complete mineralization of the substrate (Molinari et al., 2017). The catalyst can be applied in suspended form inside the reactor or attached onto the membranes (Mozia et al., 2010).

Application of the catalyst in suspended form ensures a high reaction rate; however, separation of nanoparticles by membranes results in frequent fouling which reduces the permeate flux. This is especially common in pressure-driven membranes. The fouling can be limited by employing vacuum-driven submerged membranes (Figure 2.6), cleaning membrane surfaces by air bubbles and periodical membrane permeation/backflushing (Fu et al., 2006). In PMR with suspended catalyst, the reactor is usually separated from the separation zone, and this allows the use of commercial membrane modules (Molinari et al., 2017). Different membranes for microfiltration, ultrafiltration, nanofiltration and reverse osmosis have been investigated. Of these, only reverse osmosis can remove low molecular weight substrates (Mozia et al., 2010).

The PMR with the catalyst immobilized onto the membrane modules have also been investigated. These do not suffer from catalyst fouling; however, the attached catalyst has a lower surface area. In this configuration, the membrane modules have to be specially synthesized to incorporate the catalyst (Molinari et al., 2017). They are installed in the reactor and irradiated by UV light in order to carry out photocatalysis. Application of polymeric membranes in this configuration could result in catalyst erosion and reduction of substrate degradation since these membranes suffer from gradual degradation by UV light and hydroxyl radicals. In this PMR, the catalyst loading cannot be adjusted and the whole membrane has to be replaced once the catalyst is deactivated (Mozia et al., 2010). Currently, PMR employing commercial submerged membranes with suspended catalysts are proposed for commercial application due to their simplicity and ease of scale up (Molinari et al., 2017). However, PMR

are some of the most expensive reactors due to the high capital and operating cost associated with the membranes.

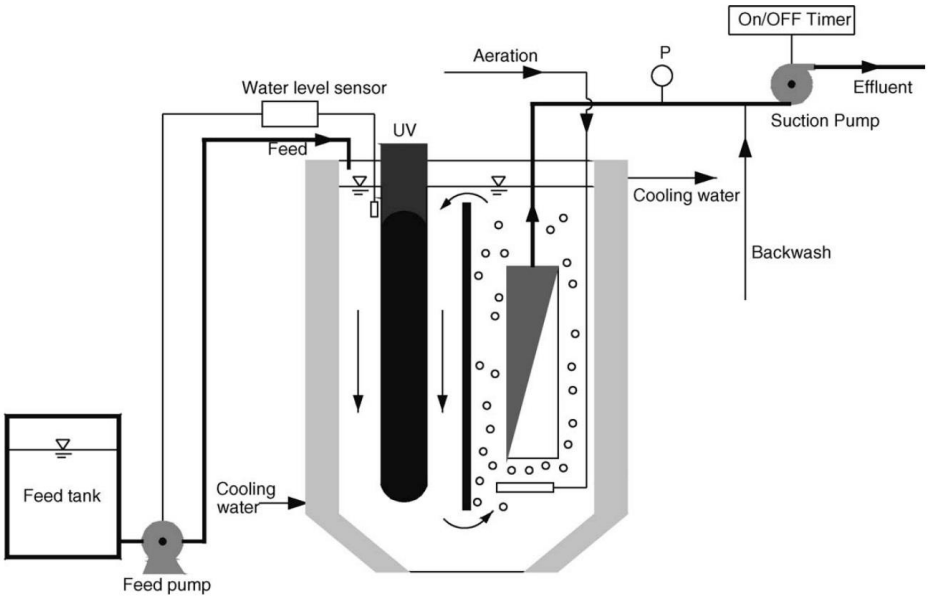

Figure 2.6: Submerged membrane photocatalytic reactor (Fu et al., 2006)

2.5.4 Tubular slurry reactors

In these reactors, a slurry of nano-catalysts is mixed with the wastewater using a mixer or a recirculating pump. Mixers are most often applied in laboratory scale reactors while pump recirculation is common in both lab-scale and pilot plants (Boyjoo et al., 2014a). The reactors are usually illuminated by lamps and/or sunlight (Spasiano et al., 2015; Dominguez et al., 2016). Lamp illuminated reactors are normally oriented vertically and can be illuminated externally or internally. The most commonly applied internally illuminated reactors are the annular reactors or immersion well reactors (Al-Rasheed and Cardin, 2003; Rabahi et al., 2019). In these reactors, the lamp is immersed in the wastewater and protected from the water by a glass sleeve. The wastewater is then confined within an annulus between the glass sleeve and the reactor wall. Annular reactors generally employ low pressure lamps such as germicidal or blacklight lamps (Rabahi et al., 2019). Light emitting diodes have also been used (Dominguez et al., 2016). In the immersion well reactors (Figure 2.7a), medium-pressure UV lamps are employed (Al-Rasheed and Cardin, 2003). In order to improve the light transmission in internally illuminated slurry reactors, multiple lamps have been used in the so-called multi-annular reactors (Boyjoo et al., 2014a). This technique allows reactor scale up by increasing the diameter of these reactors. Slurry reactors have also been illuminated externally using several low-pressure lamps distributed around the reactor (Valadés-Pelayo et al., 2015b).

In solar illuminated tubular reactors, the reactors are normally oriented horizontally. at an angle equivalent to the local latitude. To improve light utilization, reflectors have been installed on the unilluminated side of the reactor. These reflectors include parabolic concentrators, compound parabolic concentrators (CPC) (Figure 2.7b) (Spasiano et al., 2015) and surface uniform concentrators (Hou et al., 2017). Recently, a novel offset multi-tubular photoreactor has been proposed. In this reactor, several tubular reactors are installed in the space normally occupied by a CPC (Ochoa-Gutierrez et al., 2018). This reactor has been found to be better than the CPC photoreactors in terms of reaction rate, light collection and volume of wastewater treated at a comparable cost to the CPC reactor. Tubular reactors are easy to scale up and several pilot plant CPC reactors have been developed (Spasiano et al., 2015). However, due to their orientation, solar tubular reactors can only handle nano-catalysts as heavier catalysts tend to settle on the reactor walls (Malato et al., 2003). This excludes their application for heavier catalysts which may be amenable to easier separation from the wastewater.

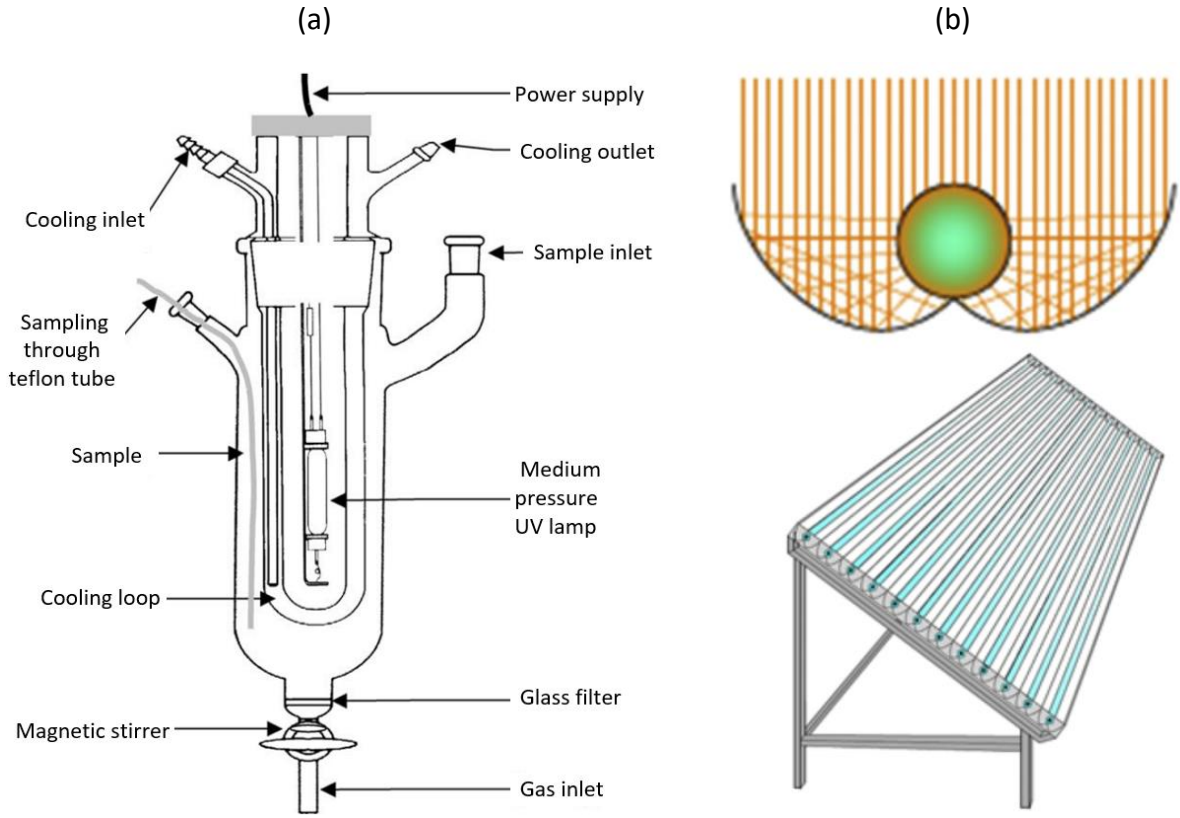

Figure 2.7: Tubular slurry reactors: (a) immersion well reactor (Al-Rasheed and Cardin, 2003); (b) compound parabolic concentrator (Spasiano et al., 2015)

2.5.5 Fluidized bed reactors

These reactors may be considered as packed bed reactors through which wastewater flows at a velocity high enough to suspend the catalysts in the wastewater stream (Tisa et al., 2014). The reactors are normally installed vertically with fluidization being provided by wastewater (Imoberdorf et al., 2008) or compressed air (Shet and Vidya, 2016; Apollo and Aoyi, 2016). Reactors which use wastewater for fluidization are usually two-phase reactors with only the catalyst and wastewater in the reactor (Figure 2.8a). In the three phase, air fluidized bed reactors, air induces motion of the wastewater which then fluidizes the catalyst particles. The use of compressed air for fluidization is especially attractive since it is less costly and has the additional advantage of supplying oxygen as an electron acceptor directly into the reactor (Gaya and Abdullah, 2008). This was demonstrated by Matsumura et al. (2007) and Chong et al. (2009) who reported an increase in the rate of photocatalysis with an increase in the air flow rate in their reactors. A modification of these reactors is the air-lift reactor in which a draft tube is installed inside the fluidized bed reactor (Xu et al., 2013) (Figure 2.8b). Air introduced into the draft tube creates a zone of low density in the draft tube with a higher density zone on the outside. Thus, the wastewater rises inside the draft tube and then comes down on the outside. This establishes uniform recirculation between the two zones (Xu et al., 2013) which has been observed to increase the reaction rate (Nam et al., 2002; Nam et al., 2009). A similar effect has been observed when the fluidized bed reactor is inclined a few degrees away from the vertical (Akach et al., 2016).

Fluidized bed reactors have been used with a wide range of catalyst sizes such as TiO_2 nanoparticles (Nam et al., 2002; Apollo and Aoyi, 2016), $Ag@TiO_2$ nanoparticles (Shet and Vidya, 2016), glass coated TiO_2 spheres (Imoberdorf et al., 2008), TiO_2 microspheres (Vega et al., 2011), TiO_2 supported on silica (Nam et al., 2009) and TiO_2-activated carbon-silica composite (Akach et al., 2016). The use of large sized catalysts is especially advantageous since such catalysts can be easily separated from the wastewater. However, in a fluidized bed reactor, catalyst particles experience multiple collisions which has been observed to result in catalyst attrition and loss of activity. Therefore, such catalysts need to be durable for effective long-term performance in the reactor (Vega et al., 2011).

Fluidized bed reactors have been illuminated internally with UV lamps (Imoberdorf et al., 2008), externally with UV lamps (Vega et al., 2011) or externally with sunlight (Shet and Vidya, 2016). The fluidized bed reactor has been found to be one of the most effective reactors for photocatalysis due to its high mass transfer characteristics and good light utilization

(Thiruvenkatachari et al., 2008; Braham and Harris, 2009; McCullagh et al., 2011). Moreover, they have a simple construction with no moving parts (Tisa et al., 2014).

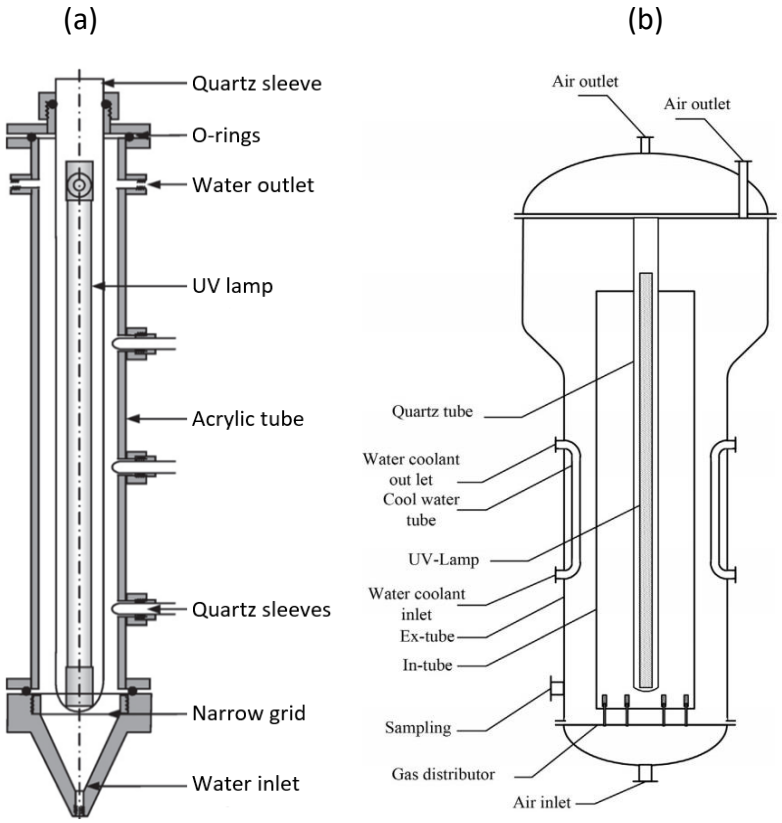

Figure 2.8: (a) Two phase fluidized bed reactors (Imoberdorf et al., 2008); (b) air-lift reactor (Xu et al., 2013)

2.6 Modelling of fluidized bed photoreactors

An air fluidized bed reactor is a multiphase contacting device in which air, introduced at the bottom of the reactor, rises as bubbles through a catalyst slurry medium. The air bubbles induce liquid motion which then fluidizes the catalyst. This results in solution mixing with high heat and mass transfer characteristics without moving parts and low maintenance (Ekambara and Dhotre, 2010). Fluidized bed photoreactors are complex due to the interplay of hydrodynamics and light distribution in such reactors. In order to design, analyse, optimize and scale up such reactors, appropriate mathematical models need to be developed. These models should account for the factors that affect the rate of photocatalysis, namely catalyst, bubble, pollutant and light distribution. Photoreactor modelling is usually divided into three parts: hydrodynamics, light distribution and reaction kinetics (Boyjoo et al., 2013a). Hydrodynamics modelling shows the distribution of catalyst particles in the reactor. Then, light distribution modelling is carried out to analyse the light distribution in the photoreactor. Reaction kinetics modelling is then carried out to determine the rate of photocatalysis.

2.7 Modelling of fluidized bed hydrodynamics

The fluidized bed photoreactor is a multiphase reactor which in many cases involve turbulent flow. As such, the hydrodynamics modelling of such a reactor is similar to that of any fluidized bed photoreactor (Boyjoo et al., 2013a). The reactor hydrodynamics is characterized by turbulence and multiple forces that influence bubble and catalyst motion resulting in very complex flows. The hydrodynamics in fluidized bed reactors have been analysed using experimental techniques such as computer-automated radioactive particle tracking (CARPT), laser doppler anemometer (LDA) and computed tomography (CT) (Kulkarni et al., 2007). These instruments are costly and available at only a few facilities. Moreover, due to time constraints, these instruments may not provide a complete analysis of the hydrodynamics at every location in the reactor. As a result, they are usually used to provide experimental data for the validation of mathematical models.

In lieu of experimental data, empirical correlations have been developed mainly for characterizing macroscopic hydrodynamic parameters such as global gas holdup, regime transition and bubble sizes (Kazakis et al., 2007). These correlations are simplistic and cannot be used to analyse spatial and temporal features of multiphase flows. Recently, with the development of faster computers, computational fluid dynamics (CFD) has emerged as an important tool for the analysis of multiphase reactors (Feng et al., 2005; Schallenberg et al., 2005; Kulkarni et al., 2007; Tabib et al., 2008; Panneerselvam et al., 2009; Ekambara and Dhotre, 2010). In CFD, the constitutive partial differential equations which govern fluid flow such as the continuity and momentum equations are converted into algebraic equations which are then solved numerically. In this way, the CFD technique results in mathematical rigour at low cost and thus provides a detailed analysis of the flow characteristics in the reactor (Ekambara and Dhotre, 2010). In order to ensure confidence in the accuracy of the models, they are validated at several spatial locations in the reactor using experimental techniques such as CARPT, CT and LDV (Kulkarni et al., 2007).

Modelling of the hydrodynamics in a fluidized bed reactor using CFD technique can be carried out using either the Euler-Langrange or Euler-Euler methods (Pan et al., 2016). In the Euler-Langrange method, the distribution of the dispersed phases is determined by tracking individual phase particles (Díaz et al., 2008). Euler-Langrange modelling is very accurate; however, it is very computationally costly when the volume fraction of the dispersed phase is high (Boyjoo et al., 2013a; Pan et al., 2016). Consequently, relatively few studies have employed the Euler-Langrange method to simulate multiphase flows (Besbes et al., 2015). The Euler-Euler model

treats the different phases as interpenetrating continua with continuity and momentum equations being solved for all phases. The interaction between the phases is accounted for using interfacial forces (Díaz et al., 2008). Most multiphase flow simulations utilize the Euler-Euler method due to its accuracy, robustness and low computational cost even when the dispersed phase volume fraction is high (Boyjoo et al., 2013a). The Euler-Euler method has been used to simulate multiphase flows in bubble column reactors (Kulkarni et al., 2007; Díaz et al., 2008; Tabib et al., 2008), slurry bed reactors (Feng et al., 2005; Ekambara and Dhotre, 2010; Li and Zhong, 2015; Zhou et al., 2017) and three phase fluidized bed reactors (Panneerselvam et al., 2009; Hamidipour et al., 2012).

Several studies use only a single bubble size especially when simulating homogeneous bubbly flows (Díaz et al., 2008; Ekambara and Dhotre, 2010) and fluidized bed reactors (Panneerselvam et al., 2009; Hamidipour et al., 2012). Recently, population balance models (PBM) in which multiple bubble sizes are considered, have attracted a lot of attention. The PBM have been solved using various methods including multiple size group (MUSIG)/Method of Classes (Bannari et al., 2008; Díaz et al., 2008; Ekambara et al., 2008) and Quadrature Method of Moments (QMOM) (Buffo et al., 2013; Gupta and Roy, 2013). These methods consider bubble coalescence and break up which are commonly observed in heterogeneous gas-liquid flows. Population balance models solve a large number of equations resulting in an increase in the computational cost as compared to single bubble models. Therefore, the use of PBM has been restricted to simulating heterogeneous flows as its application in homogeneous flows does not improve the simulation accuracy (Díaz et al., 2008; Gupta and Roy, 2013).

2.7.1 Modelling turbulence

Fluidized bed reactor flows are usually highly turbulent. In multiphase flows, large eddies extract energy from the mean flow which cascade into smaller eddies and finally dissipate due to fluid viscosity. This results in a complex flow structure with eddies of various sizes (Davidson, 2015). The largest eddies usually carry the most energy and are of most importance. Their sizes are characterized by using the length scale (Versteeg and Malalasekera, 2007). From an engineering perspective, the turbulent flow can be divided into a mean part and a fluctuating part. The mean flow characteristics is of the most interest; however, its evolution is highly influenced by the fluctuating part. Therefore, determination of turbulence is of great importance to the hydrodynamic simulation of the reactor. In order to simulate fluid turbulence, several models have been developed with varying degrees of accuracy. The most accurate of these models is based on the direct numerical simulation (DNS) of Navier-Stokes equations.

This resolves the wide range of turbulence time and length scales in operation resulting in very accurate simulation. However, DNS requires a large grid and very small time steps in order to resolve all the time and length scales (Tu et al., 2018). This makes it extremely computationally expensive even for supercomputers and thus unfeasible for application in a practical fluidized bed reactor. Its usefulness for now is restricted to the generation of turbulence data which can be used for fundamental research on turbulence and the development of simpler turbulence models (Versteeg and Malalasekera, 2007).

Much more accurate numerical schemes at manageable computational cost have been attempted by the large eddy simulation (LES). The rationale behind LES is the fact that large eddies are anisotropic and more energetic as compared to smaller eddies which are isotropic and less energetic (Versteeg and Malalasekera, 2007). In LES, the small time and length scales are eliminated from the solution of the Navier-Stokes equations. The mean flow as well as the larger turbulence structures are resolved in a time-based simulation while the effect of the smaller scale structures are modelled by sub-grid scale (SGS) models (Davidson, 2015). This approach results in an accurate solution with a lower computational cost than DNS since directly resolving the smaller time and length scales are usually the most computationally intensive. LES has been used to study instantaneous flow structures in practical reactors such as bubble column reactors (Tabib et al., 2008). The use of LES in these reactors is justified since bubble column reactors exhibit large eddies which have a marked influence on bubble diffusion and local gas holdup (Dhotre et al., 2008). However, LES requires a very fine mesh which results in a high computational cost (Kulkarni et al., 2007) while being superior to simpler turbulent models only with respect to turbulent modelling (Dhotre et al., 2008).

The most simplified and commonly applied turbulent models are based on time-averaging of the Navier-Stokes equations. This results in Reynolds-averaged Navier-Stokes (RANS) equations which describe the mean flow. These equations contain a Reynolds stress term which represents turbulent fluctuations and their effect on the mean flow. In order to close the RANS equations, the Reynolds stresses have to be evaluated as a function of the mean flow (Tu et al., 2018). The first attempt at this was by Boussinesq who hypothesized that the effect of the Reynolds stress on the mean flow was essentially to increase its viscosity. This gave rise to the eddy viscosity hypothesis in which the effective viscosity was evaluated as the sum of the molecular viscosity and the eddy viscosity. In this hypothesis, turbulent modelling could be established from evaluating the eddy viscosity (Davidson, 2015). Prandtl proposed the mixing length hypothesis in which the eddy viscosity was calculated as a function of position in the

flow field by a simple algebraic formula. This model has been found to give good results for slow moving, two-dimensional wall-bounded flows with low pressure gradients. However, it cannot accurately predict turbulence in flows with recirculation and separation (Versteeg and Malalasekera, 2007).

The mixing length concept has been further improved by the use of generalized models in which the eddy viscosity is calculated from transport equations in order to capture the dynamics of turbulence (Versteeg and Malalasekera, 2007). The most popular engineering model in this category is the k-ε model in which the eddy viscosity is evaluated from the transport equations of the turbulent kinetic energy and the turbulent dissipation rate (Davidson, 2015). This model is popular in CFD turbulent modelling due to its relative simplicity and the requirement for only boundary conditions as an input. Its general applicability has also been proved having been widely validated for a variety of flows without changing the constants of the standard model (Tu et al., 2018).

The standard k-ε model has been found to be accurate in flows within conduits and free shear flows with low pressure gradients. It gives accurate simulation in fully developed bubble column flows (Pourtousi et al., 2014). However, the assumption of isotropic eddy viscosity has resulted in poor accuracy in flows with high anisotropy, flow separation, streamline curvature, swirling and rotating frame of reference (Versteeg and Malalasekera, 2007). This is the situation in the region near the sparger in bubble column reactors where the standard k-ε model has been found to yield poor results. In order to improve the performance of the standard k-ε model, several modifications have been attempted. The most important of these variants is the Re-normalization group (RNG) k-ε model in which the production term is modified to account for multiple turbulent length scales (Masood and Delgado, 2014). This model has been found to be much better at predicting swirling flows in bubble column reactors as compared to the standard k-ε model (Laborde-Boutet et al., 2009; Gupta and Roy, 2013).

A more accurate turbulent model based on the RANS approach is the Reynolds stress model (RSM). In this model, the individual Reynolds stresses are explicitly modelled. This results in six transport equations for the individual Reynolds stresses together with a dissipation term (Ekambara et al., 2008; Davidson, 2015). The RSM has been found to be much more accurate than the k-ε model for flows with high anisotropy. However, due to the fact that it solves 7 transport equations, it is much more computationally costly than the 2-equation k-ε model. The RSM model is fairly accurate but less computationally costly as compared to LES (Versteeg

and Malalasekera, 2007). Ekambara and Dhotre (2010) found that the accuracy of RSM was comparable to that of LES near the sparger of a bubble column reactor where significant flow anisotropy was present. RSM model has been found to be better in predicting the turbulent kinetic energy profiles as compared to the k-ε model (Tabib et al., 2008). In multiphase flows, the motion of the dispersed phase also induces turbulence on the liquid with the effect of increasing the effective viscosity (Ekambara and Dhotre, 2010). In gas-liquid flows, this extra viscosity has been evaluated by an additional term provided by Sato and Sekoguchi (1975).

2.7.2 Modelling interfacial forces

In a fluidized bed reactor, the rising bubbles and solid particles experience several forces such as drag, lift, wall lubrication, turbulent dispersion and virtual mass forces (Tabib et al., 2008; Silva et al., 2012; Pourtousi et al., 2014) For a specific reactor, the magnitude and direction of these forces is a function of the bubble, liquid and solid properties and reactor geometry. In order to ensure accurate simulation at low cost, the appropriate choice of the most relevant forces need to be made (Pourtousi et al., 2014). Moreover, the inclusion of some forces may result in convergence problems during simulation (Laborde-Boutet et al., 2009). In bubble columns, some researchers have chosen to include most of the interfacial forces (Ekambara et al., 2008). Others have suggested that only the drag force should be modelled (Díaz et al., 2009; Silva et al., 2012). In three phase fluidized reactors, the interfacial forces between the dispersed phases have often been neglected while only the drag force is often modelled between the liquid and solid (Panneerselvam et al., 2009; Li and Zhong, 2015).

The drag force arises due to the resistance experienced by the dispersed phases as they move through the continuous phase. Viscous stresses around the bubble or particle create skin drag while pressure distribution around the bubble or particle results in form drag (Ekambara et al., 2008). Drag force is the most significant of the interfacial forces and must be modelled in the simulation of multiphase flows. The drag force is usually calculated from the drag coefficient for which many formulations exist (Dalla Ville, 1948; Grace et al., 1976; Ishii and Zuber, 1979; Schiller and Nauman, 1935; Ma and Ahmadi, 1990; Zhang and Vanderheyden, 2002). The equations for the drag coefficients are provided in Table A1 (Appendix A). Schiller and Nauman (1935) drag coefficient is most appropriate for solids and small spherical bubbles (Li and Zhong, 2015) while that of Grace et al. (1976) and Ishii and Zuber (1979) are normally recommended for deformable bubbles (Pourtousi et al., 2014). Several authors have found that the Ishii and Zuber (1979) drag model gives the most accurate results in bubble column simulation (Silva et al., 2012; Masood and Delgado, 2014). Other studies recommend the use

of Zhang and Vanderheyden (2002) drag model for the simulation of bubbly flows (Tabib et al., 2008; Pang and Wei, 2011) and gas-liquid drag in three-phase flows (Li and Zhong, 2015).

The lift force is attributed to the rotation of the dispersed phase and the shear stress of the continuous phase which yields a force acting perpendicular to the direction of motion of a solid particle or a bubble (Díaz et al., 2009; Pourtousi et al., 2014). The lift coefficient has been expressed as a constant in the range of -1 to 0.5 (Díaz et al., 2009) or as a function of the bubble Reynolds number (Legendre and Magnaudet, 1998; Tomiyama et al., 2002). Equations for various lift coefficients are provided in Table A2 (Appendix A). The Tomiyama et al. (2002) lift correlation specifies the sign of the lift coefficient as a function of the bubble size such that larger bubbles (d_B > 6 mm) move towards the centre of the reactor while smaller bubbles move towards the wall of the reactor (Díaz et al., 2009). This correlation is appropriate for heterogeneous flows in which bubbles have a wide size range. Other studies recommend Legendre and Magnaudet (1998) lift correlation for bubbly flows since it represents the flow physics more accurately (Pang and Wei, 2011). In homogeneous bubble flows, a constant lift coefficient between 0.1 and 0.5 has been found to be sufficient (Pourtousi et al., 2014). Some researchers have observed that the inclusion of lift force in homogeneous flows does not improve simulation accuracy (Díaz et al., 2009; Silva et al., 2012). However, the inclusion of lift force is necessary to accurately model the plume oscillation present in some gas-liquid flows (Gupta and Roy, 2013).

For bubbles, a wall lubrication force exists which tends to push bubbles away from the reactor wall. This is due to the fact that the liquid flow rate near the wall is higher than that at the centre of the reactor. The resulting pressure differences drive bubbles towards the centre of the reactor (Ekambara et al., 2008). Several models for the wall lubrication force have been proposed (Antal et al., 1991; Tomiyama et al., 2002; Frank et al., 2004). Equations for these models are provided in Table A3 (Appendix A). The model by Tomiyama et al. (2002) is only applicable for bubble columns with a circular geometry. This model was extended to non-circular geometry by Frank et al. (2004). Masood et al. (2014) compared the three wall lubrication models and found that Frank et al. (2004) model gave the best results in their square bubble column reactor.

The turbulent dispersion force arises from the movement of the dispersed phase by liquid eddies (Pourtousi et al., 2014). This force has been modelled by Lopez de Bertodano (1992) and Burns et al. (2004). It has been found to be less significant in homogeneous flows as

compared to heterogeneous flows (Tabib et al., 2008). Several studies employing Lopez de Bertodano (1992) model has found that a turbulent dispersion coefficient of 0.1 – 0.5 gives the best results (Pourtousi et al., 2014). A comparison of the two models showed that the Burns et al. (2004) model gave the best results in a square bubble column reactor (Masood et al., 2014).

The virtual mass force is due to the acceleration of the liquid in the wake of the bubble as it rises. For a spherical bubble, the virtual mass force coefficient is normally specified as 0.5 (Masood and Delgado, 2014). Several studies have shown that the virtual mass force is insignificant for gas-liquid flows in a bubble column and should be neglected during simulation (Díaz et al., 2008; Tabib et al., 2008; Masood and Delgado, 2014). This was attributed to the fact that significant acceleration effects are restricted to the ends of the column (Tabib et al., 2008).

2.7.3 CFD simulation process

Multiphase simulations have mostly been carried out using Ansys CFX (Dhotre et al., 2008; Díaz et al., 2008; Ekambara et al., 2008; Silva et al., 2012; Masood and Delgado, 2014) with a few researchers using Ansys Fluent (Laborde-Boutet et al., 2009) and openFOAM (Bannari et al., 2008; Buffo et al., 2013). Most of these codes have a user-friendly graphical interface which provides a step-by-step process through which a user may specify and solve a computational problem (Tu et al., 2018). CFD operations can be divided into three steps: pre-processing, solving and post-processing. During the pre-processing step, the geometry is defined followed by the generation of the computational grid which divides the geometry into smaller cells (Versteeg and Malalasekera, 2007). The type of mesh to use in the computational grid, whether structured or unstructured depends on the geometry (Tu et al., 2018). Grid size or the number of cells, depends on the required numerical accuracy and the available computational resources. For gas-liquid flows, it has been suggested that the smallest grid size should be at least 1.5 times the bubble size (Ekambara and Dhotre, 2010). Other researchers have suggested that grid independence can be achieved with a cell size of 50 – 100% of the Kolmogorov length scale (Díaz et al., 2008). Pre-processing also involves specification of the fluid flow problem, fluid properties and boundary conditions. The problem must be defined such that the key features of the flow physics are captured while ensuring that the solution is computationally manageable. This requires specification of the turbulence and interphase models (Versteeg and Malalasekera, 2007).

Pre-processing is usually followed by specifying numerical solution settings such as initial conditions and solution control settings such as discretization schemes, solution procedures and types of solvers. Most CFD codes use the finite volume method to integrate the governing partial differential equation over a control volume. An appropriate discretization scheme is then used to convert the integral equations into algebraic equations (Versteeg and Malalasekera, 2007). Several discretization schemes are available depending on the degree of accuracy required. These include first order upwind, second order upwind and quadratic upstream interpolation for convective kinematics (QUICK) schemes. The higher order schemes usually result in a more accurate solution at the cost of solution stability (Tu et al., 2018). The series of algebraic equations are then solved by iterative solvers such as tri-diagonal matrix algorithm (TDMA) or algebraic multigrid solver (AMG). In order to ensure correct linkage between pressure and velocity, the solver employs solution procedures such as semi-implicit method for pressure linked equations (SIMPLE) and pressure implicit split operator (PISO) (Versteeg and Malalasekera, 2007). After specifying the numerical solution settings, the CFD calculation is started and monitored to ensure solution convergence. Solution accuracy may be ascertained by monitoring the residuals due to imbalances of the conserved quantities. When the residuals drop below a specified threshold e.g. 0.0001 (Ekambara et al., 2008), the solution may be considered to be converged. During the solution, divergence of the solution may be corrected by changing the under-relaxation factors which determine how much the solution properties change from one iteration to the next (Tu et al., 2018).

The final step in a CFD solution is post-processing in which the flow properties of interest are analysed. Most CFD codes include sophisticated graphical tools for viewing such properties including X-Y, vector and contour plots. Dynamic displays can also be shown using animations (Versteeg and Malalasekera, 2007). The accuracy of any CFD solution can be ensured by carrying out a grid independence study to eliminate errors that may arise due to a course grid. This involves starting the solution with a course grid and refining it successively while monitoring the solution variables of interest. The process is continued until further grid refinement does not result in a change in the flow properties of interest (Tu et al., 2018). Grid independence and convergence can only ensure numerical accuracy. Real accuracy can only be proved through experimental validation by comparing the simulation results with those obtained from experiments done at the same boundary conditions (Versteeg and Malalasekera, 2007).

2.8 Modelling of light distribution

2.8.1 Light distribution

In a normal three phase reactor, only the hydrodynamics needs to be analysed in order to determine the reactor performance. In a three phase photoreactor, the participation of photons has to be accounted for by modelling the light distribution for a comprehensive analysis of reactor performance. An analysis of the light distribution in the reactor is crucial as it is the basis of such important photocatalytic reactor design parameters such as the local volumetric rate of energy absorption (LVREA), photocatalysis intrinsic kinetics and efficiency parameters (Moreira et al., 2010). In a photoreactor, light photons interact with catalysts, bubbles and reactor walls. This results in a highly inhomogeneous distribution of light in the photoreactor (Camera-Roda et al., 2016). Just as in the case with hydrodynamics, experimental determination of the light distribution in a photoreactor is not feasible due to time and cost constraints. Moreover, any instrument used to measure the local light intensities inside the reactor would distort the radiation field, thus making it impossible to accurately measure the light intensity profile in the reactor (Acosta-Herazo, et al., 2016). Therefore, light distribution is normally established using experimentally validated simulation (Valadés-Pelayo et al., 2014b).

The most rigorous light distribution simulations have been carried out by solving the radiation transport equation (RTE) (equation 4.1). For photocatalysis systems, the scattering terms on the right-hand side of the RTE renders an analytical solution to the RTE impossible. Therefore, numerical methods have been developed for solving the RTE. The most rigorous of these numerical methods are the deterministic discrete ordinates method (Boyjoo et al., 2013b) and the stochastic Monte Carlo method (Moreira et al., 2010; Valadés-Pelayo et al., 2014b). Methods with several simplifying assumptions such as the six-flux method (Li Puma et al., 2010) and P1 method (Orozco et al., 2009) have also been used to solve the RTE.

2.8.2 Light distribution methods

Two-flux method

This is the simplest light distribution method which considers multiple scattering effects. The method assumes that light is scattered only in the forward and backward directions. This transforms the RTE into two first order differential equations which can then be solved analytically. The two-flux method is only appropriate for reactors which may be considered to

be enclosed within two infinite parallel walls. It has been applied by Puma and Brucato (2007) to simulate the light distribution in an annular UV reactor with nanophase TiO_2 catalyst.

P1 method

The P1 method assumes that the direction of light propagation is unimportant i.e. that it is fully isotropic. This assumption transforms the RTE into a second order partial differential equation which can then be solved analytically (Orozco et al., 2012). In a typical reactor, the propagation of collimated light from such sources as sunlight may be strongly directional, especially near the light source. Therefore, the P1 method has been found to be particularly inaccurate near the reactor boundaries illuminated by sunlight (Orozco et al., 2012). The assumptions of this method also break down at low catalyst loading where there is insufficient catalyst scattering to ensure isotropic light propagation (Cuevas et al., 2007). The P1 method has been used to simulate the light distribution in annular UV (Cuevas et al., 2007) and hybrid light reactors (Orozco et al., 2009; Orozco et al., 2012) with nanophase TiO_2 as the catalyst.

Six-flux method

This method improves upon the two-flux method by assuming that incoming photons are scattered randomly by the catalyst in the six cartesian directions. The original six-flux method was developed under the assumption that light scattering could be described by the diffuse reflectance scattering phase function (Li Puma et al., 2004). The probability of light scattering in each of the six directions was then calculated from an exact solution using the Monte Carlo method. Recently, the six-flux method coupled with the Henyey-Greenstein scattering phase function has been developed and employed in several studies. This version of the six-flux method was more accurate as compared to those which employ the diffuse reflectance and isotropic scattering phase functions (Acosta-Herazo, et al., 2016). It should be noted that the six-flux method transforms into the two-flux method when all photons are backscattered.

The accuracy of the six-flux method has been investigated by comparing its results with those of the more accurate finite volume method. It was found that, under collimated light, a slight error of 5% was observed. However, under diffuse light, this error increased to 120% (Ramírez-Cabrera et al., 2017). Due to its limitation of light scattering in six directions, the six-flux method has been observed to be inaccurate in predicting the light distribution at high catalyst loading (Acosta-Herazo, et al., 2016). The six-flux method has been used to evaluate the light distribution in annular UV reactors (Li Puma et al., 2004) and solar illuminated tubular and

CPC reactors (Colina-Márquez et al., 2009; Colina-Márquez et al., 2010; Mueses et al., 2013; Acosta-Herazo et al., 2016; Ochoa-Gutiérrez et al., 2018) with nanophase TiO_2 catalysts.

Discrete ordinates method

In this method, the reactor is divided into a series of control volumes and directions. The RTE is then transformed into a series of algebraic equations according to the number of volume and angular discretizations (Boyjoo et al., 2014a). The discrete ordinates method has been included in several CFD packages such as Ansys Fluent. This method has been used to simulate the light distribution in several reactors. Casado et al. (2019) used the discrete ordinates method to simulate the light distribution in a solar illuminated compound parabolic concentrator (CPC) reactor. Moreno-SanSegundo et al. (2020) used the discrete ordinates method in Ansys Fluent and openFOAM to simulate the light distribution in an annular UV reactor, solar CPC reactor and LED illuminated reactor. Boyjoo and co-workers simulated the light distribution in an annular UV reactor (Boyjoo et al., 2014b) and multi-annular UV reactors (Boyjoo et al., 2014a; Boyjoo et al., 2013b) using the discrete ordinates method in Ansys Fluent. All these simulation studies were carried out in reactors with nanophase catalysts.

Monte Carlo method

The Monte Carlo method solves the RTE stochastically by tracking a statistically adequate number of photons from the light source until they are absorbed in the slurry or lost in the reactor wall. Monte Carlo method is preferred over other methods for complicated reactor geometries (Valades-Pelayo et al., 2014b). The accuracy of the Monte Carlo method is so well established that it is often used to validate the accuracy of other less accurate methods like the six-flux method (Acosta-Herazo, et al., 2016). The major drawback of the Monte Carlo method is that for an accurate simulation, a high number of photons need to be tracked while considering the interactions of the photons with catalyst particles and the reactor boundary (Valadés-Pelayo et al., 2014a). This is computationally intensive and requires a long simulation time. In one study, 60 million photons reportedly took 32 hours to track in a quad core computer (Valadés-Pelayo et al., 2014b).

Several studies have employed the Monte Carlo method to determine the light distribution in photocatalytic reactors. Singh et al. (2007) simulated the light distribution in a monolith reactor for air treatment using the Monte Carlo method. Imoberdorf et al. (2008) used the Monte Carlo method to determine the light distribution in a fluidized bed reactor with TiO_2 coated spheres. The Monte Carlo method has also been used to simulate the light distribution in an annular UV

reactor (Moreira et al., 2010; Valadés-Pelayo et al., 2014a, 2014b), externally illuminated annular UV reactor (Valadés-Pelayo et al., 2015a) and solar illuminated tubular and surface uniform concentrators (Hou et al., 2017) with nanoparticulate P25 TiO_2 catalysts.

2.8.3 Simulation parameters

In order to solve the RTE, the appropriate boundary conditions, scattering phase functions, absorption and scattering coefficients need to be specified.

Boundary conditions

The boundary conditions for the light distribution simulation include the spectrum of the light source and how the light interacts with the boundaries such as the lamp, lamp sleeve and reactor wall. Most light sources exhibit a wide band spectrum spanning across several wavelengths. An accurate accounting of the light spectrum is important since catalyst absorption and scattering are strong functions of the light wavelength. The most accurate simulations utilize a complete model of the light spectrum. This is common practice in Monte Carlo simulations where each photon is randomly assigned a specific wavelength according to the light spectrum (Valadés-Pelayo et al., 2014b). The six-flux method generally assumes a single wavelength and then uses wavelength-averaged optical properties. Some finite volume methods have also taken this approach. A few finite volume methods improve upon this by dividing the light spectrum into multiple zones (Boyjoo et al., 2014a).

Before simulation, it is necessary to establish how the light interacts with the boundaries. Initially Valadés-Pelayo et al. (2014b) suggested that the best boundary conditions for their annular reactor would consist of a combination of total absorption of photons by the lamp and the wall. These values were revised to 30% lamp absorption and 65% wall absorption after further refinements using a better validation technique (Valadés-Pelayo et al., 2014a). It is also important to consider how the light interacts with transparent boundaries. An accurate simulation would consider the refraction and reflection of the light across the boundaries. This is especially important for direct or collimated light sources where refraction is crucial. Acosta-Herazo et al. (2020) found that an error of up to 12% can result if refraction/reflection effects are not included in the simulation of the CPC absorber.

Boundary conditions also need to specify the intensity of the incoming radiation at the reactor boundary. For reactors illuminated by a lamp, the light intensity at the lamp sleeve depends on the type of lamp. The light intensity around the lamp can be modelled using a lamp emission model. These models are classified according to the source of photons and their direction of

propagation. According to the source of photons, lamp emission models can be classified as line source, surface source and volume source models (Figure 2.9). These can be further classified as specular and diffuse emission depending on the direction of the emitted light (Pareek et al., 2008). Line source emission models assume that the lamp can be simplified as an emitting line. These models can be used to approximate the light output of very long low-pressure lamps. The surface source models assume that the photons originate from the lamp surface. This is mostly true of black light lamps in which the UVA photons emit from the phosphor on the lamp coating. The volume source emission model treats the photons as coming from the entire volume of the lamp. This model can be used to describe the light output from arc lamps (Boyjoo et al., 2014b). The equations for line source specular emission (LSSE), line source diffuse emission (LSDE), surface source specular emission (SSSE), surface source diffuse emission (SSDE) and volume source emission (VSE) are given in Table A4 of Appendix A.

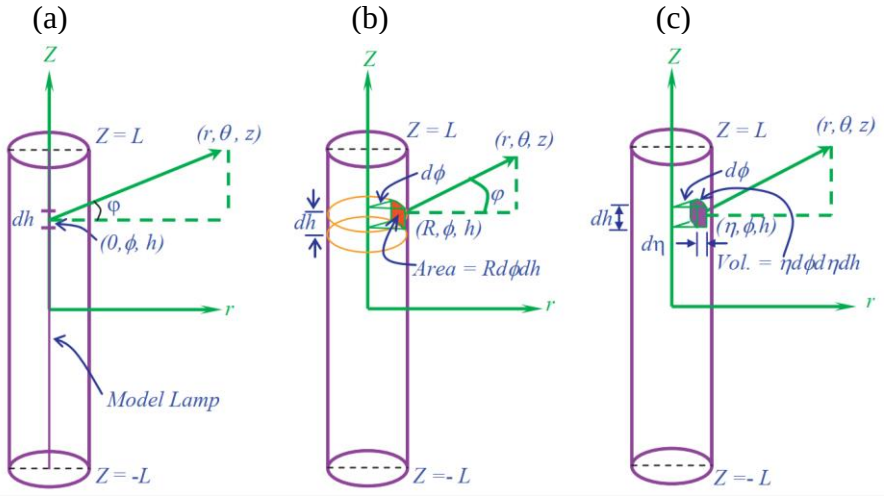

Figure 2.9: Lamp emission models (a) line source (b) surface source (c) volume source (Boyjoo et al., 2013b)

Scattering phase function

The scattering phase function defines the direction to which the catalyst particles scatter light. For very dilute heterogeneous solutions, in which a single scattering event occurs on a spherical particle, the theoretical Mie theory can apply. However, in real photocatalytic reactors, multiple scattering events occur on agglomerated catalyst particles with non-spherical shapes. In such a situation, it is more useful to apply an empirical phase function which describes the probability of scattering in a certain direction (Turolla et al., 2016). Several phase functions have been employed in photocatalytic light distribution studies including isotropic, diffuse reflecting, and Henyey-Greenstein functions.

In the isotropic phase (ISO) function, the photons have an equal probability of being scattered in any direction (Figure 2.10a-b). This phase function is expressed as:

$$p_{iso}(\theta) = \frac{1}{2} \tag{2.12}$$

where θ is the exit scattering angle.

In the diffuse reflectance (DR) phase function, the catalyst particle is assumed to reflect the light in a completely diffuse manner (Cabrera et al., 1996). This phase function scatters light mainly in a backward direction (Figure 2.10a). It is expressed mathematically as (Hou et al., 2017):

$$p_{DR}(\theta) = \frac{8}{3\pi}(\sin\theta - \theta\cos\theta) \tag{2.13}$$

The Henyey-Greenstein (HG) function can describe a wide range of scattering phenomenon using an adjustable asymmetry factor g which can take any value between -1 and 1 (Valades-Pelayo et al., 2014b):

$$p_{HG}(\theta) = \frac{1}{2}\frac{(1-\mathrm{g}^2)}{(1+\mathrm{g}^2-2\mathrm{g}\cos\theta)^{3/2}} \tag{2.14}$$

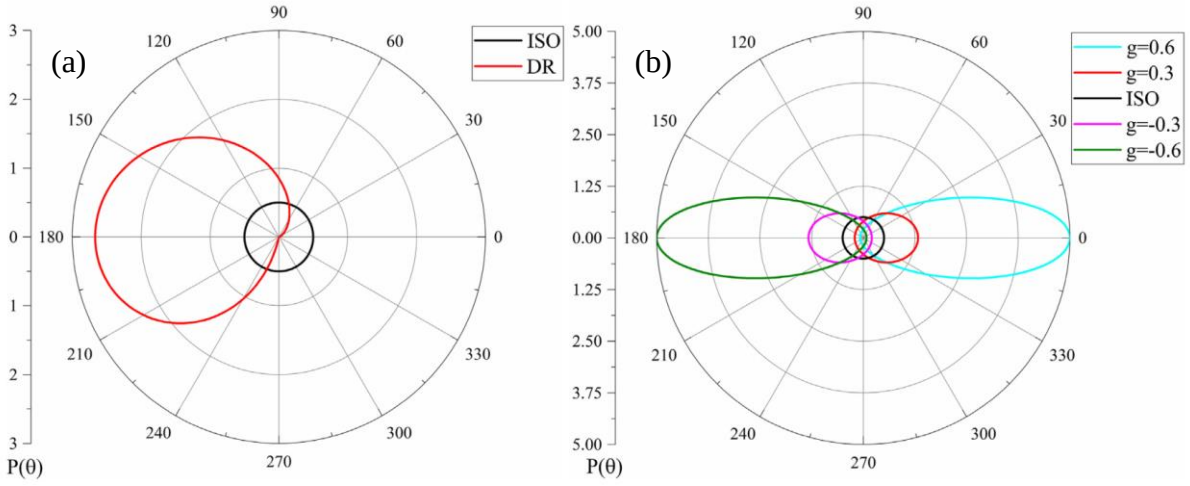

Figure 2.10: Scattering probability of (a) isotropic, diffuse reflectance and (b) Henyey-Greenstein phase functions (Hou et al., 2017)

Positive values of g specify forward scattering while negative values specify backward scattering (Figure 2.10b). When g is set to 0, eq. (2.14) reduces to eq. (2.12) and the HG phase function specifies isotropic scattering. Several studies (Valades-Pelayo et al., 2014b; Acosta-Herazo, et al., 2016; Turolla et al., 2016; Hou et al., 2017) compared several phase functions and concluded that the Henyey-Greenstein function was superior to the others. This was

attributed to the asymmetry factor whose value could be adjusted to ensure an accurate representation of scattering. This is demonstrated by the fact that *g* depends on the type of catalyst since different catalysts exhibit different scattering behaviour (Acosta-Herazo, et al., 2016). The other scattering phase functions are not able to differentiate the scattering behaviour of different catalysts which limits their accuracy.

The optimal value of *g* has been determined by comparing the experimental and simulated light intensity at specific locations in the reactor. These studies employed Aeroxide P25 TiO_2 and found that this catalyst exhibits forward scattering behaviour with different values of *g* (Table 2.3). The initial study by Satuf et al. (2005) assumed that the asymmetry factor depended only on the light wavelength. However, Turolla et al. (2016) found that *g* also depends on the catalyst loading. The asymmetry factor decreased with an increase in catalyst loading such that at very high catalyst loadings, backward scattering was observed. The rest of the studies were carried out under the assumption that *g* was independent of both light wavelength and catalyst loading. The only study which investigated the effect of pH (Valadés-Pelayo et al., 2015b) found that *g* had a lower value at acidic pH than under neutral pH showing that *g* depends on catalyst agglomeration.

Table 2.3: Henyey-Greenstein asymmetry factor from different studies

HG Asymmetry factor	Catalyst loading (g/L)	Wavelength (nm)	Reference
0.4 – 0.7	0.2 – 2	295 – 405	Satuf et al. (2005)
0.6 – 0.8	0.01 – 0.4	345 – 388	Valades-Pelayo et al. (2014b)
0.68	0.025 – 0.4	345 – 388	Valades-Pelayo et al. (2014a)
0.41	0 – 0.1	-	Valadés-Pelayo et al. (2015b)
0.64	0.08 – 0.5	-	Hou et al. (2017)
-0.399 – 0.929	0.04 – 0.4	254, 365	Turolla et al. (2016)

Absorption and scattering coefficients

These coefficients specify the amount of light that is absorbed or scattered at specific wavelengths. The sum of the absorption and scattering coefficients of a catalyst slurry is the extinction coefficient which can be easily measured using a spectrophotometer, as shown in Figure 2.11a. The extinction coefficient is not useful for the solution of the RTE. It is still necessary to extract either the absorption or scattering coefficient from the extinction coefficient. Cabrera et al. (1996) were the first researchers to tackle this challenge. They used an integrating sphere to measure the diffuse transmission through a catalyst slurry (Figure 2.11b). Then, they modelled the light transmission through the sample cell using one-

dimensional, one-directional RTE which they solved using the discrete ordinates method. By comparing the experimental and simulated transmission values, they were able to obtain the absorption and scattering coefficients. In solving the RTE, they assumed the diffuse reflectance phase function.

Subsequent studies used a similar methodology but employed the isotropic phase function (Brandi et al., 1999; Romero et al., 2003; Tolosana-Moranchel et al., 2017). All these studies reported the absorption and scattering coefficients of several commercial brands of TiO_2. Other studies have used a similar experimental methodology to determine the optical properties of $NiFe_2O_4$ (Domínguez-Arvizu et al., 2019) and $LiVMoO_6$ (Hurtado et al., 2015). These studies used the six-flux method instead of the discrete ordinates method to solve the RTE.

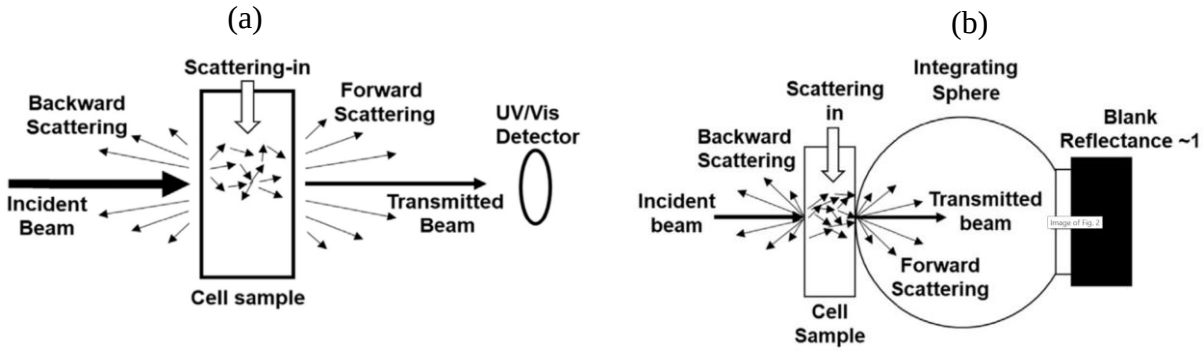

Figure 2.11: Experimental set up for (a) Extinction coefficient (b) Absorption coefficient (Domínguez-Arvizu et al., 2019)

These previous studies assumed that the catalysts scattered light according to a predetermined phase function. Instead of assuming a phase function, Satuf et al. (2005) set out to determine the appropriate phase function in addition to the scattering and absorption coefficients of several commercial TiO_2 catalysts. They used the Henyey-Greenstein phase function in the RTE and computed the asymmetry factor that resulted in the least error between measured and simulated transmittance. To do this, they measured the diffuse reflectance in addition to the light transmittance through the catalyst slurry. The optical properties of two of the catalysts from this study are shown in Figure 2.12. A similar methodology was used to determine the absorption and scattering coefficients as well as the HG asymmetry factor of commercial carbon doped TiO_2 (Manassero et al., 2013) and synthesized TiO_2-rGO (Tolosana-Moranchel et al., 2019). The latter study employed the Monte Carlo method instead of the discrete ordinates method to solve the RTE.

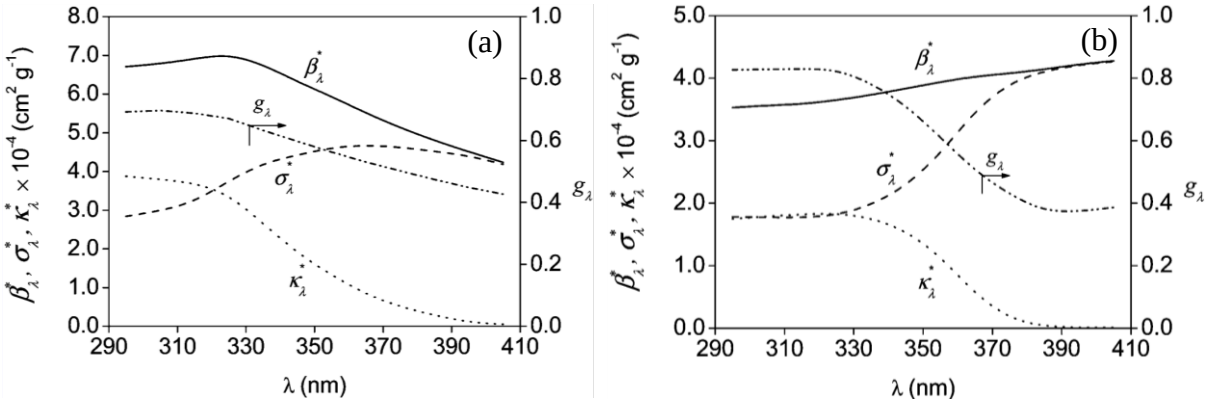

Figure 2.12: Absorption coefficient (κ_λ), scattering coefficient (σ_λ), extinction coefficients (β_λ), HG asymmetry factor (g_λ) of (a) Degussa P25 TiO_2 and (b) Aldrich TiO_2 (Satuf et al., 2005)

Simpler methods have also been employed to determine absorption and scattering coefficients. Grčić and Puma et al. (2017) measured the diffuse reflectance spectra (DRS) of the solid catalysts and the extinction coefficients of the slurry catalyst. From these two measurements, they obtained a series of simple equations from which they obtained the absorption and scattering coefficients of P25 TiO_2 and synthesized Ag@TiO_2 catalysts. Moreira et al. (2011) obtained absorption and scattering coefficients of three commercial TiO_2 catalysts using an annular reactor. They used Monte Carlo simulation with isotropic scattering to determine the wavelength-averaged absorption and scattering coefficients that resulted in the least error between experimental and measured light intensity at the reactor wall. Turolla et al. (2016) used an optical goniometer and CFD-based discrete ordinates method to estimate the absorption and scattering coefficients of Aeroxide P25 TiO_2 at a wavelength of 254 and 355 nm. A summary of the studies which have reported absorption and scattering coefficients is given in Table 2.4.

Table 2.4: Experimental determination of absorption and scattering coefficients

Catalyst	Experimental set up	Simulation model	Catalyst loading (g/L)	Wavelength (nm)	Reference
Aldrich/ Merck/ Fisher/ Fluka/ Degussa P25/ Hombikat TiO_2	Extinction Diffuse transmittance	DOM DR phase function	0.1 – 1	275 – 405	Cabrera et al. (1996)
Aldrich/ Degussa P25 TiO_2	Extinction Diffuse transmittance	DOM ISO phase function	0.025 – 5	315 – 435	Brandi et al. (1999) Romero et al. (2003)

Catalyst	Experimental set up	Simulation model	Catalyst loading (g/L)	Wavelength (nm)	Reference
P25 Aeroxide/ P90 Aeroxide/ P25/20 VP Aeroperl TiO_2	Extinction Diffuse transmittance	DOM ISO phase function	0.05 – 1.5	345 – 405	Tolosana-Moranchel et al. (2017)
Commercial $NiFe_2O_4$ Synthesized $NiFe_2O_4$	Extinction Diffuse transmittance	Six-flux ISO phase function	0.1 – 0.4	300 – 850	Domínguez-Arvizu et al. (2019)
$LiVMoO_6$	Extinction Diffuse transmittance Diffuse reflectance	Six-flux ISO phase function	0.25 – 0.75	280 – 500	Hurtado et al. (2015)
Aldrich/ Degussa P25/ Hombikat UV100 TiO_2	Extinction Diffuse transmittance Diffuse reflectance	DOM HG phase function	0.2 – 2	295 – 405	Satuf et al. (2005)
P25 Aeroxide/ Kronos vlp 7000 TiO_2	Extinction Diffuse transmittance Diffuse reflectance	DOM HG phase function	0.1 – 0.5	P25: 400 – 550 vlp: 300 – 550	Manassero et al. (2013)
TiO_2-rGO	Extinction Diffuse transmittance Diffuse reflectance	Monte Carlo HG phase function	0.05 – 0.4	315 – 415	Tolosana-Moranchel et al. (2019)
P25 Aeroxide TiO_2/ Ag@TiO_2	DRS Extinction	-	0.1 – 2	300 – 800	Grčić and Puma et al. (2017)
Degussa P25/ Aldrich/ Hombikat UV 100 TiO_2	Total transmittance Direct transmittance	Monte Carlo, ISO phase function	0 – 0.2	300 – 388 (wavelength-averaged)	Moreira et al. (2011)
P25 Aeroxide TiO_2	Angular irradiance	CFD-DOM HG phase function	0.04 – 0.4	254, 365	Turolla et al. (2016)

The three optical properties: absorption coefficient, scattering coefficient and scattering phase function are interrelated. Satuf et al. (2005) showed that using different scattering phase functions resulted in remarkably different values of the absorption and scattering coefficients. Several authors have used previously reported optical properties to simulate the light distribution in their reactors. However, the catalyst agglomeration size in the simulated reactor may not be similar to the catalyst size in the reactor that was used to generate the optical properties. This is especially true in cases where optical properties are determined under ultrasonication while the catalysts in the simulated reactor are only fluidized by wastewater recirculation. For this reason, several studies have chosen to evaluate the HG phase parameter specific to their reactor before simulating the light distribution in the reactor (Valades-Pelayo et al., 2014a; Turolla et al., 2016; Hou et al., 2017).

2.8.4 Influence of bubbles on light distribution

In a fluidized bed photoreactors, bubbles play an important part in fluidization and supply of oxygen. From the perspective of light distribution, they can be considered as inert media with a possible impact on light distribution and absorption by the catalyst. Several studies have analysed the light distribution in fluidized bed reactors in which bubbles interact with light. Boyjoo et al. (2013b) simulated the light distribution in a multi-lamp slurry bubble column reactor using the discrete ordinates method. They found that bubble scattering was negligible as compared to the catalyst scattering. Motegh et al. (2013) utilized a bi-directional scattering model to study the effect of bubbles in a theoretical three-phase reactor with suspended catalysts. They concluded that bubbles at typical sizes and gas flow rates have no significant effect on the light absorption. Trujillo et al. (2007) used the discrete ordinates method to model the light distribution on catalysts immobilized on flat plates which were immersed in a bubble column. They found that bubble scattering improved the light distribution on the flat plates.

2.8.5 Validation of light distribution models

In order to ensure that the light distribution model is accurate, validation is normally carried out by comparing the experimental and simulated light intensity at certain locations in the reactor. Initially validation was commonly carried out using actinometric techniques. In one experiment, an annular reactor was surrounded by an annular space filled with potassium ferrioxalate actinometer in order to measure the radiation exiting the wall of the reactor (Romero et al., 2003). Nowadays, light distribution models are mostly validated by measuring the forward transmitted radiation at the reactor wall using a radiometer (Figure 2.13a). This is common practice in internally illuminated annular reactors (Imoberdorf et al., 2008; Moreira

et al., 2011; Valades-Pelayo et al., 2014b). Validation has also been carried out by measuring the light intensity at different radial locations within the annulus using a spectroradiometric probe (Figure 2.13b). The measured radial intensity profiles are better data for the validation of radiation gradients within the reactor as compared to measurements only at the reactor wall (Valadés-Pelayo et al., 2014a). A similar approach was employed to establish the local light intensity at different depths of a reactor illuminated from the top with a collimated light source (Cao et al., 2014) (Figure 2.13c) and UV lamp (Hou et al., 2017) (Figure 2.13d). One of the most versatile validation methods was developed by Valadés-Pelayo et al. (2015a) to measure the light intensity at various axial locations and azimuthal directions in an externally illuminated annular reactor (Figure 2.13e).

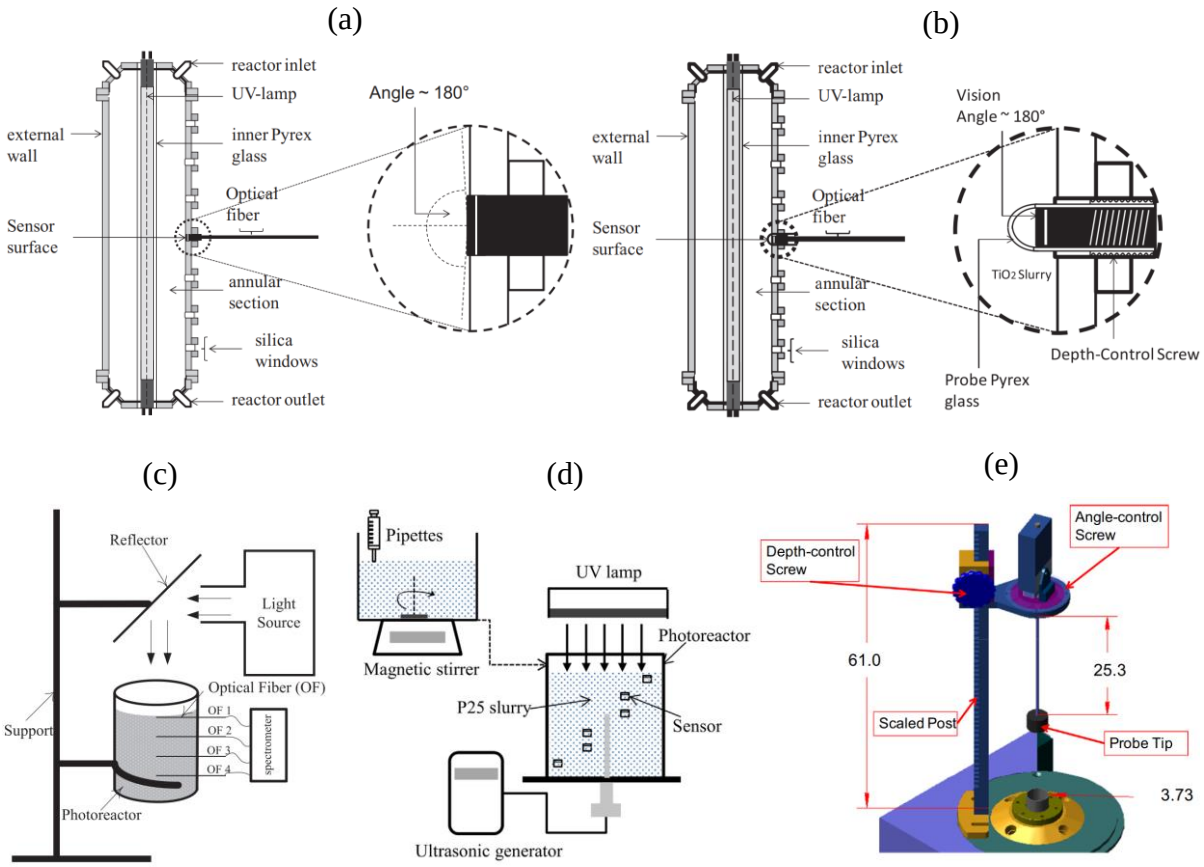

Figure 2.13: Validation methods (a) Total transmittance (Valadés-Pelayo et al., 2014b) (b) Radial intensity (Valadés-Pelayo et al., 2014a) (c) Optical fibres (Cao et al., 2014) (d) Underwater sensors (Hou et al., 2017) (e) Probe depth/angle mechanism (Valadés-Pelayo et al., 2015a)

2.9 Photocatalysis kinetics

The rate of photocatalysis generally follows the Langmuir-Hinshelwood kinetics (Gaya and Abdullah, 2008):

$$r = -\frac{dC}{dt} = \frac{kKC}{1 + KC} \tag{2.15}$$

where r is the rate of reaction, C is the substrate concentration at time t, k is the reaction rate constant and K is the Langmuir adsorption constant. Photocatalysis is normally carried out with wastewaters of a low substrate concentration of several mM. Therefore, $C \ll 1$ and eq. (2.15) simplifies to the pseudo-first order kinetics:

$$r = -\frac{dC}{dt} = kKC = k_{app}C \tag{2.16}$$

where k_{app} is the apparent first order rate constant. Integrating eq. 2.16 yields:

$$\ln\frac{C_0}{C} = k_{app}t \tag{2.17}$$

In eq. 2.17, k_{app} can be obtained as the slope of a graph of $\ln C_0/C$ vs. t where C_0 is the initial substrate concentration.

The rate of photocatalysis depends on several factors such as the solution pH, temperature, dissolved oxygen concentration, catalyst type and loading, pollutant concentration, reactor diameter and light intensity (Boyjoo et al., 2013a):

$$-r = f(pH, T, DO, cat, C, D, I) \tag{2.18}$$

In photochemical reactions, the catalyst has to absorb light in order to be activated. Consequently, the reaction rate depends on the absorbed light rather than the incident light intensity (Valadés-Pelayo et al., 2014a). Therefore, the amount of light absorbed by the catalysts in the reactor, known as the volumetric rate of energy absorption (VREA), is a more meaningful parameter than the light source intensity (Boyjoo et al., 2013a). This is due to the fact that the VREA captures aspects of the light source and reactor geometry (Li Puma et al., 2010). The rate of the reaction can then be expressed as a function of VREA and other terms as:

$$-r = f(pH, T, DO, cat, C, VREA) \tag{2.19}$$

The pseudo-first order kinetics (eq. 2.16) can be expressed using a power law dependence on the VREA (Li Puma et al., 2004; Li Puma et al., 2010) as:

$$-r = k_{int} VREA^{\alpha} C \tag{2.20}$$

where k_{int} is the intrinsic rate constant which is independent of the reactor geometry but depends on the solution pH, temperature, dissolved oxygen and catalyst type and loading. The exponent α defines how the absorbed light contributes to the successful generation and separation of electron-hole pairs. It can take any value between 0.5 and 1. At low values of VREA, $\alpha = 1$ since very little electron-hole recombination occurs. However, as VREA increases, the rate of electron-hole generation outstrips the rate of photocatalysis resulting in electron-hole recombination. In such a situation, the value of α reduces to 0.5 (Li Puma et al., 2004).

In a typical, optically thick photoreactor, several reaction regimes exist in the same reactor. At regions near the light source, half order reactions ($\alpha = 0.5$) are common due to a high value of light absorption. Deeper in the photoreactor, as light absorption reduces, full order reactions ($\alpha = 1$) dominate (Boyjoo et al., 2013a; Boyjoo et al., 2014a). Therefore, most photoreactors have a value of α between 0.5 and 1. For example, Li Puma et al. (2004) reported a value of 0.82 for a 30 mm diameter reactor illuminated by a UVA lamp.

2.10 Summary and research gaps

Several methods such as biological treatment, adsorption and various advanced oxidation processes have been developed for the treatment of aromatic compounds such as phenol (Busca et al., 2008; Mohammadi et al., 2014). Of these, the advanced oxidation process of photocatalysis has attracted a lot of attention due to its non-selective degradation of recalcitrant compounds at relatively low cost and without generating secondary waste (Ahmed et al., 2010). Nevertheless, photocatalysis still faces several challenges including lack of adequate photocatalysts, high cost and reliable light sources, efficient reactors and tools for reactor design and scale up.

Despite the development of many different types of catalysts, very few of them have been produced at industrial scale. Moreover, most studies oriented towards reactor modelling and design have employed Aeroxide P25 TiO_2 (Moreira et al., 2010; Boyjoo et al., 2014a; Valadés-Pelayo et al., 2014b). This is due to the fact that crucial optical data has only been provided for this kind of catalyst and other commercial types such as Hombikat, Tronox, Aldrich and Aeroxide P90 (Cabrera et al., 1996; Manassero et al., 2013; Tolosana-Moranchel et al., 2017).

The development of optical data such as absorption and scattering coefficients requires specialist instruments and mathematical rigour (Satuf et al., 2005). Therefore, most studies default to using the catalysts for which optical data is available. Experimental comparison of various commercial TiO_2 catalysts such as P25, Hombikat, Tronox and Aldrich has consistently revealed the higher reactivity of P25 TiO_2 (Ioannou et al., 2011; Dimitrakopoulou et al., 2012; Pelaez et al., 2012). Aeroxide P25 TiO_2 has also been extensively applied in pilot scale photocatalytic reactors (Mueses et al., 2013; Boyjoo et al., 2014a; Vela et al., 2018; Grilla et al., 2019). This also can be attributed to the fact that pilot scale studies look forward to industrial implementation and would thus employ a widely available catalysts with stable characteristics developed by a reputable company.

Several reactors have been developed for photocatalysis including thin film, rotating disk, membrane, slurry and fluidized bed reactors (McCullagh et al., 2011). Most of these reactors suffer from low throughput, complicated construction and the use of costly consumables. In this respect, the fluidized bed reactor has emerged as one of the best photocatalytic reactors due to its high mass transfer characteristics, simple construction and low cost (Braham and Harris, 2009). The air fluidized bed reactor, in particular, is attractive due to the use of air for fluidization which reduces fluidization cost while supplying oxygen directly into the reactor (Gaya and Abdullah, 2008). This reactor belongs to the family of multiphase reactors, of which a bubble column reactor may be considered a simplified version with only the liquid and gas phases. In order to design, scale up and optimize the air fluidized bed reactor, the hydrodynamics, light distribution and reaction kinetics in the reactor needs to be analysed (Boyjoo et al., 2013a). The most effective method of analysing reactor hydrodynamics is the use of CFD technique.

The CFD simulation of bubble columns (Kulkarni et al., 2007; Tabib et al., 2008; Ekambara and Dhotre, 2010) and general three phase fluidized bed reactors (Schallenberg et al., 2005; Panneerselvam et al., 2009) has been carried out. However, very little has been done on the CFD simulation of the type of the reactor employed for photocatalysis in this work: an annular fluidized bed reactor with nanoparticles. Feng et al. (2005) analysed the hydrodynamics of gas-liquid-nanoparticles in a rectangular fluidized bed using the CFD technique. They used a two-phase model for their work in which the liquid and nanoparticles comprised a single phase. As a result, they could not show the catalyst distribution which is a crucial aspect for photocatalysis. A better simulation was carried out by Qi et al. (2011) and Boyjoo et al. (2014a) in which three phase simulation was carried out in an annular fluidized bed reactor. Considering

how widely this kind of reactor has been employed for photocatalysis, much more work needs to be carried out to analyse its hydrodynamics. In the process of CFD simulation, the best models for simulating turbulence and interfacial forces needs to be evaluated.

In photocatalytic reactors, the light distribution has been analysed by solving the RTE using various numerical methods. These include the approximate P1 and six-flux methods as well as the more rigorous discrete ordinates and Monte Carlo method (Boyjoo et al., 2013a). The Monte Carlo method has been preferred by several researchers due to its accuracy and flexibility (Moreira et al., 2010; Valadés-Pelayo et al., 2014a). The light distribution in UV lamp illuminated reactors has been evaluated extensively using different methods (Orozco et al., 2009; Li Puma et al., 2010; Moreira et al., 2010; Boyjoo et al., 2013b). All these previous studies were carried out in a slurry photocatalytic reactor with no air bubbles. The Monte Carlo method has never been used to model the light distribution in a fluidized bed reactor with bubbles. An important question in a fluidized bed photoreactor is the effect of bubbles on light absorption and if it is necessary to include bubble simulation in the light distribution model (Motegh et al., 2013). The only study which attempted to answer this question, Motegh et al. (2013), concluded that bubbles have a negligible effect on light absorption by the catalysts. However, they modelled a theoretical reactor using a highly simplified model which was not validated. Clearly more work needs to be carried out in this area using validated rigorous models in order to determine the effect of bubbles on light absorption.

A similar situation has been observed in the simulation of the light distribution in solar illuminated reactors. Previous simulation studies were carried out in tubular or compound parabolic concentrator (CPC) solar reactors in which the only phases were wastewater and catalyst particles (Colina-Márquez et al., 2009; Colina-Márquez et al., 2010; Mueses et al., 2013; Acosta-Herazo et al., 2016; Ochoa-Gutiérrez et al., 2018; Casado et al., 2019). The light distribution in a solar illuminated fluidized bed reactor with bubbles has not been reported. This aspect of light distribution modelling also needs to be investigated for solar illuminated reactors since sunlight has a significant direct component in comparison to UV lamps whose output is predominantly diffuse.

Several studies on the light distribution in UV lamp illuminated reactors explicitly validated their light distribution models using light transmission measurements to establish model accuracy (Moreira et al., 2010; Valadés-Pelayo et al., 2014a, 2014b, 2015a; Hou et al., 2017). In contrast, most of the solar light distribution studies indirectly validated their models by

fitting the local volumetric rate of energy absorption (LVREA) data to the reaction rate (Colina-Márquez et al., 2009; Colina-Márquez et al., 2010). This recursive validation technique has the potential of hiding errors in the light distribution model. Moreover, most of the previous studies did not consider light refraction at the wall of the reactor which significantly affects the direction of solar light transmission in the reactor. This is a significant factor due to the fact that a significant proportion of sunlight is direct in nature and could be subject to significant refraction.

Hybrid light reactors, internally illuminated by the UV lamp and externally illuminated by sunlight, have advantages of good illumination in a compact device. Such a solar/UV lamp hybrid light reactor has been developed for gas phase photocatalysis (Portela et al., 2011, 2012; Monteiro et al., 2015). A few hybrid light reactors have been reported for wastewater treatment (Orozco et al., 2009; Durán et al., 2018a); however, none of these were typical annular reactors. The reactor developed by Durán et al. (2018a) was essentially a rotating drum reactor consisting of a catalyst coated quartz drum which was internally irradiated by a UVC lamp and externally illuminated by sunlight. Orozco et al. (2009) designed a hybrid light reactor made of an acrylic box which was internally irradiated by 6 black light lamps and illuminated by sunlight through a transparent glass at the top of the reactor. These previous studies employed low-pressure mercury lamps in their hybrid light reactors. Despite the advances made in the development of UV LED lamps, their application in photocatalysis is still limited by high cost and low efficiency (Matafonova and Batoev, 2018). Therefore, low pressure black light lamps are still recommended for use in hybrid light reactors as their output matches the solar spectrum.

Unlike UV lamp illuminated reactors and solar illuminated reactors, very few studies have investigated the light distribution in hybrid light illuminated reactors. Orozco et al. (2009) simulated the light distribution in their box-type hybrid light reactor. However, the light distribution in an annular-type hybrid solar/UV lamp reactor has not been reported. In order to establish the light distribution in a hybrid light reactor, several issues need to be addressed. First, the scattering phase function has been found to be a function of catalyst agglomeration size and light wavelength (Satuf et al., 2005; Valadés-Pelayo et al., 2015b). Consequently, the HG scattering parameter needs to be evaluated under UV lamp and solar illumination under normal conditions of reactor operation.

Secondly, the photocatalysis reaction rate depends on the light source (Li Puma et al., 2010; Joseph et al., 2016). Therefore, an analysis of the LVREA in a reactor illuminated by different light sources would not be very meaningful. An alternative parameter such as the local reaction rate (LRR) which encapsulates the effect of both light sources on catalyst reactivity would be more appropriate. As opposed to the LVREA, the LRR has been investigated by only one study in the context of UV lamp illumination (Boyjoo et al., 2014a). In order to establish the LRR, the intrinsic kinetics and the reaction order with respect to the VREA should be known. These values have only been reported for an annular UV reactor (Li Puma et al., 2004).

Solar energy is desirable for photocatalysis since it is free, renewable and contains UV light. However, sunlight is a very unpredictable source of energy as it varies by cloud cover, time of day and seasons (Natarajan et al., 2011). One way of addressing these challenges, while keeping costs low, would be to supplement sunlight with an artificial light when the solar intensity reduces. This can be carried out by a hybrid light illuminated reactor with sunlight as the primary light source and the UV lamp as the secondary light source. Such a system has been reported for gas-phase hybrid reactors which employed an ON/OFF control scheme in which the lamp was only switched on at night (Portela et al., 2011) or when the solar intensity dropped below a certain threshold (Portela et al., 2012). A better control scheme would incorporate a real-time lamp controller to continuously adjust the lamp intensity in response to the current solar intensity. Such a system has not been reported in literature.

In this thesis, the photocatalysis of phenol was carried out in a hybrid light reactor. Phenol was selected as the target substrate due to its widespread use in many industries and its recalcitrant nature. Also, phenol has emerged as one of the standard substrates for photocatalysis (Wang et al., 2004; Visa and Duta, 2013). Photocatalysis was carried out in a fluidized bed reactor due to its simplicity and high mass transfer rates. The nanophase Aeroxide P25 TiO_2 was used in the fluidized bed reactor due to its widespread use, high reactivity and the availability of its optical properties. Instead of employing a purely experimental approach, simulation and modelling with validation at every step was preferred. This methodology was considered to be more useful for reactor design, scale up and optimization as it could be more easily adapted to reactor of other sizes. The simulation approach also had the advantage of providing a detailed analysis of the hydrodynamics, light distribution and reaction kinetics in the reactor.

First, the gas-liquid-solid hydrodynamics in the annular fluidized bed reactor was analysed using the CFD technique. This was followed by the simulation of the light distribution in the

reactor under UV lamp illumination in order to determine the effect of catalyst loading and bubbles on the light distribution. Then, the simulation of the solar illuminated reactor was carried out to determine the effect of bubbles and refraction on light distribution. The LRR in the hybrid solar/UV lamp illuminated reactor was then determined at different catalyst loadings. Finally, a real-time hybrid light controller was designed using the simulation data. The Monte Carlo method was used to simulate the light distribution due to its accuracy and flexibility.

References

Acosta-Herazo, R., Monterroza-Romero, J., Mueses, M. Á., Machuca-Martínez, F., and Li Puma, G., 2016. Coupling the Six Flux Absorption–Scattering Model to the Henyey–Greenstein scattering phase function: Evaluation and optimization of radiation absorption in solar heterogeneous photoreactors. *Chemical Engineering Journal*, *302*, 86–96.

Acosta-Herazo, R., Valadés-Pelayo, P.J., Mueses, M.A., Pinzón-Cárdenas, M.H., Arancibia-Bulnes, C. and Machuca-Martínez, F., 2020. An optical and energy absorption analysis of the solar compound parabolic collector photoreactor (CPCP): The impact of the radiation distribution on its optimization. *Chemical Engineering Journal*, *395*, 125065.

Ahmed, S., Rasul, M.G., Martens, W.N., Brown, R. and Hashib, M.A., 2010. Heterogeneous photocatalytic degradation of phenols in wastewater: A review on current status and developments. *Desalination*, *261*(1–2), 3-18.

Akach, J., Onyango, M. S. and Ochieng, A., Adsorption and photodegradation of sulfamethoxazole in a three-phase fluidized bed reactor in: Singh, D.P., Kothari, R. and Tyagi, V.V. (editors), 2016. *Emerging Energy Alternatives for Sustainable Environment*. The Energy and Resources Institute (TERI), 141-152. ISBN 978-81-7993-411-1

Al-Hamdi, A.M., Rinner, U. and Sillanpää, M., 2017. Tin dioxide as a photocatalyst for water treatment: a review. *Process Safety and Environmental Protection*, *107*, 190-205.

Al-Khalid, T. and El-Naas, M. H., 2012. Aerobic biodegradation of phenols: a comprehensive review. *Critical Reviews in Environmental Science and Technology*, *42*(16), 1631-1690.

Al-Rasheed, R. and Cardin, D. J., 2003. Photocatalytic degradation of humic acid in saline waters. Part 1. Artificial seawater: influence of TiO_2, temperature, pH, and air-flow. *Chemosphere*, *51*(9), 925-933.

Antal, S.P., Lahey Jr, R.T. and Flaherty, J.E., 1991. Analysis of phase distribution in fully developed laminar bubbly two-phase flow. *International Journal of Multiphase Flow*, *17*(5), 635-652.

Apollo, S. and Aoyi, O., 2016. Combined anaerobic digestion and photocatalytic treatment of distillery effluent in fluidized bed reactors focusing on energy conservation. *Environmental Technology*, *37*(17), 2243-2251.

Ayodhya, D. and Veerabhadram, G., 2018. A review on recent advances in photodegradation of dyes using doped and heterojunction based semiconductor metal sulfide nanostructures for environmental protection. *Materials Today Energy*, *9*, 83-113.

Bannari, R., Kerdouss, F., Selma, B., Bannari, A. and Proulx, P., 2008. Three-dimensional mathematical modeling of dispersed two-phase flow using class method of population balance in bubble columns. *Computers & Chemical Engineering*, *32*(12), 3224-3237.

Baransi, K., Dubowski, Y. and Sabbah, I., 2012. Synergetic effect between photocatalytic degradation and adsorption processes on the removal of phenolic compounds from olive mill wastewater. *Water Research*, *46*(3), 789-798.

Besbes, S., El Hajem, M., Aissia, H.B., Champagne, J.Y. and Jay, J., 2015. PIV measurements and Eulerian–Lagrangian simulations of the unsteady gas–liquid flow in a needle sparger rectangular bubble column. *Chemical Engineering Science*, *126*, 560-572.

Boiarkina, I., Norris, S. and Patterson, D. A., 2013. Investigation into the effect of flow structure on the photocatalytic degradation of methylene blue and dehydroabietic acid in a spinning disc reactor. *Chemical Engineering Journal*, *222*, 159-171.

Boyjoo, Y., Ang, M. and Pareek, V., 2013a. Some aspects of photocatalytic reactor modeling using computational fluid dynamics. *Chemical Engineering Science*, *101*, 764-784.

Boyjoo, Y., Ang, M. and Pareek, V., 2013b. Light intensity distribution in multi-lamp photocatalytic reactors, *Chemical Engineering Science*, *93*, 11-21.

Boyjoo, Y., Ang, M. and Pareek, V., 2014a. CFD simulation of a pilot scale slurry photocatalytic reactor and design of multiple-lamp reactors. *Chemical Engineering Science*, *111*, 266-277.

Boyjoo, Y., Ang, M. and Pareek, V., 2014b. Lamp emission and quartz sleeve modelling in slurry photocatalytic reactors. *Chemical Engineering Science*, *111*, 34-40.

Braham, R. J. and Harris, A. T., 2009. Review of major design and scale-up considerations for solar photocatalytic reactors, *Industrial & Engineering Chemistry Research*, *48*(19), 8890-8905.

Brandi, R.J., Alfano, O.M. and Cassano, A.E., 1999. Rigorous model and experimental verification of the radiation field in a flat-plate solar collector simulator employed for photocatalytic reactions. *Chemical Engineering Science*, *54*(13-14), 2817-2827.

Buffo, A., Marchisio, D.L., Vanni, M. and Renze, P., 2013. Simulation of polydisperse multiphase systems using population balances and example application to bubbly flows. *Chemical Engineering Research and Design*, *91*(10), 1859-1875.

Burns, A.D., Frank, T., Hamill, I. and Shi, J.M., 2004, May. The Favre averaged drag model for turbulent dispersion in Eulerian multi-phase flows. In *5th international conference on multiphase flow, ICMF* (Vol. 4, 1-17). ICMF.

Busca, G., Berardinelli, S., Resini, C. and Arrighi, L., 2008. Technologies for the removal of phenol from fluid streams: a short review of recent developments. *Journal of Hazardous Materials*, *160*(2-3), 265-288.

Cabrera, M.I., Alfano, O.M. and Cassano, A.E., 1996. Absorption and scattering coefficients of titanium dioxide particulate suspensions in water. *The Journal of Physical Chemistry*, *100*(51), 20043-20050.

Camera-Roda, G., Augugliaro, V., Cardillo, A. G., Loddo, V., Palmisano, L., Parrino, F. and Santarelli, F., 2016. A reaction engineering approach to kinetic analysis of photocatalytic reactions in slurry systems, *Catalysis Today*, *259*, Part 1, 87-96.

Cao, B., Nagarajan, K. and Loh, K., 2009. Biodegradation of aromatic compounds: current status and opportunities for biomolecular approaches. *Applied Microbiology and Biotechnology*, *85*(2), 207-228.

Cao, F., Li, H., Chao, H., Zhao, L. and Guo, L., 2014. Optimization of the concentration field in a suspended photocatalytic reactor. *Energy*, *74*, 140-146.

Casado, C., García-Gil, Á., van Grieken, R. and Marugán, J., 2019. Critical role of the light spectrum on the simulation of solar photocatalytic reactors. *Applied Catalysis B: Environmental*, *252*, 1–9.

Casado, C., Marugán, J., Timmers, R., Muñoz, M. and van Grieken, R., 2017. Comprehensive multiphysics modeling of photocatalytic processes by computational fluid dynamics based on intrinsic kinetic parameters determined in a differential photoreactor. *Chemical Engineering Journal*, *310*, 368-380.

Charinpanitkul, T., Limsuwan, P., Chalotorn, C., Sano, N., Yamamoto, T., Tongpram, P., Wongsarivej, P., Soottitantawat, A. and Tanthapanichakoon, W., 2010. Synergetic removal of aqueous phenol by ozone and activated carbon within three-phase fluidized-bed reactor. *Journal of Industrial and Engineering Chemistry*, *16*(1), 91-95.

Chedeville, O., Debacq, M., Almanza, M.F. and Porte, C., 2007. Use of an ejector for phenol containing water treatment by ozonation. *Separation and Purification Technology*, *57*(2), 201-208.

Chekir, N., Tassalit, D., Benhabiles, O., Merzouk, N. K., Ghenna, M., Abdessemed, A. and Issaadi, R., 2017. A comparative study of tartrazine degradation using UV and solar fixed bed reactors. *International Journal of Hydrogen Energy*, *42*(13), 8948-8954.

Chen, X., Dai, Y. and Wang, X., 2015. Methods and mechanism for improvement of photocatalytic activity and stability of Ag_3PO_4: a review. *Journal of Alloys and Compounds*, *649*, 910-932.

Chong, M. N., Jin, B., Chow, C. W. and Saint, C., 2010. Recent developments in photocatalytic water treatment technology: a review, *Water Research*, *44*(10), 2997-3027.

Chong, M.N., Lei, S., Jin, B., Saint, C. and Chow, C.W., 2009. Optimisation of an annular photoreactor process for degradation of Congo Red using a newly synthesized titania impregnated kaolinite nano-photocatalyst. *Separation and Purification Technology*, *67*(3), 355-363.

Chowdhury, P. and Viraraghavan, T., 2009. Sonochemical degradation of chlorinated organic compounds, phenolic compounds and organic dyes–a review. *Science of the Total Environment*, *407*(8), 2474-2492.

Colina-Márquez, J., Machuca-Martínez, F. and Li Puma, G., 2009. Photocatalytic Mineralization of Commercial Herbicides in a Pilot-Scale Solar CPC Reactor: Photoreactor Modeling and Reaction Kinetics Constants Independent of Radiation Field, *Environmental Science & Technology*, *43*(23), 8953-8960.

Colina-Márquez, J., Machuca-Martínez, F. and Puma, G. L., 2010. Radiation Absorption and Optimization of Solar Photocatalytic Reactors for Environmental Applications, *Environmental Science & Technology*, *44*(13), 5112-5120.

Cuevas, S.A., Arancibia-Bulnes, C.A. and Serrano, B., 2007. Radiation field in an annular photocatalytic reactor by the P1 approximation. *International Journal of Chemical Reactor Engineering*, *5*(1).

Cutler, T. D. and Zimmerman, J. J., 2011. Ultraviolet irradiation and the mechanisms underlying its inactivation of infectious agents. *Animal Health Research Reviews*, *12*(1), 15-23.

Dalla Ville, J.M., 1948. Micrometrics. Pitman Publishing Co., New York.

Davididou, K., Nelson, R., Monteagudo, J. M., Durán, A., Expósito, A. J. and Chatzisymeon, E., 2018. Photocatalytic degradation of bisphenol-A under UV-LED, blacklight and solar irradiation. *Journal of Cleaner Production*, *203*, 13-21.

Davidson, P.A., 2015. Turbulence: an introduction for scientists and engineers. Oxford University Press.

Department of Water Affairs and Forestry, 1996. *South African Water Quality Guidelines. Volume 7: Aquatic Ecosystems.* Pretoria: Department of Water Affairs and Forestry.

Dhotre, M.T., Niceno, B. and Smith, B.L., 2008. Large eddy simulation of a bubble column using dynamic sub-grid scale model. *Chemical Engineering Journal*, *136*(2-3), 337-348.

Díaz, M.E., Iranzo, A., Cuadra, D., Barbero, R., Montes, F.J. and Galán, M.A., 2008. Numerical simulation of the gas–liquid flow in a laboratory scale bubble column: influence of bubble size distribution and non-drag forces. *Chemical Engineering Journal*, *139*(2), 363-379.

Díaz, M.E., Montes, F.J. and Galán, M.A., 2009. Influence of the lift force closures on the numerical simulation of bubble plumes in a rectangular bubble column. *Chemical Engineering Science*, *64*(5), 930-944.

Dimitrakopoulou, D., Rethemiotaki, I., Frontistis, Z., Xekoukoulotakis, N.P., Venieri, D. and Mantzavinos, D., 2012. Degradation, mineralization and antibiotic inactivation of amoxicillin by UV-A/TiO_2 photocatalysis. *Journal of Environmental Management*, *98*, 168-174.

Dominguez, S., Rivero, M. J., Gomez, P., Ibañez, R. and Ortiz, I., 2016. Kinetic modeling and energy evaluation of sodium dodecylbenzenesulfonate photocatalytic degradation in a new LED reactor. *Journal of Industrial and Engineering Chemistry*, *37*, 237-242.

Domínguez-Arvizu, J.L., Jiménez-Miramontes, J.A., Salinas-Gutiérrez, J.M., Meléndez-Zaragoza, M.J., López-Ortiz, A. and Collins-Martínez, V., 2019. Study of $NiFe_2O_4$ nanoparticles optical properties by a six-flux radiation model towards the photocatalytic hydrogen production. *International Journal of Hydrogen Energy*, *44*(24), 12455-12462.

Donaldson, A. A. and Zhang, Z., 2012. UV absorption by TiO_2 films in photocatalytic reactors: Effect of fold curvature. *AIChE Journal*, *58*(5), 1578-1587.

Durán, A., Monteagudo, J. M., San Martín, I. and Merino, S., 2018a. Photocatalytic degradation of aniline using an autonomous rotating drum reactor with both solar and UV-C artificial radiation. *Journal of Environmental Management*, *210*, 122-130.

Durán, A., Monteagudo, J.M. and San Martín, I., 2018b. Operation costs of the solar photo-catalytic degradation of pharmaceuticals in water: A mini-review. *Chemosphere*, *211*, 482-488.

Duran, J.E., Taghipour, F. and Mohseni, M., 2010. Irradiance modeling in annular photoreactors using the finite-volume method. *Journal of Photochemistry and Photobiology A: Chemistry*, *215*(1), 81-89.

Ekambara, K. and Dhotre, M.T., 2010. CFD simulation of bubble column. *Nuclear Engineering and Design*, *240*(5), 963-969.

Ekambara, K., Nandakumar, K. and Joshi, J.B., 2008. CFD simulation of bubble column reactor using population balance. *Industrial & Engineering Chemistry Research*, *47*(21), 8505-8516.

Eskandarian, M. R., Fazli, M., Rasoulifard, M. H. and Choi, H., 2016. Decomposition of organic chemicals by zeolite-TiO_2 nanocomposite supported onto low density polyethylene film under UV-LED powered by solar radiation. *Applied Catalysis B: Environmental*, *183*, 407-416.

Feng, W., Wen, J., Fan, J., Yuan, Q., Jia, X. and Sun, Y., 2005. Local hydrodynamics of gas–liquid-nanoparticles three-phase fluidization. *Chemical Engineering Science*, *60*(24), 6887-6898.

Frank, Th., Shi, J.M., Burns, A.D., 2004. Validation of Eulerian multiphase flow models for nuclear safety applications. In: *3rd International Symposium on Two-Phase Flow Modelling and Experimentation*, Pisa, Italy, 22–24.

Fu, J., Ji, M., Wang, Z., Jin, L. and An, D., 2006. A new submerged membrane photocatalysis reactor (SMPR) for fulvic acid removal using a nano-structured photocatalyst. *Journal of Hazardous Materials*, *131*(1-3), 238-242.

Gaya, U. I. and Abdullah, A. H., 2008. Heterogeneous photocatalytic degradation of organic contaminants over titanium dioxide: A review of fundamentals, progress and problems, *Journal of Photochemistry and Photobiology C: Photochemistry Reviews*, *9*(1), 1-12.

Ghosh, M., Chowdhury, P. and Ray, A.K., 2018. Study of solar photocatalytic degradation of Acesulfame K to limit the outpouring of artificial sweeteners. *Separation and Purification Technology*, *207*, 51-57.

Gogate, P. R., 2008. Treatment of wastewater streams containing phenolic compounds using hybrid techniques based on cavitation: a review of the current status and the way forward. *Ultrasonics Sonochemistry*, *15*(1), 1-15.

Gómez-Pastora, J., Dominguez, S., Bringas, E., Rivero, M.J., Ortiz, I. and Dionysiou, D.D., 2017. Review and perspectives on the use of magnetic nanophotocatalysts (MNPCs) in water treatment. *Chemical Engineering Journal*, *310*, 407-427.

Grabowska, E., Reszczyńska, J. and Zaleska, A., 2012. Mechanism of phenol photodegradation in the presence of pure and modified-TiO_2: A review. *Water Research*, *46*(17), 5453-5471.

Grace, J. R., Wairegi, T., & Nguyen, T. H., 1976. Shapes and velocities of single drops and bubbles moving freely through immiscible liquids. *Transactions of the Institution of Chemical Engineers*, *54*, 167–173.

Grilla, E., Matthaiou, V., Frontistis, Z., Oller, I., Polo, I., Malato, S. and Mantzavinos, D., 2019. Degradation of antibiotic trimethoprim by the combined action of sunlight, TiO_2 and persulfate: A pilot plant study. *Catalysis Today*, *328*, 216-222.

Grčić, I. and Puma, G.L., 2017. Six-flux absorption-scattering models for photocatalysis under wide-spectrum irradiation sources in annular and flat reactors using catalysts with different optical properties. *Applied Catalysis B: Environmental*, *211*, 222-234.

Gupta, A. and Roy, S., 2013. Euler–Euler simulation of bubbly flow in a rectangular bubble column: Experimental validation with Radioactive Particle Tracking. *Chemical Engineering Journal*, *225*, 818-836.

Hamidipour, M., Chen, J. and Larachi, F., 2012. CFD study on hydrodynamics in three-phase fluidized beds—Application of turbulence models and experimental validation. *Chemical Engineering Science*, *78*, 167-180.

Haranaka-Funai, D., Didier, F., Giménez, J., Marco, P., Esplugas, S. and Machulek-Junior, A., 2017. Photocatalytic treatment of valproic acid sodium salt with TiO_2 in different experimental devices: An economic and energetic comparison. *Chemical Engineering Journal*, *327*, 656-665.

Ho, N., Gamage, J. D. and Zhang, Z. J., 2010. Photocatalytic degradation of eriochrome black dye in a rotating corrugated drum photocatalytic reactor. *International Journal of Chemical Reactor Engineering*, *8*(1).

Hou, J., Wei, Q., Yang, Y. and Zhao, L., 2017. Experimental evaluation of scattering phase function and optimization of radiation absorption in solar photocatalytic reactors. *Applied Thermal Engineering*, *127*, 302-311.

Hurtado, L., Natividad, R., Torres-García, E., Farias, J. and Puma, G.L., 2015. Correlating the photocatalytic activity and the optical properties of $LiVMoO_6$ photocatalyst under the UV and the visible region of the solar radiation spectrum. *Chemical Engineering Journal*, *262*, 1284-1291.

Imoberdorf, G. E., Taghipour, F., Keshmiri, M. and Mohseni, M., 2008. Predictive radiation field modeling for fluidized bed photocatalytic reactors, *Chemical Engineering Science*, *63*(16), 4228-4238.

Ioannou, L. A., Hapeshi, E., Vasquez, M. I., Mantzavinos, D. and Fatta-Kassinos, D., 2011. Solar/TiO_2 photocatalytic decomposition of β-blockers atenolol and propranolol in water and wastewater. *Solar Energy*, *85*(9), 1915-1926.

Ishii, M., & Zuber, N. (1979). Drag coefficient and relative velocity in bubbly, droplet or particulate flows. *AIChE Journal*, *25*, 843–855.

Issabayeva, G., Hang, S. Y., Wong, M. C. and Aroua, M. K., 2017. A review on the adsorption of phenols from wastewater onto diverse groups of adsorbents. *Reviews in Chemical Engineering*, *34*(6), 855-873.

Jafarikojour, M., Dabir, B., Sohrabi, M. and Royaee, S. J., 2018. Application of a new immobilized impinging jet stream reactor for photocatalytic degradation of phenol: Reactor evaluation and kinetic modelling. *Journal of Photochemistry and Photobiology A: Chemistry*, *364*, 613-624.

Jiao, Y., Kovala, A. T., Shang, H. and Scott, J. A., 2019. A corrugated plate photocatalytic reactor for degradation of waterborne organic contaminants. *The Canadian Journal of Chemical Engineering*, *97*(6), 1760-1770.

Jo, W. K. and Tayade, R. J., 2014. Recent developments in photocatalytic dye degradation upon irradiation with energy-efficient light emitting diodes. *Chinese Journal of Catalysis*, *35*(11), 1781-1792.

Joseph, C. G., Taufiq-Yap, Y. H., Li Puma, G., Sanmugam, K. and Quek, K. S., 2016. Photocatalytic degradation of cationic dye simulated wastewater using four radiation sources, UVA, UVB, UVC and solar lamp of identical power output. *Desalination and Water Treatment*, *57*(17), 7976-7987.

Kazakis, N.A., Papadopoulos, I.D. and Mouza, A.A., 2007. Bubble columns with fine pore sparger operating in the pseudo-homogeneous regime: gas hold up prediction and a criterion for the transition to the heterogeneous regime. *Chemical Engineering Science*, *62*(12), 3092-3103.

Khademalrasool, M., Farbod, M. and Talebzadeh, M. D., 2016. The improvement of photocatalytic processes: Design of a photoreactor using high-power LEDs. *Journal of Science: Advanced Materials and Devices*, *1*(3), 382-387.

Khaki, M.R.D., Shafeeyan, M.S., Raman, A.A.A. and Daud, W.M.A.W., 2017. Application of doped photocatalysts for organic pollutant degradation – A review. *Journal of Environmental Management*, *198*, 78-94.

Kidak, R. and Ince, N. H., 2006. Ultrasonic destruction of phenol and substituted phenols: A review of current research. *Ultrasonics Sonochemistry*, *13*(3), 195-199.

Kuipers, J., Bruning, H., Yntema, D. and Rijnaarts, H., 2015. Wirelessly powered ultraviolet light emitting diodes for photocatalytic oxidation. *Journal of Photochemistry and Photobiology A: Chemistry*, *299*, 25-30.

Kulkarni, A.A., Ekambara, K. and Joshi, J.B., 2007. On the development of flow pattern in a bubble column reactor: experiments and CFD. *Chemical Engineering Science*, *62*(4), 1049-1072.

Kuo, W. S., Chiang, Y. H. and Lai, L. S., 2008. Solar photocatalysis of carbaryl rinsate promoted by dye photosensitization. *Dyes and Pigments*, *76*(1), 82-87.

Laborde-Boutet, C., Larachi, F., Dromard, N., Delsart, O. and Schweich, D., 2009. CFD simulation of bubble column flows: Investigations on turbulence models in RANS approach. *Chemical Engineering Science*, *64*(21), 4399-4413.

Lee, G.J. and Wu, J.J., 2017. Recent developments in ZnS photocatalysts from synthesis to photocatalytic applications—A review. *Powder Technology*, *318*, 8-22.

Legendre, D. and Magnaudet, J., 1998. The lift force on a spherical bubble in a viscous linear shear flow. *Journal of Fluid Mechanics*, *368*, 81-126.

Li Puma, G., Khor, J.N. and Brucato, A., 2004. Modeling of an annular photocatalytic reactor for water purification: oxidation of pesticides. *Environmental Science & Technology*, *38*(13), 3737-3745.

Li Puma, G., Puddu, V., Tsang, H. K., Gora, A. and Toepfer, B., 2010. Photocatalytic oxidation of multicomponent mixtures of estrogens (estrone (E1), 17β-estradiol (E2), 17α-ethynylestradiol (EE2) and estriol (E3)) under UVA and UVC radiation: Photon absorption, quantum yields and rate constants independent of photon absorption, *Applied Catalysis B: Environmental*, *99*(3–4), 388-397.

Li, K., Zhang, H., He, Y., Tang, T., Ying, D., Wang, Y., Sun, T., and Jia, J., 2015. Novel wedge structured rotating disk photocatalytic reactor for post-treatment of actual textile wastewater. *Chemical Engineering Journal*, *268*, 10-20.

Li, W. and Zhong, W., 2015. CFD simulation of hydrodynamics of gas–liquid–solid three-phase bubble column. *Powder Technology*, *286*, 766-788.

Liang, R., Fong, L. C. L. C., Arlos, M. J., Van Leeuwen, J., Shahnam, E., Peng, P., Servos, M.R. and Zhou, Y. N., 2017. Photocatalytic degradation using one-dimensional TiO_2 and Ag-TiO_2 nanobelts under UV-LED controlled periodic illumination. *Journal of Environmental Chemical Engineering*, *5*(5), 4365-4373.

Lin, C. N., Chang, C. Y., Huang, H. J., Tsai, D. P. and Wu, N. L., 2012. Photocatalytic degradation of methyl orange by a multi-layer rotating disk reactor. *Environmental Science and Pollution Research*, *19*(9), 3743-3750.

Lin, S. H. and Juang, R. S., 2009. Adsorption of phenol and its derivatives from water using synthetic resins and low-cost natural adsorbents: a review. *Journal of Environmental Management*, *90*(3), 1336-1349.

Liotta, L.F., Gruttadauria, M., Di Carlo, G., Perrini, G. and Librando, V., 2009. Heterogeneous catalytic degradation of phenolic substrates: catalysts activity. *Journal of Hazardous Materials*, *162*(2-3), 588-606.

Ljubas, D., Smoljanić, G. and Juretić, H., 2015. Degradation of Methyl Orange and Congo Red dyes by using TiO_2 nanoparticles activated by the solar and the solar-like radiation. *Journal of Environmental Management*, *161*, 83-91.

Lopez de Bertodano, M. A. (1992). Turbulent bubbly two-phase flow in a triangular duct. PhD dissertation, Rensselaer Polytechnic Institute, Troy, NY

Ma, D. and Ahmadi, G.J., 1990. A thermodynamical formulation for dispersed turbulent flows-1: basic theory. *International Journal of Multiphase Flow*, *16*, 323-340.

Malato, S., Blanco, J., Campos, A., Cáceres, J., Guillard, C., Herrmann, J. M. and Fernandez-Alba, A. R., 2003. Effect of operating parameters on the testing of new industrial titania catalysts at solar pilot plant scale. *Applied Catalysis B: Environmental*, *42*(4), 349-357.

Malato, S., Fernández-Ibáñez, P., Maldonado, M., Blanco, J. and Gernjak, W., 2009. Decontamination and disinfection of water by solar photocatalysis: Recent overview and trends, *Catalysis Today*, *147*(1), 1-59.

Manassero, A., Satuf, M.L. and Alfano, O.M., 2013. Evaluation of UV and visible light activity of TiO_2 catalysts for water remediation. *Chemical Engineering Journal*, *225*, 378-386.

Masood, R.M.A. and Delgado, A., 2014. Numerical investigation of the interphase forces and turbulence closure in 3D square bubble columns. *Chemical Engineering Science*, *108*, 154-168.

Masood, R.M.A., Rauh, C. and Delgado, A., 2014. CFD simulation of bubble column flows: An explicit algebraic Reynolds stress model approach. *International Journal of Multiphase Flow*, *66*, 11-25.

Matafonova, G. and Batoev, V., 2018. Recent advances in application of UV light-emitting diodes for degrading organic pollutants in water through advanced oxidation processes: A review. *Water Research, 132*, 177-189.

Matsumura, T., Noshiroya, D., Tokumura, M., Znad, H.T. and Kawase, Y., 2007. Simplified Model for the Hydrodynamics and Reaction Kinetics in a Gas-Liquid-Solid Three-Phase Fluidized-Bed Photocatalytic Reactor: Degradation of o-Cresol with Immobilized TiO_2. *Industrial & Engineering Chemistry Research*, *46*(8), 2637-2647.

McCullagh, C., Skillen, N., Adams, M. and Robertson, P.K., 2011. Photocatalytic reactors for environmental remediation: a review. *Journal of Chemical Technology & Biotechnology*, *86*(8), 1002-1017.

Miklos, D. B., Remy, C., Jekel, M., Linden, K. G., Drewes, J. E. and Hübner, U., 2018. Evaluation of advanced oxidation processes for water and wastewater treatment–A critical review. *Water Research, 139*, 118-131.

Mohammadi, S., Kargari, A., Sanaeepur, H., Abbassian, K., Najafi, A. and Mofarrah, E., 2014. Phenol removal from industrial wastewaters: a short review. *Desalination and Water Treatment*, *53*(8), 2215-2234.

Molinari, R., Lavorato, C. and Argurio, P., 2017. Recent progress of photocatalytic membrane reactors in water treatment and in synthesis of organic compounds. A review. *Catalysis Today, 281*, 144-164.

Monteiro, R.A., Rodrigues-Silva, C., Lopes, F.V., Silva, A.M., Boaventura, R.A. and Vilar, V.J., 2015. Evaluation of a solar/UV annular pilot scale reactor for 24 h continuous photocatalytic oxidation of n-decane. *Chemical Engineering Journal*, *280*, 409-416

Moreira, J., Serrano, B., Ortiz, A. and de Lasa, H., 2010. Evaluation of photon absorption in an aqueous TiO_2 slurry reactor using Monte Carlo simulations and macroscopic balance, *Industrial & Engineering Chemistry Research*, *49*(21), 10524-10534.

Moreira, J., Serrano, B., Ortiz, A. and de Lasa, H., 2011. TiO_2 absorption and scattering coefficients using Monte Carlo method and macroscopic balances in a photo-CREC unit. *Chemical Engineering Science*, *66*(23), 5813-5821.

Moreno-SanSegundo, J., Casado, C. and Marugan, J., 2020. Enhanced numerical simulation of photocatalytic reactors with an improved solver for the radiative transfer equation. *Chemical Engineering Journal*, *388*, 124183.

Motegh, M., van Ommen, J.R., Appel, P.W., Mudde, R.F. and Kreutzer, M.T., 2013. Bubbles scatter light, yet that does not hurt the performance of bubbly slurry photocatalytic reactors. *Chemical Engineering Science, 100*, 506-514.

Mozia, S., 2010. Photocatalytic membrane reactors (PMRs) in water and wastewater treatment. A review. *Separation and Purification Technology*, *73*(2), 71-91.

Mueses, M. A., Machuca-Martinez, F. and Li Puma, G., 2013. Effective quantum yield and reaction rate model for evaluation of photocatalytic degradation of water contaminants in heterogeneous pilot-scale solar photoreactors. *Chemical Engineering Journal*, *215–216*, 937-947.

Nafees, M. and Waseem, A., 2014. Organoclays as sorbent material for phenolic compounds: A review. *CLEAN–Soil, Air, Water*, *42*(11), 1500-1508.

Nam, W., Kim, J. and Han, G., 2002. Photocatalytic oxidation of methyl orange in a three-phase fluidized bed reactor. *Chemosphere*, *47*(9), 1019-1024.

Nam, W., Woo, K. and Han, G., 2009. Photooxidation of anionic surfactant (sodium lauryl sulfate) in a three-phase fluidized bed reactor using TiO_2/SiO_2 photocatalyst. *Journal of Industrial and Engineering Chemistry*, *15*(3), 348-353.

Nasir, A.M., Jaafar, J., Aziz, F., Yusof, N., Salleh, W.N.W., Ismail, A.F. and Aziz, M., 2020. A review on floating nanocomposite photocatalyst: Fabrication and applications for wastewater treatment. *Journal of Water Process Engineering*, *36*, 101300.

Natarajan, T.S., Thomas, M., Natarajan, K., Bajaj, H.C. and Tayade, R.J., 2011. Study on UV-LED/TiO_2 process for degradation of Rhodamine B dye. *Chemical Engineering Journal*, *169*(1–3), 126-134.

Ochoa-Gutierrez, K. S., Tabares-Aguilar, E., Mueses, M. Á., Machuca-Martínez, F. and Puma, G. L., 2018. A Novel Prototype Offset Multi Tubular Photoreactor (OMTP) for solar photocatalytic degradation of water contaminants. *Chemical Engineering Journal*, *341*, 628-638.

Orozco, S. L., Arancibia-Bulnes, C. A. and Suárez-Parra, R., 2009. Radiation absorption and degradation of an azo dye in a hybrid photocatalytic reactor, *Chemical Engineering Science* *64*(9), 2173-2185.

Orozco, S.L., Villafán-Vidales, H.I. and Arancibia-Bulnes, C.A., 2012. Photon absorption in a hybrid slurry photocatalytic reactor: Assessment of differential approximations. *AIChE Journal*, *58*(10), 3256-3265.

Oturan, M. A. and Aaron, J. J., 2014. Advanced oxidation processes in water/wastewater treatment: principles and applications. A review. *Critical Reviews in Environmental Science and Technology*, *44*(23), 2577-2641.

Pan, H., Chen, X.Z., Liang, X.F., Zhu, L.T. and Luo, Z.H., 2016. CFD simulations of gas–liquid–solid flow in fluidized bed reactors—A review. *Powder Technology*, *299*, 235-258.

Pang, M.J. and Wei, J.J., 2011. Analysis of drag and lift coefficient expressions of bubbly flow system for low to medium Reynolds number. *Nuclear Engineering and Design*, *241*(6), 2204-2213.

Panneerselvam, R., Savithri, S. and Surender, G.D., 2009. CFD simulation of hydrodynamics of gas–liquid–solid fluidised bed reactor. *Chemical Engineering Science*, *64*(6), 1119-1135.

Pareek, V., Chong, S., Tadé, M. and Adesina, A.A., 2008. Light intensity distribution in heterogenous photocatalytic reactors. *Asia-Pacific Journal of Chemical Engineering*, *3*(2), 171-201.

Pelaez, M., Nolan, N.T., Pillai, S.C., Seery, M.K., Falaras, P., Kontos, A.G., Dunlop, P.S., Hamilton, J.W., Byrne, J.A., O'shea, K. and Entezari, M.H., 2012. A review on the visible light active titanium dioxide photocatalysts for environmental applications. *Applied Catalysis B: Environmental*, *125*, 331-349.

Pereira, J.H., Vilar, V.J., Borges, M.T., González, O., Esplugas, S. and Boaventura, R.A., 2011. Photocatalytic degradation of oxytetracycline using TiO_2 under natural and simulated solar radiation. *Solar Energy*, *85*(11), 2732-2740.

Pirhashemi, M., Habibi-Yangjeh, A. and Pouran, S.R., 2018. Review on the criteria anticipated for the fabrication of highly efficient ZnO-based visible-light-driven photocatalysts. *Journal of Industrial and Engineering Chemistry*, *62*, 1-25.

Portela, R., Suárez, S., Tessinari, R.F., Hernández-Alonso, M.D., Canela, M.C. and Sánchez, B., 2011. Solar/lamp-irradiated tubular photoreactor for air treatment with transparent supported photocatalysts. *Applied Catalysis B: Environmental*, *105*(1-2), 95-102.

Portela, R., Tessinari, R., Suarez, S., Rasmussen, S., Hernandez-Alonso, M., Canela, M., Avila, P. and Sanchez, B., 2012. Photocatalysis for continuous air purification in wastewater treatment plants: from lab to reality. *Environmental Science & Technology*, *46*(9), 5040-5048.

Pourtousi, M., Sahu, J.N. and Ganesan, P., 2014. Effect of interfacial forces and turbulence models on predicting flow pattern inside the bubble column. *Chemical Engineering and Processing: Process Intensification*, *75*, 38-47.

Pradeep, N. V., Anupama, S., Navya, K., Shalini, H. N., Idris, M. and Hampannavar, U. S., 2015. Biological removal of phenol from wastewaters: a mini review. *Applied Water Science*, *5*(2), 105-112.

Puma, G.L. and Brucato, A., 2007. Dimensionless analysis of slurry photocatalytic reactors using two-flux and six-flux radiation absorption–scattering models. *Catalysis Today*, *122*(1-2), 78-90.

Qi, N., Zhang, H., Jin, B. and Zhang, K., 2011. CFD modelling of hydrodynamics and degradation kinetics in an annular slurry photocatalytic reactor for wastewater treatment. *Chemical Engineering Journal*, *172*(1), 84-95.

Rabahi, A., Assadi, A. A., Nasrallah, N., Bouzaza, A., Maachi, R. and Wolbert, D., 2019. Photocatalytic treatment of petroleum industry wastewater using recirculating annular reactor: comparison of experimental and modeling. *Environmental Science and Pollution Research*, *26*(19), 19035-19046.

Rahimi, N., Pax, R.A. and Gray, E.M., 2016. Review of functional titanium oxides. I: TiO_2 and its modifications. *Progress in Solid State Chemistry*, *44*(3), 86-105.

Ramírez-Cabrera, M.A., Valadés-Pelayo, P.J., Arancibia-Bulnes, C.A. and Ramos, E., 2017. Validity of the Six-Flux model for photoreactors. *Chemical Engineering Journal*, *330*, 272-280.

Romero, R.L., Alfano, O.M. and Cassano, A.E., 2003. Radiation field in an annular, slurry photocatalytic reactor. 2. Model and experiments. *Industrial & Engineering Chemistry Research*, *42*(12), 2479-2488.

Romero, V., Méndez-Arriaga, F., Marco, P., Giménez, J. and Esplugas, S., 2014. Comparing the photocatalytic oxidation of Metoprolol in a solarbox and a solar pilot plant reactor. *Chemical Engineering Journal*, *254*, 17-29.

Saha, N.C., Bhunia, F. and Kaviraj, A., 1999. Toxicity of phenol to fish and aquatic ecosystems. *Bulletin of Environmental Contamination and Toxicology*, *63*(2), 195-202.

Saran, S., Kamalraj, G., Arunkumar, P. and Devipriya, S. P., 2016. Pilot scale thin film plate reactors for the photocatalytic treatment of sugar refinery wastewater. *Environmental Science and Pollution Research*, *23*(17), 17730-17741.

Sato, Y. and Sekoguchi, K., 1975. Liquid velocity distribution in two-phase bubble flow. *International Journal of Multiphase Flow*, *2*(1), 79-95.

Satuf, M.L., Brandi, R.J., Cassano, A.E. and Alfano, O.M., 2005. Experimental method to evaluate the optical properties of aqueous titanium dioxide suspensions. *Industrial & Engineering Chemistry Research*, *44*(17), 6643-6649.

Schalk, S., Adam, V., Arnold, E., Brieden, K., Voronov, A. and Witzke, H. D., 2005. UV-lamps for disinfection and advanced oxidation-lamp types, technologies and applications. *IUVA news*, *8*(1), 32-37.

Schallenberg, J., Enß, J.H. and Hempel, D.C., 2005. The important role of local dispersed phase hold-ups for the calculation of three-phase bubble columns. *Chemical Engineering Science*, *60*(22), 6027-6033.

Schembri, M., 2017. An Introduction to Solar Simulator Devices. *McMaster Journal of Engineering Physics*, *2*, 1-4.

Schiller, L.A., Nauman, Z., 1935. A drag coefficient correlation. Ver. Dtsch. Ing. *77*, 138

Senthilnathan, J. and Philip, L., 2012. Elimination of pesticides and their formulation products from drinking water using thin film continuous photoreactor under solar radiation. *Solar Energy*, *86*(9), 2735-2745.

Shan, A.Y., Ghazi, T.I.M. and Rashid, S.A., 2010. Immobilisation of titanium dioxide onto supporting materials in heterogeneous photocatalysis: a review. *Applied Catalysis A: General*, *389*(1-2), 1-8.

Shangguan, Y., Yu, S., Gong, C., Wang, Y., Yang, W. and Hou, L.A., 2018. A review of microbubble and its applications in ozonation. *IOP Conference Series: Earth and Environmental Science*, *128*(1), 012149.

Sharma, S., Dutta, V., Singh, P., Raizada, P., Rahmani-Sani, A., Hosseini-Bandegharaei, A. and Thakur, V.K., 2019. Carbon quantum dot supported semiconductor photocatalysts for efficient degradation of organic pollutants in water: a review. *Journal of Cleaner Production*, *228*, 755-769

Shet, A. and Vidya, S. K., 2016. Solar light mediated photocatalytic degradation of phenol using Ag core–TiO_2 shell (Ag@ TiO_2) nanoparticles in batch and fluidized bed reactor. *Solar Energy*, *127*, 67-78.

Shin, D., Jang, M., Cui, M., Na, S. and Khim, J., 2013. Enhanced removal of dichloroacetonitrile from drinking water by the combination of solar-photocatalysis and ozonation. *Chemosphere*, *93*(11), 2901-2908.

Silva, M.K., d'Ávila, M.A. and Mori, M., 2012. Study of the interfacial forces and turbulence models in a bubble column. *Computers & Chemical Engineering*, *44*, 34-44.

Singh, M., Salvadó-Estivill, I. and Li Puma, G., 2007. Radiation field optimization in photocatalytic monolith reactors for air treatment. *AIChE Journal*, *53*, 678-686.

Singh, S., Mahalingam, H. and Singh, P.K., 2013. Polymer-supported titanium dioxide photocatalysts for environmental remediation: A review. *Applied Catalysis A: General*, *462*, 178-195.

Sousa, M.A., Lacina, O., Hrádková, P., Pulkrabová, J., Vilar, V.J., Gonçalves, C., Boaventura, R.A., Hajšlová, J. and Alpendurada, M.F., 2013. Lorazepam photofate under photolysis

and TiO_2-assisted photocatalysis: Identification and evolution profiles of by-products formed during phototreatment of a WWTP effluent. *Water Research*, *47*(15), 5584-5593.

Spasiano, D., Marotta, R., Malato, S., Fernandez-Ibanez, P. and Di Somma, I., 2015. Solar photocatalysis: materials, reactors, some commercial, and pre-industrialized applications. A comprehensive approach. *Applied Catalysis B: Environmental*, *170*, 90-123.

Stephan, B., Ludovic, L. and Dominique, W., 2011. Modelling of a falling thin film deposited photocatalytic step reactor for water purification: Pesticide treatment. *Chemical Engineering Journal*, *169*(1-3), 216-225.

Tabib, M. V., Roy, S. A. and Joshi, J. B. 2008. CFD simulation of bubble column—an analysis of interphase forces and turbulence models. *Chemical Engineering Journal*, *139*(3), 589-614.

Tapia-Tlatelpa, T., Buscio, V., Trull, J. and Sala, V., 2020. Performance analysis and methodology for replacing conventional lamps by optimized LED arrays for photocatalytic processes. *Chemical Engineering Research and Design*, *156*, 456-468.

Teh, C.M. and Mohamed, A.R., 2011. Roles of titanium dioxide and ion-doped titanium dioxide on photocatalytic degradation of organic pollutants (phenolic compounds and dyes) in aqueous solutions: A review. *Journal of Alloys and Compounds*, *509*(5), 1648-1660.

Thiruvenkatachari, R., Vigneswaran, S. and Moon, I.S., 2008. A review on UV/TiO_2 photocatalytic oxidation process (Journal Review). *Korean Journal of Chemical Engineering*, *25*(1), 64-72.

Tisa, F., Raman, A. A. A. and Daud, W. M. A. W., 2014. Applicability of fluidized bed reactor in recalcitrant compound degradation through advanced oxidation processes: a review. *Journal of Environmental Management*, *146*, 260-275.

Tolosana-Moranchel, A., Casas, J.A., Carbajo, J., Faraldos, M. and Bahamonde, A., 2017. Influence of TiO_2 optical parameters in a slurry photocatalytic reactor: Kinetic modelling. *Applied Catalysis B: Environmental*, *200*, 164-173.

Tolosana-Moranchel, Á., Manassero, A., Satuf, M.L., Alfano, O.M., Casas, J.A. and Bahamonde, A., 2019. Influence of TiO_2-rGO optical properties on the photocatalytic activity and efficiency to photodegrade an emerging pollutant. *Applied Catalysis B: Environmental*, *246*, 1-11.

Tomiyama, A., Tamai, H., Zun, I. and Hosokawa, S., 2002. Transverse migration of single bubbles in simple shear flows. *Chemical Engineering Science*, *57*, 1849–1858

Trujillo, F.J., Safinski, T. and Adesina, A.A., 2007. CFD analysis of the radiation distribution in a new immobilized catalyst bubble column externally illuminated photoreactor. *Journal of Solar Energy Engineering*, *129(1)*, 27–36

Tu, J., Yeoh, G.H. and Liu, C., 2018. Computational fluid dynamics: a practical approach. Butterworth-Heinemann.

Turolla, A., Santoro, D., de Bruyn, J.R., Crapulli, F. and Antonelli, M., 2016. Nanoparticle scattering characterization and mechanistic modelling of UV–TiO_2 photocatalytic reactors using computational fluid dynamics. *Water Research*, *88*, 117-126.

Valadés-Pelayo, P.J., del Rio, J.M., Solano-Flores, P., Serrano, B. and De Lasa, H., 2014a. Establishing photon absorption fields in a Photo-CREC Water II Reactor using a CREC-spectroradiometric probe. *Chemical Engineering Science*, *116*, 406-417.

Valades-Pelayo, P.J., Moreira, J., Serrano, B. and De Lasa, H., 2014b. Boundary conditions and phase functions in a Photo-CREC Water-II reactor radiation field. *Chemical Engineering Science*, *107*, 123-136.

Valadés-Pelayo, P.J., Sosa, F.G., Serrano, B. and de Lasa, H., 2015a. Photocatalytic reactor under different external irradiance conditions: Validation of a fully predictive radiation absorption model. *Chemical Engineering Science*, *126*, 42-54.

Valadés-Pelayo, P.J., Sosa, F.G., Serrano, B. and De Lasa, H., 2015b. Eight-lamp externally irradiated bench-scale photocatalytic reactor: Scale-up and performance prediction. *Chemical Engineering Journal*, *282*, 142-151.

Van Gerven, T., Mul, G., Moulijn, J. and Stankiewicz, A., 2007. A review of intensification of photocatalytic processes. *Chemical Engineering and Processing: Process Intensification*, *46*(9), 781-789.

Vega, A. A., Imoberdorf, G. E. and Mohseni, M., 2011. Photocatalytic degradation of 2, 4-dichlorophenoxyacetic acid in a fluidized bed photoreactor with composite template-free TiO_2 photocatalyst. *Applied Catalysis A: General*, *405*(1-2), 120-128.

Vela, N., Calín, M., Yáñez-Gascón, M.J., Garrido, I., Pérez-Lucas, G., Fenoll, J. and Navarro, S., 2018. Photocatalytic oxidation of six pesticides listed as endocrine disruptor chemicals from wastewater using two different TiO_2 samples at pilot plant scale under sunlight irradiation. *Journal of Photochemistry and Photobiology A: Chemistry*, *353*, 271-278.

Versteeg, H.K. and Malalasekera, W., 2007. An introduction to computational fluid dynamics: the finite volume method. Pearson Education.

Villegas, L. G. C., Mashhadi, N., Chen, M., Mukherjee, D., Taylor, K. E. and Biswas, N., 2016. A short review of techniques for phenol removal from wastewater. *Current Pollution Reports*, *2*(3), 157-167.

Visa, M. and Duta, A., 2013. Methyl-orange and cadmium simultaneous removal using fly ash and photo-Fenton systems. *Journal of Hazardous Materials*, *244–245*(0), 773-779.

Wang, R., Xin, J.H., Yang, Y., Liu, H., Xu, L. and Hu, J., 2004. The characteristics and photocatalytic activities of silver doped ZnO nanocrystallites. *Applied Surface Science*, *227*(1–4), 312-317.

Wu, C., Li, P., Xia, S., Wang, S., Wang, Y., Hu, J., Liu, Z. and Yu, S., 2019. The role of interface in microbubble ozonation of aromatic compounds. *Chemosphere*, *220*, 1067-1074.

Xu, H., Li, M. and Jun, Z., 2013. Preparation, characterization, and photocatalytic studies on anatase nano-TiO_2 at internal air lift circulating photocatalytic reactor. *Materials Research Bulletin*, *48*(9), 3144-3148.

Xu, M., Yang, J., Sun, C., Liu, L., Cui, Y. and Liang, B., 2020. Performance enhancement strategies of bi-based photocatalysts: A review on recent progress. *Chemical Engineering Journal*, *389*, 124402.

Yahya, N., Aziz, F., Jamaludin, N.A., Mutalib, M.A., Ismail, A.F., Salleh, W.N.W., Jaafar, J., Yusof, N. and Ludin, N.A., 2018. A review of integrated photocatalyst adsorbents for wastewater treatment. *Journal of Environmental Chemical Engineering*, *6*(6), 7411-7425.

Zeghioud, H., Khellaf, N., Djelal, H., Amrane, A. and Bouhelassa, M., 2016. Photocatalytic reactors dedicated to the degradation of hazardous organic pollutants: Kinetics, mechanistic aspects, and design–A review. *Chemical Engineering Communications*, *203*(11), 1415-1431.

Zhang, A., Zhou, M., Han, L. and Zhou, Q., 2011. The combination of rotating disk photocatalytic reactor and TiO_2 nanotube arrays for environmental pollutants removal. *Journal of Hazardous Materials*, *186*(2-3), 1374-1383.

Zhang, D.Z. and Vanderheyden, W.B., 2002. The effects of mesoscale structures on the disperse two-phase flows and their closures for dilute suspensions. *International Journal of Multiphase Flow*, *28*, 805-822.

Zhang, W., Zou, L. and Wang, L., 2009. Photocatalytic TiO_2/adsorbent nanocomposites prepared via wet chemical impregnation for wastewater treatment: A review. *Applied Catalysis A: General*, *371*(1-2), 1-9.

Zhou, R., Yang, N. and Li, J., 2017. CFD simulation of gas-liquid-solid flow in slurry bubble columns with EMMS drag model. *Powder Technology*, *314*, 466-479.

Chapter 3

3 CFD simulation of the fluidized bed reactor

3.1 Introduction

Fluidized bed reactors have been preferred for photocatalysis due to their good mixing characteristics with no moving parts and low maintenance. In such a reactor, air fluidization may be used to suspend catalyst particles and provide oxygen directly into the reactor. In an air fluidized bed reactor, air induces liquid motion which then fluidizes the bed. In order to analyse, scale up and optimize fluidized bed reactors, the reactor hydrodynamics have to be understood. The use of experimental techniques to analyse the hydrodynamics has been limited by cost and resolution. Instead, numerical methods such as computational fluid dynamics (CFD) techniques have gained popularity due to their mathematical rigour at low cost (Ekambara and Dhotre, 2010). Fluid flow in fluidized bed reactors are usually highly turbulent with the bubbles and catalysts experiencing multiple forces such as drag, lift, wall lubrication, turbulent dispersion and virtual mass forces (Tabib et al., 2008). Therefore, the choice of the models for turbulence and interfacial forces is very crucial in order to ensure good accuracy at low cost.

The CFD simulation of bubble columns (Kulkarni et al., 2007; Tabib et al., 2008; Ekambara and Dhotre, 2010) and general three phase fluidized bed reactors (Schallenberg et al., 2005; Panneerselvam et al., 2009) have been carried out. However, very little has been done on the CFD simulation of the type of the reactor employed for photocatalysis in this work: an annular fluidized bed reactor with nanoparticles (Feng et al., 2005; Qi et al., 2011; Boyjoo et al., 2014). In this chapter, the annular fluidized bed reactor employed in this study was simulated using the CFD technique. First, a bubble column reactor was simulated and validated using the experimental data of Kulkarni et al. (2007) in order to establish the most accurate turbulent models and interfacial forces. Then, the fluidized bed reactor was simulated using the turbulent model and the set of interfacial forces from bubble column simulation. The aim of this chapter was to simulate the catalyst distribution in the reactor using computational fluid dynamics.

3.2 Methodology

3.2.1 Governing equations

In this work, two reactors were simulated: a bubble column reactor for validation and the annular fluidized bed reactor. A Eulerian-Eulerian model was used to simulate the

hydrodynamics in the two reactors. The bubble column and the fluidized bed reactor were simulated using the two phase and three phase Eulerian model, respectively. The generic governing equations for the hydrodynamics model consisted of the continuity equation and the momentum equation (Panneerselvam et al., 2009).

The continuity equation is given as:

$$\frac{\partial}{\partial t}(\alpha_k \rho_k) + \nabla(\alpha_k \rho_k \boldsymbol{u}_k) = 0 \tag{3.1}$$

where α_k, ρ_k and $\boldsymbol{u}_k$ refer to the volume fraction, density and velocity of phase k.

The momentum equation for the bubble column reactor is given as:

$$\frac{\partial}{\partial t}(\alpha_k \rho_k \boldsymbol{u}_k) + \nabla(\alpha_k \rho_k \boldsymbol{u}_k \boldsymbol{u}_k + \alpha_k \tau_k) = -\nabla(\alpha_k \tau_k) - \alpha_k \nabla P + \alpha_k \rho_k g + \boldsymbol{F}_{l,g} \tag{3.2}$$

The terms on the right-hand side of the momentum equation describe the viscosity, pressure, gravity and interfacial forces acting on phase k.

For the fluidized bed reactor, the momentum equation included an additional term for the solid pressure:

$$\frac{\partial}{\partial t}(\alpha_k \rho_k \boldsymbol{u}_k) + \nabla(\alpha_k \rho_k \boldsymbol{u}_k \boldsymbol{u}_k + \alpha_k \tau_k) = -\nabla(\alpha_k \tau_k) - \alpha_k \nabla P - \nabla P_s + \alpha_k \rho_k g + \boldsymbol{F}_{l,s} \tag{3.3}$$

The sum of the volume fractions of the phases equal unity:

$$\sum_{k=g,l,s} \alpha_k = 1 \tag{3.4}$$

Turbulence

Fluid turbulence consists of a mean and fluctuating parts of the flow. The size of the largest fluctuating eddies is usually characterized by the length scale. For engineering applications, the mean flow is usually of importance. This can be obtained by averaging the Navier-Stokes equations to give Reynolds-averaged Navier-Stokes (RANS) equations that govern the flow. In order to solve the RANS equations, the components of velocity fluctuations, known as the Reynolds stress, have to be determined as a function of the mean flow. One attempt at this, the Boussinesq eddy viscosity concept, hypothesizes that Reynolds stresses can be expressed as a function of the mean strain rate. The resulting eddy viscosity model can be expressed as:

$$\tau_k = -\mu_{eff,k}\left(\nabla \boldsymbol{u}_k + (\nabla \boldsymbol{u}_k)^T - \frac{2}{3} I(\nabla \boldsymbol{u}_k)\right) \tag{3.5}$$

where τ_k is the stress tensor and $\mu_{eff,k}$ is the effective viscosity. The effective viscosity of the liquid phase ($\mu_{eff,l}$) consists of molecular viscosity ($\mu_{I,l}$), shear induced turbulent viscosity ($\mu_{t,l}$) and a term due to bubble induced turbulence ($\mu_{BIT,l}$) (Panneerselvam et al., 2009):

$$\mu_{eff,l} = \mu_{I,l} + \mu_{t,l} + \mu_{BIT,l} \tag{3.6}$$

The effective gas viscosity was calculated from the effective liquid viscosity as:

$$\mu_{eff,g} = \frac{\rho_g}{\rho_l}\mu_{eff,l} \tag{3.7}$$

The effective solid viscosity was calculated using equation (3.33).

The bubble induced turbulence ($\mu_{BIT,l}$), was calculated using the model of Sato and Sekoguchi (1975):

$$\mu_{BIT,l} = \rho_l C_{\mu,BIT}\alpha_g d_b \left|\boldsymbol{u}_g - \boldsymbol{u}_l\right| \tag{3.8}$$

where d_b is the bubble diameter and the model constant $C_{\mu,BIT}$ was 0.6.

Several models such as the standard k-ε, RNG k-ε and Reynolds Stress Model (RSM) have been proposed for computing the liquid phase shear induced turbulent viscosity ($\mu_{t,l}$).

The standard k-ε and RNG k-ε models allow to calculate the $\mu_{t,l}$ as:

$$\mu_{t,l} = \rho_l C_\mu \frac{k^2}{\varepsilon} \tag{3.9}$$

For the standard k-ε model, the turbulent kinetic energy (k) and the turbulent dissipation rate (ε) are calculated using differential transport equations:

$$\frac{\partial}{\partial t}(\alpha_l\rho_l k) + \nabla(\alpha_l\rho_l k\boldsymbol{u}_l) = -\nabla\left(\alpha_l\left(\frac{\mu_{eff,l}}{\sigma_k}\right)\nabla k\right) + \alpha_l(G - \rho_l\varepsilon) \tag{3.10}$$

$$\frac{\partial}{\partial t}(\alpha_l\rho_l k) + \nabla(\alpha_l\rho_l k\boldsymbol{u}_l) = -\nabla\left(\alpha_l\left(\frac{\mu_{eff,l}}{\sigma_\varepsilon}\right)\nabla\varepsilon\right) + \alpha_l\frac{\varepsilon}{k}(C_{\varepsilon1}G - C_{\varepsilon2}\rho_l\varepsilon) \tag{3.11}$$

where the model constants are: $C_\mu = 0.09$, $\sigma_k = 1.00$, $\sigma_\varepsilon = 1.00$, $C_{\varepsilon1} = 1.44$, $C_{\varepsilon2} = 1.92$

For the RNG k-ε model, different scales of motion are considered by making the $C_{\varepsilon2RNG}$ term a function of the local strain rate. The differential equation for k was calculated using equation (3.10) while that for ε was calculated as:

$$\frac{\partial}{\partial t}(\alpha_l\rho_l k) + \nabla(\alpha_l\rho_l k\boldsymbol{u}_l) = -\nabla\left(\alpha_l\left(\frac{\mu_{eff,l}}{\sigma_{\varepsilon RNG}}\right)\nabla\varepsilon\right) + \alpha_l\frac{\varepsilon}{k}(C_{\varepsilon1RNG}G - C_{\varepsilon2RNG}\rho_l\varepsilon) \tag{3.12}$$

where

$$C_{\varepsilon 2RNG} = 1.42 - \frac{\eta(1-\eta/4.38)}{(1+0.012\eta^3)} \tag{3.13}$$

$$\eta = \left(2S_{ij}S_{ij}\right)^{1/2}\frac{k}{\varepsilon}$$

The constants for the RNG k-ε model are: $C_\mu = 0.0845$, $\sigma_k = 0.7194$, $\sigma_\varepsilon = 0.7194$, $C_{\varepsilon 1RNG} = 1.42$

Eddy viscosity models depend on the assumption of isotropic turbulence. This assumption can be valid for some flows; however, in flows with high degrees of anisotropy, strong streamline curvature, recirculating flow and rotational effects, k-ε based models have been observed to be inaccurate. In order to address this, the RSM model was developed in which the individual Reynolds stresses ($\overline{u_i'u_j'}$) are calculated using differential transport equations. This provides the most accurate solution to the Reynolds stresses. However, this good accuracy comes with a high computational cost. Six Reynolds stress differential equations (equation 3.14) are solved along with a dissipation rate equation (equation 3.15).

$$\frac{\partial}{\partial t}\left(\alpha_l\rho_l\overline{u_i'u_j'}\right) + \frac{\partial}{\partial x_k}\left(\alpha_l\rho_l\boldsymbol{u}_k\overline{u_i'u_j'}\right) = \alpha_l P_{ij}' + \alpha_l\phi_{ij} + \frac{\partial}{\partial x_k}\left(\alpha_l\left(\mu_l + \frac{2}{3}C_s'\rho\frac{k^2}{\varepsilon}\right)\frac{\partial\overline{u_i'u_j'}}{\partial x_k}\right) - \frac{2}{3}\delta_{ij}\alpha_l\rho_l\varepsilon \tag{3.14}$$

$$\frac{\partial}{\partial t}\left(\alpha_l\rho_l\varepsilon\right) + \frac{\partial}{\partial x_k}\left(\alpha_l\rho_l\varepsilon\boldsymbol{u}_i\right) = \frac{\partial}{\partial x_j}\left(\alpha_l\left(\mu_l + \frac{\mu_{t,l}}{\sigma_\varepsilon}\right)\frac{\partial\varepsilon}{\partial x_j}\right) + \alpha_l\rho_l C_{\varepsilon 1}\left(\overline{u_i'u_k'}\frac{\partial\boldsymbol{u}_i}{\partial x_k}\right)\frac{\varepsilon}{k} - \alpha_l\rho_l C_{\varepsilon 2}\frac{\varepsilon^2}{k} \tag{3.15}$$

Gas-liquid interfacial forces

The gas-liquid interfacial forces ($\boldsymbol{F}_{l,g}$) are due to drag, lift, wall lubrication and turbulent dispersion forces:

$$\boldsymbol{F}_{l,g} = \boldsymbol{F}_D + \boldsymbol{F}_L + \boldsymbol{F}_{WL} + \boldsymbol{F}_{TD} \tag{3.16}$$

A bubble rising through a fluid experiences resistance due to drag force which is given by:

$$\boldsymbol{F}_D = \frac{3}{4}C_{D,l,g}\alpha_g\rho_l\frac{1}{d_b}|\boldsymbol{u}_G - \boldsymbol{u}_L|(\boldsymbol{u}_G - \boldsymbol{u}_L) \tag{3.17}$$

The drag coefficient ($C_{D,l,g}$) which accounts for the character of the flow around the bubble was determined using the Ishii and Zuber (1979) model which accounts for spherical, elliptical and cap regimes:

$$C_{D,l,g} = \frac{2}{3} Eo^{0.5} \tag{3.18}$$

where Eo, Eotvos number, was calculated using equation (3.24). The drag model by Ishii and Zuber (1979) has been used successfully by Ekambara and Dhotre (2010) to simulate a similar bubble column. Masood and Delgado (2014) also found the drag model to be accurate for their square bubble column reactor.

A rising bubble also experiences a lift force acting perpendicular to the direction of flow:

$$\boldsymbol{F}_L = C_L \alpha_g \rho_l \left(\boldsymbol{u}_g - \boldsymbol{u}_l\right) \times \nabla \times \boldsymbol{u}_l \tag{3.19}$$

The lift coefficient (C_L) was determined using the model by Tomiyama et al. (2002) as:

$$C_L = \begin{cases} \min[0.288 \tanh(0.121 \mathrm{Re_b}), f(Eo')], & E_o' < 4 \\ f(Eo'), & 4 < Eo' \leq 10 \\ -0.27, & 10 < Eo' \end{cases} \tag{3.20}$$

where

$$f(Eo') = 0.00105(Eo')^3 - 0.0159(Eo')^2 - 0.0204Eo' + 0.474 \tag{3.21}$$

and Eo' is the modified Eotvos number based on d_H, the long axis of the deformable bubble:

$$Eo' = \frac{g \Delta\rho d_H^2}{\sigma} \tag{3.22}$$

$$d_H = d_b (1 + 0.163 Eo^{0.757})^{1/3} \tag{3.23}$$

$$Eo = \frac{g \Delta\rho d_b^2}{\sigma} \tag{3.24}$$

where $\Delta\rho$ is the density difference between gas and liquid.

Due to the difference in liquid flow rate between the wall and at the middle of the reactor, bubbles experience a wall lubrication force which pushes them away from the wall. This effect has been modelled by Tomiyama (2002) as:

$$\boldsymbol{F}_{WL} = -C_{WL} \alpha_g \rho_l \left|\boldsymbol{u}_g - \boldsymbol{u}_l\right|_w^2 \boldsymbol{n}_w$$

where the unit normal $\boldsymbol{n}_w$ is specified in the direction away from the wall. The coefficient C_{WL} is defined as:

$$C_{WL} = C_W(Eo)\frac{d_b}{2}\left(\frac{1}{y_w^2} - \frac{1}{(D-y_w)^2}\right) \tag{3.25}$$

where D is the reactor diameter, y_w is the distance to the nearest wall and C_{WL} is a coefficient which depends on Eötvös number (Eo). C_{WL} is presented in modified form as (Ansys, 2017):

$$C_W(Eo) = \begin{cases} 0.47 & Eo < 1 \\ \exp(-0.933Eo + 0.179) & 1 \le Eo \le 5 \\ 0.00599Eo + 0.0187 & 5 \le Eo \le 33 \\ 0.179 & Eo > 33 \end{cases} \tag{3.26}$$

The turbulent dispersion force arises from the turbulent diffusion of the bubbles by liquid eddies. It has been formulated by Lopez de Bertonado (1992) as:

$$\boldsymbol{F}_{TD} = -C_{TD}\rho_l k \nabla \alpha_l \tag{3.27}$$

where k is the turbulent kinetic energy and the turbulent dispersion coefficient (C_{TD}) was specified as 0.3 as suggested by Ekambara and Dhotre (2010).

Liquid-solid interfacial forces

For the fluidized bed reactor, in addition to the gas-liquid interfacial forces, the liquid-solid interfacial drag force was modelled as:

$$\boldsymbol{F}_D = \frac{3}{4}C_{D,l,s}\alpha_s\rho_l\frac{1}{d_s}|\boldsymbol{u}_s - \boldsymbol{u}_l|(\boldsymbol{u}_s - \boldsymbol{u}_l) \tag{3.28}$$

The drag coefficient ($C_{D,l,s}$) was modelled using the Schiller and Nauman (1935) drag model as:

$$C_{D,l,s} = \max\left[\frac{24}{\mathrm{Re}}(1 + 0.15\mathrm{Re}^{0.687}), 0.44\right] \tag{3.29}$$

where

$$\mathrm{Re} = \frac{\rho_l d_s|\boldsymbol{u}_s - \boldsymbol{u}_l|}{\mu_l} \tag{3.30}$$

Solid phase hydrodynamic properties

The hydrodynamic properties of the solid phase were evaluated using the kinetic theory of granular flow (KTGF) model which is based on the analogy of the motion of gases (Ding and Gidaspow, 1990). This model accounts for the collision between particles which gives a more

accurate definition of the solid pressure and solid viscosity for use in equation (3.3) and equation (3.5), respectively.

In the KTGF model, the solid pressure is calculated as:

$$P_s = \rho_s \alpha_s \theta_s + 2\rho_s(1+e_s)\alpha_s^2 \mathrm{g}_0 \theta_s \tag{3.31}$$

where the radial distribution function (g_0) is given as:

$$\mathrm{g}_0 = \left[1 - \left(\frac{\alpha_s}{\alpha_{s,\max}}\right)^{1/3}\right]^{-1} \tag{3.32}$$

The effective solid phase viscosity ($\mu_{eff,s}$) is calculated by the KTGF model as:

$$\mu_{eff,s} = \mu_{s,col} + \mu_{s,kin} \tag{3.33}$$

where the collision viscosity ($\mu_{s,col}$) is given as:

$$\mu_{s,col} = \frac{4}{5}\alpha_s \rho_s d_s \mathrm{g}_0 (1+e_s)\left(\frac{\theta_s}{\pi}\right)^{1/2} \tag{3.34}$$

and the kinetic viscosity ($\mu_{s,kin}$) is calculated as:

$$\mu_{s,kin} = \frac{\alpha_s \rho_s d_s \sqrt{\pi\theta_s}}{6(3-e_s)}\left[1 + \frac{2}{5}(1+e_s)(3e_s-1)\alpha_s \mathrm{g}_0\right] \tag{3.35}$$

where e_s is the coefficient of restitution.

The granular temperature (θ_s) is calculated using a transport equation as:

$$\frac{3}{2}\left[\frac{\partial}{\partial t}(\rho_s \alpha_s \theta_s) + \nabla(\rho_s \alpha_s \theta_s \boldsymbol{u}_s)\right] = (-\nabla P_s I + \tau_s)\nabla \boldsymbol{u}_s + \nabla(k_{\theta_s}\nabla\theta_s) - \gamma_s - 3\boldsymbol{F}_{l,s}\theta_s \tag{3.36}$$

where the diffusion coefficient for granular energy (k_{θ_s}) is given as:

$$k_{\theta_s} = \frac{15\alpha_s \rho_s d_s \sqrt{\pi\theta_s}}{4(41-33\eta)}\left[1 + \frac{12}{5}\eta^2(4\eta-3)\alpha_s \mathrm{g}_0 + \frac{16}{15\pi}(41-33\eta)\eta\alpha_s \mathrm{g}_0\right] \tag{3.37}$$

and

$$\eta = \frac{1}{2}(1+e_s)$$

The dissipation of granular energy (γ_s) is calculated as:

$$\gamma_s = \frac{12(1-e_s^2)\mathrm{g}_0}{d_s\sqrt{\pi}}\rho_s\alpha_s^2\theta_s^{3/2} \tag{3.38}$$

3.2.2 Numerical modelling

Both the bubble column and fluidized bed reactors were simulated in 3D using ANSYS CFX 17. CFX was chosen due to its robust solver in which pressure and velocity are solved in a coupled manner.

Bubble column reactor

An air – water bubble column reactor with a diameter (D) of 150 mm and a height of 1000 mm was simulated. The initial static liquid height in the column was 900 mm. Figure 3.1 shows the coordinate system for the reactor as well as the dimension variables. A mass flow inlet boundary condition was specified at the air inlet with an air volume fraction of 1. A pressure outlet boundary condition with air backflow volume fraction of 1 was specified at the top of the reactor to keep liquid from exiting the reactor. At the reactor wall, a no-slip condition was specified for the liquid while for the gas, a free-slip condition was specified. The gas and liquid properties are listed in Table 3.1.

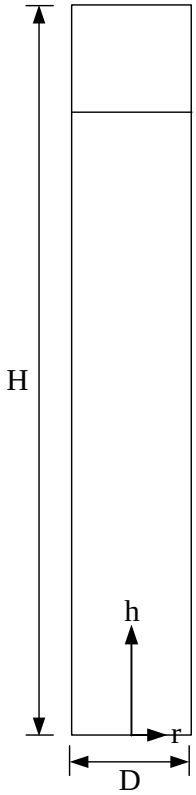

Figure 3.1: Reactor geometry coordinate

Meshing was carried out using ANSYS meshing software with a multizone scheme which utilizes hexahedral mesh for most of the reactor and tetrahedral mesh in areas in which hexahedral mesh cannot be used. The effect of grid size on simulation accuracy was investigated using grid sizes of 6837, 41356, 98264 and 231270 nodes. Due to the geometrical symmetry of the reactor, a full, half and quarter reactor geometry, along the axial direction, were investigated (Figure 3.2). The half reactor had one symmetry plane while the quarter reactor had two symmetry planes. Turbulence was modelled using the standard k-ε, RNG k-ε and Reynolds Stress Model (RSM). Most of the interfacial forces such as the drag, lift, wall lubrication and turbulence dispersion forces were modelled. Only the virtual mass force was not modelled since its effect has been found to be insignificant (Tabib et al., 2008; Masood and Delgado, 2014). This is due to the fact that the acceleration and deceleration of the liquid by bubbles which give rise to the virtual mass force are predominant mainly at the extreme ends of the bubble column.

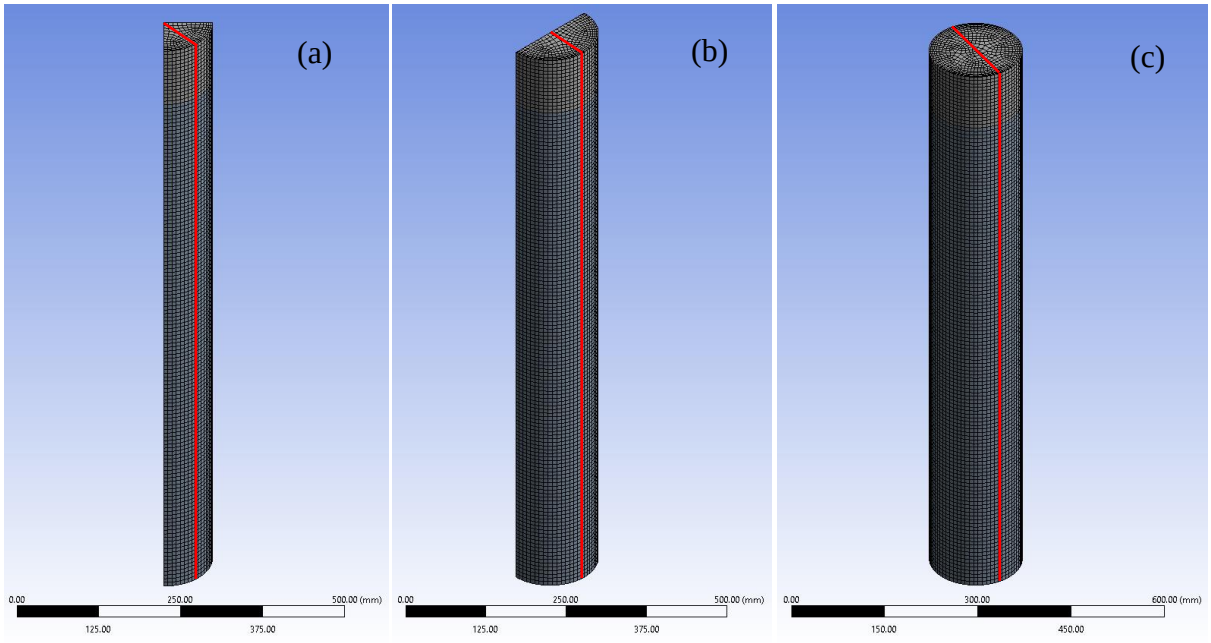

Figure 3.2: Grid of reactor geometry (a) quarter, (b) half, (c) full

The governing equations were discretized using element based finite volume method. High-resolution scheme was applied for spatial discretization while second order backward Euler scheme was used for temporal discretization. A time step of 0.001s was used for a total simulation time of 120 s with time-averaging of the flow quantities being carried out in the last 100 s. Time averaging was done in order to facilitate comparison with time-averaged experimental data. Also, time-averaged flow properties are of more relevance for engineering

purposes than instantaneous flow properties. Convergence was considered to be achieved when the mass flow residuals dropped below 1.0×10^{-4}.

Table 3.1: Liquid and gas properties

Property phase	Value
Air density (kg/m^3)	1.185
Air viscosity (kg/m s)	1.7894×10^{-5}
Bubble diameter (m)	0.006
Superficial air velocity (m/s)	0.020
Water density (kg/m^3)	997
Water viscosity (kg/m s)	0.001003
Air-water surface tension (N/m)	0.072

Fluidized bed reactor

The annular fluidized bed reactor with a wall diameter of 60.6 mm, lamp sleeve diameter of 34 mm and a height of 750 mm was simulated. The initial static liquid height in the column was 600 mm with a uniform initial solid volume fraction of 4.7×10^{-5} within the liquid phase. At the reactor wall, a free-slip condition was specified for the solid phase. In addition to the liquid and gas properties listed in Table 3.1, the required solid properties are listed in Table 3.2.

Table 3.2: Solid phase properties

Property phase	Value	Reference
Solid diameter (m)	1.34×10^{-6}	Salaices et al. (2002)
Solid density (kg/m^3)	4260	Boyjoo et al. (2013)
Solid volume fraction (-)	4.7279×10^{-5}	
Packing fraction (-)	0.55	Boyjoo et al. (2013)
Restitution coefficient (-)	0	Boyjoo et al. (2013)

Meshing was carried out using ANSYS meshing software with a multizone scheme which resulted in a grid size of 52,224 nodes for the full reactor (Figure 3.3). Turbulence was modelled using the Reynolds Stress Model (RSM) since this was the best model obtained after comparing the standard k-ε, RNG k-ε and RSM model in the bubble column reactor. Most of the gas-liquid interfacial forces such as the drag, lift, wall lubrication and turbulence dispersion forces were modelled as this was found to give the best results for the bubble column reactor. For the liquid-solid interfacial forces, only the drag force was modelled. The solids pressure due to the presence of the solid phase was modelled using the kinetic theory of granular flow in which the random movement of the solids is accounted for by an analogous comparison to similar movement of gas molecules. The solver settings for the bubble column reactor were retained during the simulation of the fluidized bed reactor.

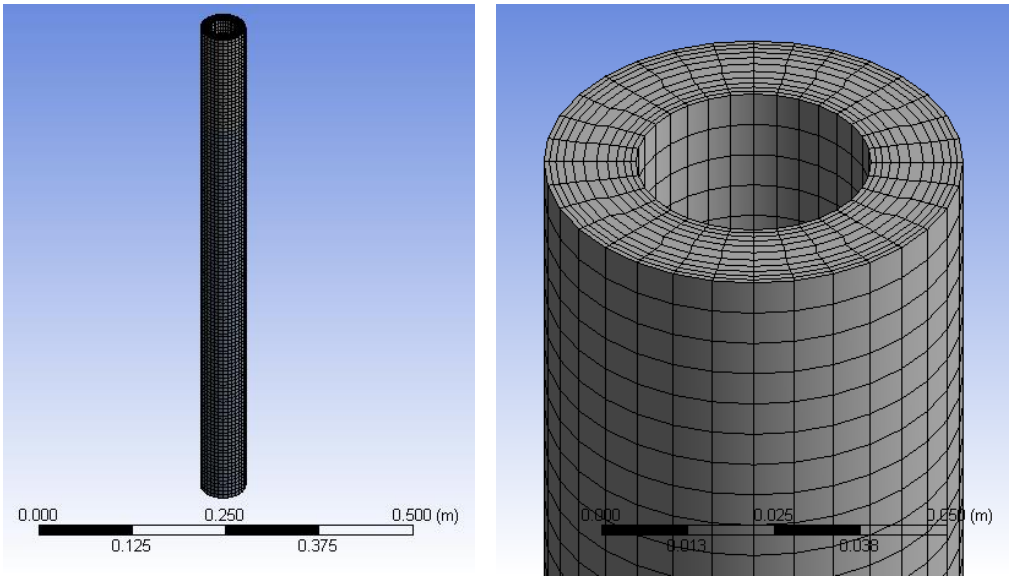

Figure 3.3: Fluidized bed reactor mesh

3.3 Results and discussion

The analysis of the bubble column reactor was carried out first in order to determine the best models which could be used to simulate the fluidized bed reactor. In the bubble column reactor, the effect of the grid size, turbulent models and interfacial forces on the simulated gas holdup, axial liquid velocity, turbulent kinetic energy and turbulent dissipation rate was investigated. The CFD simulation results of the bubble column were compared with the experimental data of Kulkarni et al. (2007). They collected time-averaged radial profiles of gas holdup, axial liquid velocity, turbulent kinetic energy and turbulent dissipation rate at different axial locations in a 150 mm diameter bubble column reactor using laser doppler anemometer (LDA).

3.3.1 Effect of reactor geometry

The tubular reactor geometry was observed to be symmetric along the axial line; therefore, only a section of the reactor could be simulated by specifying appropriate symmetry planes. In this work, three geometries were investigated: full, half and quarter reactor (Figure 3.2) using the RNG k-ε turbulent model. Simulating only a part of the reactor, if accurate, is desirable, as it could markedly reduce the simulation time by reducing the grid size. In order to investigate the effect of geometry on the simulation accuracy, experimental and simulated radial profiles of the axial liquid velocity, gas holdup, turbulent kinetic energy and turbulent dissipation rate at three axial locations were compared. This was carried out using the normalized root mean square error (NRMSE) (You et al. 2016):

$$NRMSE = \sqrt{\frac{1}{N}\sum_{i=0}^{N}(M_i - E_i)^2} \tag{3.39}$$

where N is the number of data points, M_i are the model data points, E_i are the experimental data points.

The results (Figure 3.4) show that significant errors were introduced by simulating only a part of the reactor geometry. The full reactor was the most accurate followed by the quarter reactor with the half reactor exhibiting the least accuracy. A bubble column reactor exhibits a 3D fluctuation of the rising bubble plume under operation as shown in the instantaneous liquid velocity vectors (Figure 3.7d). This suggests that, although the reactor was geometrically symmetric, it was not hydrodynamically symmetric due to spatial and temporal variation of the bubble plume (see Figure 3.7d). The half reactor was least able to capture this spatial and temporal asymmetry. The simulation accuracy depended on the geometry being able to capture as much of the fluctuating plume as possible. This was investigated by comparing the time-averaged gas holdup contours along the axial planes of the three reactors. The location of the axial planes are indicated on the diagram of the meshes (Figure 3.2). In the full geometry, the highest gas holdup was located in the middle of the column as shown in the time-averaged gas holdup contours (Figure 3.5e). This was not the case with the half geometry, in which the high gas holdup region was restricted to a region between the wall and the centre of the reactor (Figure 3.5c-d). Moreover, an increase in the averaging time from 30 s to 240 s pushed the high gas holdup region further away from the middle of the column.

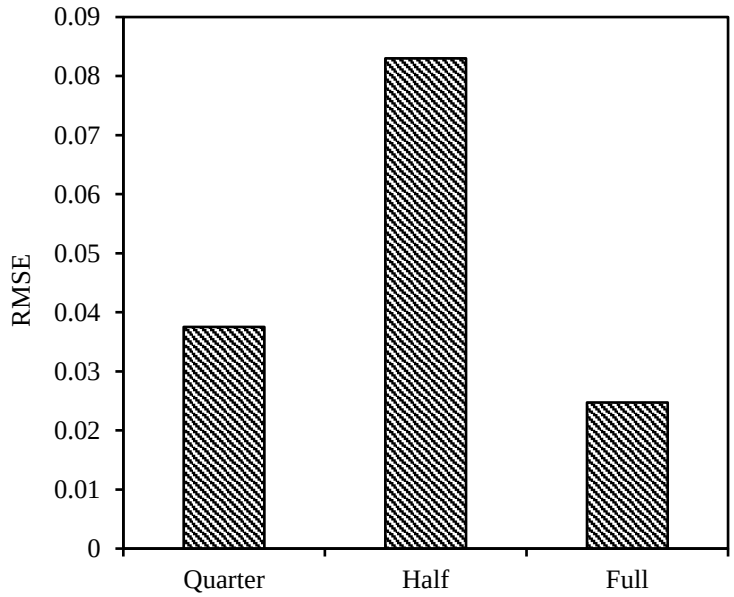

Figure 3.4: Effect of reactor geometry on simulation accuracy (RMSE)

An improvement was observed in the quarter geometry in which the high gas holdup region shifted towards the middle of the column (Figure 3.5a-b). However, the region of maximum gas holdup was located higher up the column than in the full geometry, an effect which increased with an increase in averaging time from 30 s to 240 s. Since the quarter and half reactor geometry were not able to accurately capture the flow characteristics, all further simulations were carried out using the full geometry.

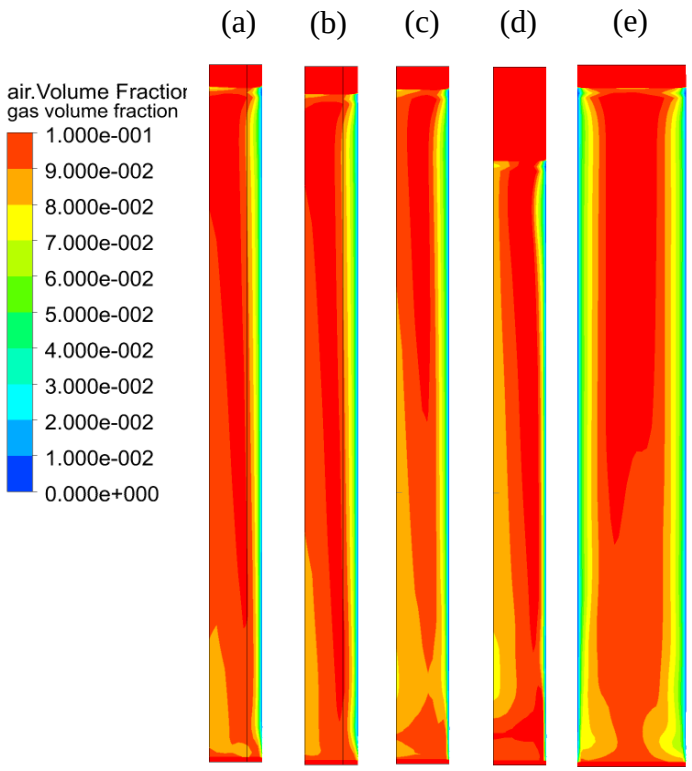

Figure 3.5: Effect of reactor geometry on the time-averaged gas holdup contours (a) quarter 30s, (b) quarter 240s, (c) half 30s, (d) half 240s, (e) full 30s

3.3.2 Effect of grid size

The accuracy of the CFD simulation using different turbulent models and grid sizes was evaluated by the comparison of experimental and simulated radial axial liquid velocity, gas holdup, turbulent kinetic energy and turbulent dissipation rate profiles at three axial locations. In order to characterize the accuracy of the models at all points of comparison, the normalized root mean square error (RMSE) criterion in section 3.3.1 was used. For all the turbulent models, the RMSE (Figure 3.6) shows a general decrease in simulation error with an increase in the grid size from 6,837 to 98,264 cells. Beyond 98,264 cells, an increase in the simulation error was observed. Therefore, the optimum grid was taken as 98,264 cells and used for all further simulations. This optimum has been observed by other researchers. For example, Ekambara and Dhotre (2010) reported that the optimum grid size was such that the cell to bubble diameter

ratio should be around 1.5. They attributed the inaccuracy of finer grid to the fact that in such cases, bubble size is larger than the average cell size. From the error analysis, the RSM model was the most accurate followed by the RNG k-ε model with the standard k-ε model showing the least accuracy. This observation will be analysed in the next section.

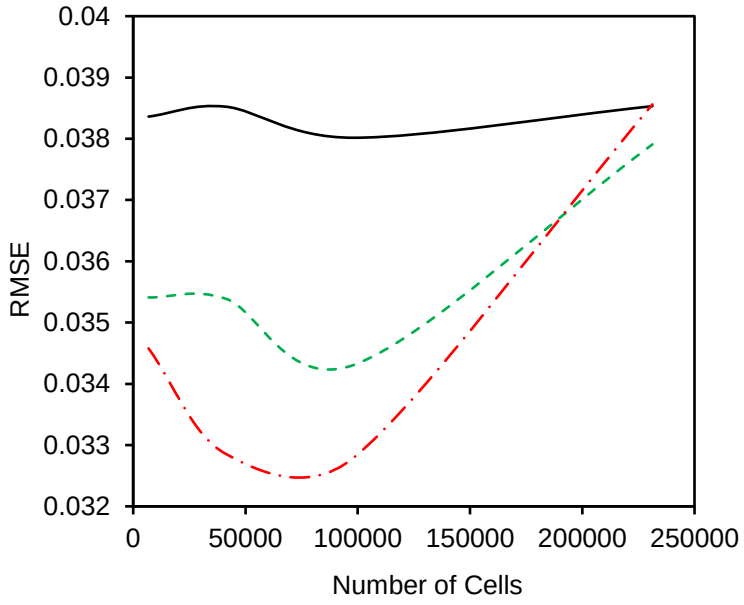

Figure 3.6: RMSE of different turbulent models and cells. Standard k-ε (——), RNG k-ε (- - -) and RSM models (—·—)

3.3.3 Effect of turbulence models

Axial liquid velocity

The axial liquid velocity is an important hydrodynamic parameter as it gives an indication of mixing efficiency and dead zones in the reactor. The effect of different turbulent models on the axial liquid velocity radial profiles at different axial locations was investigated. The time-averaged liquid velocity vectors (Figure 3.7a-c) show a well-established flow pattern in which liquid flows upwards at the middle of the reactor and downwards near the reactor wall. This is further clarified by the radial axial liquid velocity profiles (Figure 3.8). The upward flow of liquid was highest in the middle of the reactor reducing in the radial direction towards the wall. At a normalized radial location of roughly 0.7, the axial liquid velocity reduced to zero followed by a reversal in the flow direction downward before going back to zero at the wall. This kind of flow pattern is typical of a bubble column reactor as indicated by Kulkarni et al. (2007). Furthermore, as observed in the liquid velocity vectors and experimental radial axial liquid velocity profiles, the centreline axial liquid velocity increases with the height from the distributor. This is due to an increase in the bubble size with an increase in column height as a result of bubble coalescence and a decrease in hydrostatic pressure. Larger bubbles move faster

than smaller ones since larger bubbles exhibit lower surface area to volume ratio and subsequently lower skin drag. Conversely, smaller bubbles have a high surface area to volume ratio and hence experience high effective skin drag which slows their movement.

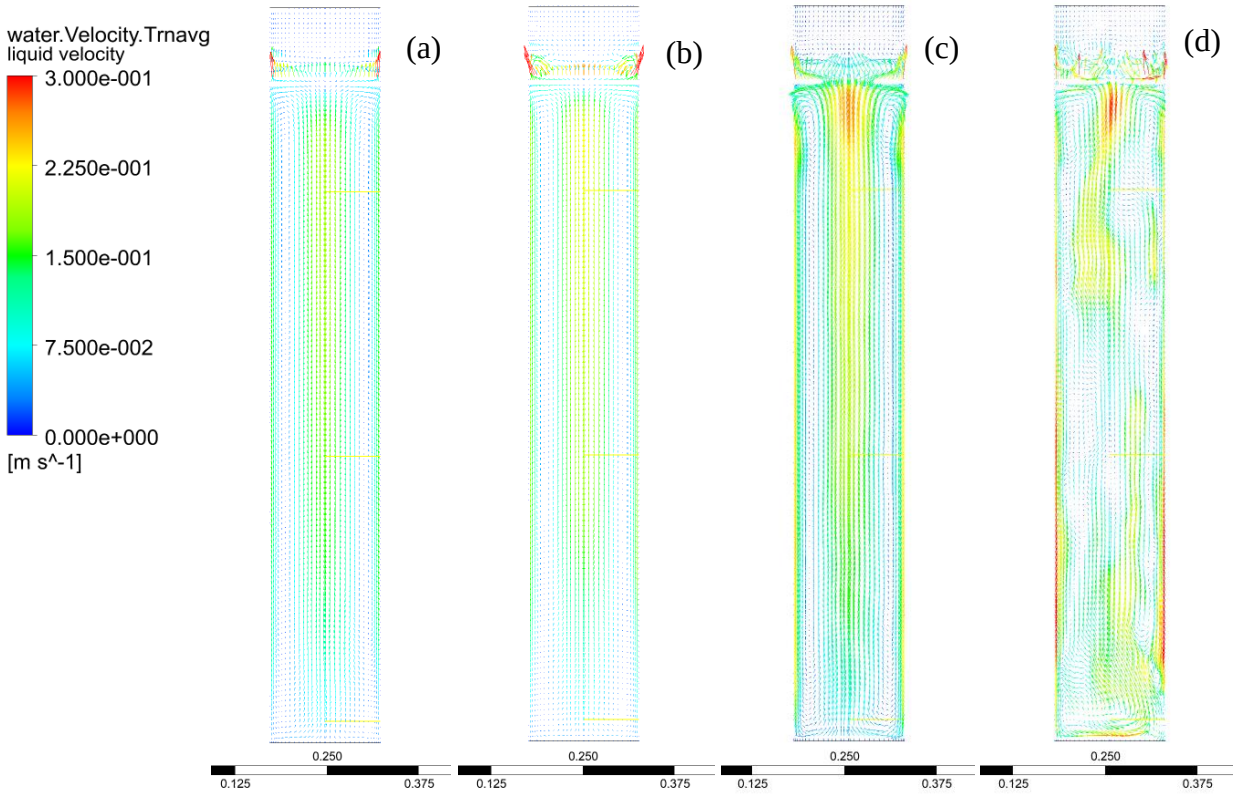

Figure 3.7: Liquid velocity vectors using different turbulence models (a) Standard k-ε (average), (b) RNG k-ε (average), (c) RSM model (average), (d) RSM model (transient)

The experimental axial liquid velocity radial profiles at different axial locations was compared to those obtained using different turbulent models. The typical axial liquid velocity radial profiles were captured by the CFD simulation. At an axial location of h/H=0.03, near the distributor, a poor agreement between the simulation and experimental profiles was observed for all the turbulent models. The prediction improved higher up in the column between h/H=0.39 and h/H=0.75 although all the turbulent models underpredicted the centreline axial velocity profiles. The RSM model showed the best prediction of the centreline axial liquid velocity while the standard k-ε had the worst prediction with the RNG k-ε model having an intermediate accuracy. This is also evident from the liquid velocity vectors which show high centreline liquid velocity using the RSM model followed by the RNG k-ε model with the standard k-ε model with the lowest values (Figure 3.7a-c). This was attributed to the better accuracy of the RSM model in the modelling of non-isotropy. The RNG k-ε turbulence model

showed a better prediction than the standard model due to a correction in the turbulence dissipation rate equation as explained in section 3.2.1.

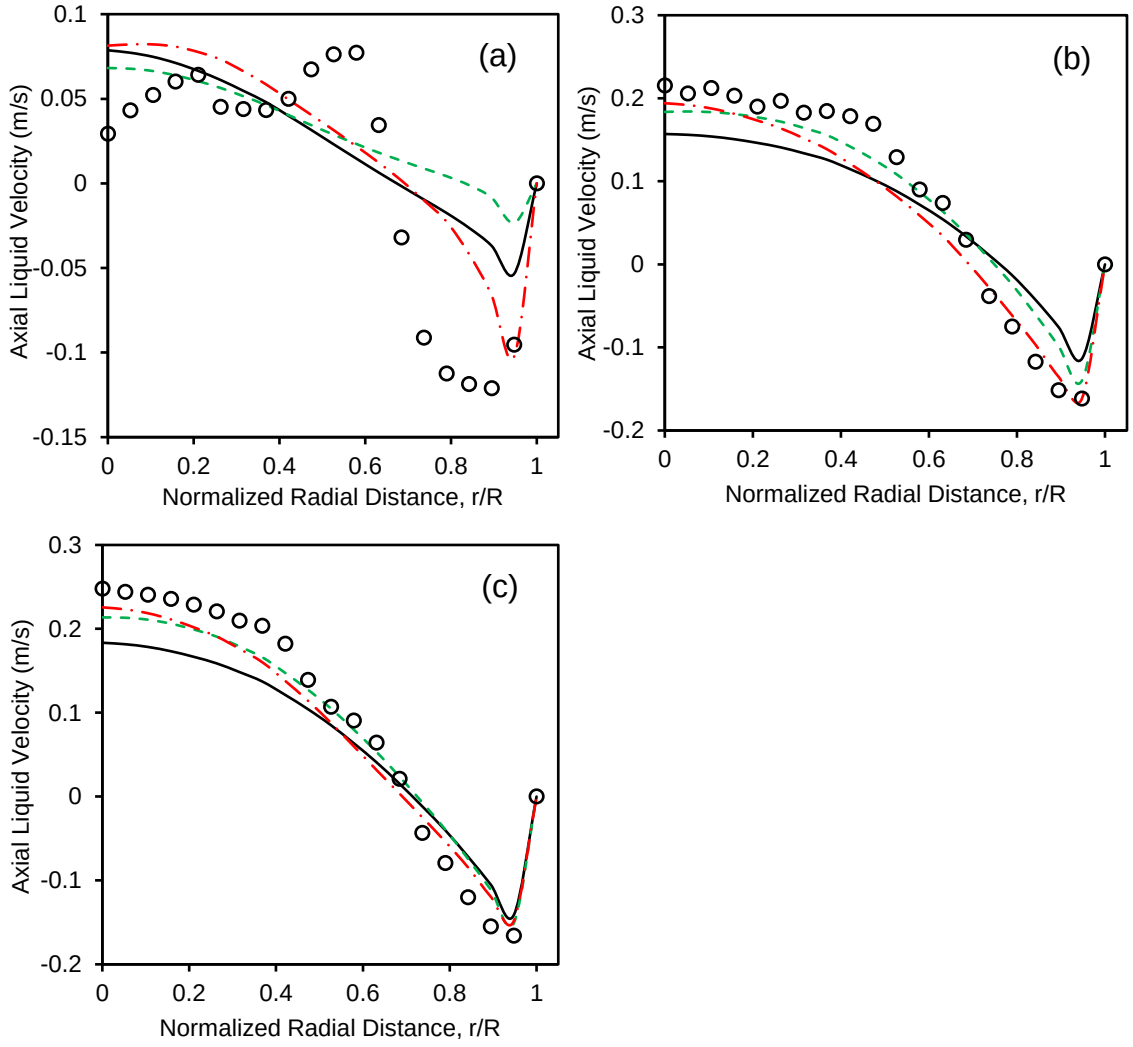

Figure 3.8: Radial profiles of the axial liquid velocity at different axial locations (a) h/H=0.03, (b) h/H=0.39, (c) h/H=0.75. Experimental (○), Standard k-ε (——), RNG k-ε (- - -) and RSM models (— · —).

With an increase in the distance from the distributor, bubbles tend to move towards the centre of the column resulting in an increase in the centreline axial liquid velocity at higher column levels (Kulkarni et al., 2007). The fact that all the turbulent models underpredicted the centreline axial liquid velocity higher up in the column could be attributed to the inaccuracy of the model which only considered a single bubble size. Significant bubble coalescence is expected in the centreline, and this would result in an increase in the bubble size. The larger bubbles would rise faster in the liquid resulting in a higher axial liquid velocity. The use of bubble coalescence and break up models would have captured this phenomenon more accurately.

Gas holdup

The effect of different turbulent models (Standard k-ε, RNG k-ε and RSM models) on the radial gas holdup at different axial locations was investigated. Radial gas holdup profiles were observed to decrease from the middle of the reactor towards the wall (Figure 3.9a-c). This is due to the fact that in a bubble column, the bubbles tend to move away from the wall and accumulate in the middle of the column. At the region near the distributor, this effect is not very pronounced, so the gas holdup radial profile appears flat. Further up the column, the gas bubbles start to move towards the centre of the column resulting in a parabolic shape when the flow is fully developed (Kulkarni et al., 2007).

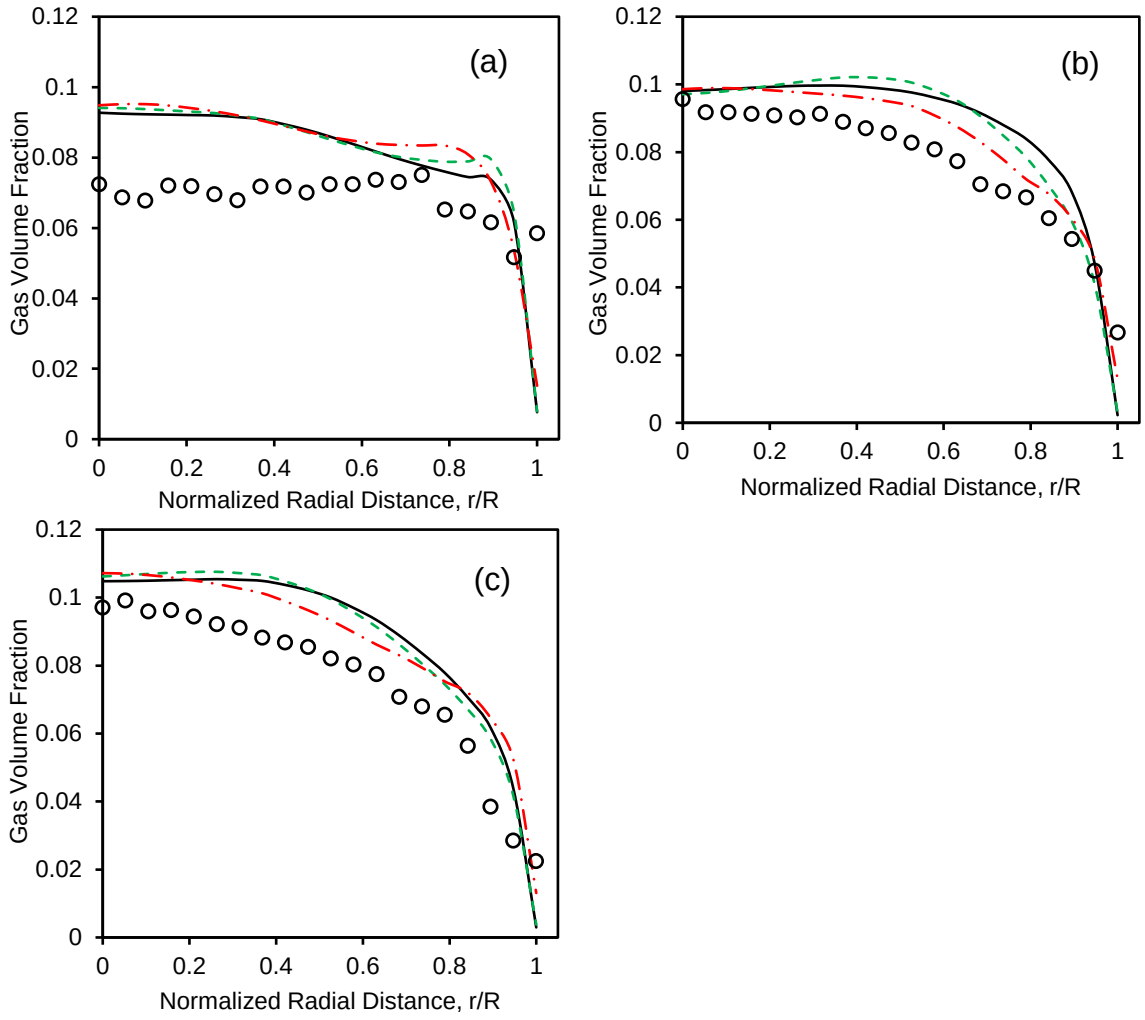

Figure 3.9: Radial profiles of the gas holdup at different axial locations (a) h/H=0.03, (b) h/H=0.39, (c) h/H=0.75. Experimental (○), Standard k-ε (——), RNG k-ε (- - -) and RSM models (—·—).

The flat profile near the distributor (h/H=0.03) was poorly captured by the different turbulent models. However, the fully developed profile between the axial location of h/H=0.39 and

h/H=0.75, was captured fairly well especially near the centreline and wall (Figure 3.9b – c). The different turbulent models had a similar degree of prediction accuracy near the centre and wall of the column. However, at the intermediate radial location near the point of flow reversal, all the turbulent models overpredicted the gas holdup. Generally, the RSM model was more accurate followed by the RNG k-ε with the standard k-ε model showing the least accurate prediction. The higher accuracy of the RSM model was due to the fact that it modelled all the six Reynolds stresses. The RNG k-ε model was found to be more accurate than the standard k-ε model which can be attributed to the fact that the RNG k-ε model could account for different turbulence scales while the standard k-ε model considers only one turbulence length scale (Masood and Delgado, 2014). The more accurate turbulence models were found to be better at predicting gas holdup. This can be attributed to the dependence of turbulent dispersion force on the turbulent kinetic energy (equation 3.27). Therefore, relatively more accurate turbulence models resulted in a more accurate prediction of the dispersion of bubbles by liquid eddies and thus the radial gas holdup profiles.

Turbulent kinetic energy

Turbulent kinetic energy gives an indication of the intensity of turbulence at different locations in the reactor. This in turn, can give valuable insight into the degree of mixing. The effect of different turbulent models on the radial turbulent kinetic energy profiles at different axial locations was investigated (Figure 3.10). The turbulent kinetic energy increases with an increase in the axial distance from the distributor. This is due to an increase in the gas velocity with height which can be attributed to the increase in bubble size as a result of the decreasing hydrostatic pressure and bubble coalescence. The larger sized bubbles rise faster since they experience less drag due to their low surface to volume ratio. At the region near the distributor (h/H=0.03), the radial turbulent kinetic energy profile is relatively flat due to a uniform gas holdup profile. At this region, a significant difference in the prediction using the different turbulent models was observed. At this region of high anisotropy, only the RSM model provided accurate simulation. The 2-equation k-ε models overpredicted the turbulent kinetic energy due to the fact that these models were developed under the assumption of isotropic flow. Higher up the column, where the flow is well developed, gas holdup increases near the centreline, resulting in high turbulent kinetic energy at the centre of the column. A second high turbulence kinetic energy zone is observed at the point of flow reversal which drops drastically near the wall. The high turbulent kinetic energy at the point of flow reversal has been attributed to the large gradients and fluctuations in the liquid velocity (Ekambara et al., 2008). Simulation

using the different turbulent models managed to capture the high turbulent kinetic energy at the point of flow reversal and the reduction at the wall; however, all the models underpredicted the high turbulent kinetic energy at the centreline (Figure 3.10). This could be attributed the low axial liquid velocity predicted by the turbulence models (Figure 3.8) which could be due to inaccurate prediction of the interfacial forces.

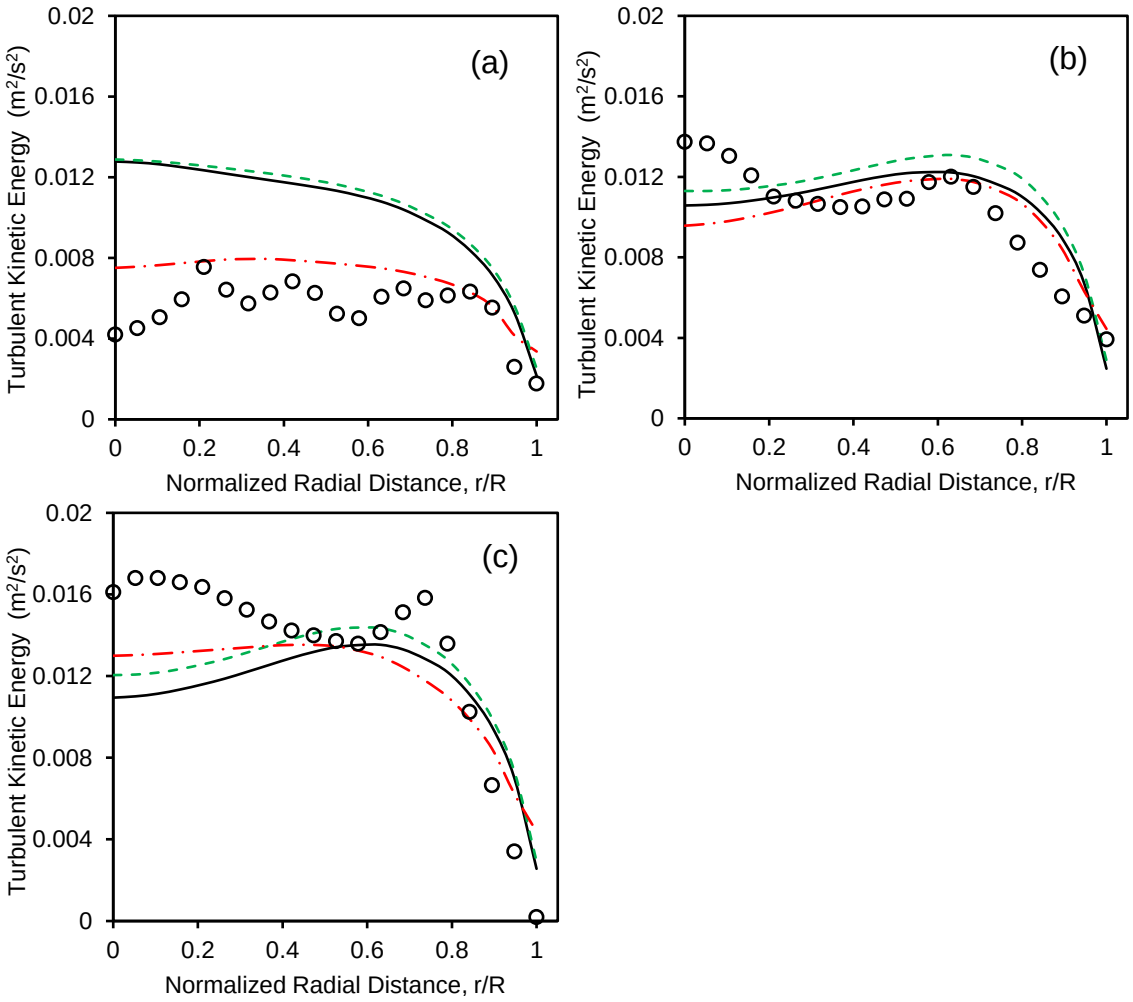

Figure 3.10: Radial profiles of the turbulent kinetic energy at different axial locations (a) h/H=0.03, (b) h/H=0.39, (c) h/H=0.75. Experimental (○), Standard k-ε (——), RNG k-ε (- - -) and RSM models (—·—).

Turbulent dissipation rate

The effect of different turbulent models on the radial turbulent dissipation rate profiles at different axial locations was also investigated (Figure 3.11). The turbulent dissipation rate profile is usually low in the middle of the reactor and increases rapidly near the reactor wall. The dissipation rate is also observed to increase with an increase in axial distance from the distributor as the flow becomes more developed. All the turbulent models captured the low turbulent dissipation rate at the reactor centreline; however, a poor agreement was observed at

intermediate radial locations and at the centre line (Figure 3.11). While all the models underpredicted the dissipation rate at intermediate radial locations, the RSM model overpredicted the turbulent dissipation rate at the wall while the k-ε based models underpredicted it. All the turbulent models failed to capture the hump observed near the region of flow reversal. Other studies have reported the difficulty in capturing this hump (Ekambara et al., 2008).

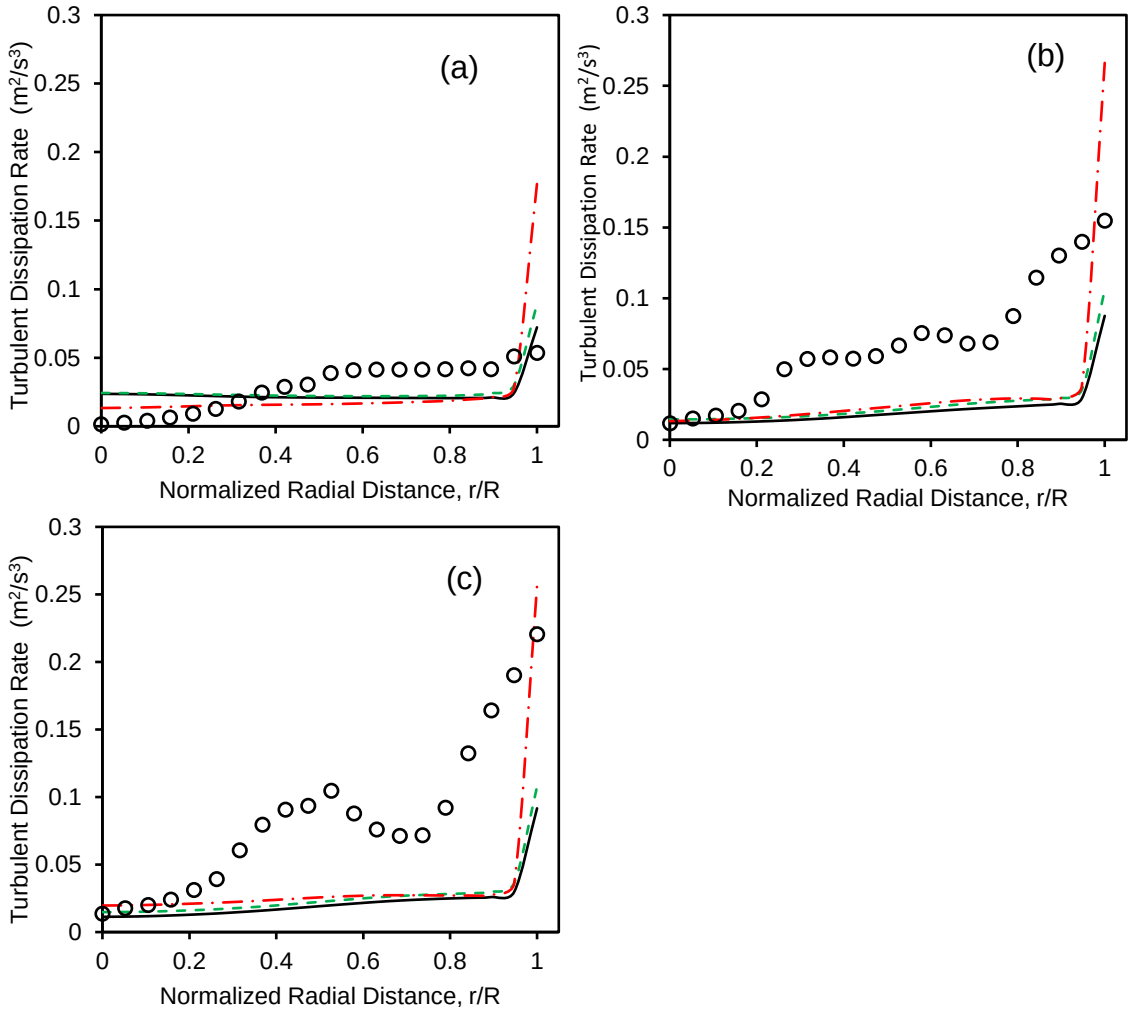

Figure 3.11: Radial profiles of the turbulent dissipation rate at different axial locations (a) h/H=0.03, (b) h/H=0.39, (c) h/H=0.75. Experimental (○), Standard k-ε (——), RNG k-ε (- - -) and RSM models (—·—).

Generally, the RNG k-ε turbulence model predicted a higher turbulence dissipation rate than the standard k-ε model. This was due to the $C_{\varepsilon 2RNG}$ term in the dissipation rate equation (equation 3.12) which is set to a constant in the standard k-ε turbulence model. However, in the RNG k-ε turbulence model, that term is a function of the local strain rate and enables the RNG k-ε turbulence model to capture turbulence effects at different length scales (Masood and

Delgado, 2014). As a result, the RNG k-ε turbulence model predicts a higher turbulent dissipation rate and a lower turbulent viscosity since dissipation rate is inversely proportional to the induced turbulent viscosity (equation 3.9). The effective liquid velocity consists of molecular and turbulent viscosity. Therefore, lower turbulent viscosity results in lower effective liquid viscosity which allows gas bubbles to rise faster in the liquid which leads to a high centreline liquid velocity using RNG k-ε as compared to standard k-ε (Laboude-Boutet et al., 2009). This also explains why the RSM model with the highest dissipation rate also predicted a high centreline liquid velocity (Figure 3.8).

3.3.4 Effect of interfacial forces

Axial liquid velocity

The effect of a combination of interfacial forces on the axial liquid velocity was also investigated. The results (Figure 3.12) shows that modelling drag and lift forces resulted in a general overprediction of the axial liquid velocity near the distributor. Further up the column, the combination of drag and lift forces underpredicted the centreline axial liquid velocity while overpredicting the velocity near the reactor wall. This could be due to the high gas holdup region near the reactor wall after including the lift force (Figure 3.13). A further improvement on the prediction was observed by combining the drag, lift and wall lubrication forces. This improvement was possibly due to the shift in the bubbles from the reactor wall to the bulk as a result of the low pressure zone created at the centre of the reactor by the fast moving liquid. The bubble redistribution resulted in an increase in the centreline axial velocity. The most accurate prediction was given when all the four forces (drag, lift, wall lubrication and turbulent forces) were modelled where only a slight underprediction was observed at the reactor centreline. Addition of the turbulent dispersion force ensured that the effect of liquid turbulence on the bubble movement was captured, resulting in a more accurate liquid velocity profile.

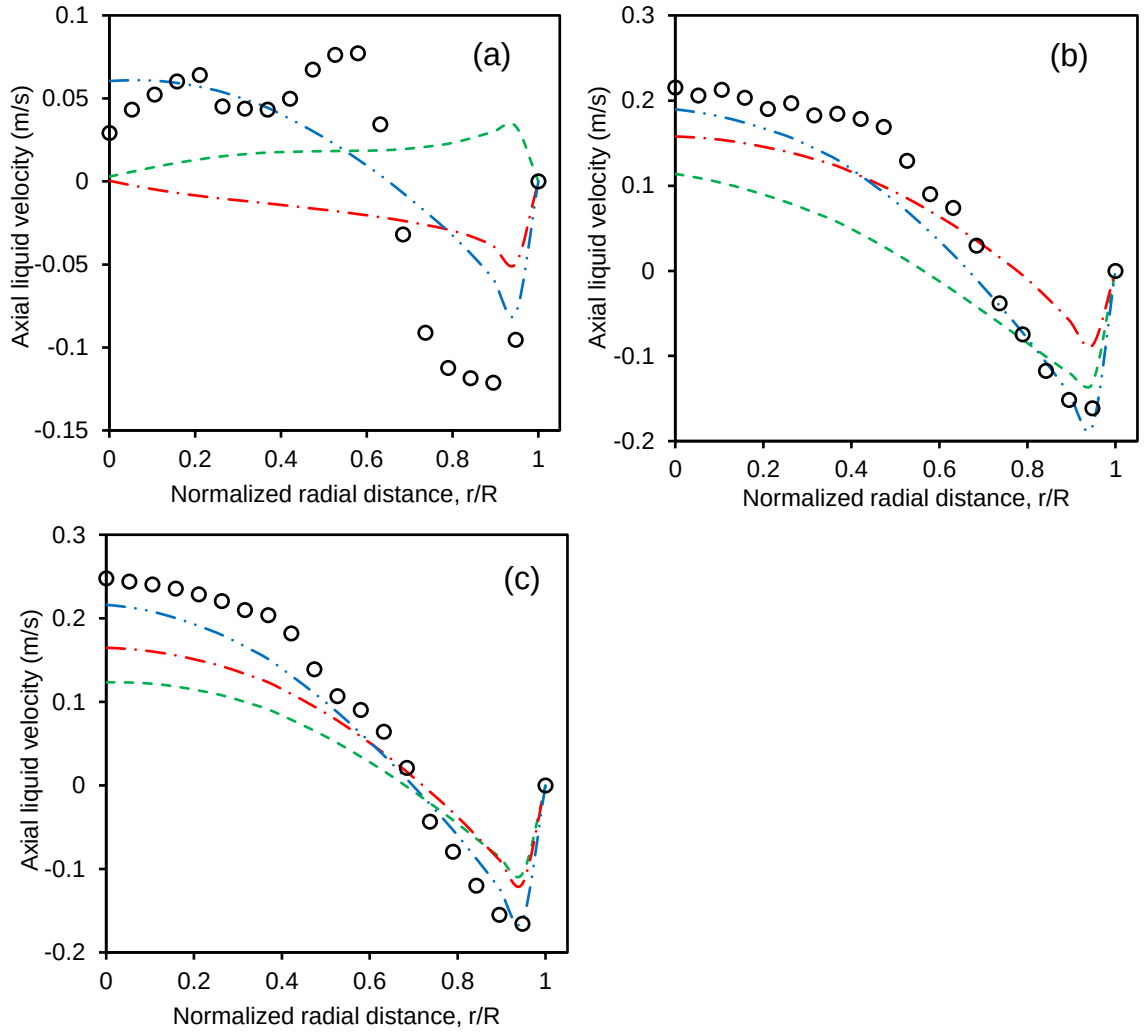

Figure 3.12: Radial profiles of the axial liquid velocity at different axial locations (a) h/H=0.03, (b) h/H=0.39, (c) h/H=0.75. Experimental (○), Drag+Lift (- - -), Drag+Lift+Wall lubrication (— · —), Drag+Lift+Wall lubrication+Turbulent dispersion (— · · —).

Gas holdup

Interfacial forces modify the movement of the bubble swarm in the reactor and this effect is most evident in the radial gas holdup profiles. The influence of a combination of different interfacial forces on the radial gas holdup profiles was investigated at different axial locations. The results (Figure 3.13) show that modelling the drag and lift forces resulted in a parabolic gas holdup profile, at the fully developed region, with accurate simulation at the central and intermediate locations. However, using the drag and lift force resulted in an increase of the gas holdup near the reactor wall. In this work, a bubble diameter of 6 mm was specified. The lift force model of Tomiyama et al. (2002), specifies a negative lift coefficient for bubbles which are 6 mm and larger. Such a negative lift coefficient results in the movement of bubbles towards the reactor centreline; however, some bubbles remain near the reactor wall.

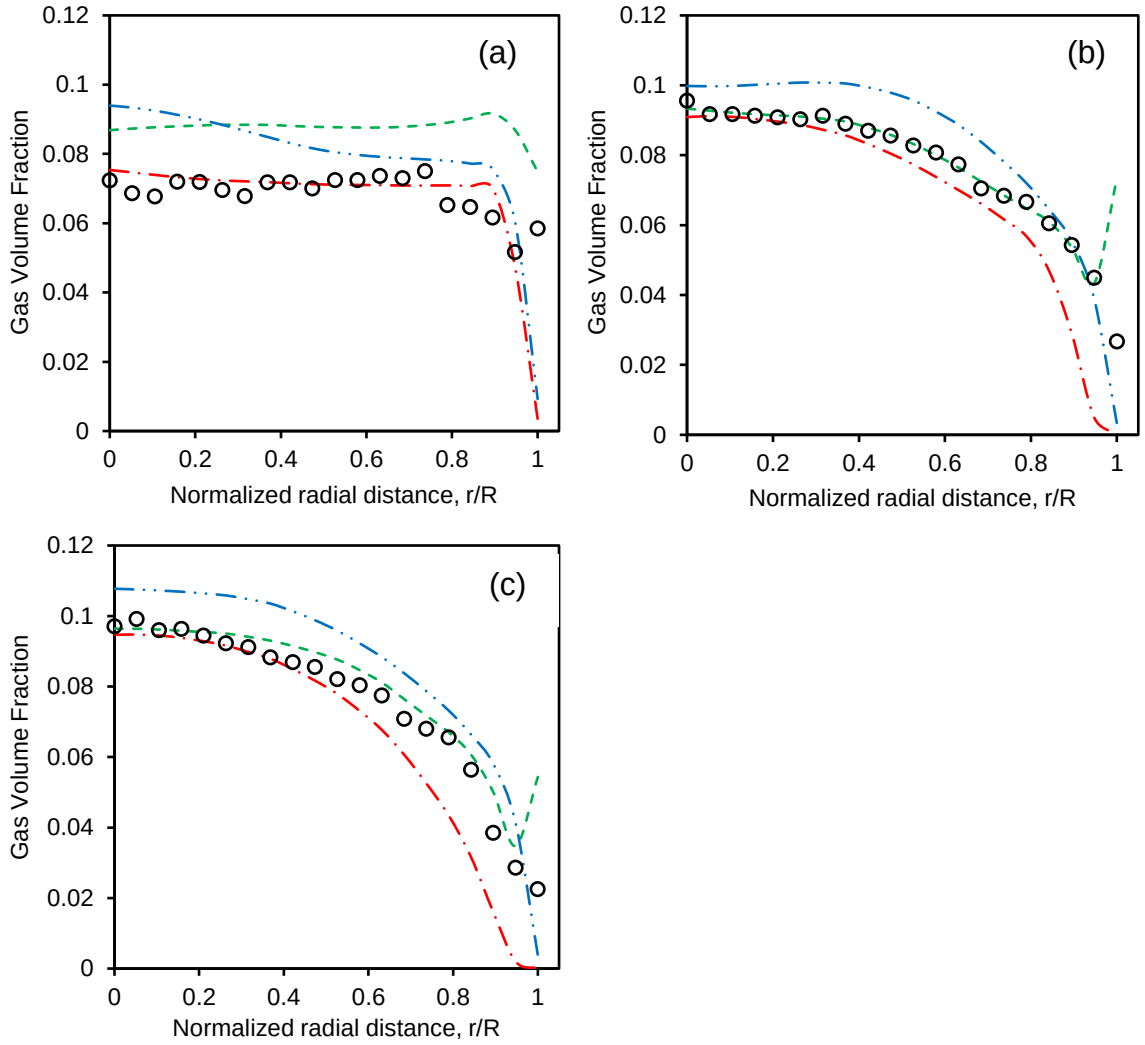

Figure 3.13: Radial profiles of the gas holdup at different axial locations (a) h/H=0.03, (b) h/H=0.39, (c) h/H=0.75 Experimental (○), Drag+Lift (- - -), Drag+Lift+Wall lubrication (—·—), Drag+Lift+Wall lubrication+Turbulent dispersion (—··—).

Modelling the drag, lift and wall lubrication forces improved gas holdup prediction near the distributor. Further up the column, the addition of the wall lubrication force to the drag and lift forces pushed the bubbles that remained near the wall towards the centreline which resulted in accurate prediction of the gas holdup near the reactor centreline and an underprediction near the reactor wall. This can be attributed to a very strong wall lubrication force which pushed the bubbles away from the wall. Inclusion of all four forces (drag, lift, wall lubrication and turbulent dispersion forces) resulted in a general overprediction of the gas holdup at the centreline and intermediate locations, with a fairly accurate prediction near the wall. The parabolic gas holdup profile along the radial direction was less steep as compared to the profile which was obtained using a combination of drag, lift and wall lubrication forces. This can be attributed by the tendency of the turbulence dispersion force to redistribute bubbles towards the reactor wall (Tabib et al., 2008).

Turbulent kinetic energy

The effect of different interfacial forces on the radial turbulent kinetic energy profiles was also investigated. The results (Figure 3.14) show that the combination of drag and lift forces generally resulted in accurate prediction of the turbulent kinetic energy at the different axial locations. However, combining drag, lift and wall lubrication forces grossly overpredicted the turbulent kinetic energy at all locations. This can be attributed to the high centreline gas holdup predicted by this combination of forces. A further addition of the turbulent dispersion force

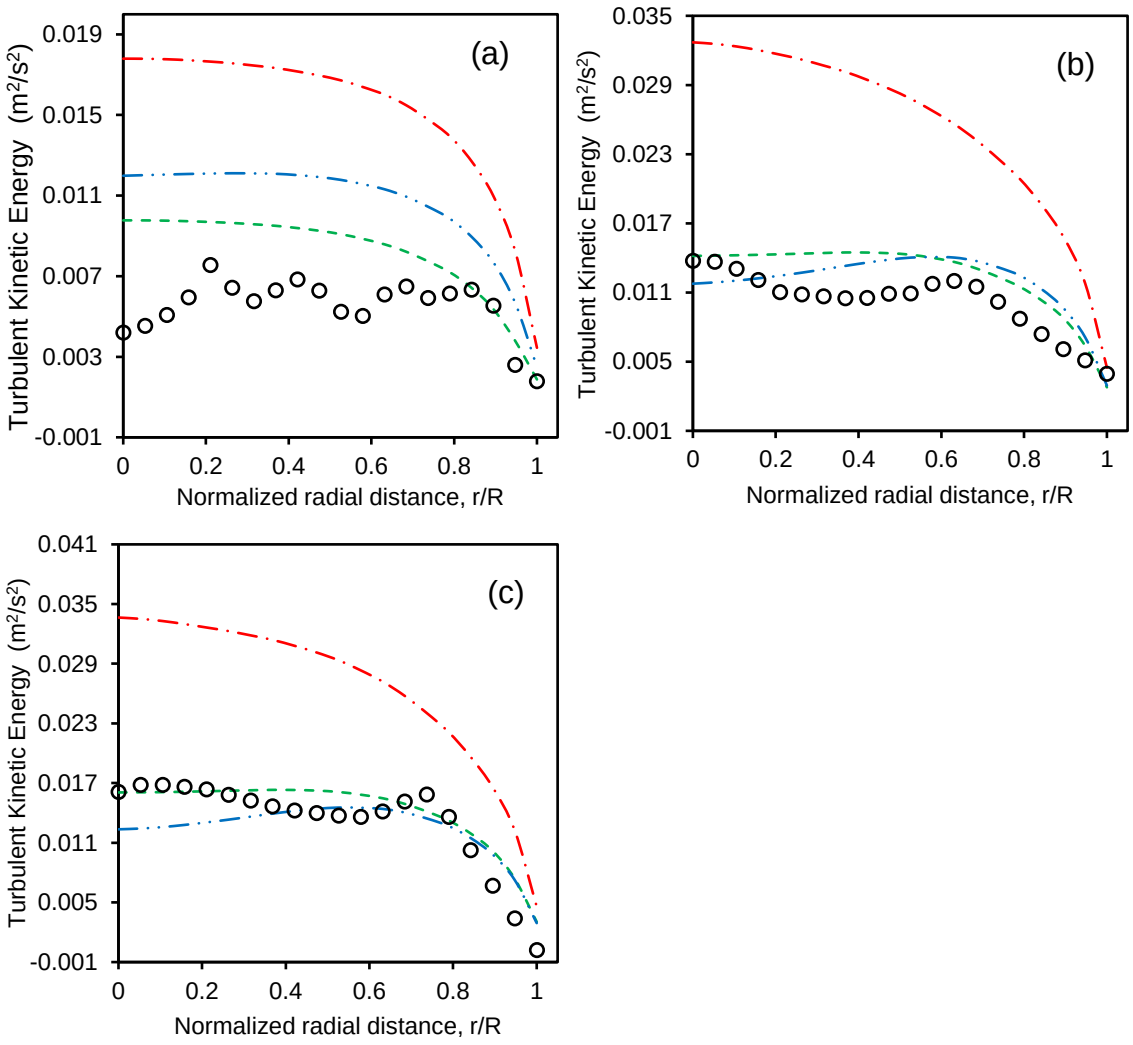

Figure 3.14: Radial profiles of the turbulent kinetic energy at different axial locations (a) h/H=0.03, (b) h/H=0.39, (c) h/H=0.75. Experimental (○), Drag+Lift (- - -), Drag+Lift+Wall lubrication (—·—), Drag+Lift+Wall lubrication+Turbulent dispersion (—··—).

significantly improved the prediction due to better redistribution of bubbles. The good prediction observed using drag+lift and drag+lift+wall lubrication+turbulent dispersion can be attributed to the broader distribution of gas holdup while using this combination of forces. This reduced the shear stresses, resulting in a lower turbulent kinetic energy profiles.

Turbulent dissipation rate

The influence of different combination of forces on the radial turbulent dissipation rate profiles was investigated. The results (Figure 3.15) show that the turbulent dissipation rate at the centreline was predicted accurately by most of the combinations of interfacial force (except drag+lift+wall lubrication). Most of the combinations of interfacial forces, except drag+lift combination, overpredicted the turbulent dissipation rate at the wall of the reactor near the distribution. Further up the column, all other combinations of interfacial forces underpredicted the turbulent dissipation rate at the wall of the reactor except drag+lift+wall lubrication forces. The unique prediction by the combination of drag+lift+wall lubrication forces can be attributed to its relatively rapid change in gas volume fraction in the radial direction as shown by the steep gas holdup profile. This resulted in high shear stresses.

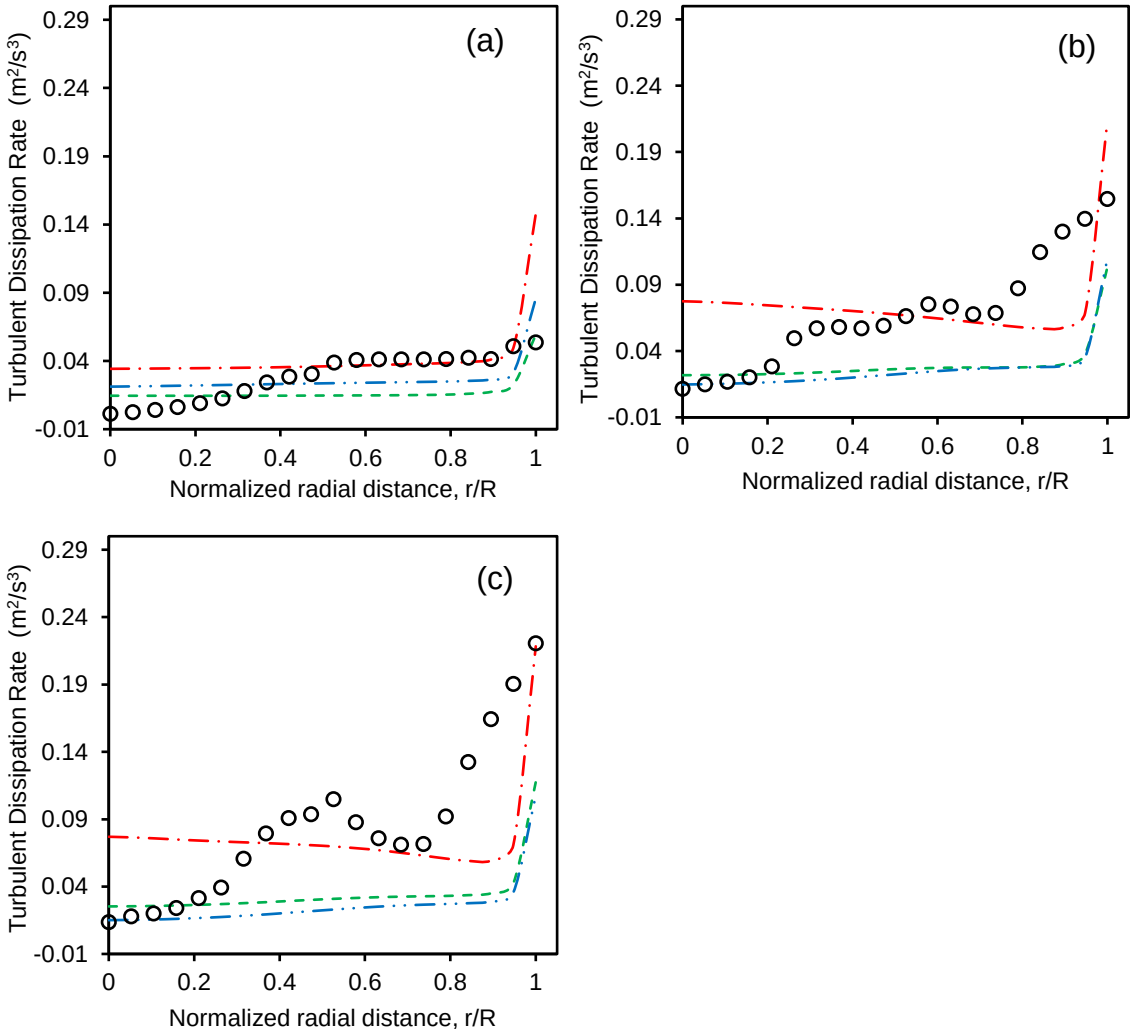

Figure 3.15: Radial profiles of the turbulent dissipation rate at different axial locations (a) h/H=0.03, (b) h/H=0.39, (c) h/H=0.75. Experimental (○), Drag+Lift (- - -), Drag+Lift+Wall lubrication (—·—), Drag+Lift+Wall lubrication+Turbulent dispersion (—··—).

3.3.5 Fluidized bed reactor

The CFD model for simulating the fluidized bed reactor was validated using the bubble column of Kulkarni et al. (2007) in order to determine the best turbulent model and interfacial forces. The bubble column was chosen for validation of the CFD model instead of a typical three phase fluidized bed reactor for several reasons. First, most of the three phase fluidized bed reactors for which experimental data was available, utilized very large particles at high solid loading. For example, Panneerselvam et al. (2009) and Hamidipour et al. (2012) simulated fluidized bed reactors with a typical solid particle size of 2.3 – 3 mm and a solid volume fraction of 0.6. The three-phase reactor simulated by Zhou et al. (2017) had a solid volume fraction of 0.091 – 0.4 and particle size of 100 – 140μm while that simulated by Li and Zhong (2015) had particle size of 35 – 450 μm and a solid volume fraction of 0.05 – 0.2. In contrast, the fluidized bed reactor used in this work had a particle size of 1340 nm and a catalyst loading of 0.2 g/L corresponding to a solid volume fraction of 4.7×10^{-5}. Moreover, from Stokes law, the terminal velocity of TiO_2 agglomerates in water was calculated as 1.29 cm/h which is significantly lower than the terminal velocity observed in most fluidized bed reactors. In some of the previously simulated fluidized bed reactors, both the gas and liquid flowed in and out of the reactor (Schallenberg et al., 2005; Panneerselvam et al., 2009). However, in the fluidized bed reactor used in this work, both the liquid and solid were retained within the reactor.

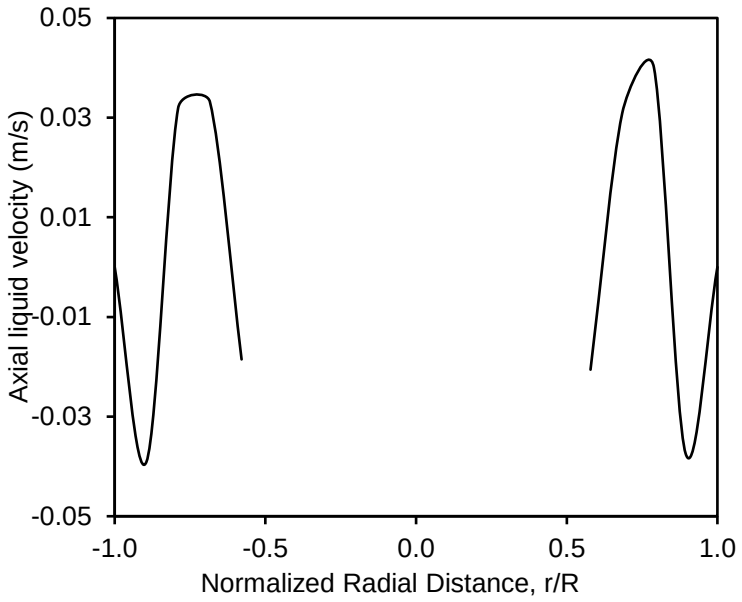

Figure 3.16: Radial axial liquid velocity profile

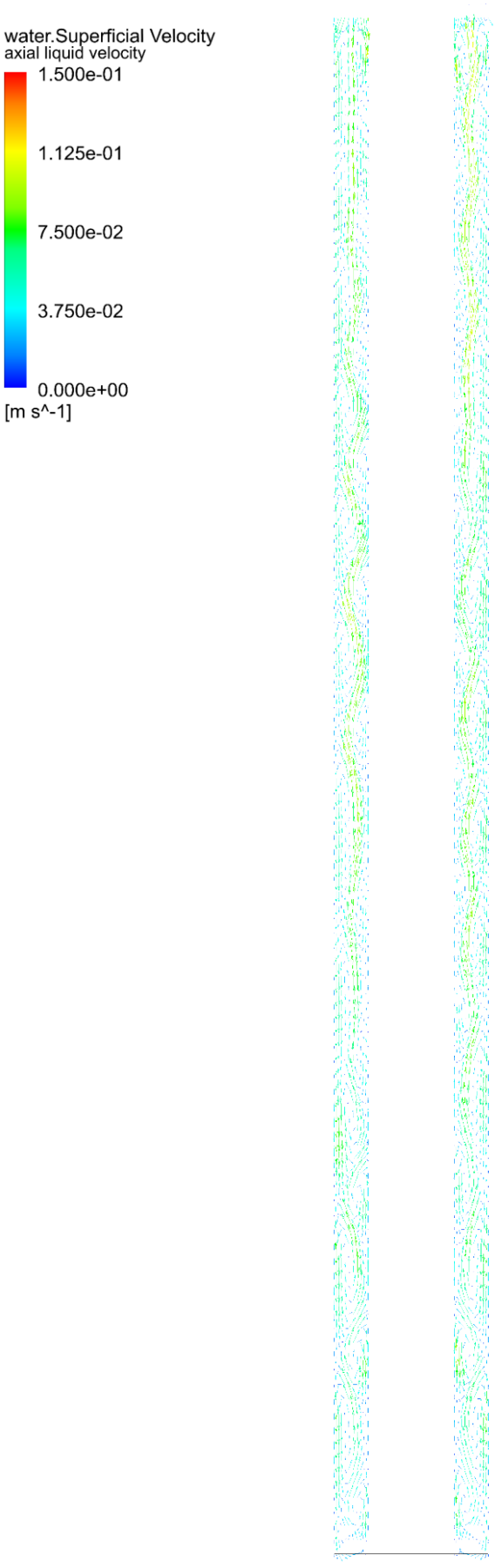

Figure 3.17: Liquid velocity vectors

In view of the factors discussed above, the reactor in this work was much similar hydrodynamically to a bubble column than previously simulated three phase fluidized bed reactors. Boyjoo et al. (2013) also noted this similarity between a bubble column reactor and a fluidized bed reactor with nanoparticles. This fact has also been recognized by Feng et al. (2005) who simulated their gas-liquid-nanoparticle reactor essentially as a bubble column with the liquid properties modified in order to account for the nanoparticles. This work improved upon the work of Feng et al. (2005) by adapting the bubble column CFD model to three phase simulation by adding the catalyst as a separate solid phase.

The simulation settings for the bubble column reactor which gave the best results were found to be the Reynolds Stress Model and the use of a combination of drag, lift, wall lubrication and turbulent dispersion forces. These settings were applied in the simulation of the annular fluidized bed reactor. In an annular reactor, all the fluid is confined in the annulus between the inner and outer reactor wall. The axial liquid velocity plot along the radial coordinate (Figure 3.16) shows the liquid flowing upwards in the middle of the annulus and downwards towards both walls of the annulus. This flow reversal profile near the wall has been observed in tubular reactors such as the bubble column reactor simulated in this work. The liquid velocity vectors (Figure 3.17) show serpentine upward flow restricted within the annulus with downward flow near the annulus walls.

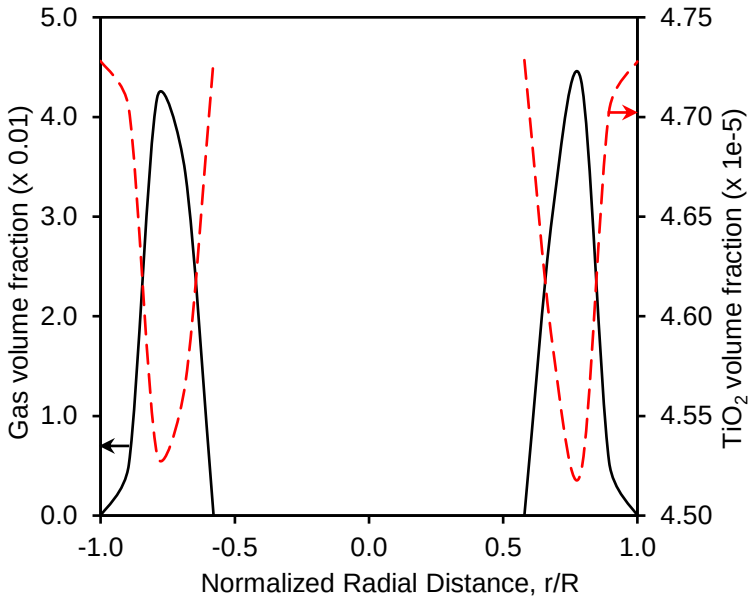

Figure 3.18: Radial gas and solid holdup profiles

The radial gas holdup profile (Figure 3.18) shows the highest gas holdup in the middle of the annulus which dropped to zero at both walls of the reactor. This is further clarified by the axial

and radial gas holdup contours (Figure 3.19a,c) which shows a high gas holdup in the middle of the annulus. Vincent et al. (2011) reported a similar gas holdup profile in their annular reactor. This profile is due to the tendency of bubbles to move away from both walls as a result of the wall lubrication force. The opposite trend was observed in the solid holdup profile in which the highest solid holdup was observed at the reactor walls with the solid holdup reducing towards the middle of the reactor (Figure 3.18; Figure 3.19b,d). A similar radial solid holdup profile has been observed in other three-phase fluidized bed reactors (Li and Zhong, 2015; Zhou et al., 2017). From a photocatalysis perspective, the higher catalyst loading at the reactor walls is desirable since this would expose more catalyst to the light from sunlight and UV lamp.

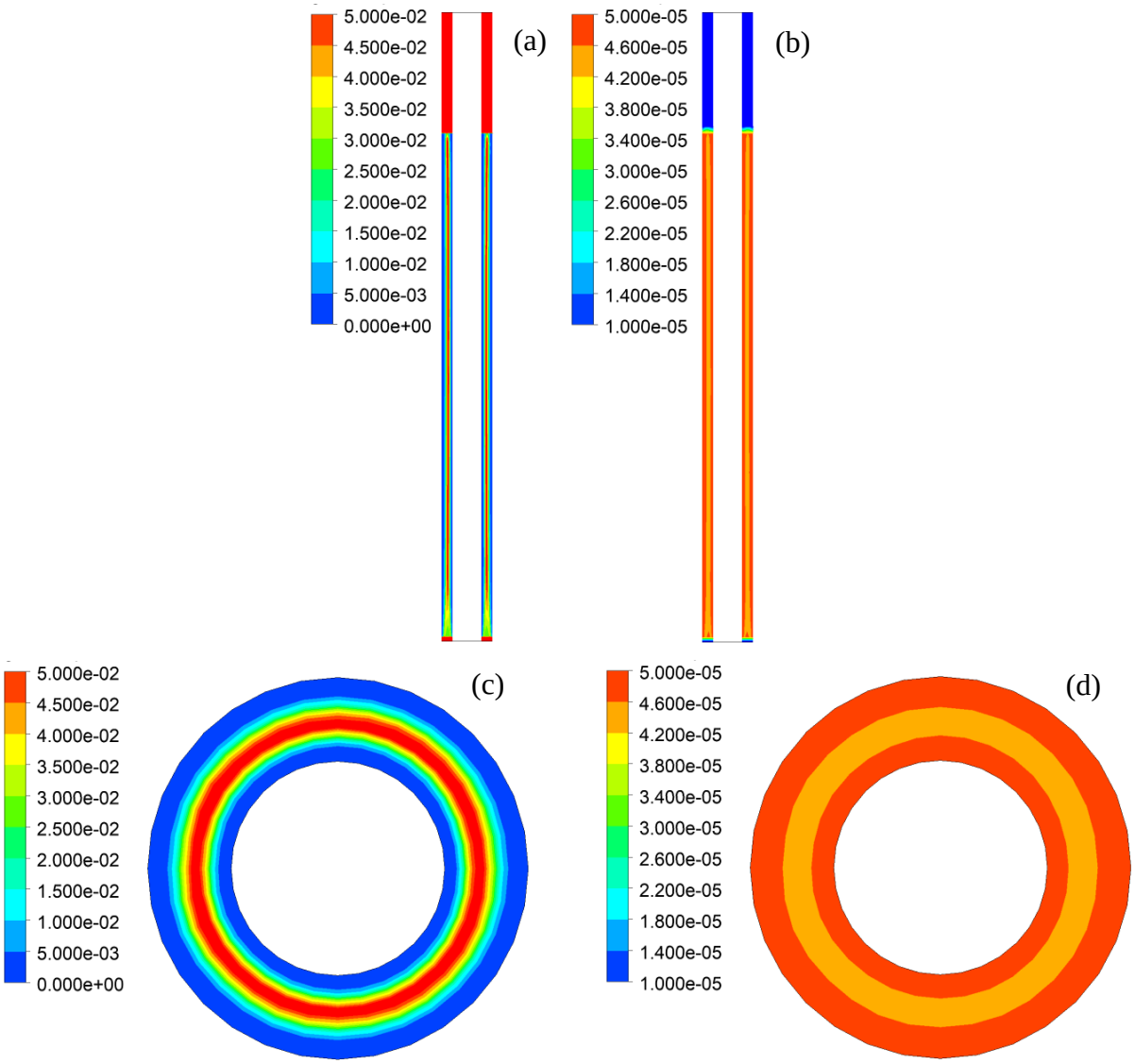

Figure 3.19: Contour plots of phase holdups (a) axial gas holdup (b) axial solid holdup (c) radial gas holdup (d) radial solid holdup

Generally, the radial variation of the catalyst loading was not significant. For instance, in the radial section represented by Figure 3.18, the difference between the highest and lowest solid

holdup was only 4%. The axial variation of the solid holdup along the column was also observed to be insignificant (Figure 3.19b). The insignificant variation of the solid holdup in the reactor was due to the fact that the catalyst was nanoparticulate in nature and could be easily fluidized in the reactor. Consequently, an assumption of uniform catalyst distribution in the reactor can be made. The simulation of the photocatalytic reactor involves the modelling of the hydrodynamics, light distribution and reaction. In such a simulation, the most important information to be obtained from hydrodynamics is the catalyst distribution. Therefore, an assumption of uniform catalyst distribution means that detailed hydrodynamics modelling can be neglected. This can significantly simplify photocatalytic reactor simulation with significant time savings since hydrodynamics simulation is usually very time consuming.

3.4 Conclusion

In this chapter, the hydrodynamics in a bubble column reactor was simulated using computational fluid dynamics (CFD). After preliminary evaluation of the optimum grid and geometry size, the effect of turbulence model and interfacial forces were investigated. A grid of 98,000 nodes was found to be optimum while simulating the full reactor geometry was deemed necessary in order to eliminate errors due to the physics of the flow. The Reynolds stress model (RSM) was found to be the most accurate. A combination of different interfacial forces resulted in different levels of accuracy depending on the hydrodynamic parameter under investigation. Nevertheless, modelling the drag, lift, wall lubrication and turbulent dispersion forces was observed to result in a fairly accurate simulation of all the different hydrodynamic parameters. Using the CFD model from the bubble column simulation and adjusting for the presence of a solid phase, the hydrodynamics in the fluidized bed reactor could be simulated. The simulation revealed a slight increase in the catalyst loading near the reactor walls. This would result in an increased light absorption during photocatalysis. Nevertheless, the catalyst distribution in the reactor was found to be fairly uniform. Consequently, hydrodynamics simulation in the fluidized bed reactor could be neglected so that the focus be on the light distribution and reaction kinetics. In this respect, the light distribution in the UV lamp illuminated reactor with uniform catalyst loading will be analysed in the next chapter.

References

Ansys, C.F.X., 2017. Solver theory guide. *Ansys CFX Release, 18*.

Boyjoo, Y., Ang, M. and Pareek, V., 2013. Some aspects of photocatalytic reactor modeling using computational fluid dynamics. *Chemical Engineering Science, 101*, 764-784.

Boyjoo, Y., Ang, M. and Pareek, V., 2014. CFD simulation of a pilot scale slurry photocatalytic reactor and design of multiple-lamp reactors, *Chemical Engineering Science*, *111*, 266-277.

Ekambara, K. and Dhotre, M.T., 2010. CFD simulation of bubble column. *Nuclear Engineering and Design*, *240*(5), 963-969.

Feng, W., Wen, J., Fan, J., Yuan, Q., Jia, X. and Sun, Y., 2005. Local hydrodynamics of gas–liquid-nanoparticles three-phase fluidization. *Chemical Engineering Science*, *60*(24), 6887-6898.

Ding, J. and Gidaspow, D., 1990. A bubbling fluidization model using kinetic theory of granular flow. *AIChE journal*, *36*(4), 523-538.

Hamidipour, M., Chen, J. and Larachi, F., 2012. CFD study on hydrodynamics in three-phase fluidized beds—Application of turbulence models and experimental validation. *Chemical Engineering Science*, *78*, 167-180.

Ishii, M. and Zuber, N., 1979. Drag coefficient and relative velocity in bubbly, droplet or particulate flows. *AIChE Journal*, *25*(5), 843-855.

Kazakis, N.A., Papadopoulos, I.D. and Mouza, A.A., 2007. Bubble columns with fine pore sparger operating in the pseudo-homogeneous regime: gas hold up prediction and a criterion for the transition to the heterogeneous regime. *Chemical Engineering Science*, *62*(12), 3092-3103.

Kulkarni, A.A., Ekambara, K. and Joshi, J.B., 2007. On the development of flow pattern in a bubble column reactor: experiments and CFD. *Chemical Engineering Science*, *62*(4), 1049-1072.

Lopez de Bertodano, M.A., 1992. Turbulent bubbly two-phase flow in a triangular duct. Ph.D. Dissertation, Rensselaer Polytechnic Institute.

Li, W. and Zhong, W., 2015. CFD simulation of hydrodynamics of gas–liquid–solid three-phase bubble column. *Powder Technology*, *286*, 766-788.

Masood, R.M.A. and Delgado A., 2014. Numerical investigation of the interphase forces and turbulence closure in 3D square bubble columns, *Chemical Engineering Science*, *108*, 154-168

Panneerselvam, R., Savithri, S. and Surender, G., 2009. CFD simulation of hydrodynamics of gas–liquid–solid fluidised bed reactor. *Chemical Engineering Science*, *64*(6), 1119-1135.

Qi, N., Zhang, H., Jin, B. and Zhang, K., 2011. CFD modelling of hydrodynamics and degradation kinetics in an annular slurry photocatalytic reactor for wastewater treatment. *Chemical Engineering Journal*, *172*(1), 84-95.

Salaices, M., Serrano, B. and De Lasa, H.I., 2002. Experimental evaluation of photon absorption in an aqueous TiO2 slurry reactor. *Chemical Engineering Journal*, *90*(3), 219-229.

Sato, Y. and Sekoguchi, K., 1975. Liquid velocity distribution in two-phase bubble flow. *International Journal of Multiphase Flow*, *2*(1), 79-95.

Schallenberg, J., Enß, J.H. and Hempel, D.C., 2005. The important role of local dispersed phase hold-ups for the calculation of three-phase bubble columns. *Chemical Engineering Science*, *60*(22), 6027-6033.

Schiller, L.A., Nauman, Z., 1935. A drag coefficient correlation. *Ver. Dtsch. Ing*. *77*, 138

Tabib, M. V., Roy, S. A. and Joshi, J. B., 2008. CFD simulation of bubble column—an analysis of interphase forces and turbulence models. *Chemical Engineering Journal*, *139*(3), 589-614.

Tomiyama, A., Tamai, H., Zun, I. and Hosokawa, S., 2002. Transverse migration of single bubbles in simple shear flows. *Chemical Engineering Science*, *57*(11), 1849-1858.

Vincent, G., Schaer, E., Marquaire, P.M. and Zahraa, O., 2011. CFD modelling of an annular reactor, application to the photocatalytic degradation of acetone. *Process Safety and Environmental Protection*, *89*(1), 35-40.

You, R., Chen, J., Shi, Z., Liu, W., Lin, C.H., Wei, D. and Chen, Q., 2016. Experimental and numerical study of airflow distribution in an aircraft cabin mock-up with a gasper on. *Journal of Building Performance Simulation*, *9*(5), 555-566.

Zhou, R., Yang, N. and Li, J., 2017. CFD simulation of gas-liquid-solid flow in slurry bubble columns with EMMS drag model. *Powder Technology*, *314*, 466-479.

Chapter 4

4 Simulation of the light distribution in a UV lamp illuminated reactor

4.1 Introduction

In the design, analysis and scale up of a fluidized bed photoreactor, all the factors that could affect the rate of photocatalysis, namely catalyst, bubble, pollutant and light distribution should be accounted for. Very good mixing is possible in a fluidized bed photoreactor; therefore, an assumption of homogeneous catalyst distribution in the reactor can be made (Boyjoo et al., 2014a). This hypothesis has been proven in chapter 3, in which catalyst distribution was shown to be reasonably homogeneous. Such an assumption is not valid for light distribution which is always inhomogeneous (Camera-Roda et al., 2016). As a result, most photocatalytic reactor modelling has focused on light distribution.

The light distribution in two-phase annular UV reactors has been investigated extensively (Li Puma et al., 2010; Moreira et al., 2010; Valadés-Pelayo et al., 2014). However, only a few studies have evaluated the light distribution in a three-phase annular UV reactor. Boyjoo et al. (2013) simulated the light distribution in a multi-lamp slurry bubble column reactor using the discrete ordinates method. Motegh et al. (2013) utilized a bi-directional scattering model to study the effect of bubbles in a theoretical three-phase reactor with suspended catalysts. Clearly more work needs to be done in this area using rigorous validated models in order to establish the conclusions made by other authors. In this chapter, a rigorous model based on the Monte Carlo method was validated and then used to simulate the light distribution in a three-phase annular UV reactor. The Monte Carlo method is well known for its accuracy; however, it has never been used to simulate the light distribution in a three-phase annular UV reactor. The aim of this chapter was to investigate the effect of catalyst and bubbles on the light distribution in a UV lamp illuminated fluidized bed photoreactor.

4.2 Methodology

4.2.1 Reactor set up

The fluidized bed photoreactor (Figure 4.1) consisted of a 2.2 mm thick reactor wall and a 1.4 mm thick glass sleeve made of clear borosilicate glass. The reactor wall outer diameter and the glass sleeve outer diameter were 65 and 34 mm, respectively. Air was supplied to the reactor from an oil free compressor (Jun-Air) through a borosilicate glass porous distributor with a

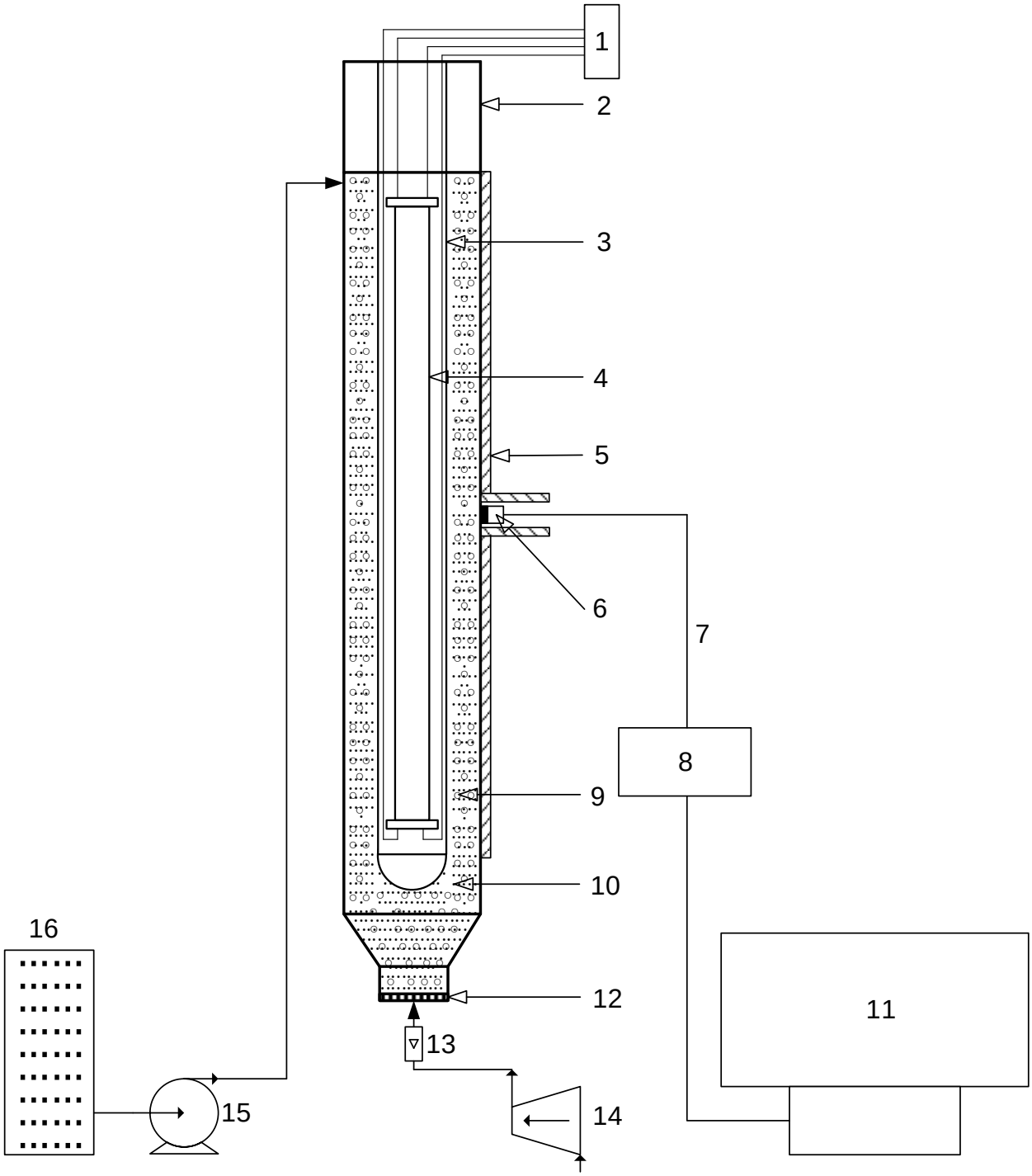

Figure 4.1: Light distribution measurement setup. (1) Power supply, (2) reactor wall, (3) lamp sleeve, (4) black light lamp, (5) radiation sensor support, (6) radiometric sensor, (7) fibre optic cable, (8) spectroradiometer, (9) air bubble, (10) catalyst slurry, (11) computer, (12) porous distributor, (13) rotameter, (14) air compressor, (15) peristaltic pump, (16) feed tank

pore size of 10 – 16 µm. A rotameter was provided to control the flow rate of the air entering the reactor. The total height of the reactor was 820 mm with a working height of 600 mm and a liquid capacity of 1.25 L. The reactor was operated in continuous mode for the air and batch

mode for the liquid and catalyst. Technical drawings of the reactor body and lamp sleeve are provided in Figure B1 and Figure B2 of Appendix B.

Reactor illumination was provided by an 18 W low pressure black light blue lamp (Philips) installed inside the glass sleeve. The lamp had a diameter of 26 mm, arc length of 515 mm and a photon emission rate of 2.1×10^{-5} Einsteins/s. The light passing through the reactor wall, referred to as the total transmitted radiation (TTR) was measured using a radiation sensor fitted on the reactor wall at the reactor axial centreline. The radiation sensor used in this study was the CR2 cosine receptor with a ¼ inch diameter supplied by Stellarnet. The light collected by the radiation sensor was measured using a calibrated spectroradiometer (Stellarnet, Black Comet SR) which was connected to the sensor by a fibre optic cable.

4.2.2 Monte Carlo model

For an absorbing and scattering medium, the radiation energy balance across a thin block of catalyst slurry has been described using the radiation transport equation (RTE) (Romero et al., 2003):

$$\frac{dI_\lambda(s,\Omega)}{ds} = -\kappa_\lambda I_\lambda(s,\Omega) - \sigma_\lambda I_\lambda(s,\Omega) + \frac{1}{4\pi}\sigma_\lambda \int_0^{4\pi} p(\Omega' \to \Omega) I_\lambda(s,\Omega') d\Omega' \quad (4.1)$$

where I_λ is a beam of light of wavelength λ travelling in direction Ω and distance s; κ_λ and σ_λ are the absorption and scattering coefficients of the medium, respectively; $p(\Omega' \to \Omega)$ is the scattering phase function which determines the probability that light from direction Ω' will be scattered to direction Ω. In this work, the RTE was solved stochastically using the Monte Carlo method which is described next.

Bubble location

The reactor was operated in a homogenous flow regime, in which the bubbles were observed to be spherical with a fairly uniform distribution. This flow regime could best be modelled by assuming a random distribution of spherical bubbles. An algorithm adapted from Imoberdorf et al. (2008) was used to specify the random location of bubble centroids under the following restrictions and assumptions: (i) all bubbles were assumed to be spherical with a uniform diameter, (ii) to keep a bubble from intersecting a reactor boundary, bubble centroids were offset from all reactor boundaries by a distance of one bubble radius, (iii) the minimum distance

between two bubble centroids was specified to be equal to the bubble diameter to prevent bubble overlap. The number of bubbles (n_b) was calculated from the gas holdup as:

$$n_b = \frac{6\varepsilon_g V}{\pi d_b^3} \tag{4.2}$$

where ε_g is the global gas holdup, V is the reactor volume and d_b is the bubble diameter. The bubble diameter was measured from photographs of the reactor under operation and found to be 6 mm on average. Global gas holdup was measured using the quick-stop method (Ochieng et al., 2002; 2003).

A random bubble centroid location in cartesian coordinates (x_B, y_B, z_B) was specified using equations (4.3) – (4.6) under constraint (ii). Once a random bubble centroid was specified, its distance to all other bubbles was checked. If the specified bubble was found to overlap another bubble, it was discarded and then another random bubble was generated. This process was continued until the required number of non-overlapping bubbles was specified.

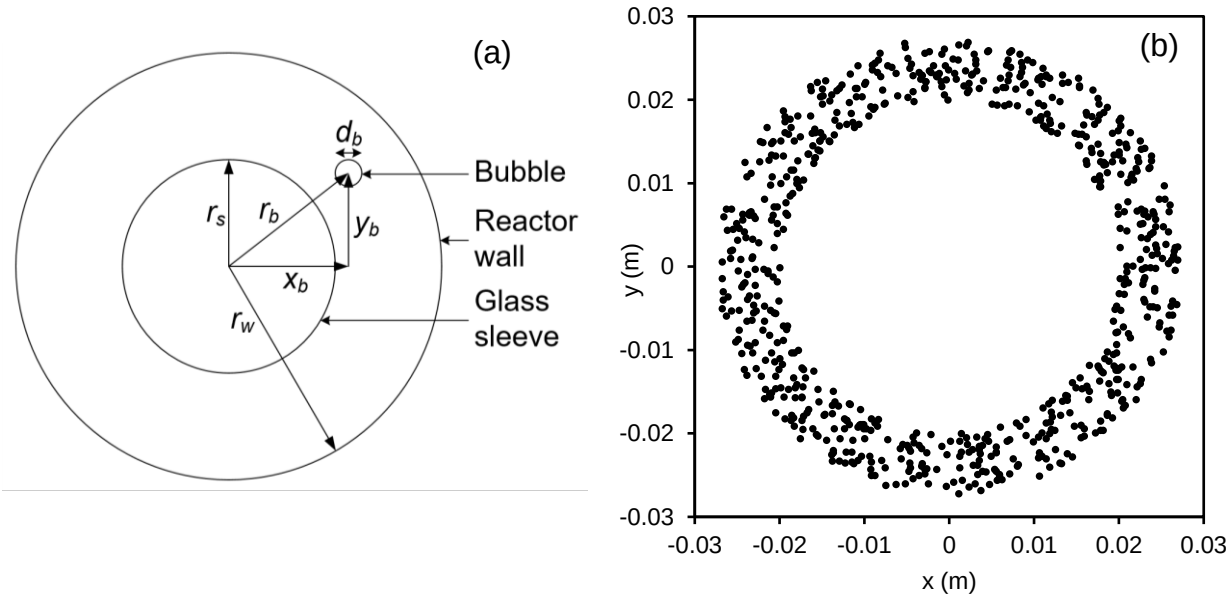

Figure 4.2: (a) Coordinate system in bubble distribution, (b) Random bubble centroid distribution

$$r_b = (r_s + 0.5d_b) + (r_w - r_s - d_b)R_1 \tag{4.3}$$

$$x_b = r_b \cos(2\pi R_2) \tag{4.4}$$

$$y_b = r_b \sin(2\pi R_2) \tag{4.5}$$

$$z_b = d_b + (h_w - d_b)R_3 \tag{4.6}$$

where r_b is the bubble radial location, r_s is the outer glass sleeve radius, r_w is the reactor wall radius, h_w is the reactor height and R_1, R_2, R_3 are random numbers. The coordinate system used for bubble distribution is shown in Figure 4.2a while Figure 4.2b shows the random bubble centroid distribution obtained using equations (4.1) – (4.6). The simulated bubble centroids were randomly distributed within the reactor annulus (Figure 4.1) as required.

Lamp emission

In a low pressure black light lamp, UVC photons generated in the lamp volume hit the phosphor coating on the lamp surface resulting in the generation of UVA photons. The UVA photons are then emitted diffusely in all directions. As a result, the lamp emission was modelled using the surface source with diffuse emission (SSDE) model (Pareek et al., 2008):

$$G_\lambda = \frac{K_\lambda}{4\pi}\int_{h=0}^{h=h_L}\int_{\phi=0}^{\phi=\pi}\frac{(r\cos\theta - r_L\cos\phi)\,r_L \mathrm{d}\phi \mathrm{d}h}{(r\cos\theta - r_L\cos\phi)^2 + (r\sin\theta - r_L\sin\phi)^2 + (z-h)^2} \tag{4.7}$$

where G_λ is the spectral incident radiation, K_λ is the rate of photon emission per unit surface of lamp, h is the axial coordinate of lamp element, z is the axial coordinate, r is the radial coordinate, h_L is the length of the lamp, r_L is the radius of the lamp, ϕ is the angular coordinate and θ is the zenith angle.

Equation (4.7) was solved stochastically by emitting photons at random locations on the lamp surface which were then transmitted diffusely in random directions. The random angular emission location (ϕ_L) within the lamp volume was determined as:

$$\phi_L = 2\pi R_4 \tag{4.8}$$

from which the lamp emission location in cartesian coordinates (x_L, y_L) was given as:

$$x_L = r_L\,R_5\cos(\phi_L) \tag{4.9}$$

$$y_L = r_L\,R_5\sin(\phi_L) \tag{4.10}$$

where r_L is the lamp radius and R_4, R_5 are random numbers.

The lamp emission intensity along the axial coordinate has been found to be highest at the middle of the lamp and lowest at the lamp extremities. Tsekov and Smirniotis (1997) represented this trend using the probability density function:

$$P_z = 0.5\left[\frac{z-a}{\sqrt{r_L^2 + (z+a)^2}} - \frac{z-a-h_L}{\sqrt{r_L^2 + (z-a-h_L)^2}}\right] \tag{4.11}$$

where P_z is the probability of a photon being emitted from an axial location z on the lamp surface, a is the axial distance between the lamp and the reactor end cap, r_L is the lamp radius while h_L is the height of the lamp. The axial emission location was randomly selected using a cumulative probability density function derived from the model by Tsekov and Smirniotis (1997).

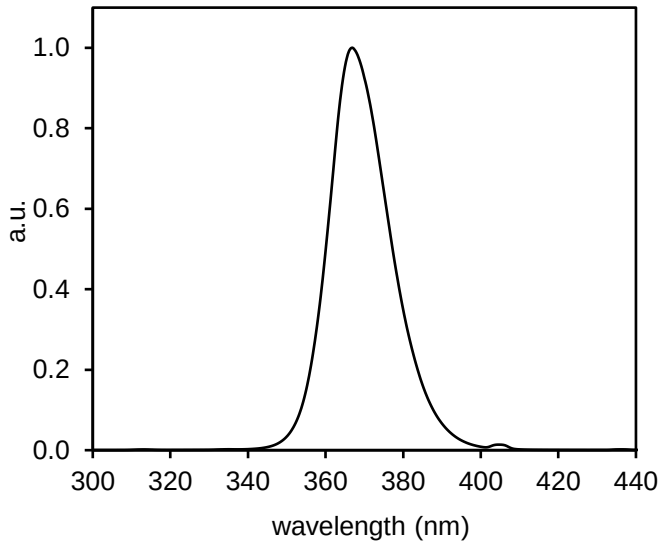

Figure 4.3: Black light lamp spectrum

Figure 4.3 shows the emission spectrum of the lamp which was measured experimentally using the spectroradiometer. The measured spectrum is very similar to that provided by the manufacturer (Lighting.philips.com, 2017). From the spectrum, it can be observed that the lamp emits photons between 340 and 410 nm with most of the photons having a wavelength of 367 nm. In this simulation, only the lamp spectrum between 340 and 387 nm was considered since the catalyst used in this simulation, Aeroxide P25 TiO_2, does not absorb light beyond 387 nm (Boyjoo et al., 2013). The wavelength of an emitted photon was randomly chosen using a cumulative probability density function derived from the lamp spectrum.

After specifying the photon emission location and wavelength, the initial direction of photon flight was specified using random azimuth and zenith angles. In the coordinate system employed in this model (Figure 4.4), the origin was positioned at the bottom of the reactor with the zenith angle measured clockwise from the z-axis and the azimuth angle measured anti-clockwise from the x-axis. The random azimuth angle (ϕ) of photon flight was specified under the condition that the emitted photon does not move back into the lamp (Zekri and Colbeau-Justin, 2013). Therefore, the azimuth angle was specified as a function of the angular photon emission location (ϕ_L) as:

$$\phi = \phi_L - 0.5\pi + \pi R_6 \tag{4.12}$$

The random zenith angle (θ) of photon flight was specified as (Moreira et al., 2010):

$$\theta = \text{acos}(2R_7 - 1) \tag{4.13}$$

where R_6 and R_7 are random numbers.

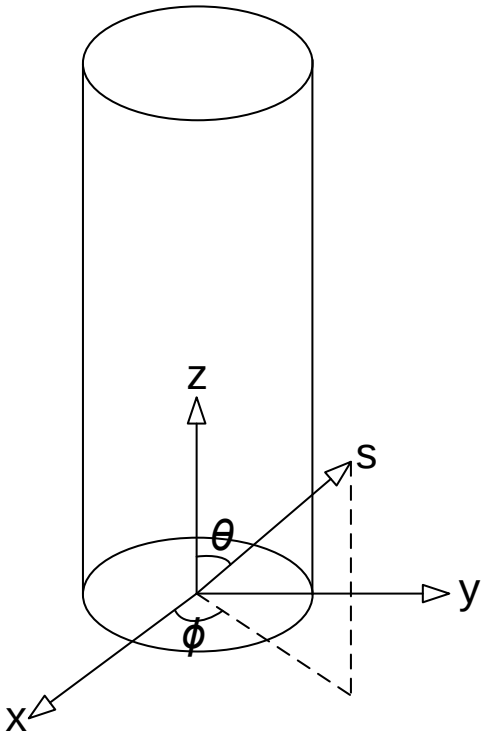

Figure 4.4: Reactor coordinate system

Photon path

Once the initial direction of photon flight was specified, the photon was moved across the air gap until it hit the inner glass sleeve. The transparency of the 1.4 mm thick borosilicate glass to light was determined to be 94.83%. Therefore, at the glass sleeve, the probability of the photon being absorbed by the glass sleeve was specified as 5.17%. This absorption event was determined using another random number R_8 such that If $R_8 < 0.0517$, the photon was absorbed; otherwise, the photon was transmitted through the glass sleeve with refraction. The change in direction due to refraction was computed using Snell's law (De Greve, 2006). After crossing the glass sleeve, the photon flight through the slurry was evaluated.

The free photon path length (l_P) in the slurry during which time no absorption or scattering events occurred was determined as (Pareek et al., 2008):

$$l_P = -\frac{\ln(R_9)}{\kappa_\lambda + \sigma_\lambda} \tag{4.14}$$

where R_9 is a random number while κ_λ and σ_λ are the spectral absorption and scattering coefficients of the medium, respectively. The spectral scattering and absorption coefficients of the catalyst used in this work were obtained from Romero et al. (2003) and are listed in Table 4.1.

Table 4.1: P25 TiO_2 spectral scattering and absorption coefficients (Romero et al., 2003)

λ (nm)	κ_λ (cm^2 g^{-1})	σ_λ (cm^2 g^{-1})
315	18722	50418
325	15872	54528
335	11775	55877
345	8082	55056
355	4777	54583
365	2548	52547
375	1293	50013
385	433	47567
395	0	45071
405	0	42343
415	0	40000
435	0	36000

Once the photon had travelled a distance l_P within the slurry, its new location in cartesian coordinates was determined as:

$$x_N = x_O + (\sin\theta \cos\phi)\, l_P \tag{4.15}$$

$$y_N = y_O + (\sin\theta \cos\phi)\, l_P \tag{4.16}$$

$$z_N = z_O + (\cos\theta)\, l_P \tag{4.17}$$

where x_N, y_N, z_N were the new updated cartesian coordinates while x_O, y_O, z_O were the previous coordinates.

Absorption and scattering events

At the end of the free photon path length, the photon could either be absorbed or scattered. The probability of an absorption event was determined as (Changrani and Raupp, 1999):

$$R_{10} < \frac{\kappa_\lambda}{\kappa_\lambda + \sigma_\lambda} \tag{4.18}$$

where R_{10} is a random number while κ_λ and σ_λ are the spectral absorption and scattering coefficients of the medium, respectively. The reactor volume was divided into a grid consisting of 10 radial and 60 axial regions. If equation (4.18) evaluated true, the photon was absorbed and its energy per unit volume was stored in a corresponding location in the grid. The local

volumetric rate of energy absorption (LVREA) was computed as the sum of the energy of all photons absorbed per unit volume at a specified grid location (Valadés-Pelayo et al., 2014). The volumetric rate of energy absorption (VREA) was then determined as the average of LVREA values at all locations.

If the photon was not absorbed, it was scattered. Scattering involved a change in the photon azimuth and zenith angles. The new angles were determined from coordinate transformations based on the scattering azimuth and zenith angles. The scattering azimuth direction (ϕ_s) was calculated as:

$$\phi_s = 2\pi R_{11} \tag{4.19}$$

The scattering zenith direction was determined using the Henyey-Greenstein (HG) phase function (Moreira et al., 2010) as:

$$\cos(\theta_s) = \begin{cases} \frac{1}{2g}\left[1 + g^2 - \left(\frac{1-g^2}{1-g+2gR_{12}}\right)^2\right], & if\ g \neq 0 \\ 2R_{12} - 1, & if\ g = 0 \end{cases} \tag{4.20}$$

where R_{10}, R_{11}, R_{12} are random numbers and g is the HG phase function scattering parameter whose value lies between -1 and 1. A scattering parameter of -1, 0 and 1 refers to completely backward, isotropic and completely forward scattering, respectively. The zenith scattering angle (θ_s) was then calculated as:

$$\theta_s = \text{acos}(\cos(\theta_s)) \tag{4.21}$$

In case the photon hit a bubble, the photon was reflected on the bubble or transmitted by refraction through the bubble. The reflection or transmission event was determined as a function of the incident angle on the bubble. The change in photon direction due to refraction was computed using Snell's law (De Greve, 2006). The reflected or transmitted photon then continued its flight through the slurry. The series of absorption and scattering events in the slurry and bubbles was continued until the photon was absorbed or hit the outer glass sleeve, reactor wall or end caps. On hitting the outer glass sleeve, the photon could be absorbed or transmitted with refraction to the air gap from where it could hit the lamp. A photon which hit the lamp was reflected off the lamp surface (Moreira et al., 2010). A photon which hit the reactor wall could be absorbed (with a probability of 8%) or transmitted with refraction to the air outside the reactor. The transmitted photon could hit the radiometer sensor or escape the reactor. If the photon hit the sensor, its energy was added to the TTR variable. Figure 4.5 shows

a section of the fluidized bed photoreactor illustrating photon flight from the lamp to the radiometer sensor. Any photon which escaped the reactor wall and reactor end cap or was absorbed in the slurry, glass sleeve, reactor wall or sensor was considered lost; therefore, a new photon was emitted from the lamp and tracked.

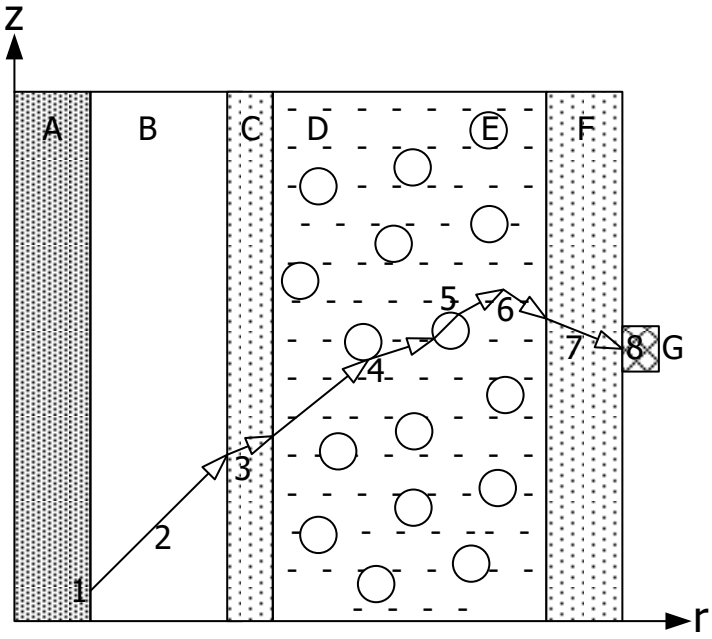

Figure 4.5: Photon flight in the reactor (1) emission location, (2) air gap photon flight, (3) glass sleeve refraction, (4) bubble scattering, (5) bubble transmission, (6) slurry scattering, (7) reactor wall refraction, (8) sensor absorption. (A) lamp, (B) air gap, (C) glass sleeve, (D) catalyst slurry, (E) bubble, (F) reactor wall, (G) radiometer sensor

A large number of photons packets (10^7) was emitted and tracked through the reactor. In a stochastic simulation like Monte Carlo, simulation accuracy increases with an increase in the number of tracked photon packets. However, an increase in the photon packets also increases the simulation time. The optimum number of photon packets was determined by analyzing the values of the TTR at different catalyst loadings and photon packets. As can be seen in Figure 4.6, at low photon packets, a wide variation in the TTR was observed. This wide variation drastically reduced at 10^7 photon packets; therefore, this number was chosen as the optimum. All simulations were carried out by tracking 10^7 photon packets, the number of packets which was also used by Moreira et al. (2010). By tracking a large number of photon packets, the light distribution in the reactor was established by analysing the LVREA at different locations in the slurry. In order to account for the continuous change in bubble locations in the reactor, a new bubble centroid matrix was generated for every 10^4 emitted photons. The Monte Carlo algorithm was written and solved in MATLAB R2015a. A sample program is provided in Appendix C.

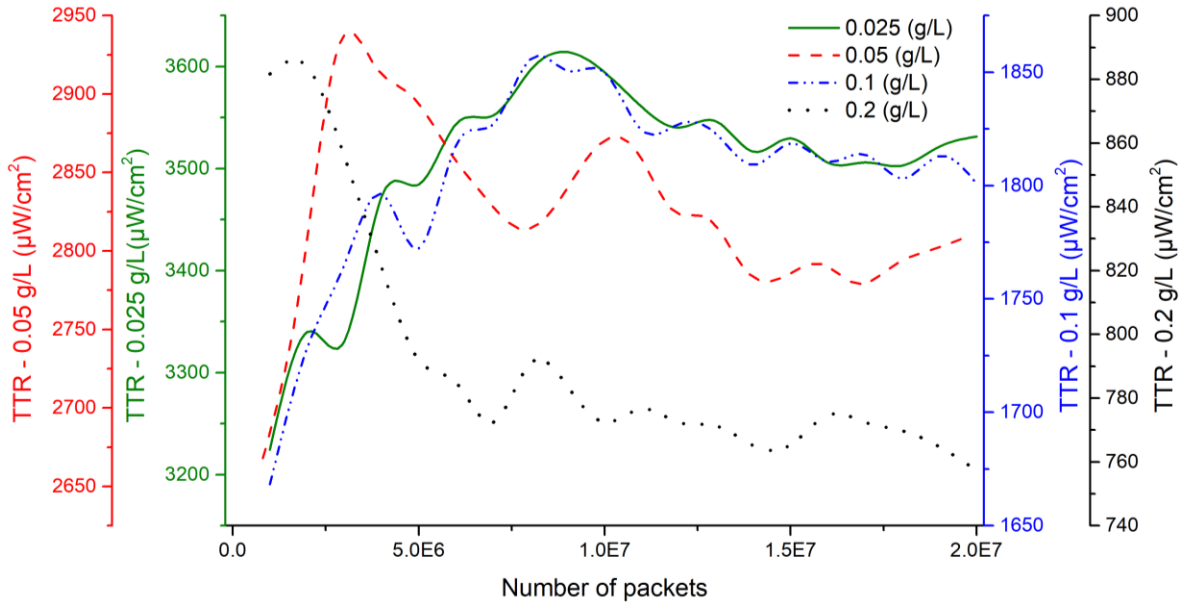

Figure 4.6: Effect of the number of photon packets tracked on the TTR at different catalyst loadings

4.2.3 TTR Experiments

The total transmitted radiation (TTR) refers to the fraction of emitted photons which hit the sensor positioned on the reactor wall. The TTR was measured using a radiometer sensor fixed on the outer wall of the reactor. A catalyst slurry was prepared in the feed tank by mixing a measured quantity of Aeroxide P25 TiO_2 purchased from Acros Organics in 1250 mL of deionized water (Millipore DirectQ 8). The catalyst, P25 TiO_2, has a primary particle size of 20 – 30 nm, specific surface area of 52 m^2 g^{-1} and a composition of 78% anatase and 22% rutile (Li Puma et al., 2004). In water, sonicated suspensions form aggregates of 700 nm (Cabrera et al., 1996) while unsonicated suspensions form larger aggregates of 1181 – 2277 nm (Li Puma et al., 2004). The slurry with a catalyst loading of 0.025 g/L was then pumped into the reactor and then compressed air was introduced into the reactor at a flow rate of 40 L/h. The UV lamp was then switched on and left to warm for 30 minutes. Afterwards, TTR measurements were taken by automatically averaging a set of radiation readings over a duration of 5 minutes using Stellarnet Spectrawiz software. After measuring the TTR at a catalyst loading of 0.025 g/L, the catalyst loading in the reactor was increased by introducing measured quantities of catalyst into the reactor. In this way, the TTR was measured at catalyst loadings of 0.025, 0.05, 0.1, 0.2, 0.4 and 0.6 g/L.

4.3 Results and discussion

4.3.1 Total transmitted radiation

Total transmitted radiation (TTR) measurements are a convenient method of validating the Monte Carlo model by measuring the light escaping through the reactor wall. TTR measurements at the reactor wall were carried out at different catalyst loadings (0.025 – 0.6 g/L). The experimental results (Figure 4.7a) show an exponential decrease in the TTR from 3596 to 53 µW/cm^2 with an increase in the catalyst loading from 0.025 to 0.6 g/L. The decrease in the TTR with an increase in catalyst loading can be attributed to the increase in light obstruction due to scattering and absorption (Moreira et al., 2010; Valadés-Pelayo et al., 2014).

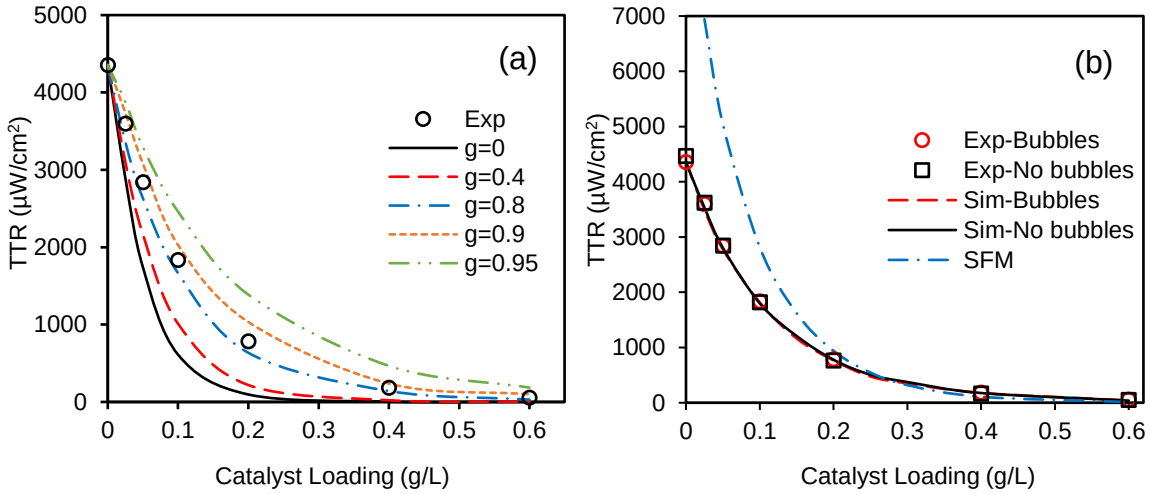

Figure 4.7: (a) Effect of scattering parameter (g) on Monte Carlo simulation (b) comparison of experimental TTR and simulated TTR with and without bubbles at a scattering parameter of 0.84

The TTR from the reactor at different catalyst loadings was simulated using the Monte Carlo method. In order to characterize the nature of catalyst scattering, the effect of the Henyey-Greenstein phase function parameter (g) was investigated. The simulation results (Figure 4.7a) show an increase in the TTR with an increase in the scattering parameter from 0 to 0.95 at all catalyst loadings. The Henyey-Greenstein scattering parameter determines the direction in which light is scattered by the catalyst particles. The scattering parameter can range from -1 to 1. A scattering parameter of -1 refers to complete backward scatter while 1 refers to complete forward scatter and 0 refers to isotropic scatter in all directions. Therefore, the increase in the forward scattering parameter resulted in more photons moving towards the reactor wall leading to the observed increase in the TTR. Figure 4.7a also shows that the increase in the TTR with an increase in the scattering parameter was more significant at higher catalyst loadings. For example, an increase in the scattering parameter from 0 to 0.95 resulted in an increase in the

simulated TTR by 25% and 99% at a catalyst loading of 0.025 and 0.4 g/L, respectively. This was due to the fact that at high catalyst loading, the number of photon scattering centres increased, significantly affecting photon trajectories and the TTR.

In order to determine the best scattering parameter, the accuracy of the different scattering parameters was calculated using a root mean square error (RMSE) criterion:

$$RMSE = \frac{1}{n}\sum_{i=0}^{n}\sqrt{(E_i - S_i)^2} \tag{4.22}$$

where n was the total number of data points, E_i was the *i*th experimental data point while S_i was the *i*th simulated data point. The least error was observed at a scattering parameter of 0.84, where a very good agreement between experimental and simulated TTR values was observed (Figure 4.7b). This shows that the P25 TiO_2 catalyst scattered UV light in the forward direction, an observation which is consistent with the reports of several authors (Satuf et al., 2005; Valadés-Pelayo et al., 2014). However, the value of the scattering parameter obtained in this work was slightly higher than those reported by other authors. For example, Valadés-Pelayo et al. (2014) reported a scattering parameter value of 0.68 for P25 TiO_2. This can be attributed to the fact that Valadés-Pelayo et al. (2014) used the TiO_2 optical properties reported by Romero et al. (1997) while this work used the data set published by Romero et al. (2003). Satuf et al. (2005) showed that the choice of a scattering phase function has a marked effect on the TiO_2 optical properties and vice-versa. For the same model, the use of different optical properties would require different scattering parameters in order to achieve accurate simulation.

TTR values were also measured in the presence and absence of bubbles at different catalyst loadings (Figure 4.7b). The TTR values in the presence of bubbles were slightly lower than those in the absence of bubbles. For example, at a catalyst loading of 0.025 g/L, the TTR values in the presence and absence of bubbles were 3596 and 3617 μW/cm^2, respectively. This was expected since light attenuation due to bubble scatter has been found to be very low as a result of the insignificant contribution of bubble scattering to the extinction coefficient (Boyjoo et al., 2013). For example, at a catalyst loading of 0.025 g/L, the optical thickness in the absence and presence of bubbles was estimated to be 1.83 cm and 1.87 cm, respectively. Therefore, the presence of bubbles attenuates light only slightly which reflects on the insignificant differences in the TTR. A different situation has been observed in a gas-solid reactor by Iatridis et al. (1990) and Brucato et al. (1992) in which light transmission increased with an increase in the

gas flow rate. This was due to the fact that the gas bubbles provided pathways in the solid bed through which light was transmitted.

The Monte Carlo simulation was able to predict fairly accurately the TTR both in the presence and absence of bubbles using the same scattering parameter of 0.84 (Figure 4.7b). This suggests that during TTR measurements, the agglomeration state of the catalyst under fluidization was similar to that in the reactor without bubbles. Otherwise a change in the scattering parameter would have been necessary to achieve accurate simulation (Valadés-Pelayo et al., 2015). The catalyst did not have enough time to agglomerate since TTR measurements in the absence of bubbles was carried out immediately after shutting off the air supply for fluidization.

Figure 4.7b also compares the experimental TTR with the value predicted by the six-flux model (SFM) (Toepfer et al., 2006). The SFM was observed to over-estimate the TTR especially at low catalyst loadings. This could be attributed to the fact that the TTR uses the line source specular emission (LSSE) model for the lamp while the surface source diffuse emission (SSDE) model was used in this work. The predicted lamp output by the LSSE has been observed to be almost double the values predicted by the SSDE since diffuse emission follows a cosine law (Boyjoo et al., 2014b). A fluorescent lamp like the one used in this work emits diffuse light and its emission should be modelled using the SSDE instead of the LSSE (Boyjoo et al., 2014b). However, the SFM uses the LSSE since it is the only lamp model for which an analytical solution exists. As a result, for a reactor with a fluorescent lamp, it overpredicts the lamp output, resulting in high TTR values at low catalyst loadings when light transmittance is high. This comparison highlights the importance of rigorous models like the Monte Carlo model for light distribution simulation.

4.3.2 Local volumetric rate of energy absorption

The Monte Carlo model, validated using TTR data, was used to investigate the light distribution in the reactor. For photocatalysis, the most useful light distribution parameter is the local volumetric rate of energy absorption (LVREA) which refers to the amount of light absorbed by the catalyst at a specific location in the reactor (Valadés-Pelayo et al., 2014). The LVREA was calculated by summing the energy of all photons absorbed at a particular location in the reactor. LVREA profiles at different locations in the reactor at various catalyst loadings were investigated using the best scattering parameter of 0.84. At the different catalyst loadings, the LVREA profiles (Figure 4.8a – f) show uniform LVREA along the axial direction between axial location 0.18 to 0.82. Below axial location 0.18 and above axial location 0.82, the LVREA

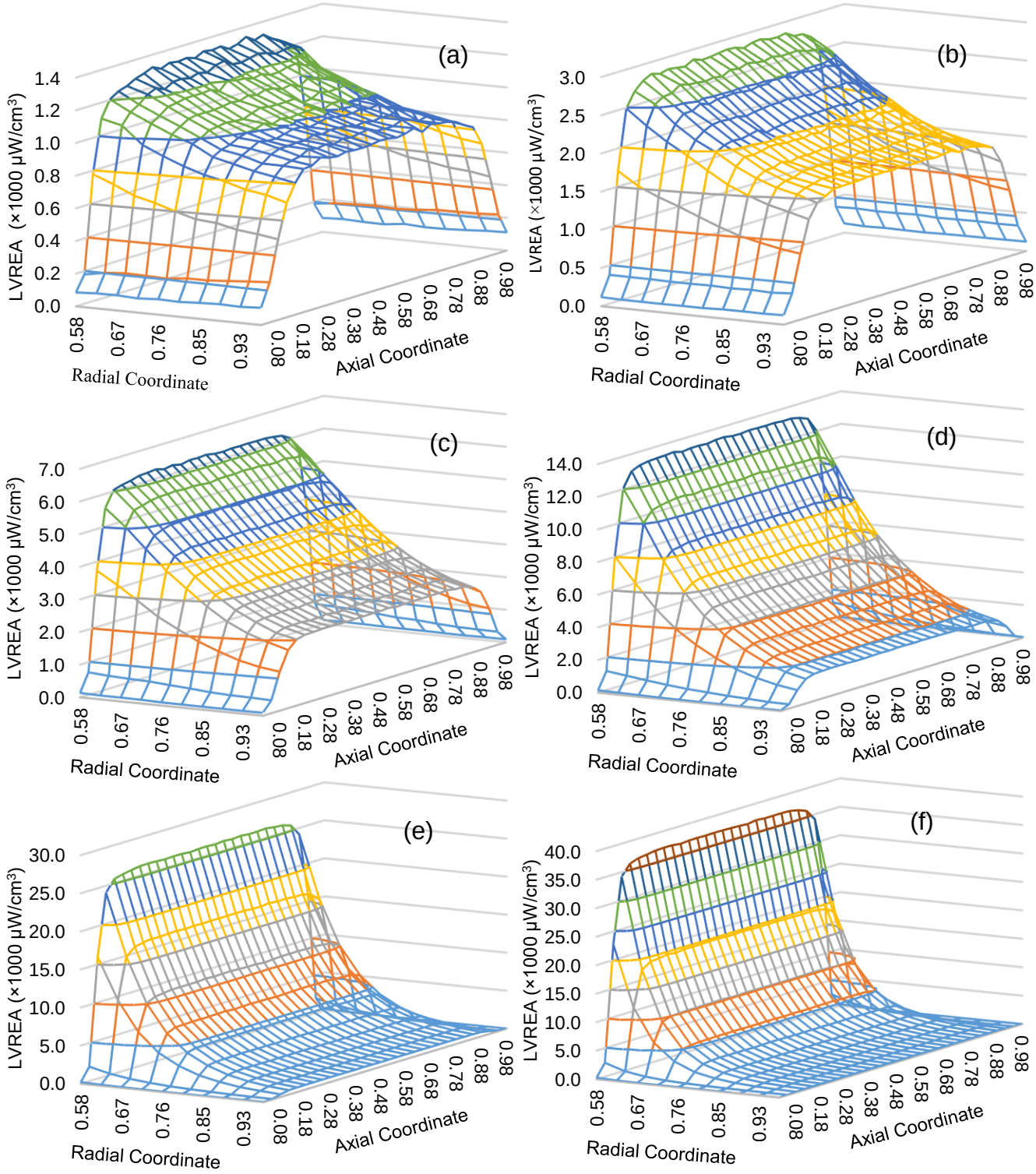

Figure 4.8: LVREA profiles at different catalyst loadings. (a) 0.025 g/L, (b) 0.05 g/L, (c) 0.1 g/L, (d) 0.2 g/L, (e) 0.4 g/L, (f) 0.6

values dropped sharply to 0 at the reactor end caps. The lamp emission model by Tsekov and Smirniotis (1997) specified uniform maximum emission between axial location 0.1 and 0.9 along the lamp length which reduced gradually to half the maximum output at the extremities.

Moreover, the axial gap between the reactor end caps and the lamp end caps were not illuminated. A combination of the non-uniform lamp emission profile and unilluminated parts of the reactor was responsible for the observed axial LVREA profiles.

The LVREA profiles (Figure 4.8a – f) also show an exponential decrease in the LVREA along the radial direction from the glass sleeve to the reactor wall. The radial LVREA profiles were further clarified using a 2D plot of the LVREA along the radial coordinate at the reactor axial centreline (axial location = 0.5). From the 2D plot (Figure 4.9), most of the light was absorbed near the glass sleeve (radial location = 0.58) with the amount of light absorbed decreasing towards the reactor wall. For example, at a catalyst loading of 0.2 g/L, an increase in the radial coordinate from 0.58 to 0.98 resulted in a decrease in LVREA from 13334 $\mu W/cm^3$ to 1718 $\mu W/cm^3$. This can be attributed to the absorption and scattering of light by the catalyst as it travels from the lamp towards the reactor wall. From Figure 4.8a – f and Figure 4.9, it can be observed that an increase in the catalyst loading resulted in an increase in the LVREA values closest to the glass sleeve. The increase in the LVREA with an increase in the catalyst loading was most pronounced near the glass sleeve since the light received at that location had not been attenuated by the catalyst. For example, an increase in the catalyst loading from 0.025 g/L to 0.6 g/L resulted in an increase in the LVREA from 1314 $\mu W/cm^3$ to 37037 $\mu W/cm^3$ at radial location 0.58. This was due to the fact that an increase in the catalyst loading resulted in an increase light absorption.

From the radial LVREA profiles, it can also be observed that an increase in the catalyst loading resulted in a steeper decay of the LVREA profile along the radial direction (Figure 4.8a – f; Figure 4.9). This was due to the increased light absorption near the glass sleeve at high catalyst loadings which drastically reduced the amount of light reaching the reactor wall (Valadés-Pelayo et al., 2014). A consequence of the radial profiles was the formation of dark zones near the reactor wall at high catalyst loadings. These dark zones are characterized by catalysts which are never activated and are thus wasted. During reactor design, it is desirable to illuminate the reactor as uniformly as possible without considerable loss in radiation. Therefore, a well illuminated reactor would have few dark zones and low TTR. The LVREA and TTR simulation has shown that an increase in the catalyst loading resulted in a decrease in the TTR and an increase in the dark zones. This suggests that an optimum catalyst loading exists which balances LVREA and TTR resulting in good reactor illumination. This optimum catalyst loading can be determined using the volumetric rate of energy absorption (VREA) which is calculated by averaging the LVREA values in the whole reactor.

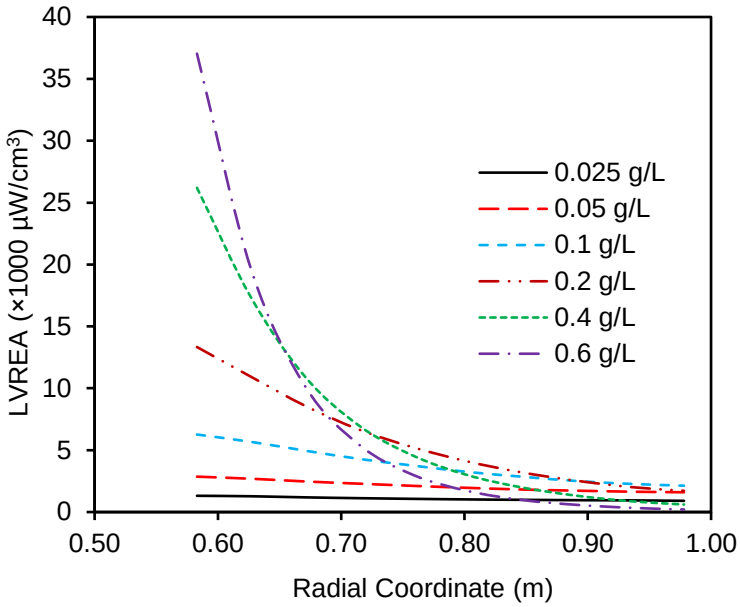

Figure 4.9: Radial LVREA profiles at different catalyst loadings

4.3.3 Volumetric rate of energy absorption

The VREA results (Figure 4.10) showed an exponential increase in the VREA with an increase in the catalyst loading. For example, an increase in the catalyst loading from 0.025 to 0.4 g/L resulted in an increase in the VREA from 827 to 4948 µW/cm^3. A further increase in the catalyst loading to 0.6 g/L resulted in a marginal increase in the VREA to 5139 µW/cm^3. From an analysis of the effect of catalyst loading on the VREA (Figure 4.10), the optimum catalyst loading can be determined as the amount of catalyst beyond which no significant increase in the VREA is observed. At the optimum catalyst loading, the maximum amount of light is utilized at the lowest catalyst loading. The optimum catalyst loading has been determined from the VREA plot as the catalyst loading at the onset of the asymptote with a VREA value equivalent to 95% of the maximum VREA (Valadés-Pelayo et al., 2014). For the reactor and light source used in this study, the optimum catalyst loading was found to be 0.4 g/L which was similar to the optimum catalyst loading of 0.4 g/L reported by Li Puma et al. (2004). The reactor by Li Puma et al. (2004) had a narrower annulus (6 mm) with a weaker lamp (8 W) compared to the thicker annulus (13 mm) and stronger lamp (18 W) used in this work. The lamp in the reactor by Li Puma et al. (2004), produced much fewer photons which travelled a much shorter distance before reaching the reactor wall. Therefore, the optimum catalyst loading required to minimize photon loss was found to be comparable to that in this work.

The effect of gas holdup on the VREA was also investigated by carrying out Monte Carlo simulations at gas holdups of 0, 0.0482, 0.0687 and 0.0895 at bubble diameters of 0, 6, 4 and 2 mm, respectively. These gas holdups were experimentally measured in the fluidized bed

reactor using different distributor plates to generate a variety of bubble sizes and gas holdups. The results (Figure 4.10), show an increase in the VREA with an increase in the gas holdup which was slightly more pronounced at lower catalyst loadings. For example, at a catalyst loading of 0.1 g/L, an increase in the gas holdup from 0 to 0.0895 resulted in an increase in the VREA from 2824 to 3064 μW/cm^3. However, at a catalyst loading of 0.4 g/L, an increase in the gas holdup from 0 to 0.0895 resulted in a marginal increase in the VREA from 4949 to 4957 μW/cm^3.

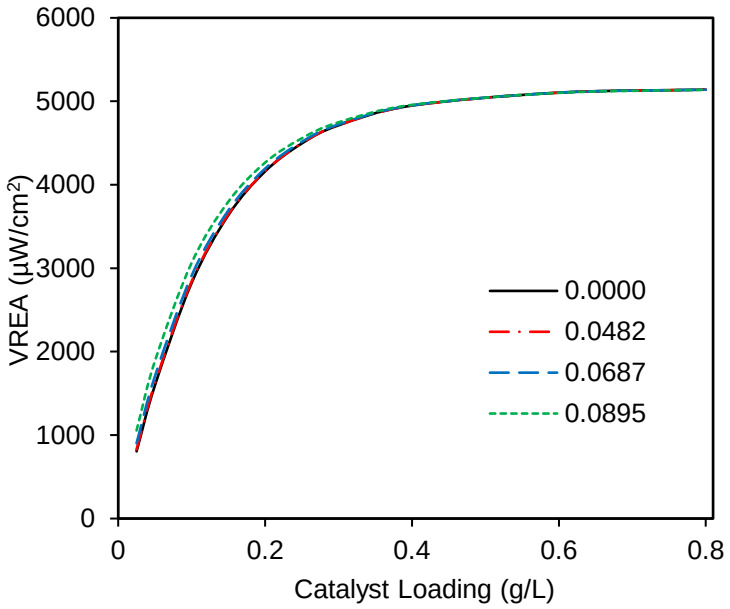

Figure 4.10: Effect of catalyst loading and gas holdup on VREA

At higher catalyst loadings, bubble scattering was negligible as compared to catalyst scattering. As a result, the overall influence of bubbles on the light distribution and VREA was also insignificant. However, at lower catalyst loadings, the contribution of bubbles to light scattering increased. This resulted in light distribution which prolonged the residence time of photons in the reactor thus increasing the probability of their absorption by catalysts. This effect increased with an increase in the gas holdup. These results show that at the optimum catalyst loading, bubbles have negligible effect on light absorption even at high gas holdups. However, at sub-optimal catalyst loadings, bubbles slightly improve light absorption. This suggests that in Monte Carlo simulation, photon-bubble interactions can be neglected without considerable loss in accuracy. Neglecting the photon-bubble interactions has the advantage of increasing the speed of the Monte Carlo simulation since simulating photon-bubble interactions is computationally costly. Furthermore, in the Chapter 3, gas holdup was observed to significantly vary along the radial coordinate of the reactor (Figure 3.18). However, for the sake of simplicity, in the Monte Carlo simulation, a random bubble distribution was specified.

Therefore, the fact that photon-bubble interactions can be neglected further shows that hydrodynamic considerations are unimportant in the fluidized bed reactor simulated in this work.

The results in this work contradict some aspects of the findings of Motegh et al. (2013). Although they also found that the effect of bubbles was only significant at low catalyst loadings, they concluded that an increase in the gas holdup resulted in a reduction in light absorption. This contradiction can be attributed to the fact that their model did not account for the interaction between the lamp and backscattered photons. In their work, backscattered photons were assumed to be lost resulting in a reduction in absorbed photons. In this work, the interaction between backscattered photons and the lamp was simulated by considering photons which hit the lamp as reflected back into the slurry. Therefore, bubbles did not contribute to backward photon loss. Instead, the bubbles distributed the photons in the slurry which increased their probability of being absorbed by the catalysts.

4.4 Conclusion

In this chapter, a Monte Carlo model was developed for simulating the light distribution in a fluidized bed photoreactor under UV lamp illumination. Total transmitted radiation (TTR) measurements at the wall of the reactor was used to validate the Monte Carlo model. The best agreement between experimental and simulated TTR data was obtained at a scattering parameter of 0.84 showing that the catalyst exhibited forward scattering behaviour. The Monte Carlo model was found to be more accurate than the six-flux model due to the use of the diffuse lamp emission model. Local volumetric rate of energy absorption profiles revealed fairly uniform axial light distribution profiles while the radial light distribution was highly non-uniform. The optimum catalyst loading was found to be 0.4 g/L using the light distribution analysis. The presence of bubbles slightly decreased the TTR but increased light absorption especially at low catalyst loadings. At the optimum catalyst loading, the effect of bubbles on light absorption was found to be negligible. Therefore, accurate Monte Carlo simulation could be achieved without accounting for bubble-photon interactions. The negligible effect of bubbles on light distribution further demonstrates that hydrodynamic effects can be neglected in the simulation of the photocatalytic reactor.

In this chapter, the light distribution in a UV lamp illuminated reactor was investigated. A hybrid light reactor is illuminated externally by sunlight and internally by UV light. In order to analyse the light distribution in such a reactor, an analysis of both UV and solar effects need to

be carried out. In the next section, the Monte Carlo simulation of the light distribution in a solar illuminated reactor is discussed.

References

Boyjoo, Y., Ang, M. and Pareek, V., 2013. Light intensity distribution in multi-lamp photocatalytic reactors, *Chemical Engineering Science*, *93*, 11-21.

Boyjoo, Y., Ang, M. and Pareek, V., 2014a. CFD simulation of a pilot scale slurry photocatalytic reactor and design of multiple-lamp reactors, *Chemical Engineering Science*, *111*, 266-277.

Boyjoo, Y., Ang, M. and Pareek, V., 2014b. Lamp emission and quartz sleeve modelling in slurry photocatalytic reactors. *Chemical Engineering Science*, *111*, 34-40.

Brucato, A., Iatridis, D., Yue, P.L. and Rizzuti, L., 1992. Modelling of light transmittance and reflectance in flat fluidized photoreactors. *Canadian Journal of Chemical Engineering*, *70*, 1063-1070.

Cabrera, M.I., Alfano, O.M. and Cassano, A.E., 1996. Absorption and scattering coefficients of titanium dioxide particulate suspensions in water. *Journal of Physical Chemistry*, *100*, 20043-20050.

Camera-Roda, G., Augugliaro, V., Cardillo, A. G., Loddo, V., Palmisano, L., Parrino, F. and Santarelli, F., 2016. A reaction engineering approach to kinetic analysis of photocatalytic reactions in slurry systems, *Catalysis Today*, *259*, Part 1, 87-96.

Changrani, R. and Raupp, G. B., 1999. Monte Carlo simulation of the radiation field in a reticulated foam photocatalytic reactor, *AIChE Journal*, *45*(5), 1085-1094.

De Greve, B., 2006. *Reflections and refractions in ray tracing*. https://graphics.stanford.edu /courses/cs148-10-summer/docs/2006--degreve--reflection_refraction.pdf

Iatridis, D., Yue, P.L., Rizzuti, L. and Brucato, A., 1990. The absorption of light energy in flat fluidized photoreactors. *Chemical Engineering Journal*, *45*, 1-8.

Imoberdorf, G. E., Taghipour, F., Keshmiri, M. and Mohseni, M., 2008. Predictive radiation field modeling for fluidized bed photocatalytic reactors, *Chemical Engineering Science*, *63*(16), 4228-4238.

Li Puma, G., Khor, J.N. and Brucato, A., 2004. Modeling of an annular photocatalytic reactor for water purification: oxidation of pesticides. *Environmental Science & Technology*, *38*, 3737-3745.

Li Puma, G., Puddu, V., Tsang, H. K., Gora, A. and Toepfer, B., 2010. Photocatalytic oxidation of multicomponent mixtures of estrogens (estrone (E1), 17β-estradiol (E2), 17α-

ethynylestradiol (EE2) and estriol (E3)) under UVA and UVC radiation: Photon absorption, quantum yields and rate constants independent of photon absorption, *Applied Catalysis B: Environmental*, *99*(3–4), 388-397.

Lighting.philips.com., 2017. TL-D 18W BLB 1SL/25 TL-D Blacklight Blue - Philips Lighting. [online] Available at: http://www.lighting.philips.com/main/prof/conventional-lamps/fluorescent-lamps-and-starters/tl-d/tl-d-blacklight-blue/928048010805_EU/product [Accessed 22 May 2017].

Moreira, J., Serrano, B., Ortiz, A. and de Lasa, H., 2010. Evaluation of photon absorption in an aqueous TiO_2 slurry reactor using Monte Carlo simulations and macroscopic balance, *Industrial & Engineering Chemistry Research*, *49*(21), 10524-10534.

Motegh, M., Ruud van Ommen, J., Appel, P. W., Mudde, R. F. and Kreutzer, M. T., 2013. Bubbles scatter light, yet that does not hurt the performance of bubbly slurry photocatalytic reactors, *Chemical Engineering Science*, *100*, 506-514.

Ochieng, A., Odiyo, J. O. and Mutsago, M., 2003. Biological treatment of mixed industrial wastewaters in a fluidised bed reactor, *Journal of Hazardous Materials*, *96*(1), 79-90.

Ochieng, A., Ogada, T., Sisenda, W. and Wambua, P., 2002. Brewery wastewater treatment in a fluidised bed bioreactor, *Journal of Hazardous Materials*, *90*(3), 311-321.

Pareek, V., Chong, S., Tadé, M. and Adesina, A. A., 2008. Light intensity distribution in heterogenous photocatalytic reactors, *Asia-Pacific Journal of Chemical Engineering*, *3*(2), 171-201.

Romero, R. L., Alfano, O. M. and Cassano, A. E., 1997. Cylindrical photocatalytic reactors. Radiation absorption and scattering effects produced by suspended fine particles in an annular space, *Industrial & Engineering Chemistry Research*, *36*(8), 3094-3109.

Romero, R. L., Alfano, O. M. and Cassano, A. E., 2003. Radiation field in an annular, slurry photocatalytic reactor. 2. Model and experiments, *Industrial & Engineering Chemistry Research*, *42*(12), 2479-2488.

Satuf, M. L., Brandi, R. J., Cassano, A. E. and Alfano, O. M., 2005. Experimental method to evaluate the optical properties of aqueous titanium dioxide suspensions, *Industrial & Engineering Chemistry Research*, *44*(17), 6643-6649.

Toepfer, B., Gora, A. and Puma, G.L., 2006. Photocatalytic oxidation of multicomponent solutions of herbicides: Reaction kinetics analysis with explicit photon absorption effects. *Applied Catalysis B: Environmental*, *68*, 171-180.

Tsekov, R. and Smirniotis, P. G., 1997. Radiation field in continuous annular photocatalytic reactors: role of the lamp finite size, *Chemical Engineering Science*, *52*(10), 1667-1671.

Valadés-Pelayo, P. J., Guayaquil Sosa, F., Serrano, B. and de Lasa, H., 2015. Eight-lamp externally irradiated bench-scale photocatalytic reactor: Scale-up and performance prediction, *Chemical Engineering Journal*, *282*, 142-151.

Valadés-Pelayo, P. J., Moreira, J., Serrano, B. and de Lasa, H., 2014. Boundary conditions and phase functions in a Photo-CREC Water-II reactor radiation field, *Chemical Engineering Science*, *107*, 123-136.

Zekri, M. e. M. and Colbeau-Justin, C., 2013. A mathematical model to describe the photocatalytic reality: What is the probability that a photon does its job? *Chemical Engineering Journal*, *225*, 547-557.

Chapter 5

5 Simulation of the light distribution in a solar illuminated reactor

5.1 Introduction

Conventional photocatalysis has been carried out with mercury UV lamps as the light source. However, such lamps are costly to run as they need electricity and this has motivated the use of sunlight for photocatalysis (Malato et al., 2009). In order to design, optimize and scale up a solar illuminated reactor, the light distribution in the reactor needs to be determined. Several studies have investigated the light distribution in two-phase solar illuminated tubular and compound parabolic concentrator (CPC) reactors (Colina-Márquez et al., 2009; Colina-Márquez et al., 2010; Mueses et al., 2013; Acosta-Herazo et al., 2016; Hou et al., 2017; Ochoa-Gutiérrez et al., 2018; Casado et al., 2019). Most of these studies had several shortcomings. None of them carried out an explicit validation of their light distribution model using light transmission measurement. Most of the studies did not consider light refraction at the wall of the reactor. Clearly, more needs to be done to accurately simulate the light distribution in solar illuminated reactors.

In the previous chapter, the light distribution in a UV lamp illuminated fluidized bed photoreactor was modelled. In this chapter, the Monte Carlo model which was developed for the annular UV reactor in chapter 4 was adapted for simulation of the light distribution in a solar illuminated three-phase reactor. The light distribution in this reactor has not been reported in literature. The light distribution model was validated by comparing the intensity of the light refracted on the unilluminated wall with that predicted by the model. In addition to modelling the interaction of photons with bubbles and catalyst particles, the rigorous Monte Carlo model accounted for the solar diffuse fraction as well as wall refraction. The objective of this chapter was to determine the effect of catalyst loading, air bubbles and solar diffuse fraction on the light distribution in a solar illuminated reactor.

5.2 Methodology

5.2.1 Experimental set up

The solar illuminated photocatalytic reactor (Figure 5.1) was made of a clear borosilicate glass with an outer diameter of 65 mm and a thickness of 2.2 mm. Air was supplied through a porous distributor with a pore size of 10 – 16 μm positioned at the bottom of the reactor. The reactor height was 600 mm with a liquid capacity of 1800 mL. The reactor was set up vertically on a

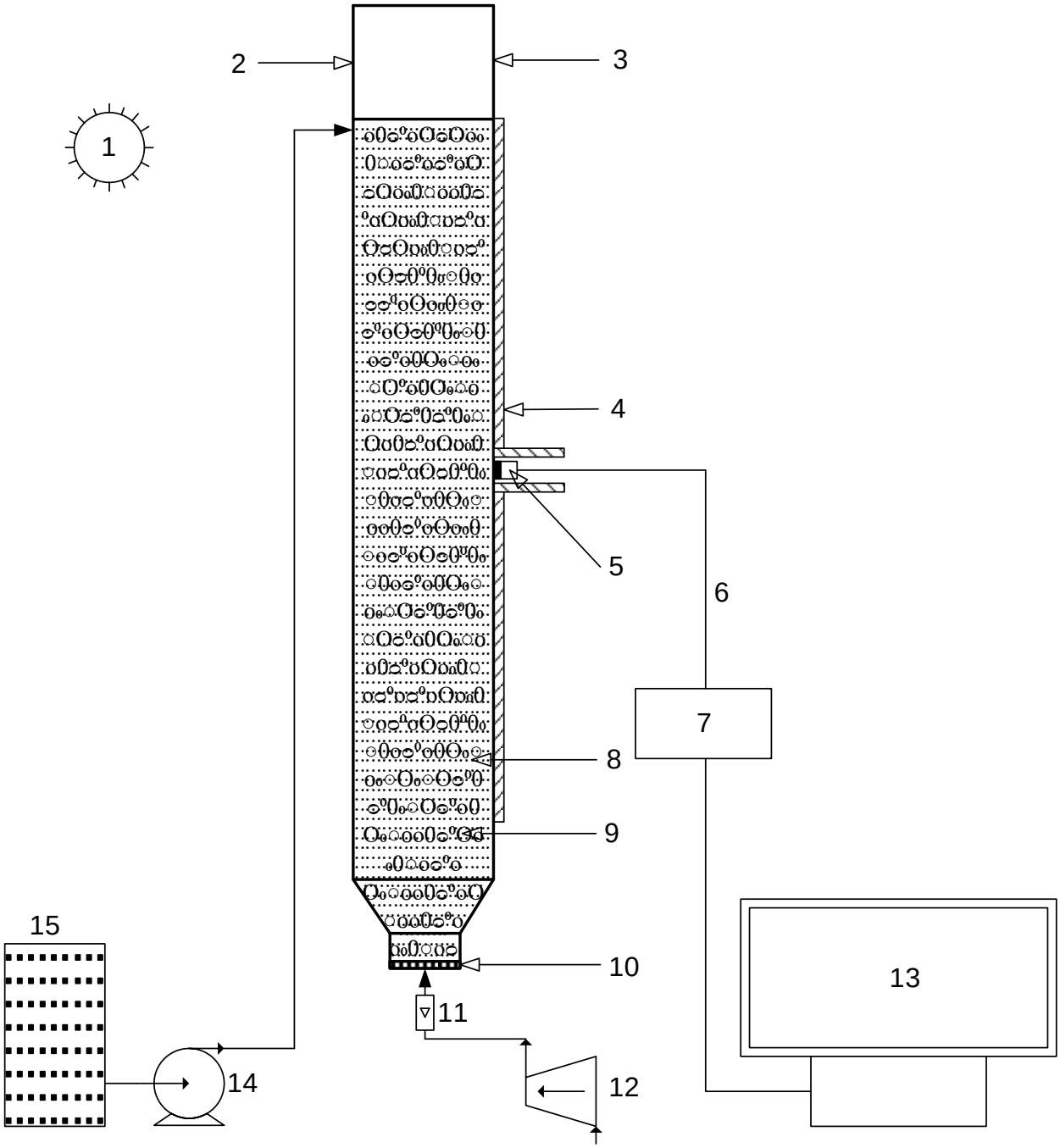

Figure 5.1: Light distribution measurement setup. (1) sun, (2) illuminated reactor wall, (3) unilluminated reactor wall, (4) radiation sensor support, (5) radiation sensor, (6) fibre optic cable, (7) spectroradiometer, (8) catalyst slurry, (9) air bubble, (10) porous air distributor, (11) rotameter, (12) air compressor, (13) computer, (14) peristaltic pump, (15) feed mixing tank

roof top where it was illuminated on one side by sunlight. It was observed that sunlight was refracted through the reactor in such a way that a narrow strip of light was formed axially along the unilluminated wall of the reactor (Figure 5.6a). This total refracted radiation (TRR) was measured by a radiation sensor (Stellarnet CR2 cosine receptor) positioned on the

unilluminated reactor wall. Light from the sensor was channelled to a calibrated Stellarnet Black Comet SR spectroradiometer using a fibre optic cable.

5.2.2 Monte Carlo model

The radiation energy balance in a scattering and absorbing medium can be described by the radiation transport equation (RTE) (Romero et al., 2003) as:

$$\frac{dI_\lambda(s,\Omega)}{ds} = -\kappa_\lambda I_\lambda(s,\Omega) - \sigma_\lambda I_\lambda(s,\Omega) + \frac{1}{4\pi}\sigma_\lambda \int_0^{4\pi} p(\Omega' \rightarrow \Omega) I_\lambda(s,\Omega') d\Omega' \quad (5.1)$$

where I_λ refers to the specific intensity of a ray of light of wavelength λ travelling a distance s in direction Ω. The symbols κ_λ and σ_λ are the medium absorption and scattering coefficients, respectively. $p(\Omega' \rightarrow \Omega)$ is the scattering phase function. In this work, the Monte Carlo method was used to solve equation (5.1) as described next.

Bubble distribution

The reactor was operated in a homogenous flow regime, in which the distribution of bubbles was fairly uniform. Bubbles were observed to be nearly spherical with an average diameter of 4 mm. This flow regime could best be modelled by assuming a random distribution of spherical bubbles. The number of bubbles (n_b) was calculated as a function of the gas holdup as:

$$n_b = \frac{6\varepsilon_g V}{\pi d_b^3} \quad (5.2)$$

where d_b is the bubble diameter, V is the reactor volume and ε_g is the global gas holdup. The global gas holdup was found to be 0.018 using the quick-stop method in which the gas holdup was calculated from the difference between the aerated liquid height and the gas-free height (Ochieng et al., 2002; 2003).

The bubble radial location (r_b) was given as:

$$r_b = 0.5d_b + (r_w - d_b)R_1 \quad (5.3)$$

from where the random bubble centroid (x_b, y_b, z_b) was specified by equations (5.4) – (5.6) as:

$$x_b = r_b \cos(2\pi R_2) \quad (5.4)$$

$$y_b = r_b \sin(2\pi R_2) \quad (5.5)$$

$$z_b = d_b + (h_w - d_b)R_3 \quad (5.6)$$

where r_w is the reactor wall radius, h_w is the reactor height and R_1, R_2, R_3 are random numbers uniformly distributed between 0 and 1. Figure 5.2a shows the bubble distribution coordinate system.

After specifying the bubble centroid, its distance to other bubbles and the reactor boundaries was evaluated as described elsewhere (Imoberdorf et al., 2008). If a boundary or bubble overlap was found, the specified bubble centroid was discarded and another one generated until the required number of bubbles was obtained.

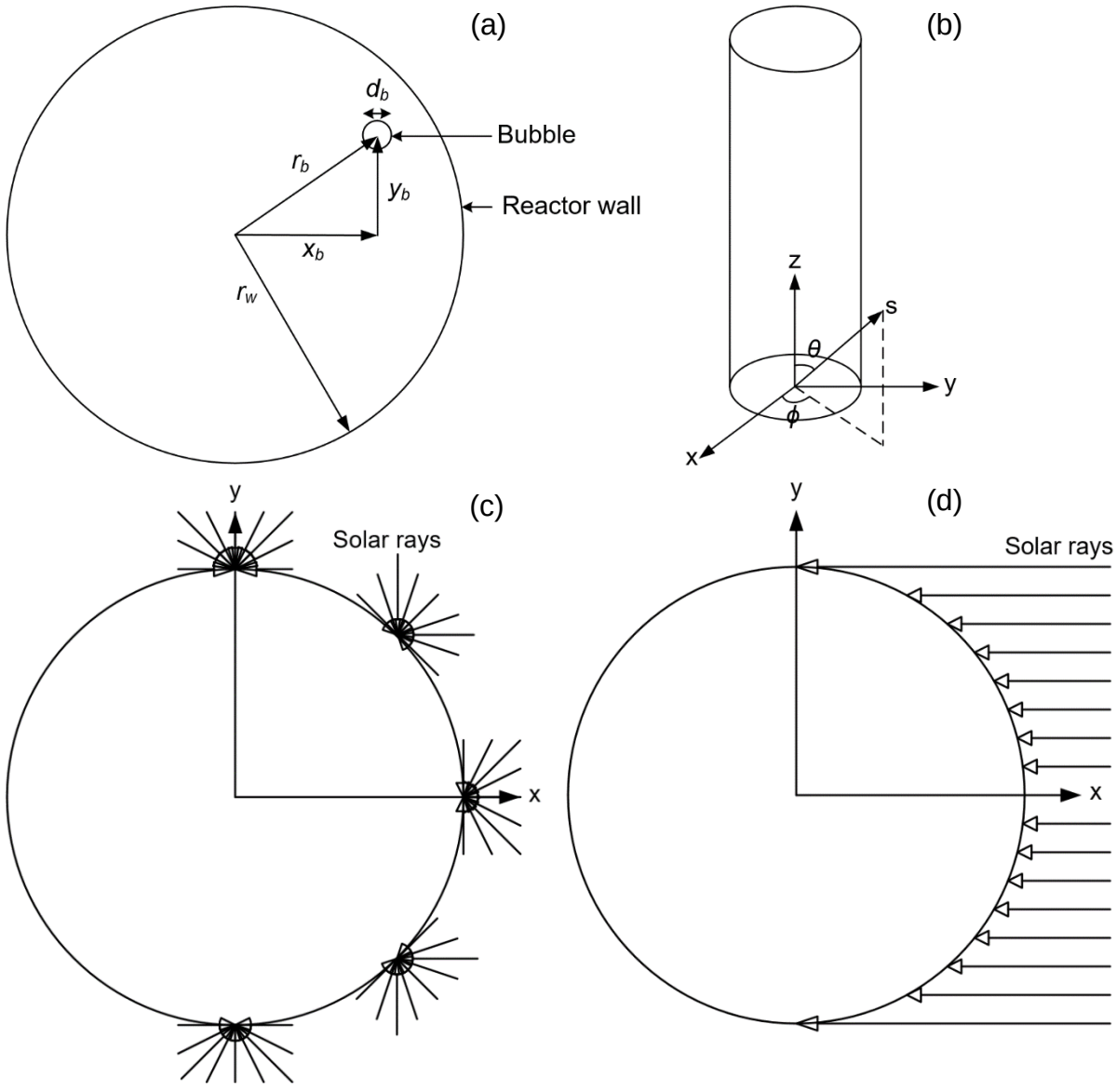

Figure 5.2: Coordinate systems for (a) Bubbles (b) Reactor (c) Diffuse light illumination (d) Direct light illumination

Incident solar irradiance and diffuse fraction

The incident solar irradiance, normal to the reactor ($G_{i,N}$), was calculated using an equation adapted from the Hay, Davies, Klucher and Reindl (HDKR) tilt irradiance model (Duffie and Beckman, 2013):

$$G_{i,N} = \frac{(G_{be} + G_d\, G_{be}/G_0)}{\cos\theta_s} + G_d\left(1 - \frac{G_{be}}{G_0}\right)\left(\frac{1+\cos\beta}{2}\right)\left[1 + \sqrt{\frac{G_{be}}{G}}\sin^3\left(\frac{\beta}{2}\right)\right] + G\rho_G\left(\frac{1-\cos\beta}{2}\right) \quad (5.7)$$

where θ_s is the solar zenith angle, β is the reactor tilt angle and G is the global horizontal UV irradiance. The first, second and third terms on the right-hand side of equation (5.7) refer to the beam, sky diffuse and ground reflected diffuse irradiation, respectively.

The extra-terrestrial solar irradiance on a horizontal plane (G_0) was calculated as:

$$G_0 = G_{sc,UV}\left(1 + 0.033\cos\frac{360\, n_D}{365}\right)\cos\theta_s \quad (5.8)$$

where n_D is the day of the year and $G_{sc,UV}$ is the solar UV constant which was evaluated as 2.6164×10^4 moles m^{-2} s^{-1} from the ASTM standard extra-terrestrial spectrum reference E-490-00 between 0.1195 and 0.3875 μm (Solar Spectra: Standard Air Mass Zero, 1999).

The horizontal diffuse irradiance (G_d) was calculated as:

$$G_d = Gk_d \quad (5.9)$$

where the horizontal diffuse fraction (k_d) was calculated using the correlation proposed by Boland et al. (2008):

$$k_d = 1/(1 + \exp(-5.00 + 8.60k_t)) \quad (5.10)$$

where the clearness index (k_t) is given as:

$$k_t = \frac{G}{G_0} \quad (5.11)$$

The horizontal beam irradiance (G_{be}) was then determined as:

$$G_{be} = G - G_d \quad (5.12)$$

The value of the ground reflectance (ρ_G) used in equation (5.7) was estimated using the HDKR model (Duffie and Beckman, 2013):

$$G_T = \left(G_{be} + G_d \frac{G_{be}}{G_0}\right)\frac{\cos\theta}{\cos\theta_s} + G_d\left(1 - \frac{G_{be}}{G_0}\right)\left(\frac{1+\cos\beta}{2}\right)\left[1 + \sqrt{\frac{G_{be}}{G}}\sin^3\left(\frac{\beta}{2}\right)\right] + G\rho_G\left(\frac{1-\cos\beta}{2}\right) \quad (5.13)$$

where θ is the incident angle of sunlight with respect to the orientation of the reactor. In equation (5.13), the values of the global tilt UV irradiance (G_T) and the global horizontal UV irradiance (G) were experimentally measured using the spectroradiometer in the 300 – 387 nm wavelength band.

Direct rays from the sun are scattered by clouds, aerosols and dust in the atmosphere resulting in the formation of diffuse rays. The proportion of diffuse solar rays in sunlight is referred to as the diffuse fraction. Usually, the diffuse fraction is evaluated on the horizontal surface since the incident solar irradiance is measured on the horizontal plane. However, in this simulation, the incident solar irradiance was specified at an angle normal to the reactor. Instead of using the horizontal diffuse fraction in the calculations, a normal diffuse fraction, based the incident normal solar irradiance ($G_{i,N}$) was considered to be more appropriate. This normal diffuse fraction ($k_{d,N}$) was derived from equation (5.7) as:

$$k_{d,N} = \left\{G_d\left(1 - \frac{G_{be}}{G_0}\right)\left(\frac{1+\cos\beta}{2}\right)\left[1 + \sqrt{\frac{G_{be}}{G}}\sin^3\left(\frac{\beta}{2}\right)\right] + G\rho_G\left(\frac{1-\cos\beta}{2}\right)\right\} \Big/ G_{i,N} \quad (5.14)$$

Photon location and wavelength

In a tubular solar photocatalytic reactor, only one side of the reactor is illuminated (Figure 5.2c – d). The random angular photon location on the reactor wall (φ_w) was calculated as:

$$\varphi_w = \pi R_4 - 0.5\pi \quad (5.15)$$

from which the radial photon location (x_w, y_w) was specified as:

$$x_w = r_w R_5 \cos(\varphi_w) \quad (5.16)$$

$$y_w = r_w R_5 \sin(\varphi_w) \quad (5.17)$$

The axial photon location (z_w) was determined as:

$$z_w = h_w R_6 \tag{5.18}$$

where R_4, R_5, R_6 are random numbers uniformly distributed between 0 and 1.

The photon wavelength was specified randomly between 300 and 387 nm from a cumulative probability density function derived from the solar spectrum. This wavelength range was specified due to the fact that there was little solar intensity below 300 nm and the catalyst does not absorb light above 387 nm.

Initial photon direction

After specifying the wavelength and location of the photon on the reactor surface, its direction of propagation was then specified. The direction of solar rays depends on the position of the sun in the sky which is a function of the time of day and year. Solar position is described using two angles: solar azimuth and solar zenith. Also, the direction of propagation of direct and diffuse light is markedly different. Diffuse photons arrive on the reactor from several directions (Figure 5.2c) while direct photons arrive at the reactor from a single direction (Figure 5.2d). Therefore, the identity of the photon, whether it is diffuse or direct, was first determined using another random number as:

$$k_{d,N} > R_7 \tag{5.19}$$

If equation (5.19) was evaluated as true, the photon was considered diffuse and the photon flight azimuth angle (ϕ) was determined randomly as:

$$\phi = \phi_w + 0.5\pi + \pi R_8 \tag{5.20}$$

Also, the random photon flight zenith angle (θ) was given as:

$$\theta = \pi R_9 \tag{5.21}$$

If equation (5.19) was evaluated as false, the photon was considered to be a direct photon. Its photon flight azimuth angle (ϕ) was specified as a function of the solar azimuth angle (ϕ_s) as:

$$\phi = \phi_s + 0.0436(2R_{10} - 1) + \pi \tag{5.22}$$

Since the reactor was oriented vertically, solar rays did not arrive at the reactor perpendicularly. Instead, sunlight arrived at the reactor at the current zenith angle of the sun. The photon flight zenith angle (θ) was specified as a function of the solar zenith angle (θ_s) as:

$$\theta = \theta_s + 0.0436(2R_{11} - 1) + 0.5\pi \tag{5.23}$$

where R_7, R_8, R_9, R_{10} and R_{11} are random numbers uniformly distributed between 0 and 1. The term $0.0436(2R-1)$ in equation (5.22) and (5.23) was added to account for the fact that direct photons are circumsolar in nature. Figure 5.2b shows the reactor coordinate system with the origin at the base of the reactor, the azimuth angle (ϕ) measured anticlockwise from the *x*-axis and the zenith angle (θ) measured clockwise from the *z*-axis.

Photon path

After specifying the initial photon flight direction, the photon flight across the reactor wall was evaluated. The reactor wall had a transparency of 92% to solar UV light which corresponds to a photon absorption probability of 8%. This value was obtained from the light transmission data provided by Schott-Duran, the manufacturers of the borosilicate glass used to fabricate the reactor (Schott, n.d.). The probability of a photon being absorbed by the reactor wall was evaluated by the inequality $0.08 > R_{12}$, where R_{12} is a random number uniformly distributed between 0 and 1. If the photon was not absorbed, it was refracted across the reactor wall with the change in direction being determined by Snell's law (De Greve, 2006). Due to the curved nature of the reactor surface and the refractive indices of air, glass and water, all photons were refracted as the incidence angles were below the critical angles. This is true even for those rays which are tangent to the reactor wall.

Once inside the reactor, the photon could travel for a certain distance before striking a bubble or being absorbed/scattered by the catalyst. Since bubbles were relatively few, photon-bubble interactions were modelled directly by considering the reflection on or transmission through the bubble. Catalyst particles, on the other hand, are numerous, and this precludes a direct modelling of photon-catalyst interactions. Instead, these interactions were modelled by considering the catalyst optical characteristics (absorption coefficients, scattering coefficients and scattering phase function) to establish the fate of the photon once it strikes a catalyst. The spectral absorption and scattering coefficients for Aeroxide P25 TiO_2 were obtained from Romero et al. (2003). The Henyey-Greenstein phase function, popular for its versatility (Valades-Pelayo et al., 2014b), was used in this work. This phase function employs an asymmetry factor whose value lies between -1 and 1 which enables the function to represent a wide variety of scattering scenarios from complete backward to complete forward scattering.

In the reactor, the moving photon could either strike a bubble or a catalyst depending on their distance to the photon. Based on the bubble distribution, the distance to the nearest bubble, l_b,

was evaluated by considering the distance between the photon and nearby bubble surfaces. The distance between the photon and a catalyst particle, l_c, was evaluated as (Pareek et al., 2008):

$$l_c = -\frac{\ln(R_{13})}{\kappa_\lambda + \sigma_\lambda} \tag{5.24}$$

where R_{13} is a random number uniformly distributed between 0 and 1, κ_λ is the spectral absorption coefficient and σ_λ is the spectral scattering coefficient of the catalyst.

The photon travelled a distance l which is the shorter distance between l_b or l_c. The new location of the photon, in cartesian coordinates, was determined as:

$$x_n = x_o + (\sin\theta \cos\phi)\, l \tag{5.25}$$

$$y_n = y_o + (\sin\theta \cos\phi)\, l \tag{5.26}$$

$$z_n = z_o + (\cos\theta)\, l \tag{5.27}$$

where x_n, y_n, z_n are the new coordinates and x_o, y_o, z_o are the previous coordinates.

Absorption and scattering events

If $l = l_c$, the photon struck a catalyst and would either be absorbed or scattered. The probability of being absorbed was evaluated by the inequality (Moreira et al., 2010):

$$\frac{\kappa_\lambda}{\kappa_\lambda + \sigma_\lambda} > R_{14} \tag{5.28}$$

where R_{14} is a random number uniformly distributed between 0 and 1. If the photon was absorbed by the catalyst, its energy was stored in a grid of 11,520 cells consisting of 16 radial, 36 angular and 20 axial regions. The local volumetric rate of energy absorption (LVREA) was determined as the sum of the energy of all photons absorbed at a certain grid cell per unit volume of the cell (Valades-Pelayo et al., 2014b). The volumetric rate of energy absorption (VREA) was then calculated as the sum of the LVREA in all the grid cells as:

$$VREA = \frac{1}{V} \int LVREA\, dV \tag{5.29}$$

where V is the reactor volume.

If the photon was not absorbed, it was scattered, resulting in a change in the azimuth and zenith angle of photon flight. The scattering azimuth direction (ϕ_{sc}) was evaluated as:

$$\phi_{sc} = 2\pi R_{15} \tag{5.30}$$

The scattering zenith direction was evaluated from the Henyey-Greenstein (HG) phase function as (Moreira et al., 2010):

$$\cos(\theta_{sc}) = \begin{cases} \frac{1}{2g}\left[1 + g^2 - \left(\frac{1 - g^2}{1 - g + 2gR_{16}}\right)^2\right], & if\ g \neq 0 \\ 2R_{16} - 1, & if\ g = 0 \end{cases} \quad (5.31)$$

where R_{15}, R_{16} are random numbers and g is the HG phase function asymmetry factor. The zenith scattering angle (θ_{sc}) was then calculated as:

$$\theta_{sc} = \text{acos}(\cos(\theta_{sc})) \quad (5.32)$$

If $l = l_b$, the photon struck a bubble and would either be reflected on the surface of the bubble or transmitted by refraction through the bubble. The reflection or refraction event was a function of the photon incident angle as determined by Snell's law (De Greve, 2006). Both reflection and refraction resulted in a change in the direction of photon flight and thus could be considered as scattering events.

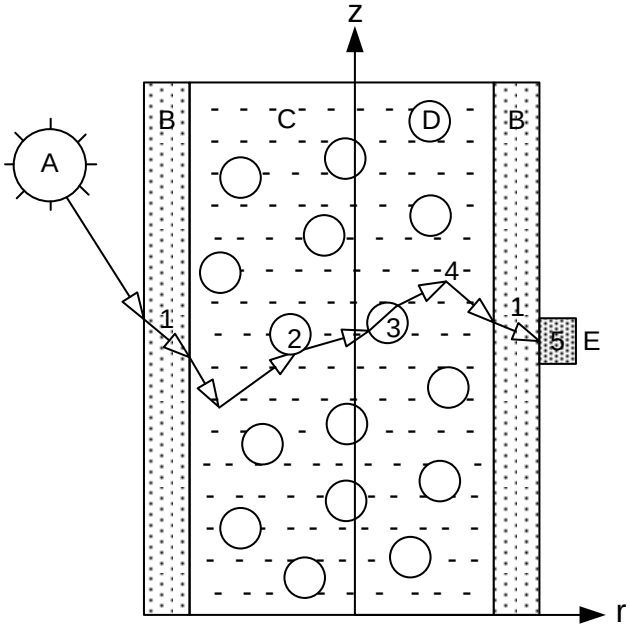

Figure 5.3: Flight of a photon in the reactor (1) reactor wall refraction, (2) bubble scattering, (3) bubble transmission, (4) catalyst scattering, (5) sensor absorption. (A) solar position, (B) reactor wall, (C) catalyst slurry, (D) bubble, (E) radiometer sensor

The photon continued its flight in the reactor, being scattered by bubbles and catalyst until it was absorbed by the catalyst. From inside the reactor, a photon could hit the reactor wall, at which point it would be absorbed or refracted through the wall. Beyond the wall, the photon could escape to the air or it could hit the radiation sensor, in which case the energy of the

photon would be added to the TRR variable. A photon was considered lost if it crossed the reactor boundaries or was absorbed by the catalyst, sensor or wall. Consequently, another photon was emitted and tracked through the reactor. This process continued until 10^7 photon packets were emitted in order to establish the average TRR and LVREA profiles in the reactor. In chapter 4, 10^7 photon packets was found to be the optimal number for Monte Carlo simulations. In order to account for the continuous movement of bubbles, the bubble distribution was updated after every 10^5 photons had been tracked. Figure 5.3 illustrates the flight of a photon from the reactor wall to the radiation sensor. The algorithm for Monte Carlo simulation was written and solved in MATLAB R2015a (Appendix C). The random numbers were generated using MATLAB's default random number generator: Mersenne twister. This generator has a period of 2^{19937}-1 which far exceeds any possible number of events in this Monte Carlo method thus ensuring a truly random simulation.

5.2.3 Validation experiments

The Monte Carlo model was validated using the total refracted radiation (TRR) measurements at the unilluminated wall of the reactor. Validation experiments were carried out in the month of April between 12 and 1 pm in Vanderbijlpark, South Africa (GPS coordinates: 26.7034° S, 27.8077° E). At the time of the experiment, the sky was clear with an average global horizontal UV irradiance of 31.4 W/m^2. A catalyst slurry with a loading of 0.005 g/L Aeroxide P25 TiO_2 was prepared in the feed tank using deionized water from a Millipore DirectQ unit. A volume of 1800 mL of the catalyst slurry was then pumped into the reactor. Catalyst mixing was achieved by bubbling compressed air into the reactor. After 5 min of catalyst mixing, the TRR, global horizontal UV irradiance and global tilt UV irradiance were measured by positioning the radiation sensor on the unilluminated reactor wall, horizontal plane and vertical plane, respectively. The TRR readings without aeration were taken immediately after shutting the air flow before any appreciable catalyst sedimentation had occurred. To measure the TRR at other catalyst loadings, the catalyst in the reactor was increased gradually and TRR readings taken at catalyst loadings of 0.01, 0.025, 0.05, 0.1 and 0.2 g/L with and without aeration. In order to account for any variation in the TRR due to bubble movement, 100 samples of the light intensity were taken consecutively and then averaged to obtain the TRR.

5.3 Results and discussion

5.3.1 Model validation

Total refracted radiation (TRR) measurement is a novel technique of measuring the forward transmitted radiation. TRR measurements were made at several catalyst loadings (0.005 – 0.2

g/L) and aeration states. The experimental results (Figure 5.4a) show that increasing the catalyst loading from 0.005 to 0.2 g/L led to a decrease in the TRR from 3238 to 29 µW/cm^2 in the reactor without aeration. This was due to the obstruction of light as a result of catalyst scattering and absorption which reduced the light intensity on the sensor. The extent of light obstruction increased with an increase in catalyst loading as the number of catalyst particles in solution increased. The presence of bubbles reduced the TRR, especially at low catalyst loadings (<0.025 g/L). For instance, at a low catalyst loading of 0.005 g/L, aeration decreased the TRR from 3238 to 2423 µW/cm^2. However, at a higher catalyst loading of 0.2 g/L, aeration resulted in a slight decrease in the TRR from 29 to 28 µW/cm^2. This trend was due to bubble scattering

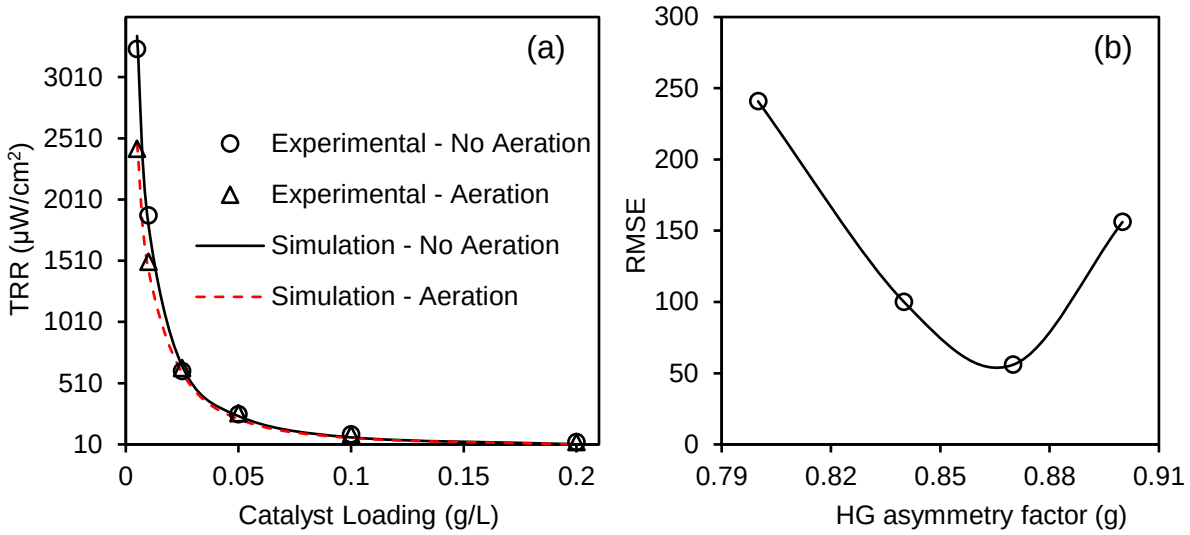

Figure 5.4: (a) Comparison of Monte Carlo simulation with experimental TRR values at different catalyst loading and aeration states (b) Effect of HG asymmetry factor on simulation accuracy

which directed the light away from the sensor thus reducing the measured TRR. Bubble scattering was more evident at low catalyst loading since it was the predominant scattering mechanism as a result of the reduced light attenuation by catalyst absorption and scattering. A similar finding has been reported in aerated photobioreactors in which bubble scattering was observed to be significant only at low algal concentrations (Wheaton and Krishnamoorthy, 2012; McHardy et al., 2018).

The effect of bubbles on the TRR can be further explained by considering the nature of sunlight which consists of direct and diffuse light. Bubbles influence the propagation of direct and diffuse light in different ways. To illustrate this, Monte Carlo simulation of the reactor under direct or diffuse light illumination of the same intensity was carried out. This was achieved by

setting the normal diffuse fraction to 0 or 1 for direct light or diffuse light illumination, respectively. Simulation was carried out at different catalyst loadings (0.005 – 0.2 g/L) and aeration states. The TRR was generally found to be higher under direct light than under diffuse light illumination, especially at low catalyst loadings (Figure 5.5). This trend could be explained by tracing the path of 1000 photons in the reactor filled with only water (Figure 5.6a – d). In the reactor without bubbles, the diffuse light arriving from several directions (Figure 5.2c) was uniformly distributed on the unilluminated wall of the reactor (Figure 5.6c). The unidirectional direct light (Figure 5.2d) was refracted onto a thin strip on the unilluminated wall where the sensor was positioned (Figure 5.6a). Consequently, under direct illumination, most of the light was focused on the sensor, and this resulted in higher TRR measurements as compared to diffuse illumination. This effect was more pronounced at low catalyst loadings in which light transmission was less affected by catalyst scattering and absorption.

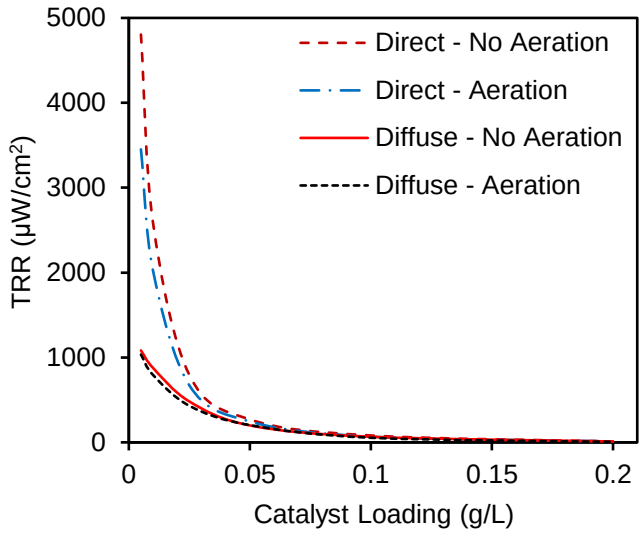

Figure 5.5: Effect catalyst loading and aeration state on the TRR under direct and diffuse light illumination

The simulation results (Figure 5.5) also show that the presence of bubbles reduced the TRR especially at low catalyst loadings. This reduction in the TRR was much more pronounced under direct light illumination than under diffuse light illumination. Due to its directional nature, direct light is very sensitive to bubble scattering which changes its direction away from the radiation sensor. This is clearly shown in the ray tracing diagram where bubbles are observed to scatter some of the direct light away from the refraction point where the TRR sensor is located (Figure 5.6b). In contrast, diffuse light travels in all directions such that any change in the direction by bubble scattering has a very limited impact on the overall direction of propagation. This is evident from the minimal differences observed in the ray traces in the

reactor with bubbles as compared to that without bubbles (Figure 5.6c – d). Since sunlight has an appreciable amount of direct light, its overall transmission is significantly affected by the presence of bubbles. This is markedly different from the situation in reactors illuminated by diffuse light sources like the low-pressure mercury UV lamps. In such reactors, the effect of bubbles on the forward transmitted radiation has been found to be negligible (chapter 4).

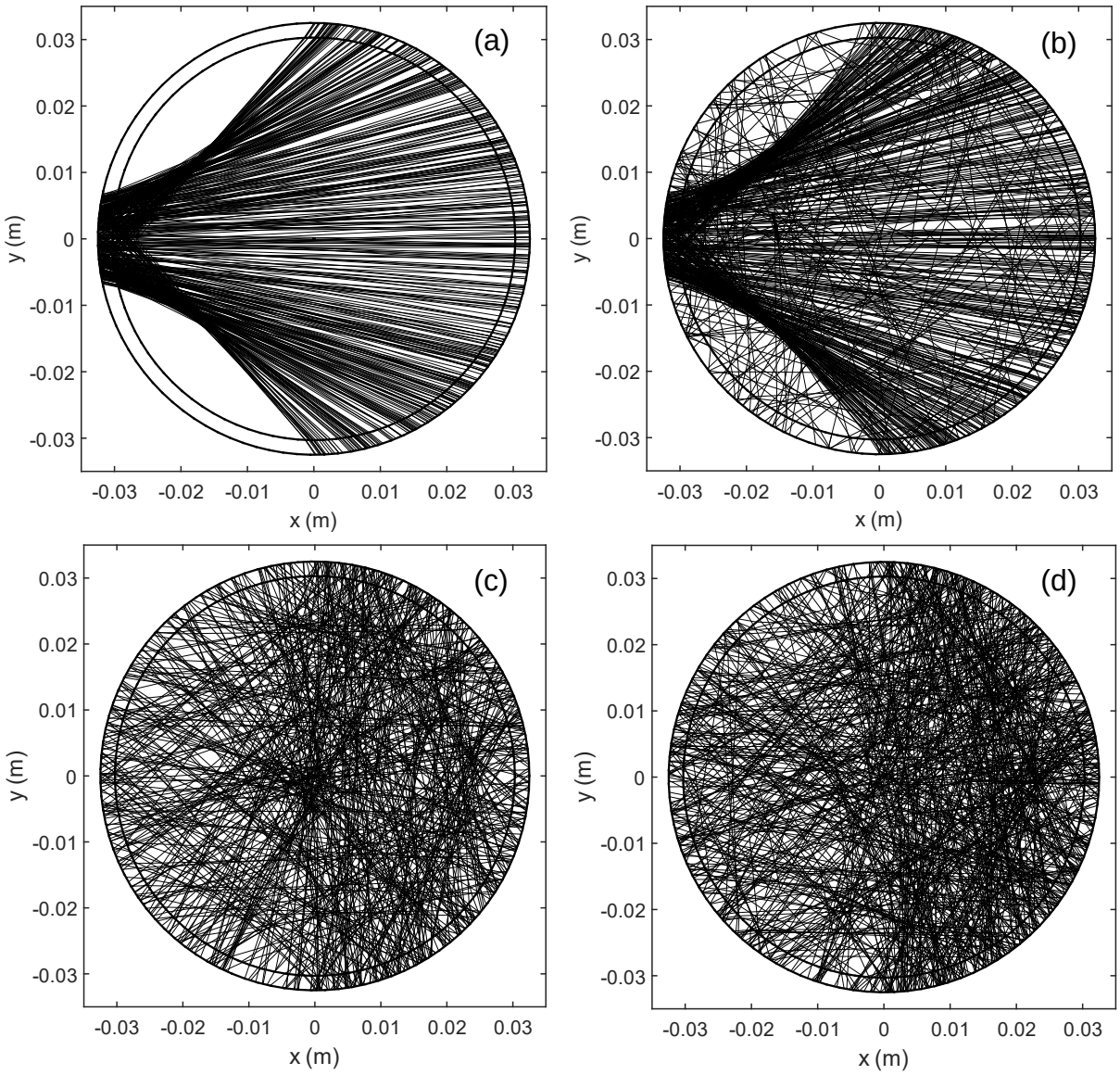

Figure 5.6: Ray tracing diagrams: (a) diffuse fraction of 0 without bubbles (b) diffuse fraction of 0 with bubbles (c) diffuse fraction of 1 without bubbles, (d) diffuse fraction of 1 with bubbles

The presence of a significant amount of direct light in sunlight resulted in an interesting refraction phenomenon in the reactor. The curved geometry of the reactor wall refracted the direct light across the air/glass/water interface such that the light was focused onto a narrow strip along the unilluminated wall (Figure 5.6a). This created a fixed point with respect to the incident light direction where the forward transmitted light intensity could be measured. By

considering wall refraction in the Monte Carlo model, the intensity of the refracted light could be used to validate the model in the presence of bubbles and catalyst particles. It should be noted that in most of the previous simulations of light distribution in solar photoreactors (Colina-Márquez et al., 2009; Colina-Márquez et al., 2010; Mueses et al., 2013; Acosta-Herazo et al., 2016; Ochoa-Gutiérrez et al., 2018), the wall refraction was not considered. Also, in those studies, the light distribution models were not validated intrinsically using forward transmitted radiation. Instead, most of the models were validated using experimental reaction kinetics data, a process which involves the use of fitting constants from experimental photocatalysis data. Such a recursive validation process may yield an accurate fit with kinetic data even if the light distribution model is inaccurate. Consequently, the accuracy of any light distribution model should only be established by validating it intrinsically by measuring the transmitted light. So far, such validation has been carried out only in reactors illuminated by UV lamps (Moreira et al., 2010; Valades-Pelayo et al., 2014a; Valadés-Pelayo et al., 2014b) and a xenon lamp (Cao et al., 2014).

In order to determine the nature of catalyst scattering under solar illumination, the effect of the Henyey-Greenstein asymmetry factor on the TRR was investigated. This was carried out by comparing the error in simulation of the TRR at different catalyst loadings in the reactor without aeration. The error in simulation was evaluated using the root mean square error (RMSE):

$$RMSE = \sqrt{\sum_{i=0.005\ \mathrm{g/L}}^{0.2\ \mathrm{g/L}} \left[TRR_{Exp}(i) - TRR_{Sim}(i)\right]^2} \tag{5.33}$$

where $TRR_{Exp}(i)$ and $TRR_{Sim}(i)$ are the experimental and simulated TRR at catalyst loading i, respectively. The results (Figure 5.4 b) show a decrease in the simulation error from g = 0.8 to g = 0.87 beyond which the error increases. An asymmetry factor of 0.87 was thus established for this catalyst under solar illumination. This value is slightly higher than the value of 0.84 which was found for this same catalyst under UV lamp illumination in chapter 4. This could be attributed to the differences in the wavelengths of UV and solar light. Satuf et al. (2005) observed that g was a function of the light wavelength. Using their data, the wavelength averaged g was calculated and found to be 0.52 and 0.56 under UV lamp and solar illumination, respectively. Therefore, g should be slightly higher under solar than under UV lamp illumination which is consistent with the findings in this work.

In this study, the light distribution model was validated by comparing the experimental TRR values with those obtained from Monte Carlo simulation at different catalyst loadings (0.005 – 0.2 g/L) and aeration states (Figure 5.4 a). The simulations were carried out using an asymmetry factor of 0.87. The results show that the Monte Carlo method could predict the TRR fairly accurately at the different catalyst loadings and aeration states. The main source of error in the Monte Carlo simulation can be attributed to inaccurate specification of the solar diffuse fraction. As shown in Figure 5.5, the diffuse fraction has a significant effect on the TRR. Therefore, an accurate simulation can only be achieved with correct values of the diffuse fraction. The most accurate method of evaluating the diffuse fraction involves the use of at least two radiometers for measuring the diffuse and global solar UV radiation. Such specialized instruments are costly and have only been installed in a few locations around the world (Khorasanizadeh and Mohammadi, 2016).

Several empirical correlations for the diffuse fraction have been developed for the locations with the appropriate instruments (Khorasanizadeh and Mohammadi, 2016). However, most of these correlations do not cover the UV range and are very location specific. In this work, the correlation by Boland et al. (2008) was used to estimate the diffuse fraction. This correlation was chosen due to its simplicity and the fact that it was developed in Australia (34.9° S) which is closer in latitude to South Africa (26.7° S) as compared to locations in North America, Europe and Asia. The error in the diffuse fraction was minimized by measuring the global horizontal UV irradiance and global tilt UV irradiance followed by adjusting the ground reflectance in the HDKR model. This approach was found to be fairly accurate and low cost, resulting in good prediction of the experimental TRR by the Monte Carlo model.

5.3.2 Overall radiation absorption

The volumetric rate of energy absorption (VREA) is the amount of light absorbed by all the catalyst in the reactor (Valades-Pelayo et al., 2014b). The VREA is usually proportional to the reaction rate constant and has been used by several authors (Moreira et al., 2010; Valades-Pelayo et al., 2014b; Hou et al., 2017) to determine the optimum catalyst loading without running photocatalytic experiments. The results of the VREA (Figure 5.7a) showed that the VREA increased exponentially as the catalyst loading was increased. For instance, without aeration, the VREA increased from 264 to 967 $\mu W/cm^3$ as the catalyst loading was increased from 0.005 to 0.2 g/L. Increasing the catalyst loading to 0.6 g/L increased the VREA marginally to 999 $\mu W/cm^3$. This trend is due to the increase in light absorption with an increase in the number of catalyst particles in solution. However, at very high catalyst loadings, the catalysts

particles near the light source shielded the light from illuminating the rest of the reactor. As a result, a large number of catalyst particles were not illuminated and did not participate in light absorption. The optimum catalyst loading is the lowest value of the catalyst loading at which the maximum amount of light is absorbed. At this value, increasing the catalyst loading leads to a marginal increase in the VREA (Valades-Pelayo et al., 2014b). In this reactor, the optimum catalyst loading was determined from Figure 5.7a as 0.15 g/L.

At all catalyst loadings, the presence of bubbles led to a negligible drop in the light absorption. For instance, at 0.1 g/L catalyst loading, aeration resulted in a slight decrease in the VREA from 911 to 908 $\mu W/cm^3$ (Figure 5.7a). Bubble scattering redirected only a few photons outside the reactor with the rest being redistributed in the reactor where they were absorbed by the catalyst. The negligible effect of bubbles on light absorption compared to the significant contribution of air to catalyst fluidization and in-situ oxygen supply demonstrate the positive role of air fluidization in photocatalysis. The insignificant effect of bubbles on VREA also suggest that, during Monte Carlo simulations, the interactions of photons and bubbles can be neglected in order to reduce simulation time as found in chapter 4.

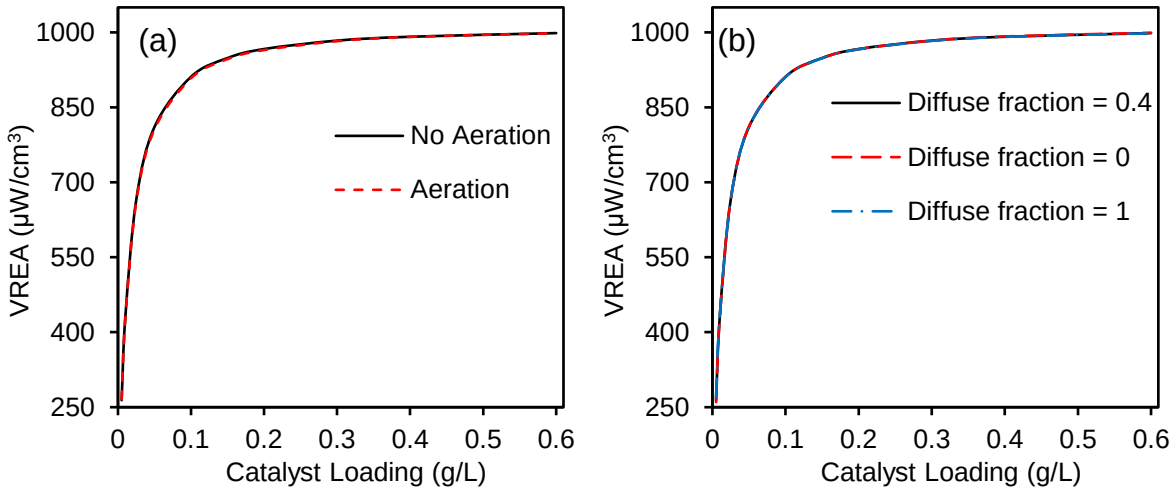

Figure 5.7: Effect of (a) Aeration state (b) Solar diffuse fraction on the VREA at different catalyst loadings

The influence of the type of radiation (direct or diffuse light) on the light absorption was also investigated. The results (Figure 5.7b) show that the diffuse fraction generally had no effect on the light absorption. For instance, at 0.1 g/L catalyst loading, the VREA was found to be 911 $\mu W/cm^3$ under both direct and diffuse light illumination. This was due to the fact that photon absorption by the catalyst does not depend on the direction of incidence. As a result, for the same light intensity and catalyst loading, the light absorption would be the same even if all the

photons followed a similar trajectory (direct light) or different paths (diffuse light). The diffuse fraction significantly affects the TRR and model validation; however, it had very little influence on light absorption. The aim of light distribution modelling is to obtain the VREA for estimation of the optimum catalyst or use in kinetic analysis. Thus, once the model has been validated, it can be used to determine the VREA without the need for an accurate value of the diffuse fraction. This is desirable considering the extra equipment and/or modelling needed for the estimation of the diffuse fraction. An accurate value of the normal solar irradiance would still be required, but this can easily be calculated from measurement of the global horizontal UV irradiance and the global tilt UV irradiance as described in section 2.2.2.

5.3.3 Light distribution

The validated Monte Carlo model was used to analyse the local volumetric rate of energy absorption (LVREA) profiles in the reactor. The Monte Carlo model was simplified by neglecting bubble-photon interactions. Analysis of the LVREA provides a useful metric for estimating the local kinetics in the reactor. In this respect, it could be used to optimize the reaction rate by identifying poorly illuminated regions in the reactor with lower reaction rates. The LVREA along the axial direction was analysed using contour plots along the x, z coordinate at different catalyst loadings (Figure 5.8a – f). These plots show a general uniformity in the LVREA along the axial coordinate, except for a narrow region at the top and bottom of the reactor in which the contours slope diagonally. The reactor was positioned vertically such that solar rays arrived at the reactor at the solar zenith angle. Consequently, the LVREA profiles at the top and bottom of the reactor were observed to follow a diagonal profile consistent with the path of the photons. At axial regions between the top and bottom surfaces, catalyst scattering redistributed the photons, resulting in a fairly uniform axial profiles. Along the radial coordinate, a significant shift in the LVREA profiles were observed. This was best analysed using polar plots at axial location z = 300 mm (Figure 5.9a – f). In the polar plots, 0° lies on the illuminated side of the reactor while 180° lies on the unilluminated side.

The polar plots shows non-uniform LVREA values at all catalyst loadings and a shift in the region of highest LVREA as the catalyst loading was increased. At a low catalyst loading of 0.005 g/L (Figure 5.9a), the highest LVREA values were observed between angular location of 120° and 240° and radial location of 15 and 25 mm on the unilluminated side of the reactor. This shifted to a region on the sides of the reactor spanning angular location 210 – 330° and angular location 30 – 150° at 0.01 g/L catalyst loading (Figure 5.9b). At higher catalyst loadings (> 0.01 g/L), increasing the catalyst loading gradually shifted the location of the

highest LVREA to a narrow strip between angular location 90° and 270° on the illuminated side of the reactor. Also, at these high catalyst loadings, the depth of the high LVREA region decreased as the catalyst loading was increased.

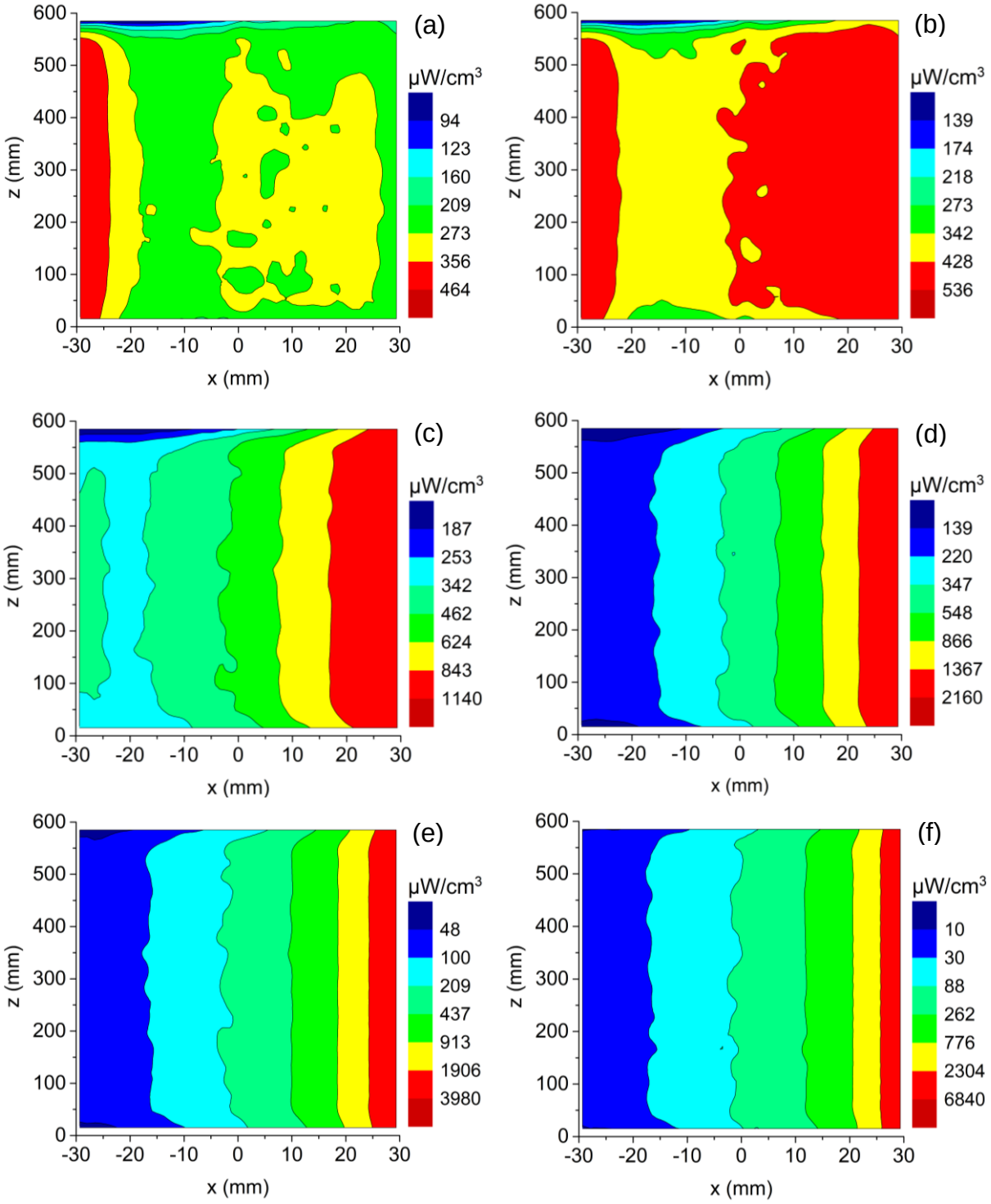

Figure 5.8: Axial (x, z) contour plots of the LVREA at different catalyst loadings. (a) 0.005 g/L, (b) 0.01 g/L, (c) 0.025 g/L, (d) 0.05 g/L, (e) 0.1 g/L, (f) 0.2 g/L

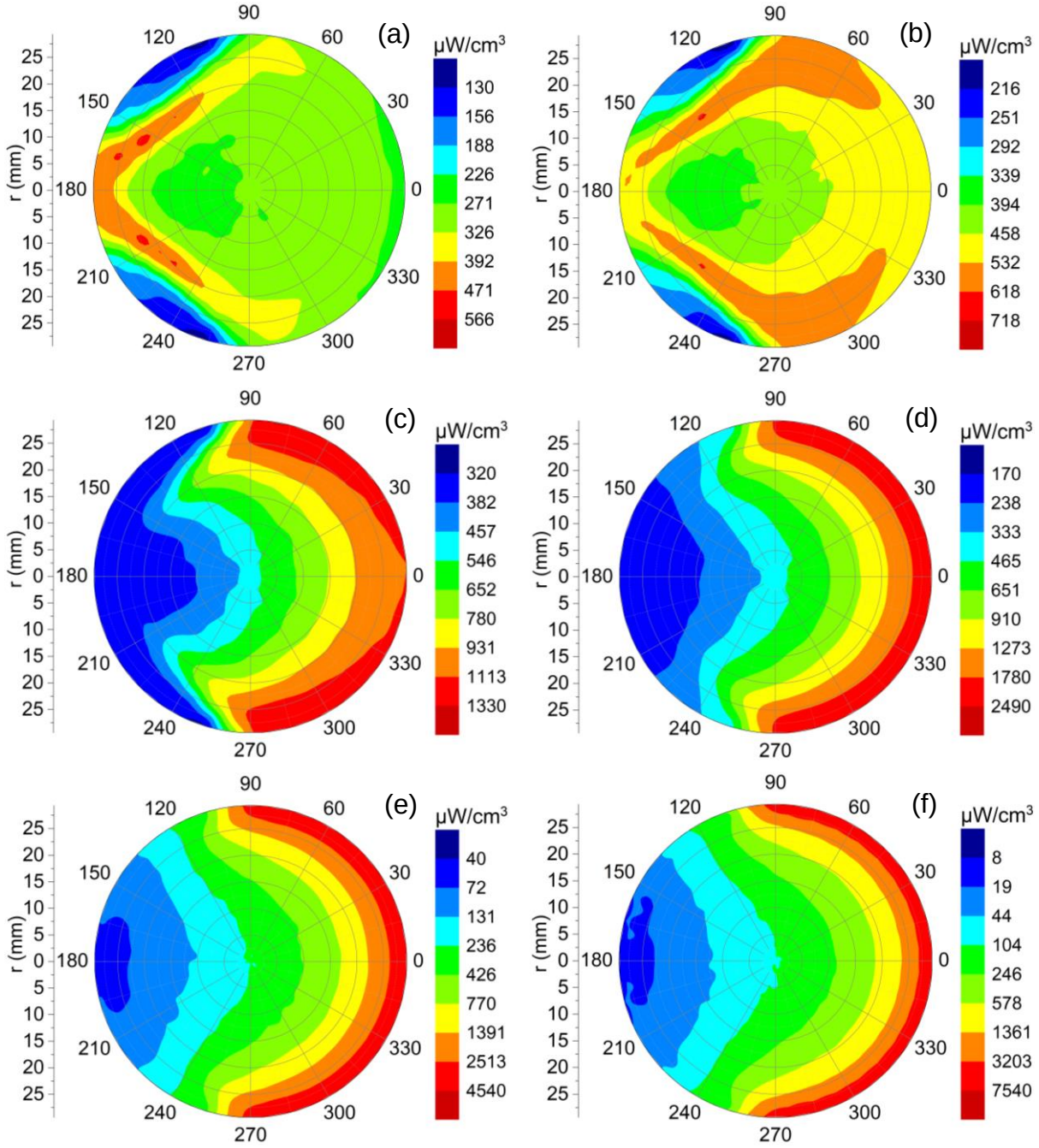

Figure 5.9: LVREA polar plots at different catalyst loadings. (a) 0.005 g/L, (b) 0.01 g/L, (c) 0.025 g/L, (d) 0.05 g/L, (e) 0.1 g/L, (f) 0.2 g/L

To obtain a better understanding of the radial LVREA profiles, 2D plots were generated from the axial plots (Figure 5.10). The 2D plot represented a line at z-location 300 mm drawn from x-coordinate -30 mm to 30 mm. The plots show an increase in the exponential decay of the LVREA along the radial coordinate as the catalyst loading was increased. At low catalyst loading (0.005 – 0.01 g/L), little differences in the LVREA values along the radial coordinate was observed. For instance, at 0.01 g/L catalyst loading, values of the LVREA ranged from 360 to 534 μW/cm^3 along the radial coordinate. This contrasts with the trend at higher catalyst

loadings (> 0.01 g/L) in which a markedly steeper drop in the LVREA along the radial coordinate was observed. For instance, at 0.1 g/L catalyst loading, the LVREA decreased from 3915 μW/cm^3 to 65 μW/cm^3 from radial coordinate -29 to 29 mm, respectively. Figure 5.10 also shows an increase in the LVREA at the illuminated wall as the catalyst loading was increased. For instance, at radial coordinate 29 mm, increasing the catalyst loading from 0.025 to 0.2 g/L led to an increase in the LVREA from 1115 to 6810 μW/cm^3.

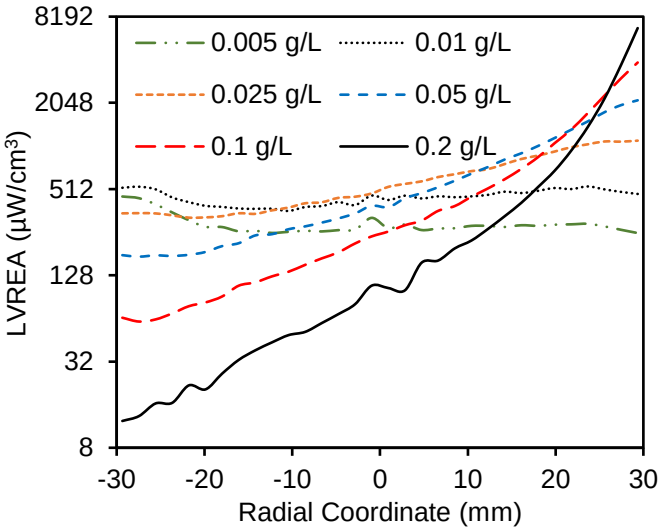

Figure 5.10: Radial LVREA profiles at different catalyst loadings

At low catalyst loading (0.005 – 0.01 g/L), the insignificant light absorption in the reactor resulted in uniform LVREA values along the radial coordinate. At these catalyst loadings, the light propagation followed the pattern of refraction observed in the reactor without any catalyst (Figure 5.6a). This concentrated the incident light to a narrow spot near the unilluminated side of the reactor. Increasing the catalyst loading above 0.01 g/L resulted in a gradual increase in the light absorption. The catalyst particles near the illuminated wall absorbed most of the light which shielded the catalyst particles deeper in the reactor. This resulted in an exponential decrease in the LVREA along the radial coordinate, increased the LVREA near the illuminated wall and reduced the depth of the illuminated zone (Valades-Pelayo et al., 2014b). Furthermore, the increased absorption and scattering of photons along the direction of light propagation gradually blunted the pattern of refraction as the catalyst loading increased.

5.4 Conclusion

In this chapter, the light distribution in a solar illuminated photoreactor was simulated using the Monte Carlo method. A new method, based on the total refracted radiation (TRR) at the unilluminated wall, was developed for validating the Monte Carlo model. Good agreement was obtained between simulated and experimental TRR values at all catalyst loadings and aeration

states. The optimum catalyst loading was found to be 0.15 g/L from an analysis of the volumetric rate of energy absorption (VREA). Simulation showed that air bubbles affected the transmission of direct light much more than diffuse light. Bubbles, at low catalyst loading, decreased the TRR; however, at all catalyst loadings, bubbles had negligible effect on the light absorption. This showed that air was a good fluidization method as it achieved good catalyst mixing (Chapter 3) and provided oxygen electron acceptor without negatively impacting light absorption. Solar diffuse fraction significantly affected the TRR at low catalyst loading but did not affect the light absorption. Therefore, a fairly accurate Monte Carlo simulation could be obtained without specifying the diffuse fraction and bubble-photon interactions. A general uniformity in the LVREA along the axial direction was observed except near the top and bottom of the reactor. Radial profiles of the local volumetric rate of energy absorption (LVREA) showed non-uniform light distribution due to refraction and light absorption. The maximum LVREA region shifted from the unilluminated to the illuminated side as the catalyst loading was increased. This study demonstrated the rigour and accuracy of the Monte Carlo method and its usefulness for gaining insight into light absorption at different locations and in the presence of inert media such as air bubbles. Moreover, the Monte Carlo method could be used to provide reactor design data such as the optimum catalyst loading without running costly photocatalysis experiments.

In this chapter, the light distribution in a solar illuminated reactor was investigated. The light distribution in a UV lamp illuminated reactor was reported in the previous section. In a hybrid light reactor, both light sources illuminate the reactor simultaneously and the UV and solar effects are additive. It is also expected that the different light sources will result in different reaction rates. In order to analyse the reaction rate under hybrid light illumination, the influence of light intensity and type of illumination on the reaction rate needs to be analysed. Such analyses and the reaction rate profiles under hybrid light illumination will be discussed in the next chapter.

References

Acosta-Herazo, R., Monterroza-Romero, J., Mueses, M. Á., Machuca-Martínez, F., and Li Puma, G., 2016. Coupling the Six Flux Absorption–Scattering Model to the Henyey–Greenstein scattering phase function: Evaluation and optimization of radiation absorption in solar heterogeneous photoreactors. *Chemical Engineering Journal*, *302*, 86–96.

Boland, J., Ridley, B., and Brown, B., 2008. Models of diffuse solar radiation. *Renewable Energy*, *33*(4), 575–584.

Cao, F., Li, H., Chao, H., Zhao, L., and Guo, L., 2014. Optimization of the concentration field in a suspended photocatalytic reactor. *Energy*, *74*(C), 140–146.

Casado, C., García-Gil, Á., van Grieken, R., and Marugán, J., 2019. Critical role of the light spectrum on the simulation of solar photocatalytic reactors. *Applied Catalysis B: Environmental*, *252*, 1–9.

Colina-Márquez, J., Machuca-Martínez, F., and Li Puma, G., 2009. Photocatalytic mineralization of commercial herbicides in a pilot-scale solar CPC reactor: photoreactor modeling and reaction kinetics constants independent of radiation field. *Environmental Science & Technology*, *43*(23), 8953–8960.

Colina-Márquez, J., Machuca-Martínez, F., and Puma, G. L., 2010. Radiation absorption and optimization of solar photocatalytic reactors for environmental applications. *Environmental Science & Technology*, *44*(13), 5112–5120.

De Greve, B., 2006. *Reflections and refractions in ray tracing*. https://graphics.stanford.edu /courses/cs148-10-summer/docs/2006--degreve--reflection_refraction.pdf

Duffie, J. A., and Beckman, W. A., 2013. *Solar engineering of thermal processes* (4th Edition). Wiley New York.

Hou, J., Wei, Q., Yang, Y., and Zhao, L., 2017. Experimental evaluation of scattering phase function and optimization of radiation absorption in solar photocatalytic reactors. *Applied Thermal Engineering*, *127*, 302–311.

Imoberdorf, G. E., Taghipour, F., Keshmiri, M., and Mohseni, M., 2008. Predictive radiation field modeling for fluidized bed photocatalytic reactors. *Chemical Engineering Science*, *63*(16), 4228–4238.

Khorasanizadeh, H., and Mohammadi, K., 2016. Diffuse solar radiation on a horizontal surface: Reviewing and categorizing the empirical models. *Renewable and Sustainable Energy Reviews*, *53*, 338–362.

Malato, S., Fernández-Ibáñez, P., Maldonado, M. I., Blanco, J., and Gernjak, W., 2009. Decontamination and disinfection of water by solar photocatalysis: Recent overview and trends. *Catalysis Today*, *147*(1), 1–59.

McHardy, C., Luzi, G., Lindenberger, C., Agudo, J. R., Delgado, A., and Rauh, C., 2018. Numerical analysis of the effects of air on light distribution in a bubble column photobioreactor. *Algal Research*, *31*, 311–325.

Moreira, J., Serrano, B., Ortiz, A., and de Lasa, H., 2010. Evaluation of photon absorption in an aqueous TiO_2 slurry reactor using Monte Carlo simulations and macroscopic balance. *Industrial & Engineering Chemistry Research*, *49*(21), 10524–10534.

Mueses, M. A., Machuca-Martinez, F., and Li Puma, G., 2013. Effective quantum yield and reaction rate model for evaluation of photocatalytic degradation of water contaminants in heterogeneous pilot-scale solar photoreactors. *Chemical Engineering Journal*, *215–216*, 937–947.

Ochieng, A., Odiyo, J. O., and Mutsago, M., 2003. Biological treatment of mixed industrial wastewaters in a fluidised bed reactor. *Journal of Hazardous Materials*, *96*(1), 79–90.

Ochieng, A., Ogada, T., Sisenda, W., and Wambua, P., 2002. Brewery wastewater treatment in a fluidised bed bioreactor. *Journal of Hazardous Materials*, *90*(3), 311–321.

Ochoa-Gutiérrez, K. S., Tabares-Aguilar, E., Mueses, M. Á., Machuca-Martínez, F., and Li Puma, G., 2018. A Novel Prototype Offset Multi Tubular Photoreactor (OMTP) for solar photocatalytic degradation of water contaminants. *Chemical Engineering Journal*, *341*, 628–638.

Pareek, V., Chong, S., Tadé, M., and Adesina, A. A., 2008. Light intensity distribution in heterogenous photocatalytic reactors. *Asia-Pacific Journal of Chemical Engineering*, *3*(2), 171–201.

Romero, R. L., Alfano, O. M., and Cassano, A. E., 2003. Radiation field in an annular, slurry photocatalytic reactor. 2. Model and experiments. *Industrial & Engineering Chemistry Research*, *42*(12), 2479–2488.

Satuf, M. L., Brandi, R. J., Cassano, A. E. and Alfano, O. M., 2005. Experimental method to evaluate the optical properties of aqueous titanium dioxide suspensions, *Industrial & Engineering Chemistry Research*, *44*(17), 6643-6649.

Schott., n.d.. *Schott tubing bronchure*. Retrieved July 13, 2020, from https://www.schott.com/d/tubing/9d60ae04-a9db-4b63-82b3-7aebd5bad71e/1.6/schott-tubing_brochure_duran_english-en.pdf

Solar Spectra: Standard Air Mass Zero., 1999. https://rredc.nrel.gov/solar//spectra/am0/ASTM2000.html

Valadés-Pelayo, P. J., Moreira del Rio, J., Solano-Flores, P., Serrano, B., and de Lasa, H., 2014a. Establishing photon absorption fields in a Photo-CREC Water II Reactor using a CREC-spectroradiometric probe. *Chemical Engineering Science*, *116*, 406–417.

Valades-Pelayo, P. J., Moreira, J., Serrano, B., and De Lasa, H., 2014b. Boundary conditions and phase functions in a Photo-CREC Water-II reactor radiation field. *Chemical Engineering Science*, *107*, 123–136.

Wheaton, Z. C., and Krishnamoorthy, G., 2012. Modeling radiative transfer in photobioreactors for algal growth. *Computers and Electronics in Agriculture*, *87*, 64–73.

Chapter 6

6 Simulation of the reaction rate profiles in a hybrid solar/UV lamp illuminated reactor

6.1 Introduction

Traditionally, photocatalysis has been carried out using nanophase TiO_2 illuminated by mercury ultraviolet (UV) lamps. Most of the reactors used in conventional photocatalysis have been the annular type in which the UV lamp is positioned in the middle of the reactor. The most popular UV lamp for lab scale installations has been the low-pressure black light and germicidal lamps (Apollo and Aoyi, 2016). In such a reactor, most of the light is absorbed in a narrow region near the lamp sleeve which results in poor illumination in the rest of the reactor (Valades-Pelayo et al., 2014). The least illuminated region is usually near the reactor wall where the catalysts are poorly illuminated resulting in catalyst wastage and a low reaction rate. To improve the reaction rate and optimize catalyst use, the region near the reactor wall needs to be illuminated. This can be done by employing an external light source such as sunlight. The resulting hybrid light reactor, internally illuminated by the UV lamp and externally illuminated by sunlight, has advantages of good illumination in a compact device. Moreover, the use of free and renewable solar energy significantly reduces the operation cost of the hybrid light reactor.

A few hybrid light reactors have been developed for wastewater treatment including a box-type reactor (Orozco et al., 2009) and a rotating drum reactor (Durán et al., 2018). However, a hybrid light annular three-phase reactor has not been reported for wastewater treatment. In order to design, scale up and optimize such a reactor, the light distribution needs to be evaluated. Since a hybrid light reactor is illuminated by two light sources, the LVREA as a design parameter would not be appropriate as the catalyst reactivity is affected by the light wavelength and intensity. A better design parameter would be the local reaction rate which encapsulates the effect of both light sources on catalyst reactivity.

In this chapter, previously validated Monte Carlo methods for the reactor illuminated by a UV lamp (chapter 4) and sunlight (chapter 5) were merged and then employed for the simulation of light distribution in the hybrid light reactor. Reaction parameters for the reactor under solar and UV lamp illumination were determined from the volumetric rate of energy absorption (VREA) and phenol photocatalysis reaction rate data. The simulated VREA and reaction

parameters were then used to establish the local reaction rate (LRR) profiles in the reactor under UV lamp, solar and hybrid light illumination. Finally, the optimum catalyst loading, based on the light absorption and LRR distribution, were determined for different reactor configurations. The aim of this chapter was to determine the effect of light source (UV lamp, solar, hybrid solar/UV lamp) and catalyst loading on the local reaction rate profiles.

6.2 Methodology

6.2.1 Reactor set up

The hybrid solar/UV lamp reactor (Figure 6.1) was similar in construction, dimensions and operation to the annular slurry bubble column reactor in chapter 4. The reactor was illuminated internally by a 15 W black light UV lamp which was protected from the liquid using a borosilicate glass lamp sleeve. A similar borosilicate glass was used to construct the reactor wall to let in sunlight. This type of glass had a high transmittance to both solar and long wave UV light. During experiments, the reactor was set up on a roof top with a clear view to the sun. The reactor was operated in batch mode for the catalyst slurry with compressed air being used to fluidize the catalyst.

Solar intensity was measured using a calibrated spectroradiometer (Stellarnet, Black Comet SR) system. This consisted of a radiation sensor (CR2 cosine receptor) which was connected to the spectroradiometer via a fibre-optic cable. The radiation data from the spectoradiometer was analysed using spectrawiz software on a computer. A special bracket enabled the radiation sensor to be positioned vertically and horizontally to measure the global horizontal UV irradiance (GHI) and the global tilt UV irradiance (GTI), respectively.

6.2.2 Monte Carlo method

The light distribution in the hybrid light reactor was simulated stochastically using a combination of the Monte Carlo methods developed previously for the reactor illuminated by the UV lamp (chapter 4) and sunlight (chapter 5). In the hybrid light reactor, the photon can originate from the UV lamp or sunlight. Consequently, the source of the photon was determined as:

$$\frac{G_{UV}}{G_{UV} + G_{i,N}} > R_1 \tag{6.1}$$

where G_{UV} is the UV lamp intensity measured at the lamp surface while $G_{i,N}$ is the normal incident solar irradiance which was determined using the correlations reported in chapter 5. R_1 is a random number uniformly distributed between 0 and 1.

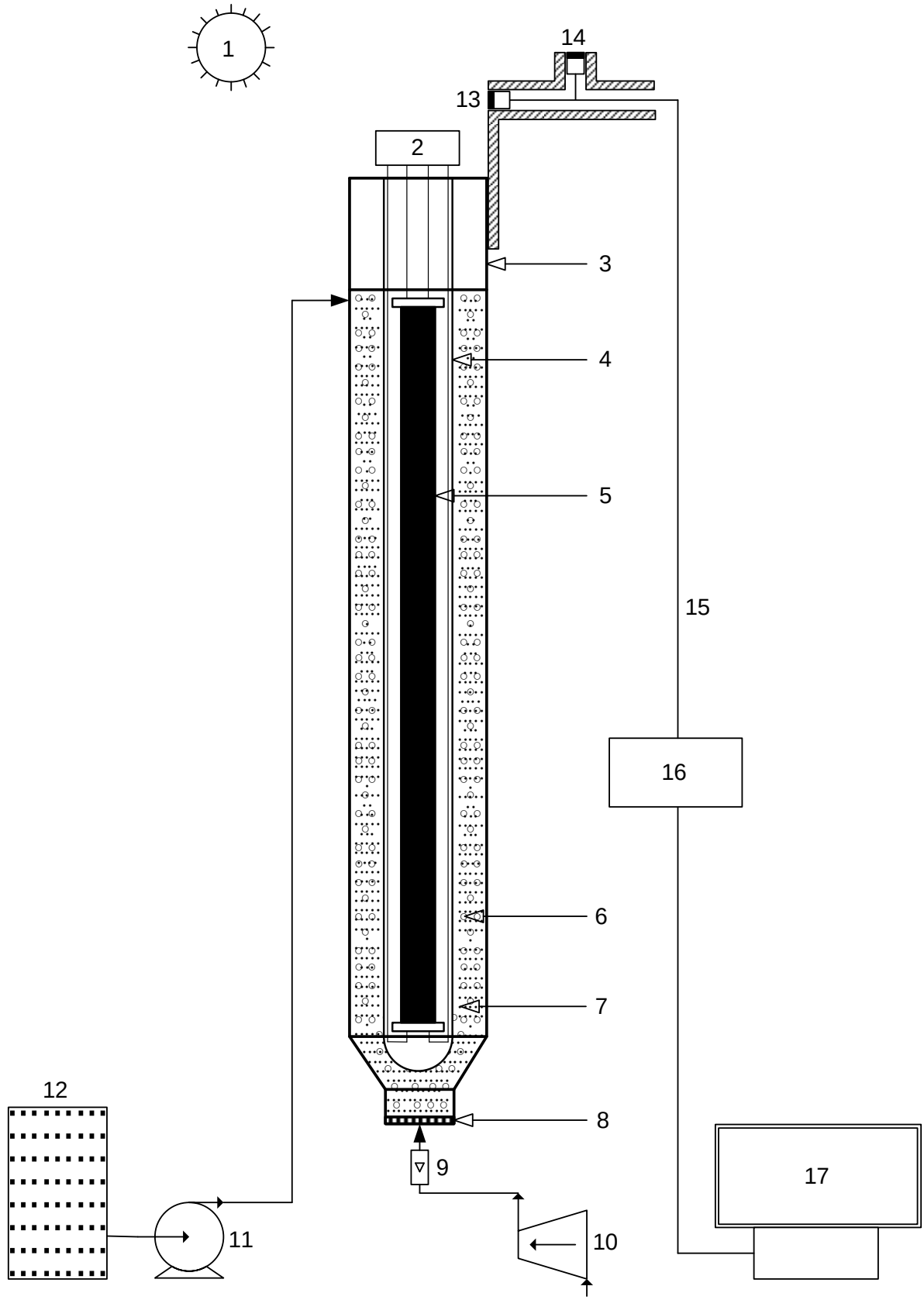

Figure 6.1: Hybrid solar/UV lamp reactor (1) sun, (2) lamp power supply, (3) reactor wall, (4) lamp sleeve, (5) black light lamp, (6) air bubble, (7) catalyst particle, (8) porous distributor, (9) air rotameter, (10) air compressor, (11) peristaltic pump, (12) feed tank, (13) GTI sensor, (14) GHI sensor, (15) fibre optic cable, (16) spectroradiometer, (17) computer

If equation (6.1) was evaluated as true, the photon originated from the UV lamp and its flight through the reactor was tracked using the Monte Carlo algorithm for the UV lamp illuminated reactor (chapter 4). However, if equation (6.1) was evaluated as false, the photon was a solar photon and its flight through the reactor was described using the algorithm for the solar illuminated reactor (chapter 5). The photon flight through the reactor continued until the photon was either absorbed by the catalyst, lamp sleeve, wall or went beyond the reactor boundaries.

The reactor volume was divided into 11,520 cells consisting of 16 radial, 36 angular and 20 axial regions. Two identical local volumetric rate of energy absorption (LVREA) grids were employed; one to store the energy of solar photons and the other for UV lamp photons. If the photon was absorbed by the catalyst, its energy was stored in one of the two LVREA grids depending on its identity and location. The LVREA at a certain grid cell was then determined as the sum of the energy of all photons absorbed at that grid cell per unit volume of the cell (Valades-Pelayo et al., 2014). The volumetric rate of energy absorption (VREA) for each of the two energy storage grids was then calculated as the sum of the LVREA in all the grid cells as:

$$VREA_{sol} = \frac{1}{V} \int LVREA_{sol}\, dV \tag{6.2}$$

$$VREA_{UV} = \frac{1}{V} \int LVREA_{UV}\, dV \tag{6.3}$$

where V is the reactor volume and the subscripts sol and UV refer to solar and UV lamp photons, respectively.

Table 6.1: Monte Carlo simulation parameters and values

Parameter	Simulation values
Reactor wall	ID: 60.6 mm, OD: 65 mm, Height: 600 mm, Absorbance: 8%
Lamp sleeve	ID: 31.2 mm, OD: 34 mm, Height: 600 mm, Absorbance: 5.17%
Black light lamp	OD: 26 mm, Height: 600 mm
Refractive indices	Air: 1.00029, Glass: 1.473 (Schott, n.d.), Water: 1.332986
HG asymmetric factor	UV lamp: 0.84 solar: 0.87

Photocatalysis is normally used to treat dilute wastewater streams in which the substrate concentration is in the order of a few mM. Therefore, photocatalysis reaction can be assumed to follow the pseudo-first order kinetics:

$$r = -\frac{dC}{dt} = k_{app} C \tag{6.4}$$

where r is the rate of reaction, C is the substrate concentration at time t and k_{app} is the apparent first order rate constant. The effect of light intensity on the rate constant can be expressed using a power law dependence on the VREA (Li Puma et al., 2004) as:

$$k_{app} = k_{int} VREA^{\alpha} \tag{6.5}$$

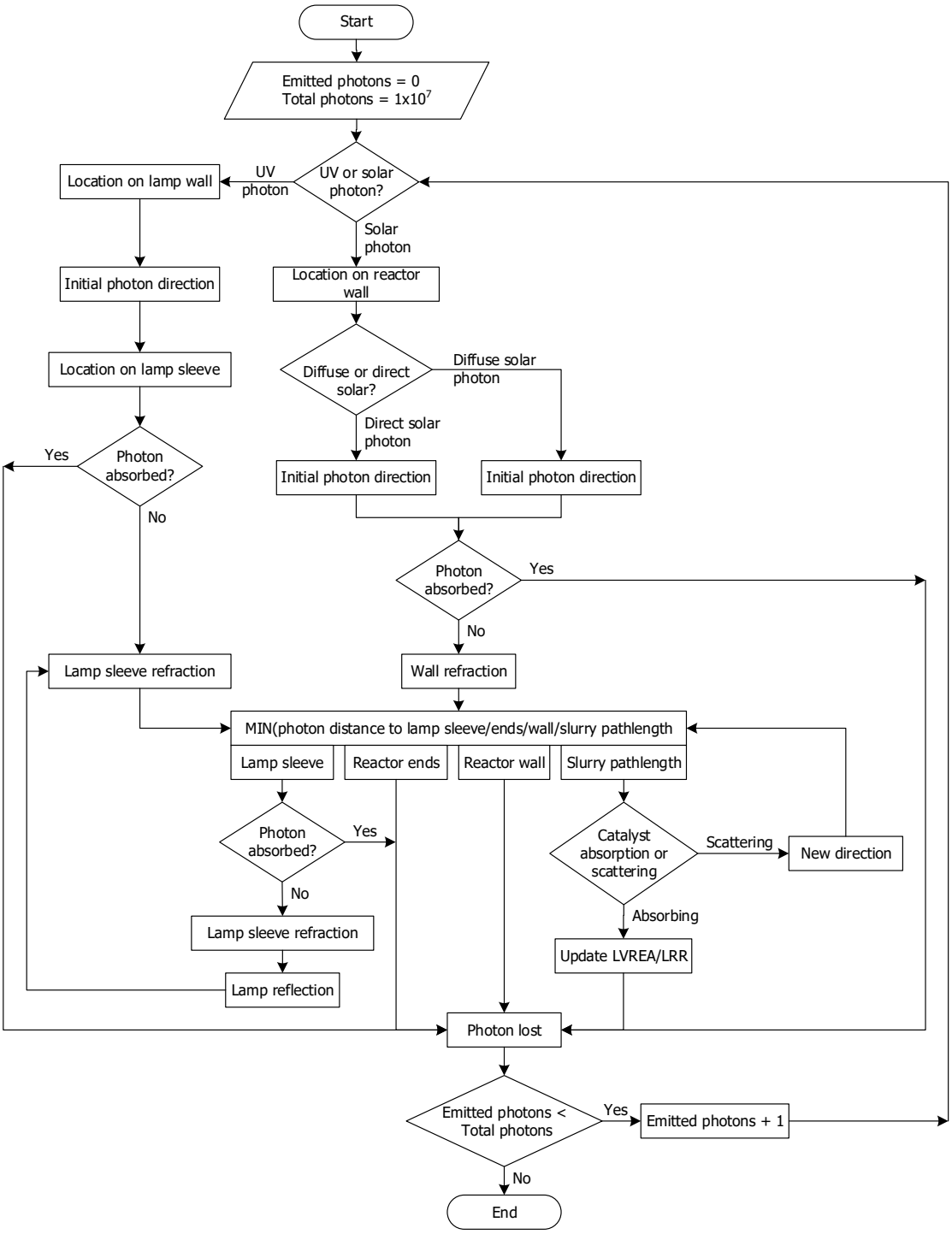

Figure 6.2: Monte Carlo algorithm flow sheet

where k_{int} is the intrinsic rate constant and α is the reaction order with respect to the VREA. Since solar and UV lamp photons were considered separately, equation (6.5) can also be written as:

$$k_{app} = k_{int\_sol}(VREA_{sol})^{\alpha\_sol} + k_{int\_UV}\,(VREA_{UV})^{\alpha\_UV} \tag{6.6}$$

where the suffixes sol and UV refer to solar and UV lamp photons, respectively. The local reaction rate (LRR) was established using another grid of similar dimensions to the LVREA grids. The LRR in each of the grid cells was determined using an equation derived from equations (6.4 – 6.6) as:

$$LRR = \left[k_{int\_sol}(LVREA_{sol})^{\alpha\_sol} + k_{int\_UV}\,(LVREA_{UV})^{\alpha\_UV}\right]C \tag{6.7}$$

Some of the key Monte Carlo simulation parameters such as the reactor dimensions, refractive indices and the Henyey-Greenstein asymmetric factors are listed in Table 6.1. The Monte Carlo algorithm for the photon flight through the hybrid light reactor is illustrated in Figure 6.2. Figure 6.3 is a cross section of the hybrid light reactor illustrating the photon flight from the lamp or the sun through the reactor. During reactor operation, catalyst particles were fluidized using air bubbles. However, photon-bubble interactions were not considered in the simulation since it had been shown previously that bubbles do not have a significant effect on the light absorption under both solar and UV lamp illumination (chapter 4 and chapter 5). The Monte Carlo method was also used to establish the light distribution in simplified reactors which were illuminated by either sunlight or the UV lamp.

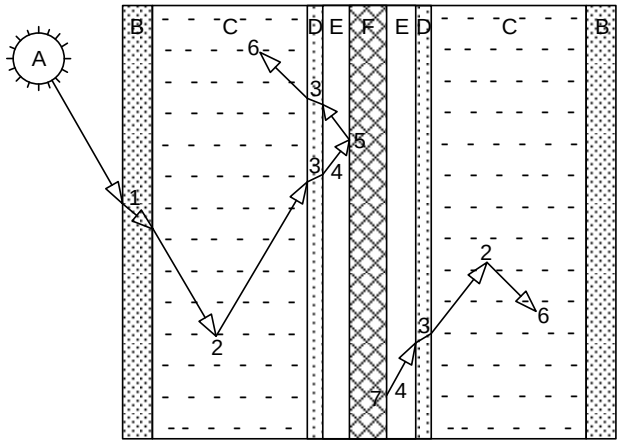

Figure 6.3: Photon flight in the hybrid light reactor (1) reactor wall refraction, (2) slurry scattering, (3) lamp sleeve refraction, (4) air gap photon flight, (5) lamp wall reflection, (6) catalyst absorption, (7) UV lamp photon emission. (A) solar position, (B) reactor wall, (C) catalyst slurry, (D) lamp sleeve, (E) air gap, (F) UV lamp

6.2.3 Photocatalysis experiments

During photocatalysis experiments, three different reactor configurations were employed based on the type of illumination. The annular UV lamp and annular solar reactors were illuminated by the UV lamp and sunlight, respectively while the hybrid light reactor was illuminated by both light sources. Pictures of these reactors are shown in Appendix B. The catalyst employed in this work was Aeroxide P25 TiO_2 purchased from Acros Organics. This catalyst was characterized by Carbajo et al. (2018) and found to have an anatase phase content of 86% with a primary particle size of 21 nm and a rutile phase content of 14% whose primary particle size is 33 nm. The specific surface area of the catalyst as measured by the BET technique was found to be 55 m^2/g. Furthermore, in de-ionized water at pH 6 which corresponds to the pH of phenol solution, the catalysts were observed to form aggregates of up to 3.5 μm.

Photocatalysis experiments were carried out at different catalyst loadings in each of these reactor configurations. First, the reactor was covered with a black canvas to shut off sunlight. Then, the reactor was filled with 1250 mL phenol solution with a concentration of 50 mg/L and a measured amount of catalyst loading between 0.25 g/L and 0.6 g/L. The catalyst slurry solution was kept under mixing in the dark for 30 minutes to ensure adsorption-desorption equilibrium. At the same time, the UV lamp was switched on and left to warm for 30 minutes outside the reactor. For the annular UV lamp reactor, the lamp was inserted into the reactor lamp sleeve to start the reaction. In case of the annular solar reactor, the canvas covering the reactor was removed to expose the reactor to sunlight and start the photocatalysis reaction. For the hybrid light reactor, the reaction was started by simultaneously inserting the lamp into the lamp sleeve and removing the canvas to illuminate the reactor with both the UV lamp and sunlight.

The substrate solution was sampled every 10 minutes, filtered with a 0.45 μm nylon syringe filter to remove the catalyst. Then, the concentration of the phenol solution was analysed using a Perkin-Elmer high performance liquid chromatography (HPLC). The HPLC was equipped with a C18 column (Perkin-Elmer) and a diode array detector (DAD) set at a wavelength of 270 nm. The mobile phase consisted of HPLC grade acetonitrile and water at a ratio of 60:40 and a flow rate of 1 mL/min. During substrate sampling, the global horizontal UV irradiance and the global tilt UV irradiance were recorded. An average of these values was used to compute the normal solar intensity incident upon the reactor during the photocatalysis experiment using the correlations reported previously (chapter 5). The intensity of the light

incident upon the reactor boundaries and the solar conditions during the experiments in the different reactor configurations are listed in Table 6.2:

Table 6.2: Light intensity of different reactor configurations

Reactor configuration	Light intensity (mol/s)	Solar zenith angle (°C)	Solar diffuse fraction
Annular UV lamp	2.159×10^{-5}		
Annular solar	9.035×10^{-6}	21.8	0.153
Hybrid solar/UV lamp	2.159×10^{-5} (UV lamp) 7.670×10^{-6} (solar)	29.5	0.337

6.3 Results and discussion

6.3.1 Reaction rate parameters

The value of α and k_{int} are usually determined by fitting VREA to experimentally determined values of k_{app} (Li Puma et al., 2004). This is carried out by plotting k_{app} and VREA on a log-log scale from which the values of k_{int} and α can easily be determined from the intercept and slope, respectively. In this work, experimental values of k_{app} were determined from the photocatalysis of phenol at different catalyst loadings in the annular UV lamp and annular solar reactors. The values of the VREA were determined from Monte Carlo simulation of the light distribution in those same reactor configurations. The simulations were carried out at the experimental catalyst loading and the intensity of the UV lamp/sunlight at the time of the experiments.

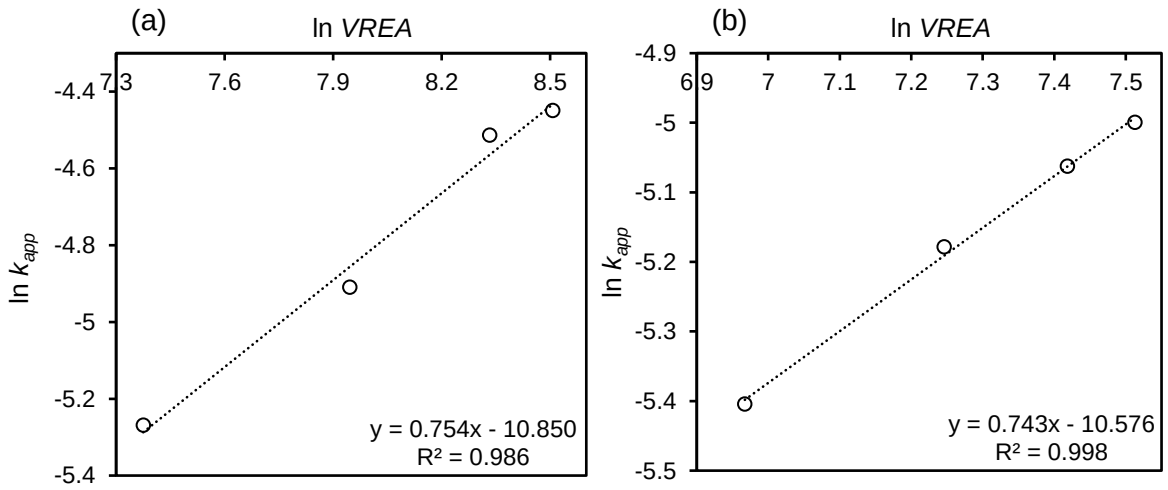

Figure 6.4: Log-log plot of $VREA$ vs k_{app} for (a) Annular UV lamp reactor (b) Annular solar reactor

The plots of k_{app} vs VREA in the annular UV lamp and annular solar reactors are shown in Figure 6.4. Under UV lamp illumination, α and k_{int} were found to be 0.75 and 1.94×10^{-5} $cm^{2.25}$ $\mu W^{-0.75}$ min^{-1}, respectively. The value of α is close to the value of 0.82 reported by (Li Puma

et al., 2004) for an annular UV lamp reactor containing P25 TiO_2 catalyst irradiated with an 8W black light lamp. The values of α and k_{int} under solar illumination were found to be 0.74 and 2.55×10^{-5} $cm^{2.22}$ $\mu W^{-0.74}$ min^{-1}, respectively. The value of α usually lies between 0.5 and 1. At low values of VREA, very little electron-hole recombination occurs; therefore, most of the absorbed radiation results in reaction. In this situation, the value of α approximates 1. As the value of VREA increases, the rate of electron-hole generation outstrips the rate of photocatalysis resulting in electron-hole recombination. This decreases the value of α to 0.5 (Li Puma et al., 2004). A value of α between 0.5 and 1 is common in optically thick reactors in which both first order and half order regimes exist in the same reactor (Boyjoo et al., 2013).

For both the annular solar and UV lamp reactors, the value of α was between 0.5 and 1 which shows that both first order and half order regimes were present in the reactor. It is conceivable that the region near the light source had half order reaction which increased to first order reaction further away from the light sources (Boyjoo et al., 2013). The value of α under solar illumination was slightly lower than the corresponding value under UV lamp illumination. This can be attributed to the relatively high energy photons in the 300 – 345 nm wavelength range in sunlight which were not present in the UV lamp photons, all of which have wavelengths above 345 nm (Figure 6.5). These high energy photons could generate much more electrons and holes resulting in a higher rate of electron-hole recombination under solar illumination as compared to UV lamp illumination. A similar finding has been reported by (Orozco et al., 2009).

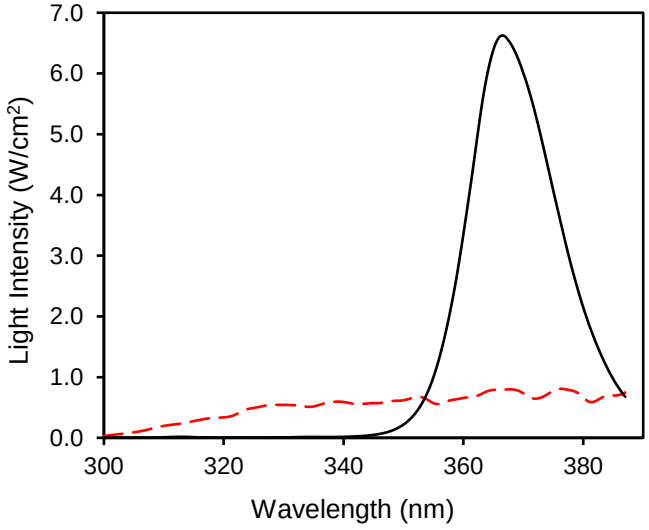

Figure 6.5: Light spectra of sunlight (– – –) and UV lamp (——) between 300 and 387 nm

Generally, the reaction rate under UV lamp illumination was higher than that under solar illumination. For example, at a catalyst loading of 0.2 g/L, the reaction rate under UV lamp and solar illumination was 0.548 and 0.337 mg L^{-1} min^{-1}, respectively (Figure 6.6). This could be attributed to two factors. First, the intensity of the UV lamp was higher than that of sunlight (Table 6.2). This resulted in higher values of the VREA and reaction rate under UV lamp illumination. Secondly, as shown by the respective values of α, the efficiency of conversion of the absorbed UV lamp photons into viable electron-hole pairs was better than that of solar photons, and this resulted in a higher reaction rate. Other studies have also found that the rate of photocatalysis depends on the type of light source (Li Puma et al., 2010; Joseph et al., 2016).

The reaction rate under both light sources was generally higher than the reaction rate under either solar or UV lamp illumination. This was mainly attributed to the dual illumination of the reactor from both the inside and outside which minimized dark zones and improved overall catalyst activation. It should be noted that the sum of the reaction rate under solar and UV lamp illumination did not equal the reaction rate under dual illumination. For example, at a catalyst loading of 0.2 g/L, the sum of the reaction rate under UV lamp and solar illumination was 0.885 $mgL^{-1}min^{-1}$ while that under hybrid light illumination was 0.788 $mgL^{-1}min^{-1}$. This discrepancy was due to the fact that the solar and hybrid light photocatalysis experiments were carried out on different days with different solar intensities.

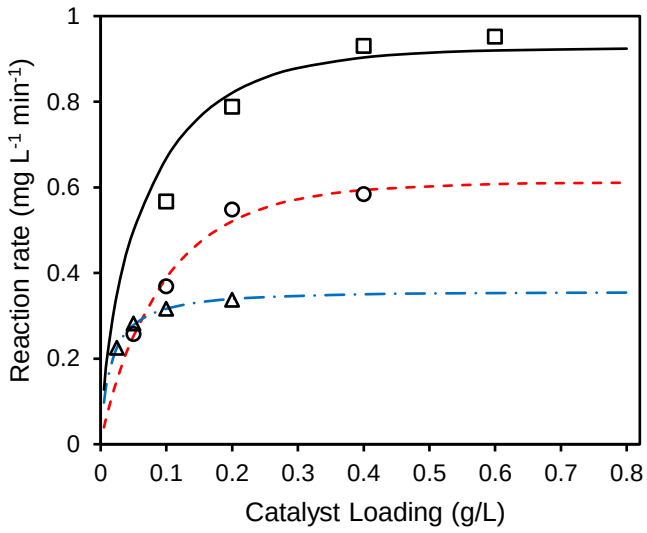

Figure 6.6: Experimental and simulated rate of phenol photocatalysis under different light sources. Solar-simulated (—·—), solar-experimental (Δ), UV lamp-simulated (— — —), UV lamp-experimental (○), hybrid light-simulated (——), hybrid light-experimental (□).

Figure 6.6 shows a very good fit between the experimental and simulated reaction rate under UV lamp, solar and hybrid light illumination. The good fit of the simulated reaction rate under

UV lamp and solar illumination was expected since the simulated rate profiles were evaluated from experimental data. The reaction parameters (α and k_{int}) obtained under UV lamp and solar illumination were used to determine the simulated reaction rate profiles under hybrid light illumination without any other adjustable parameters. The good fit between the experimental and simulated reaction rate under hybrid light illumination shows the accuracy and reliability of Monte Carlo simulation.

6.3.2 Local reaction rate profiles

After evaluating the intrinsic reaction rate constants (k_{int}) and the reaction order with respect to the VREA (α), these values were used to determine the local reaction rate (LRR) profiles in the reactor. Previous studies had shown that changes in the light absorption were insignificant along the axial axis in this reactor under both solar and UV lamp illumination (chapter 4 and chapter 5). Therefore, LRR profiles were only investigated on the radial plane. LRR profiles at three catalyst loadings (0.25, 1.0 and 4.0 g/L) in four reactor configurations (tubular solar, annular solar, annular UV lamp and hybrid light) were analysed using polar plots across the reactor centre-line (z = 300 mm) (Figure 6.7a – l).

The LRR values were presented on a dimensionless scale with the maximum LRR indicated on each sub-figure. The tubular and annular solar reactors were illuminated from the right side of the polar plots while the annular UV lamp reactor was illuminated internally. The hybrid light reactor was illuminated from the right side of the polar plot by sunlight and also internally by the UV lamp. To facilitate comparison among the different reactor configurations, Monte Carlo simulations were carried out using the same set of light intensity values measured during the hybrid light experiments (Table 6.2). A pair of 2D plots were also used to show the radial LRR profiles across the polar plots. The radial LRR profiles for the tubular and annular solar reactors were presented in Figure 6.8a while those for the UV lamp and hybrid light illuminated reactors were shown in Figure 6.8b.

In the solar and UV lamp illuminated reactors (Figure 6.7a – i), the LRR decreased from the illuminated side of the reactor to the unilluminated side. The radial profiles showed an exponential decay of the LRR along the light path with the gradient of the decay increasing with an increase in the catalyst loading (Figure 6.8a,b). At the lowest catalyst loading (0.025 g/L), a fairly uniform but low LRR profile was observed in the reactor. For example, in the tubular solar reactor, the radial LRR ranged from 0.106 to 0.245 $mgL^{-1}min^{-1}$ at 0.025 g/L catalyst loading (Figure 6.8a). At the highest catalyst loading (0.4 g/L), very high values of the

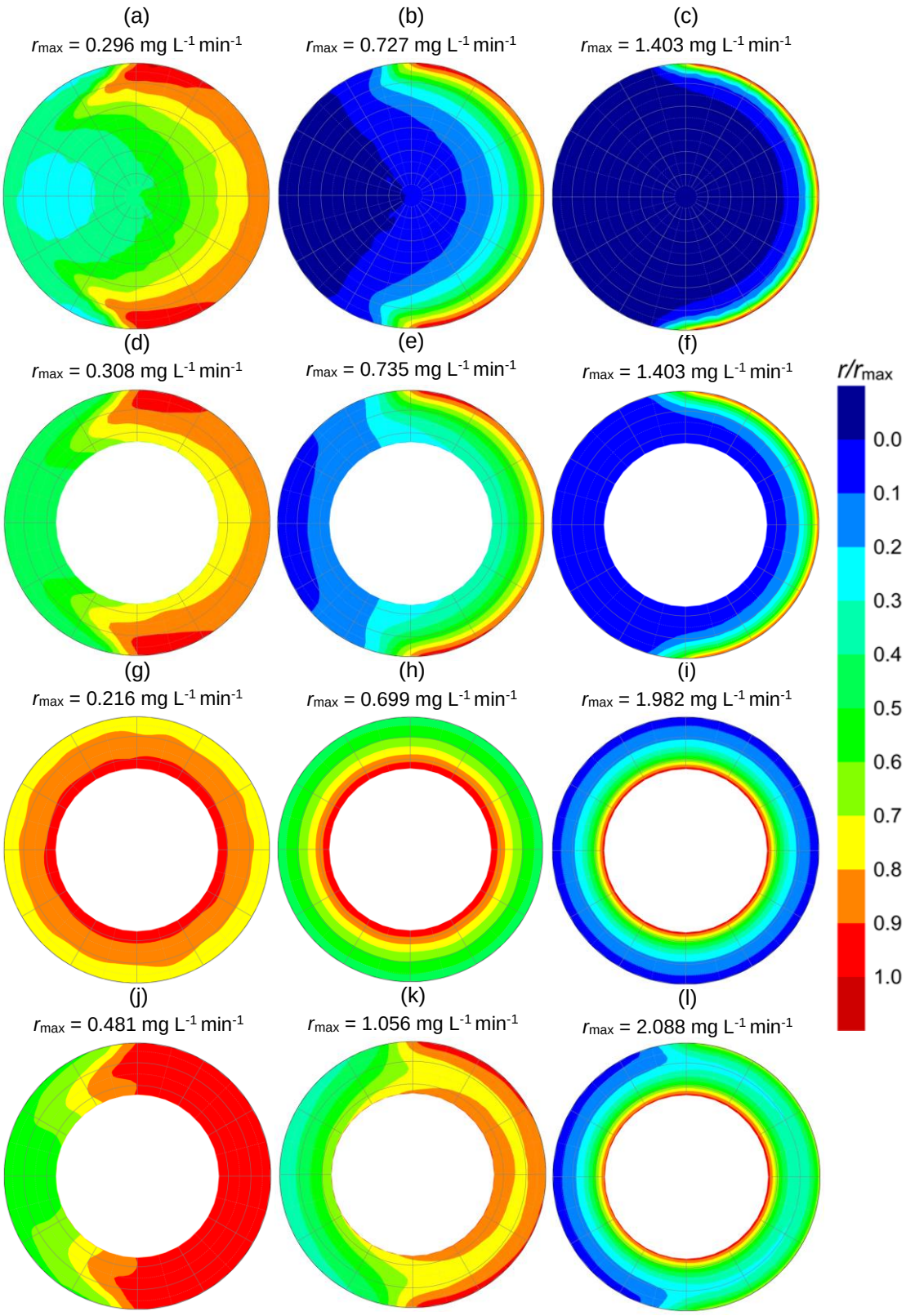

Figure 6.7: Local reaction rate for different reactors and catalyst loadings. (a) Tubular solar-0.025 g/L (b) Tubular solar-0.1 g/L (c) Tubular solar-0.4 g/L (d) Annular solar-0.025 g/L (e) Annular solar-0.1 g/L (f) Annular solar-0.4 g/L (g) Annular UV lamp-0.025 g/L (h) Annular UV lamp-0.1 g/L (i) Annular solar-0.4 g/L (j) Hybrid-0.025 g/L (k) Hybrid-0.1 g/L (l) Hybrid-0.4 g/L

LRR were observed near the illuminated region with most of the reactor exhibiting very low LRR values. For example, at a catalyst loading of 0.4 g/L, the radial LRR dropped from 1.324 $mgL^{-1}min^{-1}$ at the illuminated wall to 0.002 $mgL^{-1}min^{-1}$ at the unilluminated wall of the tubular solar reactor (Figure 6.8a). The exponential decay in the LRR was due to light attenuation along the light path due to catalyst absorption and scattering. An increase in the catalyst loading has been observed to increase the light attenuation (Valades-Pelayo et al., 2014), and this increased the decay of the LRR along the light path.

The radial LRR profiles showed that the annular solar reactor had a better LRR distribution than the tubular solar reactor. Whilst the LRR profiles near the illuminated wall were similar for both solar reactors, the LRR values near the unilluminated wall was higher in the annular reactor at all catalyst loadings. For example, at a catalyst loading of 0.4 g/L, the radial LRR ranged from 0.002 to 1.324 $mgL^{-1}min^{-1}$ in the tubular reactor and from 0.007 to 1.324 $mgL^{-1}min^{-1}$ in the annular reactor (Figure 6.8a). Light absorption by catalyst particles at the centre of the tubular reactor reduced the amount of light reaching the unilluminated region. In contrast, the centre of the annular reactor was filled with air which did not absorb any light, and this increased the incident light reaching the unilluminated region. The good light utilization in the annular configuration provided a platform for even better light utilization in the hybrid light reactor.

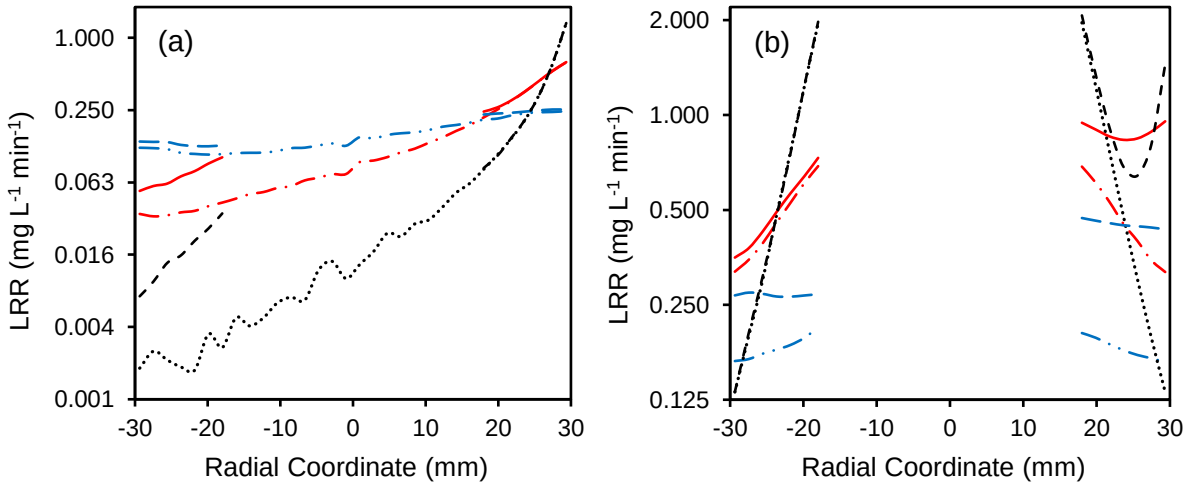

Figure 6.8: Radial LRR profiles (a) Tubular solar-0.025 g/L (—···—), Tubular solar-0.1 g/L (—·—), Tubular solar-0.4 g/L (·····), Annular solar-0.025 g/L (— — —), Annular solar-0.1 g/L (——), Annular solar-0.4 g/L (- - -); (b) Annular UV lamp-0.025 g/L (—···—) Annular UV lamp-0.1 g/L (—·—) Annular UV lamp-0.4 g/L (·····) Hybrid light-0.025 g/L (— — —) Hybrid light-0.1 g/L (——) Hybrid light-0.4 g/L (- - -).

Generally, higher LRR values were observed in the annular UV lamp reactor as compared to the solar illuminated reactors. For example, at a catalyst loading of 0.1 g/L, the minimum radial

LRR values were 0.053 and 0.318 $mgL^{-1}min^{-1}$ in the annular solar and UV lamp reactors, respectively (Figure 6.8a,b). This was due to the higher intensity and better catalyst utilization of UV lamp photons as compared to solar photons. Deeper penetration of UV lamp photons would be advantageous for hybrid light operation as this would provide good illumination to the solar dark zone, the side of the reactor that was not illuminated by sunlight.

In the hybrid light reactor, the LRR in the solar illuminated zone was strongly influenced by the two light sources. At low catalyst loading (0.025 g/L), a fairly uniform LRR was observed in this zone (Figure 6.7j). At this low catalyst loading, both solar and UV lamp photons could penetrate deep into the catalyst slurry, resulting in the illumination of all catalysts by both light sources. As the catalyst loading increased, the highest LRR values were restricted to a narrow region near the solar illuminated wall and the lamp sleeve (Figure 6.7k – l). This was characterized by the U-shaped curve of the radial LRR in the solar illuminated zone which became very steep at the highest catalyst loading (Figure 6.8b). This trend was attributed to an increase in the light attenuation with catalyst loading which reduced the path length of light in the reactor (Moreira et al., 2010). As a result, most of the light was absorbed in the region near both light sources resulting in high LRR in these regions.

It can also be observed from Figure 6.7l that the reaction rate near the lamp sleeve was markedly higher than that near the solar-illuminated wall. At such high catalyst loadings, rapid light attenuation ensured that the reaction rate near the boundaries was due to a specific light source. As compared to sunlight, light from the UV lamp had a higher intensity and reaction order with respect to the VREA. As a result, the more numerous UV lamp photons were also more likely to form electron-hole pairs in the catalysts, and this resulted in a higher LRR near the lamp sleeve.

The lowest LRR in the hybrid light reactor was observed in the solar dark zone (Figure 6.7j – l). For example, at a catalyst loading of 0.1 g/L, the lowest radial LRR was 0.834 $mgL^{-1}min^{-1}$ in the solar illuminated zone and 0.353 $mgL^{-1}min^{-1}$ in the solar dark zone (Figure 6.8b). This was due to the fact that the solar dark zone was not directly illuminated by sunlight and the solar photons from the solar illuminated zone were blocked by the catalyst and UV lamp. The solar photons reaching the solar dark zone decreased with an increase in catalyst loading. At the highest catalyst loading, very little solar photons could reach the dark zone; consequently, most of the illumination in the solar dark zone was provided by the UV lamp. This is clearly evident from the radial LRR profiles in the solar dark zone at a catalyst loading of 0.4 g/L

which shows similar LRR profiles in the annular UV lamp and hybrid light reactors (Figure 6.8b).

6.3.3 Optimum catalyst loading

Catalyst loading is one of the most critical parameters in evaluating the performance of a photoreactor since it affects hydrodynamics, irradiation, mass transfer and reaction kinetics. The optimum catalyst loading was investigated from the simulated reaction rate in the four reactor configurations (Figure 6.9a). For all reactor configurations, increasing the catalyst loading resulted in an increase in the overall reaction rate up to an optimal value beyond which any further increase in the catalyst loading resulted in only a marginal increase in the reaction rate. In this respect, the optimum catalyst loading in the tubular solar, annular solar, annular UV lamp and hybrid light reactors were found to be 0.15, 0.2, 0.4, and 0.4 g/L, respectively (Figure 6.9a). It should be noted that similar values were obtained using the VREA data in the annular UV lamp reactor (chapter 4) and tubular solar reactor (chapter 5). This further proves the hypothesis that VREA data can be used to predict the optimum catalyst loading without the need for photocatalysis experiments.

From the simulation studies, it was observed that the optimum catalyst loading in the annular solar reactor was higher than that in the tubular solar reactor. This can be attributed to better penetration of solar photons in the annular solar reactor. Also, the annular UV lamp reactor had a higher optimum catalyst loading as compared to the solar reactors. This was due to the higher light output from the UV lamp as compared to sunlight. The optimum catalyst loading in the annular UV lamp and hybrid light reactors were equal. In the hybrid light reactor, the influence of the UV lamp was much stronger than that of sunlight since UV lamp photons could penetrate deeper into the catalyst slurry. Therefore, the optimum catalyst loading was predominantly determined by the pathlength of UV lamp photons which explains the similar optimum catalyst loading in the two reactor configurations. Despite the similarity in the optimum catalyst loading in the two reactors, the reaction rate in the hybrid light reactor was much higher due to solar illumination. Solar illumination also markedly improved the reaction rate distribution in the hybrid light reactor.

In a photocatalytic reactor, an increase in the catalyst loading has been observed to increase the overall light absorption and decrease the light distribution (Valades-Pelayo et al., 2014). The conventional method of evaluating the optimum catalyst loading using the reaction rate or VREA, therefore, yields a value that maximizes the overall reaction rate or light absorption

without reference to the light distribution and catalyst utilization. At this optimum catalyst loading, it is often the case that a lot of the catalyst in the reactor are poorly irradiated and therefore wasted. This could present an opportunity for further optimization in cases where the cost of the catalyst far exceeds the photon cost. In such a situation, it would be necessary to consider the optimum catalyst loading with respect to the light distribution or the LRR distribution. Recently, Acosta-Herazo et al. (2020) proposed a new parameter, the energy absorption distribution index (EADI), which could be used to evaluate the highest catalyst loading that would ensure the best possible light distribution. The EADI was evaluated as:

$$EADI = \frac{VREA}{RSD_{LVREA}} \tag{6.8}$$

where the RSD_{VREA} is the relative standard deviation of the local volumetric rate of energy absorption (LVREA). In this work, an analogous parameter, the reaction rate distribution index (RRDI) is proposed. The RRDI is based on the LRR and is computed as:

$$RRDI = \frac{r}{RSD_{LRR}} \tag{6.9}$$

where r is the overall reaction rate and RSD_{LRR} is the relative standard deviation of the LRR.

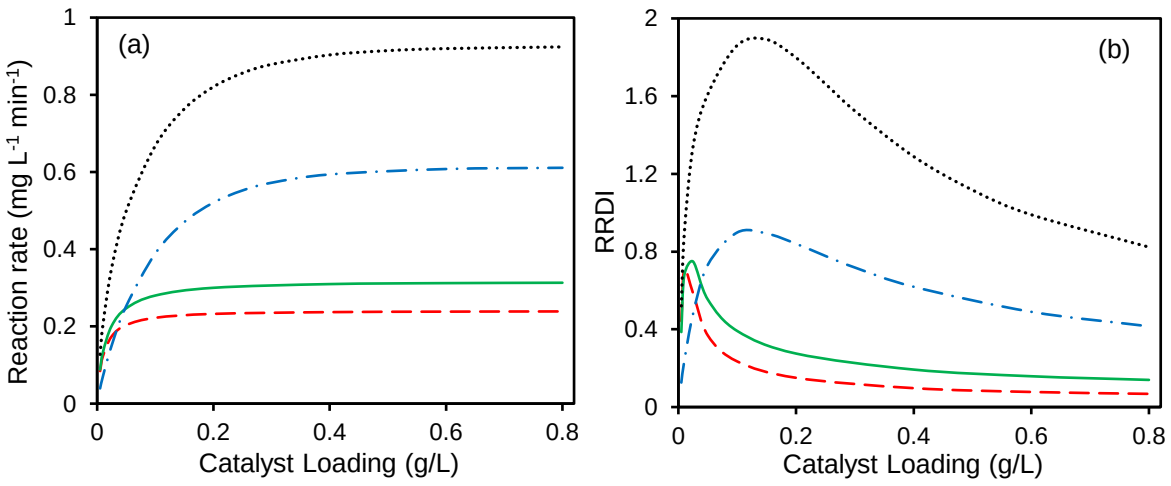

Figure 6.9: Effect of catalyst loading on the (a) overall reaction rate (b) RRDI in different reactor configurations. Tubular solar (– – –), Annular solar (——), Annular UV lamp (– · –), Hybrid light (·····).

A graph of RRDI vs catalyst loading reveals a distinct peak which identifies the optimum catalyst loading for the best reaction rate distribution. Based on the RRDI, the optimum catalyst loading in the tubular solar, annular solar, annular UV lamp and hybrid light reactor was found to be 0.01, 0.025, 0.1 and 0.15 g/L, respectively (Figure 6.9b). These values are significantly

lower than the optimum catalyst loading based on the overall reaction rate. This is expected since the lower catalyst loading would ensure a better light distribution. Higher values of the RRDI are indicative of better distribution in the LRR. In this respect, the annular solar reactor was observed to exhibit better LRR distribution than the tubular solar reactor. Furthermore, the UV lamp illuminated reactor had a better LRR distribution than the solar illuminated reactors, especially at catalyst loadings above 0.05 g/L. These observations reinforce similar findings from an evaluation of the LRR (section 6.3.2). The RRDI in the hybrid light reactor was much higher than the sum of the RRDI in the annular solar and annular UV lamp reactors. For example, at a catalyst loading of 0.15 g/L, the RRDI in the annular solar and annular UV lamp reactors were 0.315 and 0.893, respectively, with a combined value of 1.208. This was significantly lower than the RRDI of 1.892 in the hybrid light reactor at a catalyst loading of 0.15 g/L. This highlights the drastic improvement in the LRR distribution that was achieved by the hybrid light illumination.

6.4 Conclusion

In this chapter, previously developed Monte Carlo models were adapted for simulation of the light distribution in a hybrid solar/UV lamp photocatalytic reactor. The reaction order with respect to the VREA was found to be 0.75 and 0.74 under UV lamp and solar illumination, respectively. This showed that both first and half-order regimes existed in the reactor and that solar illumination resulted in a higher degree of electron-hole recombination than UV illumination. Illumination by the UV lamp resulted in a higher reaction rate as compared to solar illumination. The reaction rate under both light sources was generally higher than that under either solar or UV lamp illumination. A good fit between simulated and experimental reaction rate under hybrid light illumination was obtained which highlighted the accuracy of Monte Carlo simulation.

The optimum catalyst loading, based on the overall reaction rate, was found to be 0.15 g/L (tubular solar), 0.2 g/L (annular solar), 0.4 g/L (annular UV lamp), and 0.4 g/L (hybrid light). Using the reaction rate distribution index (RRDI), the optimum catalyst loading, based on the reaction rate distribution was found to be 0.01 g/L (tubular solar), 0.025 g/L (annular solar), 0.1 g/L (annular UV lamp), and 0.15 g/L (hybrid light). The radial reaction rate profiles showed a non-uniform distribution of the reaction rate which worsened with an increase in catalyst loading. In the hybrid light reactor, the regions nearest to the light sources had the highest reaction rate while the solar dark side had the lowest reaction rate. The local reaction rate (LRR) profiles and the RRDI in the different reactors revealed that the LRR distribution followed the

order: hybrid light > annular UV lamp > annular solar > tubular solar reactors. The RRDI also showed a drastic improvement in the LRR distribution due to hybrid light illumination.

This chapter highlighted the accuracy and reliability of the Monte Carlo method for simulating the reaction rate profiles in a hybrid solar/UV lamp reactor. Illumination by the UV lamp resulted in a higher reaction rate as compared to solar illumination, and this showed that the UV lamp could be used to supplement the solar energy. As a result, the Monte Carlo model can be used to design the lamp controller for adjusting the output of the UV lamp in response to changes in the solar intensity, which is the subject of the next chapter.

References

Acosta-Herazo, R., Valadés-Pelayo, P. J., Mueses, M. A., Pinzón-Cárdenas, M. H., Arancibia-Bulnes, C., and Machuca-Martínez, F., 2020. An optical and energy absorption analysis of the solar compound parabolic collector photoreactor (CPCP): The impact of the radiation distribution on its optimization. *Chemical Engineering Journal, 395,* 125065.

Apollo, S., and Aoyi, O., 2016. Combined anaerobic digestion and photocatalytic treatment of distillery effluent in fluidized bed reactors focusing on energy conservation. *Environmental Technology, 37*(17), 2243–2251.

Boyjoo, Y., Ang, M., and Pareek, V., 2013. Some aspects of photocatalytic reactor modeling using computational fluid dynamics. *Chemical Engineering Science, 101,* 764–784.

Carbajo, J., Tolosana-Moranchel, A., Casas, J.A., Faraldos, M. and Bahamonde, A., 2018. Analysis of photoefficiency in TiO2 aqueous suspensions: Effect of titania hydrodynamic particle size and catalyst loading on their optical properties. *Applied Catalysis B: Environmental*, *221*, 1-8.

Durán, A., Monteagudo, J. M., San Martín, I. and Merino, S., 2018. Photocatalytic degradation of aniline using an autonomous rotating drum reactor with both solar and UV-C artificial radiation. *Journal of Environmental Management*, *210*, 122-130.

Joseph, C. G., Taufiq-Yap, Y. H., Li Puma, G., Sanmugam, K., and Quek, K. S., 2016. Photocatalytic degradation of cationic dye simulated wastewater using four radiation sources, UVA, UVB, UVC and solar lamp of identical power output. *Desalination and Water Treatment*, *57*(17), 7976–7987.

Li Puma, G., Khor, J. N., and Brucato, A., 2004. Modeling of an Annular Photocatalytic Reactor for Water Purification: Oxidation of Pesticides. *Environmental Science & Technology*, *38*(13), 3737–3745.

Li Puma, G., Puddu, V., Tsang, H. K., Gora, A., and Toepfer, B., 2010. Photocatalytic

oxidation of multicomponent mixtures of estrogens (estrone (E1), 17β-estradiol (E2), 17α-ethynylestradiol (EE2) and estriol (E3)) under UVA and UVC radiation: Photon absorption, quantum yields and rate constants independent of photon absorption. *Applied Catalysis B: Environmental*, *99*(3–4), 388–397.

Moreira, J., Serrano, B., Ortiz, A., and de Lasa, H., 2010. Evaluation of photon absorption in an aqueous TiO_2 slurry reactor using Monte Carlo simulations and macroscopic balance. *Industrial & Engineering Chemistry Research*, *49*(21), 10524–10534.

Orozco, S. L., Arancibia-Bulnes, C. A., and Suárez-Parra, R., 2009. Radiation absorption and degradation of an azo dye in a hybrid photocatalytic reactor. *Chemical Engineering Science*, *64*(9), 2173–2185.

Schott., n.d. *Schott tubing bronchure*. Retrieved July 13, 2020, from https://www.schott.com/d/tubing/9d60ae04-a9db-4b63-82b3-7aebd5bad71e/1.6/schott-tubing_brochure_duran_english-en.pdf

Valades-Pelayo, P. J., Moreira, J., Serrano, B., and De Lasa, H., 2014. Boundary conditions and phase functions in a Photo-CREC Water II reactor radiation field. *Chemical Engineering Science*, *107*, 123–136.

Chapter 7

7 Design of a UV lamp output controller for hybrid light photocatalysis

7.1 Introduction

Conventional photocatalysis has been carried out using UV lamps. The cost of running the UV lamps contribute significantly to the cost of photocatalysis. As a result, alternative light sources such as sunlight have been proposed (Malato et al., 2009). Solar energy is desirable for photocatalysis since it is free, renewable and contains UV light. However, sunlight is a very unpredictable source of energy as it varies by cloud cover, time of day, region and seasons (Natarajan et al., 2011). One way of addressing these challenges, while keeping costs low, would be supplementing sunlight with an artificial light source when the solar intensity reduces. Such a hybrid light system has been developed for gas-phase photocatalytic reactors in which black light UV lamps were used as the artificial light source (Portela et al., 2011; Portela et al., 2012; Monteiro et al., 2015).

These gas-phase hybrid light reactors were equipped with an ON/OFF control scheme in which the reactors were illuminated by sunlight during the day with the lamp being switched on at night (Portela et al., 2011; Portela et al., 2012). Such a system could potentially be costly without addressing the daytime variation in the solar intensity. A better control scheme would incorporate a real-time lamp controller to continuously adjust the lamp intensity in response to the current solar intensity. Such a system has not been reported in literature. In this chapter, the design of a UV lamp output controller that can be used for hybrid light photocatalysis was described. A representative solar data was collected on a clear day and used to design and demonstrate the operation of the lamp controller. For the design, the reaction rate data and Monte Carlo model from chapter 6 was employed. The aim of this chapter was to design a lamp controller for hybrid light photocatalysis.

7.2 Methodology

7.2.1 Monte Carlo method

The light distribution was simulated in the annular UV, annular solar and hybrid light reactor according to the Monte Carlo methods developed in Chapter 4, Chapter 5 and Chapter 6, respectively. The photon flight through the reactor was tracked from the light source until the photon was either absorbed by the catalyst, lamp sleeve, wall or went beyond the reactor boundaries. The total light absorbed by the catalyst, the volumetric rate of energy absorption

(VREA) was evaluated and employed as a parameter to calculate the rate of reaction in each of the three reactors.

7.2.2 Solar radiation measurement

Solar intensity can be characterized by several parameters. In this work, two measurements were taken with a radiometer and the rest estimated from mathematical correlations. The global horizontal irradiance (GHI) refers to the global (direct and diffuse) solar intensity incident on a horizontal surface. It was measured by mounting the radiometer sensor on a spirit level which was then carefully aligned to the horizontal plane. The global tilt irradiance (GTI) is the global solar intensity which is incident on any plane tilted from the horizontal. In this work, the GTI was measured by aligning the radiometer sensor to the vertical plane on which the reactor was positioned.

The GHI and GTI were measured from 8:00 am to 4:00 pm on a clear day in Vanderbijlpark, South Africa (GPS coordinates: 26.7034° S, 27.8077° E). The measurements were taken using a calibrated spectroradiometer (Stellarnet, Black Comet SR) which was connected to the CR2 cosine sensor by a fibre optic cable. Using the GHI, GTI and the solar zenith angle, the global normal irradiance (GNI) was calculated using the correlations in chapter 5 provided by Duffie and Beckman (2013). The GNI is the incident global solar radiation normal to the surface of the vertical reactor. This parameter was chosen as it encapsulates all the parameters of solar irradiance in one number while taking into account the direct and diffuse solar radiation as well as the solar zenith angle.

7.3 Results and discussion

7.3.1 Solar intensity measurement

The solar intensity was characterized by the measured global horizontal irradiance (GHI) and the global tilt irradiance (GTI) and a calculated global normal irradiance (GNI). From Figure 7.1, it can be observed that the GHI increased gradually from morning hours and peaked at midday before reducing as the day progressed. The GTI also increased from morning hours and peaked at around 10:00 am after which it reduced to its lowest level at 1:00 pm before rising slightly and then dropping off during the afternoon. This trend is typical of the irradiance on a tilted surface, in which, as the sun rises high in the sky, the GTI measured on the surface reduces.

The GNI increased during the morning hours and peaked at noon, after which it reduced as the day progressed. This trend approximately followed that of the GHI but was modulated a little

by the GTI. This is expected since the GNI was calculated from the GHI, GTI and the solar zenith angle. Figure 7.1 also shows lower values of GHI, GTI and GNI readings in the afternoon as compared to corresponding hours in the morning. Although clear skies were observed during the whole day, it is possible that during the afternoon, the atmospheric water vapour increased which absorbed and diffused the sunlight resulting in a reduction in the recorded solar intensity.

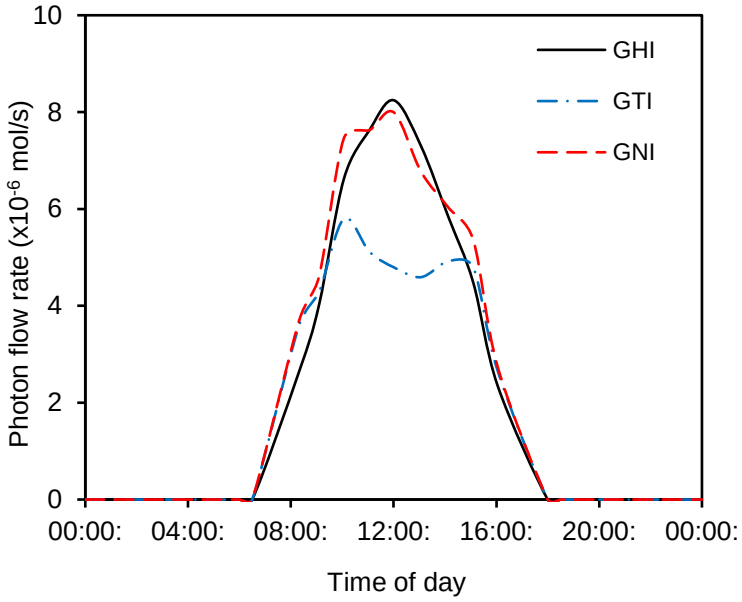

Figure 7.1: Global Horizontal Irradiance, Global Tilt Irradiance and Global Normal Irradiance at different times of the day

7.3.2 Effect of time of day on light absorption

In the previous section, it was shown that the solar light intensity incident on the reactor changes throughout the day. It is also necessary to determine the effect of the changing solar intensity on the light absorption as characterized by the volumetric rate of energy absorption (VREA). The VREA is a crucial parameter as it is commonly used to determine the intrinsic reaction rate. Before evaluating the light absorption, the operating catalyst loading needs to be evaluated. During hybrid light photocatalysis, it is expected that the catalyst loading will be kept constant while adjusting the lamp output. Since sunlight is the primary light source, the operating catalyst loading should be chosen as the optimum catalyst loading under solar illumination. In chapter 6, the optimum catalyst loading under solar illumination in the annular reactor was found to be 0.2 g/L. Using this optimum catalyst loading, Monte Carlo simulations were carried out to evaluate the VREA at different hours of the day.

The results (Figure 7.2) shows almost identical graphs of the GNI and VREA. This is due to the fact that, at the high catalyst loading of 0.2 g/L used in the simulation, almost all the photons were absorbed by the catalyst as clearly shown in Figure 6.9a. Therefore, the absorbed light (VREA) was proportional to the solar intensity (GNI). For hybrid light photocatalysis, this observation raises several possibilities. The VREA is computationally expensive to determine using Monte Carlo simulation and would require very fast and costly computers to calculate in real-time. It would be much more desirable to replace VREA with the GNI in the reaction rate equation. This approach would be advantageous as it would enable near real-time adjusting of the UV lamp output as a function of the incident solar intensity without the need to compute the VREA. Furthermore, since there would be no need to compute the VREA, the overall cost of the hybrid light controller hardware would be much lower.

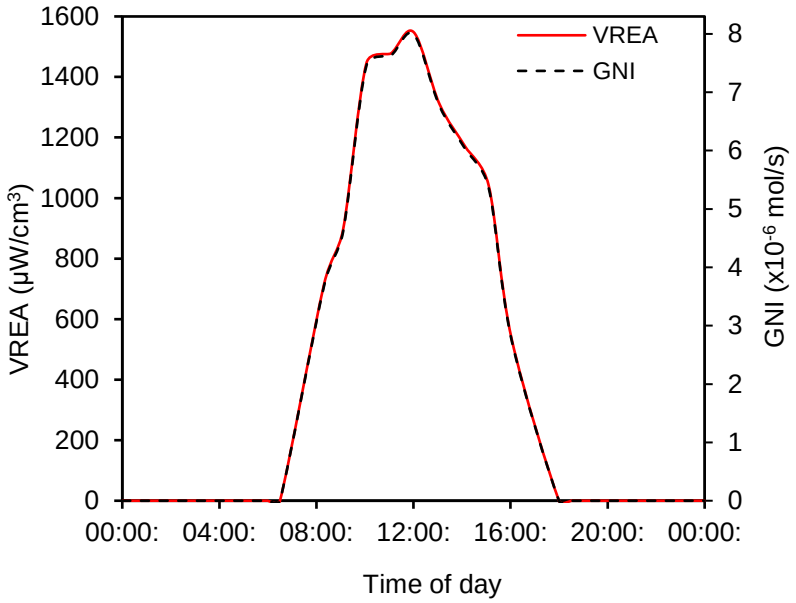

Figure 7.2: VREA and photon flow rate at different times of the day

7.3.3 Lamp output controller design

The solar reaction rate ($-r_{solar}$) as a function of the GNI ($G_{i,n}$) can be adapted from equation (6.4 – 6.6) as:

$$-r_{solar} = k_{int,solar}\left(k_{VREA}G_{i,n}\right)^{\alpha_{solar}}C \tag{7.1}$$

where k_{VREA} is a multiplication factor such that:

$$VREA = k_{VREA}G_{i,n} \tag{7.2}$$

From linear regression, the value of k_{VREA} was found to be 1.94E+8 µW.s/(cm^3.mol) with an R^2 value of 1.0 (Figure 7.3). The perfect linear fit between the VREA and GNI further proves that, at the catalyst loading of 0.2 g/L, almost all solar photons were absorbed in the reactor.

The rate of reaction at different catalyst loadings, under solar illumination, was carried out in chapter 6. Using Monte Carlo simulation and the experimental data, the rate of reaction at a catalyst loading of 0.2 g/L was determined as 0.3 mg L^{-1} min^{-1}. This value was specified as the reference reaction rate. The aim of hybrid light photocatalysis was then to maintain the rate of photocatalysis at the reference level, irrespective of the solar intensity. Consequently, the UV lamp output would be adjusted as required to maintain the rate of reaction at the reference value. As was shown in Chapter 6, the rate of reaction is additive. Therefore, a simple formula was employed to determine the additional rate of reaction due to the UV lamp (r_{UV}) which would be required to achieve the reference reaction rate ($r_{reference}$):

$$r_{UV} = r_{reference} - r_{solar} \tag{7.3}$$

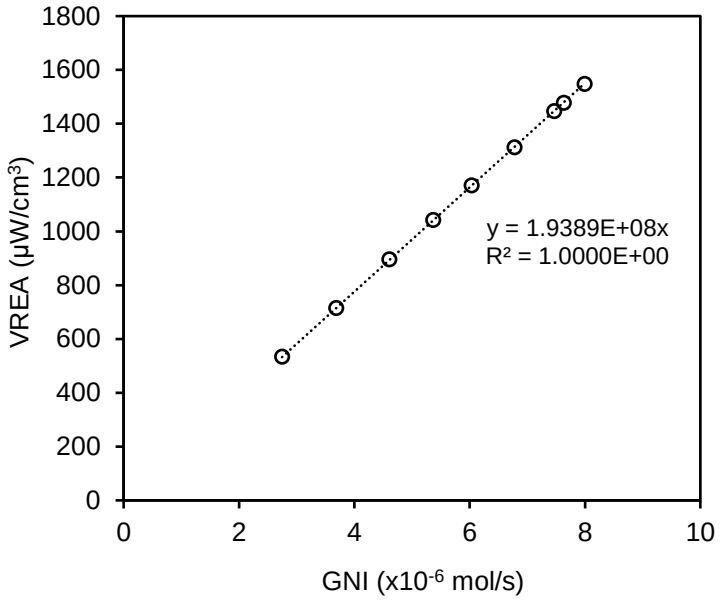

Figure 7.3: Linear regression of VREA with photon flow rate

The VREA due to the UV lamp is proportional to the UV lamp intensity which is proportional to the percentage lamp output. Therefore, the additional reaction rate due to the UV lamp, can be evaluated by modifying equation (6.4 – 6.6) as:

$$-r_{UV} = k_{int,UV}(I_{UV}VREA_{UV})^{\alpha_{UV}}C \tag{7.4}$$

where I_{UV} is the percentage lamp output. Using equations (7.1 – 7.4), the lamp output (I_{UV}) could be adjusted as a function of the GNI to maintain the overall reaction rate at the reference.

7.3.4 Hybrid light photocatalysis

This work envisions a hybrid light system with a continuous single-pass flow of the wastewater through the reactor. In this scheme, the wastewater flow rate is set such that the discharge limit would be achieved at the reference reaction rate. Adjusting the lamp output in real-time to compensate for any drop in the solar intensity would ensure that the discharge limit is always

achieved with a fixed phenol concentration in the effluent. Figure 7.4 shows the lamp output that would be required to maintain the overall reaction rate at the reference level. At midday, the required lamp output would be 0.25%. This value would increase gradually towards the night on either side of midday up to a maximum of 55% at night. The lower lamp output at night was due to the higher intensity of the UV lamp as compared to sunlight (Figure 6.5).

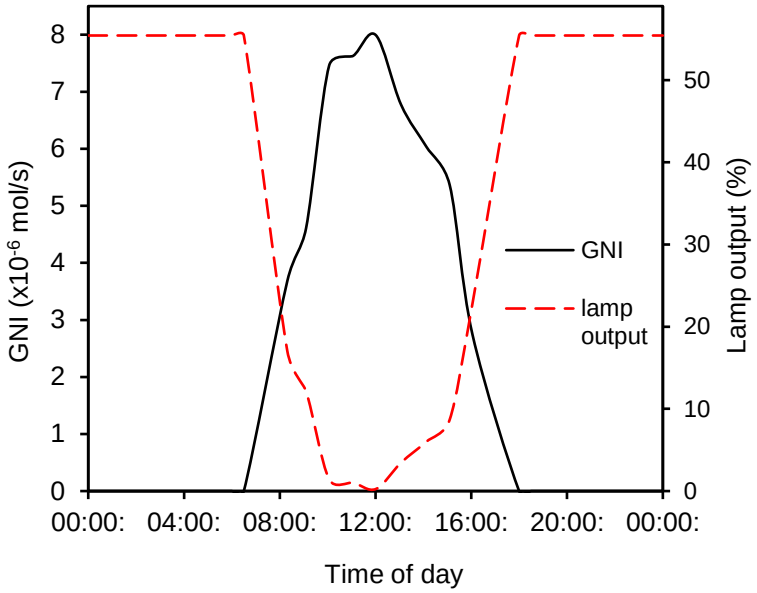

Figure 7.4: The lamp output at different photon flow rates

This hybrid light system is more effective than the one employed by Portela et al. (2012) in which an ON/OFF control scheme was used to switch on the UV lamp at 100% output at night while switching off the lamp during the day. Since the lamp was only operated at night, Portela et al. (2012) experienced variation in the effluent concentration of H_2S during the day as a result of variations in the solar intensity. If a similar ON/OFF controller was used in this work, a significant variation in the phenol reaction rate would be observed as shown in Figure 7.5.

At night, the ON/OFF controller resulted in a high and constant reaction rate of 0.45 mg L^{-1} min^{-1}. However, during the day, the reaction rate fluctuated from 0.15 mg L^{-1} min^{-1} at 16:00 hrs to 0.31 mg L^{-1} min^{-1} at midday. This contrasts with the hybrid controller in which a uniform reaction rate of 0.3 mg L^{-1} min^{-1} could be maintained by continuously adjusting the lamp output in response to a change in the incident solar intensity. Therefore, the hybrid light controller was superior to the ON/OFF controller in terms of effectiveness in eliminating variations in the reaction rate and subsequent effluent concentration.

A comparison of the electric energy consumption of the lamp under the hybrid controller vs the ON/OFF controller like the one reported by Portela et al. (2012) was made. It was found that the hybrid lamp controller and the ON/OFF controller would result in 3.9 kWh and 6.5kWh

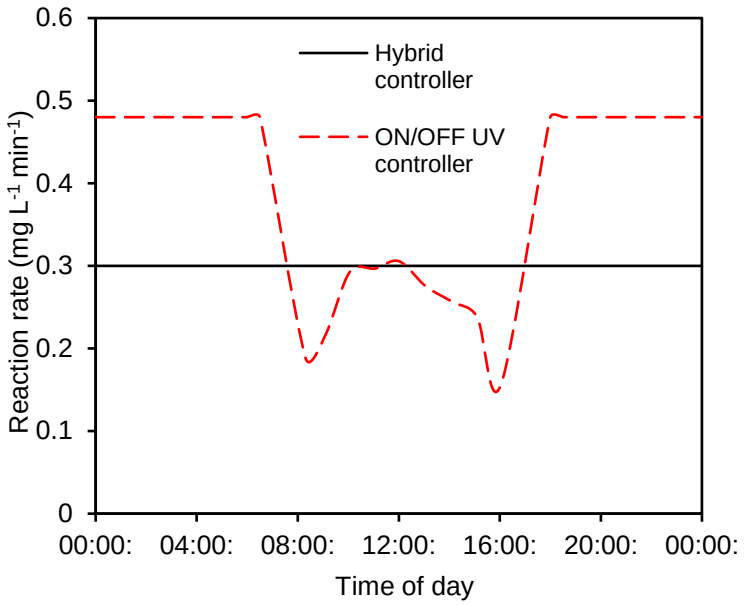

Figure 7.5: Reaction rate under hybrid and ON/OFF lamp controller

of energy consumed by the lamp, respectively (Figure 7.6). This represents a cost savings of 40% with the hybrid lamp controller over the ON/OFF controller. The lower energy consumption under hybrid light control can be attributed to the fact that, at night, the lamp would be switched on at only 55% of its full output with a corresponding reduction in its power consumption. In contrast, although the ON/OFF controller switched off the lamp during the day, it would switch on the lamp to its full output at night. With such a huge cost savings, investing in the miscellaneous hardware for the hybrid lamp controller is expected to be cost effective in the long run.

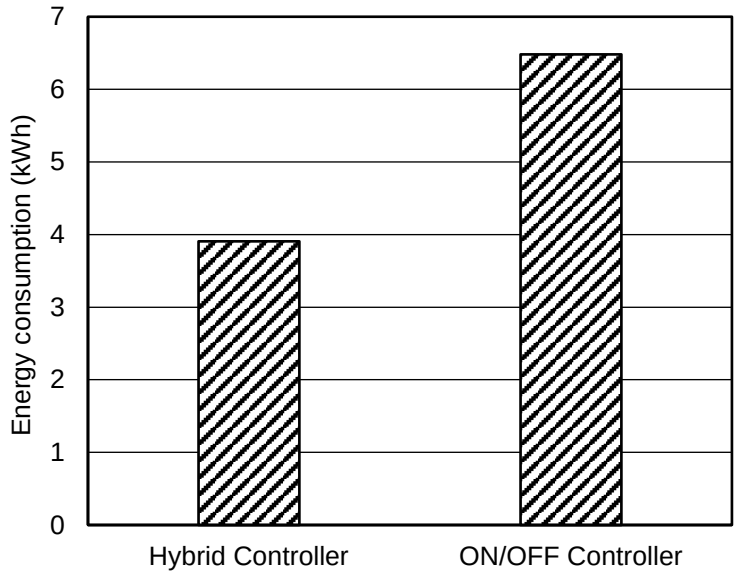

Figure 7.6: Energy consumption of the lamp under hybrid and ON/OFF controller

7.3.5 Economic analysis

The cost of electricity for running the UV lamps represents a major portion of the total operating cost of photocatalysis. In order to compare the cost associated with different photocatalytic reactors, a figure-of-merit, the electrical energy per order (EEO), is often employed (Vishnuganth et al., 2016):

$$EEO = \frac{38.4 \times P_0}{V \times k_{app}} \tag{7.4}$$

where P_0 is the average power consumption, V is the volume of the wastewater, k_{app} is the apparent first order rate constant. Table 7.1 shows the EEO of phenol photocatalysis under UV lamp illumination, hybrid illumination with an on/off controller and hybrid light illumination with the hybrid controller. Average values of hourly P_0 and k_{app} were used in the calculations for the hybrid light systems. The results show that using hybrid light instead of pure UV lamp reduced the EEO by 23% for the on/off controller and 40% for the hybrid controller. This was due to the fact that, during the day, the hybrid light systems used free sunlight to illuminate the reactor.

Table 7.1: Electrical Energy per Order of different illumination sources

Light source	P_0 (kW)	V (L)	$k_{app}(\text{min}^{-1})$	EEO (kWh m^{-3} order^{-1})
UV lamp	0.018	1.25	0.0096	57.6
Hybrid (on/off controller)	0.0113	1.25	0.00786	44.16
Hybrid (hybrid controller)	0.0678	1.25	0.006	34.71

7.4 Conclusion

In this chapter, a procedure for designing the hybrid lamp controller was shown. First, the hourly solar intensity for a representative day was recorded. It was found that, at the optimum catalyst of 0.2 g/L, the graph for light absorption and the global normal irradiation (GNI) were similar as almost all the incident light was absorbed. Therefore, instead of directly computing the volumetric rate of energy absorption (VREA), the GNI could be used to estimate the reaction rate under sunlight. A simple correlation could then be used to relate the required lamp output as a function of the GNI. Such a correlation would be more suitable for real-time control as it would be much faster than Monte Carlo computations with the additional advantage of lowering the cost of the controller hardware. The resulting hybrid light controller was found to be more effective in maintaining the effluent discharge limit with a much less lamp energy consumption as compared to the ON/OFF controller. Furthermore, the EEO of the hybrid light

reactor was 40% lower than that of the UV lamp reactor. Therefore, hybrid light photocatalysis is a promising method of carrying out photocatalysis efficiently at a low cost.

References

Duffie, J.A. and Beckman, W.A., 2013. Solar engineering of thermal processes 4th Edition. New York: Wiley

Malato, S., Fernández-Ibáñez, P., Maldonado, M., Blanco, J. and Gernjak, W., 2009. Decontamination and disinfection of water by solar photocatalysis: Recent overview and trends, *Catalysis Today*, *147*(1), 1-59.

Monteiro, R.A., Rodrigues-Silva, C., Lopes, F.V., Silva, A.M., Boaventura, R.A. and Vilar, V.J., 2015. Evaluation of a solar/UV annular pilot scale reactor for 24 h continuous photocatalytic oxidation of n-decane. *Chemical Engineering Journal*, *280*, 409-416

Natarajan, T.S., Thomas, M., Natarajan, K., Bajaj, H.C. and Tayade, R.J., 2011. Study on UV-LED/TiO_2 process for degradation of Rhodamine B dye. *Chemical Engineering Journal, 169*(1–3), 126-134.

Portela, R., Suárez, S., Tessinari, R.F., Hernández-Alonso, M.D., Canela, M.C. and Sánchez, B., 2011. Solar/lamp-irradiated tubular photoreactor for air treatment with transparent supported photocatalysts. *Applied Catalysis B: Environmental*, *105*(1-2), 95-102.

Portela, R., Tessinari, R., Suarez, S., Rasmussen, S., Hernandez-Alonso, M., Canela, M., Avila, P. and Sanchez, B., 2012. Photocatalysis for continuous air purification in wastewater treatment plants: from lab to reality. *Environmental Science & Technology*, *46*(9), 5040-5048.

Vishnuganth, M.A., Remya, N., Kumar, M. and Selvaraju, N., 2016. Photocatalytic degradation of carbofuran by TiO_2-coated activated carbon: model for kinetic, electrical energy per order and economic analysis. *Journal of Environmental Management*, *181*, 201-207.

Chapter 8

8 Conclusion and recommendations

8.1 Conclusion

In this study, a fluidized bed reactor was designed for solar/UV lamp photocatalysis of phenol. The hydrodynamics, light distribution and reaction kinetics in the reactor were simulated. Then, this data was used to design a UV lamp controller which could be used for photocatalysis of phenol throughout the day and night irrespective of solar intensity. In order to carry out the hydrodynamics of the fluidized bed reactor, the CFD model was validated using data from a bubble column reactor. The bubble column model showed that simulating a full reactor using the Reynolds stress model (RSM) and a combination of drag, lift, wall lubrication and turbulent dispersion forces was the most accurate approach. The bubble column CFD model was modified by adding the solid phase and then it was used to model the annular fluidized bed reactor. The simulation revealed a slight increase in the catalyst loading near the reactor walls which would result in an increased light absorption during photocatalysis. Nevertheless, the catalyst distribution in the reactor was found to be fairly uniform. Consequently, simulation of the hydrodynamics in the fluidized bed reactor could be neglected so that the focus be on the light distribution and reaction kinetics.

The light distribution in the reactor under UV lamp, solar and hybrid light illumination was analysed using the Monte Carlo model. The model was validated using total transmitted radiation (TTR) and total refracted radiation (TRR) measurements at the wall of the reactor under UV lamp and solar illumination, respectively. Validation of the solar illuminated reactor using the TRR, which was based on the refraction of light through the reactor, was a novel validation method developed in this study. Very good agreement between the experimental and measured TTR/TRR values was observed in both the annular UV and tubular solar reactors. The Aeroxide P25 TiO_2 catalyst was confirmed to exhibit forward scattering behaviour with a Henyey-Greenstein scattering parameter of 0.84 and 0.87 under UV lamp and solar illumination, respectively. An increase in catalyst loading was observed to markedly reduce the light transmission through the reactor. In the UV lamp illuminated reactor, the Monte Carlo model was found to be more accurate than the six-flux model as it could better represent the lamp emission. It was shown that bubbles affected the transmission of sunlight more than that of UV light.

For the UV lamp and solar illuminated reactors, the local volumetric rate of energy absorption (LVREA) profiles were analysed. The results revealed a fairly uniform axial light distribution profiles while the radial light distribution profiles were highly non-uniform, and this worsened with an increase in catalyst loading. A similar trend was observed for the radial local reaction rate profiles in the hybrid light reactor. The optimum catalyst loading, based on the simulated reaction rate, was found to be 0.15 g/L (tubular solar), 0.2 g/L (annular solar), 0.4 g/L (annular UV lamp), and 0.4 g/L (hybrid light). Similar values were obtained using only the volumetric rate of energy absorption (VREA), and this shows that the optimum catalyst loading could be estimated from Monte Carlo simulation without running photocatalysis experiments. At these optimum catalyst loadings, the effect of bubbles on the light absorption was found to be negligible. This further proved the finding that hydrodynamics could be neglected in the simulation and accurate Monte Carlo simulation could be achieved without accounting for bubble-photon interactions. This study showed that air was a good fluidization method as it achieved good catalyst mixing and provided oxygen electron acceptor without negatively impacting light absorption.

The reaction order with respect to the VREA was found to be 0.75 and 0.74 under UV lamp and solar illumination, respectively. This showed that both first and half-order regimes existed in the reactor and that solar illumination resulted in a higher degree of electron-hole recombination. Illumination by the UV lamp resulted in a higher reaction rate as compared to solar illumination, and this showed that the UV lamp could be used to supplement the solar energy. For a typical sunny day, the graph of light absorption and the global normal irradiation (GNI) were similar. Therefore, instead of directly computing the VREA, the GNI could be used to estimate the reaction rate under solar illumination. A simple correlation could then be used to relate the required lamp output as a function of the GNI. Such a correlation would be more suitable for real-time control as it would be much faster than Monte Carlo computations with the additional advantage of lowering the cost of the controller hardware. The resulting hybrid light controller was found to be more effective in maintaining the effluent discharge limit with a much less lamp energy consumption as compared to an ON/OFF controller. Compared to the UV lamp reactor, the hybrid light reactor had a 40% lower electrical energy per order (EEO). This shows that hybrid light photocatalysis is a promising method of carrying out photocatalysis efficiently at a low cost.

Recalcitrant wastes such as phenols have been shown to be toxic and persistent in the environment. Their removal from wastewaters before discharge is crucial to sustainable

manufacturing. Photocatalysis has been found to be a very versatile method of treating such wastes at the tertiary stage of wastewater treatment. However, its commercialization has been limited due to the high electricity cost associated with running UV lamps. Reducing this cost by employing sunlight has resulted in an unreliable source of light. These drawbacks were addressed by the hybrid UV/lamp fluidized bed reactor developed in this work which could drastically reduce the cost of photocatalysis. This has the potential to make photocatalysis commercially viable and a candidate for the elimination of recalcitrant wastes from the environment.

8.2 Recommendations

In the hydrodynamics analysis, the gas-liquid-solid hydrodynamics in the fluidized bed reactor was simulated using a CFD model which was validated from a bubble column reactor. The two reactors had different phases, geometry and configuration. Therefore, the three phase CFD model may not have yielded the best accuracy. A more accurate model would have been obtained if validation data was available for a similar reactor. The annular fluidized bed has been used widely for photocatalysis. Considering how popular this reactor is, it is recommended that future studies should determine the experimental hydrodynamics data for this reactor. This would provide the foundation for a robust and rigorous analysis of the hydrodynamics in such a reactor using simulation tools like CFD.

The Monte Carlo model for the solar illuminated reactor required the diffuse fraction as a parameter. An approximation of the diffuse fraction was made using correlations and measurements of the global horizontal and global tilt irradiance data. This method was found to be fairly accurate. However, it contributed to some inaccuracy in the Monte Carlo model such that the experimental and measured total refracted radiation (TRR) was not a perfect match. This error could have arisen from the choice of the diffuse fraction correlation which was based on Australian data in the visible solar band. Although many correlations in the visible band has been developed at several locations globally, a similar correlation for the UV diffuse fraction has not been developed. A future research area should focus on developing such correlations to be used in modelling photoreactors.

The light transmission in the hybrid solar/UV lamp reactor was not validated with both light sources. This was due to difficulties in locating the point of convergence of the refracted photons. An alternative methodology was used to validate the Monte Carlo algorithm by assuming that light sources are additive. This assumption was later proved to be valid as the

Monte Carlo method predicted the reaction rate fairly accurately. The hybrid light reactor was validated by measuring the transmission of both light sources separately. However, an even more accurate Monte Carlo model could have been possible if the light transmission was measured in the presence of both light sources. This could be carried out using a wide aperture light collector such as an integrating tube. It is recommended that future studies should develop such a validation method.

In this work, the reactor was illuminated internally by a mercury UV lamp and externally by sunlight on one side. Considering the high energy consumption of the mercury UV lamp, an alternative low energy lamp such as the UV LED could be used. Also, it was also observed that one side of the reactor was poorly illuminated by sunlight. This could have been improved by the use of a reflector such as the compound parabolic concentrator (CPC). The use of such illumination systems was outside the scope of this work. Due to their advantages, future studies should develop such a hybrid UV LED/solar CPC reactor.

This work focused on the use of modelling and simulation to design the hybrid solar/UV lamp reactor. The UV lamp controller was designed and expected results under 24 hours operation was shown. The Monte Carlo model was validated throughout so the accuracy of the results could be assured. For practical purposes, it would be necessary to use these results to run a hybrid light reactor for several days. This would shine light on some operational issues that may not have been captured by the models. It is recommended that future studies should carry out a pilot study on hybrid light photocalysis.

Appendix A

Table A1: Drag Coefficients

Drag coefficient model	Reference
$C_D = \frac{24}{\mathrm{Re}_b}\left(1 + 0.15\,\mathrm{Re}_b^{0.687}\right), \quad \text{if} \quad \mathrm{Re}_b < 1000$ $C_D = 0.44, \quad \text{if} \quad \mathrm{Re}_b > 1000$	Schiller and Nauman (1935)
$C_D = \left(0.63 + \frac{4.8}{\sqrt{\mathrm{Re}_b}}\right)^2$	Dalla Ville (1948)
$C_D = \frac{4}{3}\frac{\mathrm{g}d_b}{V_T^2}\frac{(\rho_L - \rho_G)}{\rho_L}$	Grace et al. (1976)
$C_D = \frac{2}{3}Eo^{0.5}$	Ishii and Zuber (1979)
$C_D = \frac{24}{\mathrm{Re}_b}\left(1 + 0.1\,\mathrm{Re}_b^{0.75}\right)$	Ma and Ahmadi (1990)
$C_D = 0.44 + \frac{24}{\mathrm{Re}_b} + \frac{6}{1+\sqrt{\mathrm{Re}_b}}$	Zhang and Vanderheyden (2002)

Table A2: Lift coefficients

Lift coefficient model	Reference
$C_L = \begin{cases} \min[0.288\tanh(0.121\mathrm{Re}_b), f(Eo_d)] & Eo_d < 4 \\ f(Eo_d) & 4 \le Eo_d \le 10.7 \end{cases}$ $Eo_d = \frac{\mathrm{g}\left(\rho_\mathrm{f} - \rho_\mathrm{g}\right)d_H^2}{\sigma}$ $f(Eo_d) = 0.00105Eo_d^3 - 0.0159Eo_d^2 - 0.0204Eo_d + 0.474$ $d_H = d_b(1 + 0.163\,Eo^{0.757})$	Tomiyama et al. (2002)
$C_L = k\sqrt{\left\{C_L^{lowRe}(\mathrm{Re}_b, Sr_b)\right\}^2 + \left\{C_L^{highRe}(\mathrm{Re}_b)\right\}^2}$ $C_L^{lowRe}(\mathrm{Re}_b, Sr_b) = \frac{6}{\pi^2}(\mathrm{Re}_b \cdot Sr_b)^{-0.5}\left[\frac{2.255}{(1+0.2\varepsilon^{-2})^{1.5}}\right]$ $C_L^{highRe}(\mathrm{Re}_b) = \frac{1}{2}\left(\frac{1 + 16/\mathrm{Re}_b}{1 + 29/\mathrm{Re}_b}\right)$ $k = 2 - \exp\left(2.92d_b^{2.21}\right)$	Legendre and Magnaudet (1998)

Table A3: Wall lubrication coefficients

Wall lubrication coefficient model	Reference
$C_{WL} = \max\left\{0, \frac{C_{W1}}{d_b} + \frac{C_{W2}}{y_w}\right\}$ $C_{W1} = -0.01, C_{W2} = 0.05$	Antal et al. (1991)
$C_{WL} = C_W(E_o)\frac{d_b}{2}\left(\frac{1}{y_w^2} - \frac{1}{(D-y_w)^2}\right)$ $C_W(E_o) = \begin{cases} 0.47 & E_o < 1 \\ \exp(-0.933E_o + 0.179) & 1 \le E_o \le 5 \\ 0.00599E_o + 0.0187 & 5 \le E_o \le 33 \\ 0.179 & E_o > 33 \end{cases}$	Tomiyama et al. (2002)
$C_{WL} = C_W(E_o) \cdot \max\left\{0, \frac{1}{C_{WD}} \cdot \frac{1 - \frac{y_w}{C_{WC}d_b}}{y_w \cdot \left[\frac{y_w}{C_{WC}d_b}\right]^{p-1}}\right\}$ $C_{WC} = 10, C_{WD} = 6.8, p = 1.7$	Frank et al. (2004)

Table A4: Lamp emission models (Boyjoo et al., 2014b)

Model	Equation
line source specular emission (LSSE)	$E = \frac{K_l}{4\pi}\int_{-L}^{L}\frac{dh}{(r^2 + (z-h)^2)}$ $E = \frac{K_l}{4\pi r}\left[\tan^{-1}\left(\frac{z+L}{r}\right) - \tan^{-1}\left(\frac{z-L}{r}\right)\right]$
line source diffuse emission (LSDE)	$E = \frac{K_l}{4\pi}\int_{-L}^{L}\frac{r dh}{[r^2 + (z-h)^2]^{3/2}}$
surface source specular emission (SSSE)	$E = \frac{K_s}{4\pi}\int_{-L}^{L}\int_{-\pi/2}^{\pi/2}\frac{R\, d\phi\, dh}{[(\mathrm{r}\cos\theta - R\cos\phi)^2 + (\mathrm{r}\sin\theta - R\sin\phi)^2 + (z-h)^2]}$
surface source diffuse emission (SSDE)	$E = \frac{K_s}{4\pi}\int_{-L}^{L}\int_{-\pi/2}^{\pi/2}\frac{\cos\varphi\, R\, d\phi\, dh}{[(\mathrm{r}\cos\theta - R\cos\phi)^2 + (\mathrm{r}\sin\theta - R\sin\phi)^2 + (z-h)^2]}$
volume source emission (VSE)	$E = \frac{K_V}{4\pi}\int_{-L}^{L}\int_{0}^{R}\int_{-\pi}^{\pi}\frac{\eta\, d\eta\, d\phi\, dh}{[(\mathrm{r}\cos\theta - \eta\cos\phi)^2 + (\mathrm{r}\sin\theta - \eta\sin\phi)^2 + (z-h)^2]}$

Appendix B

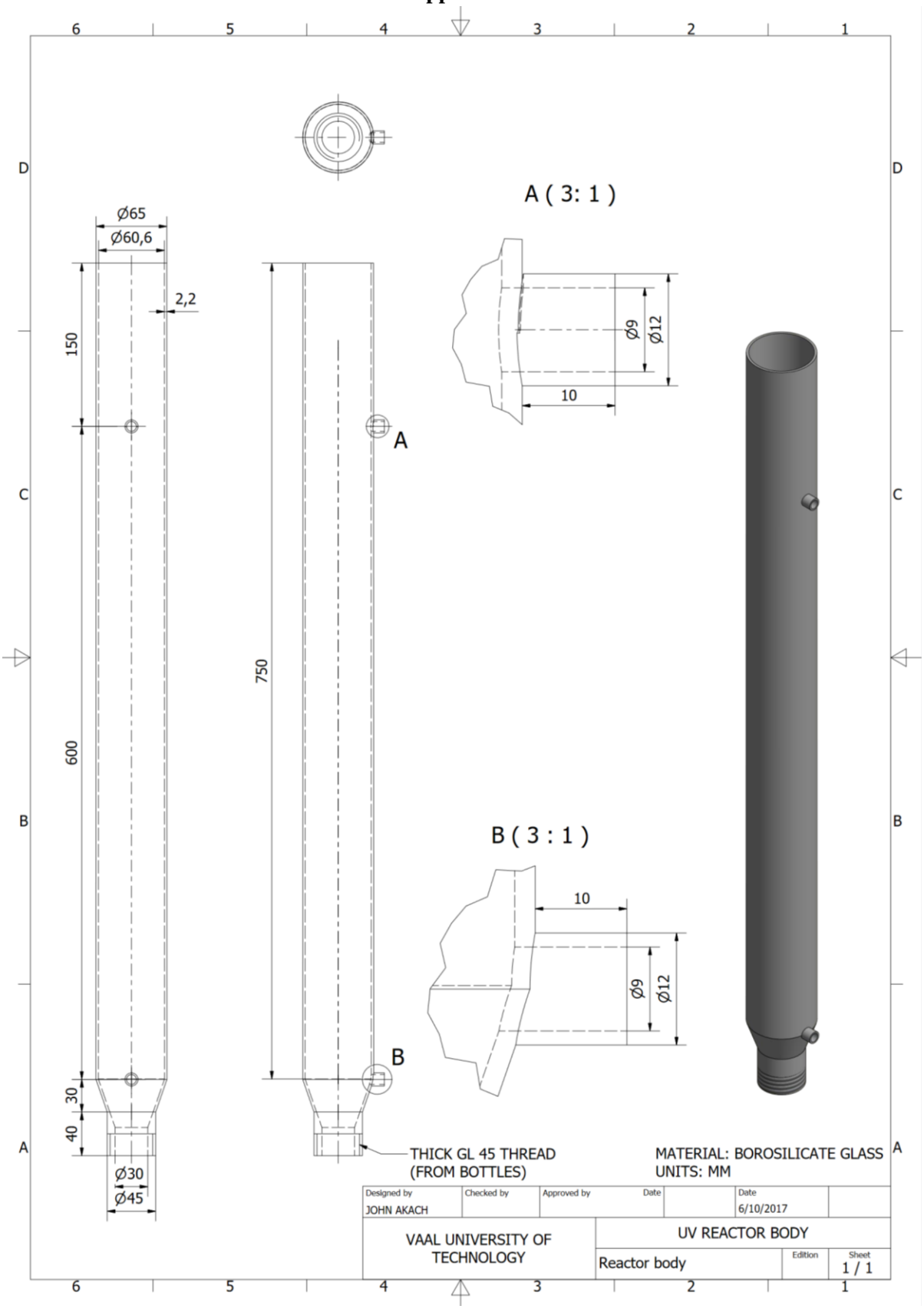

Figure B1: Detailed specifications of the fluidized bed reactor body

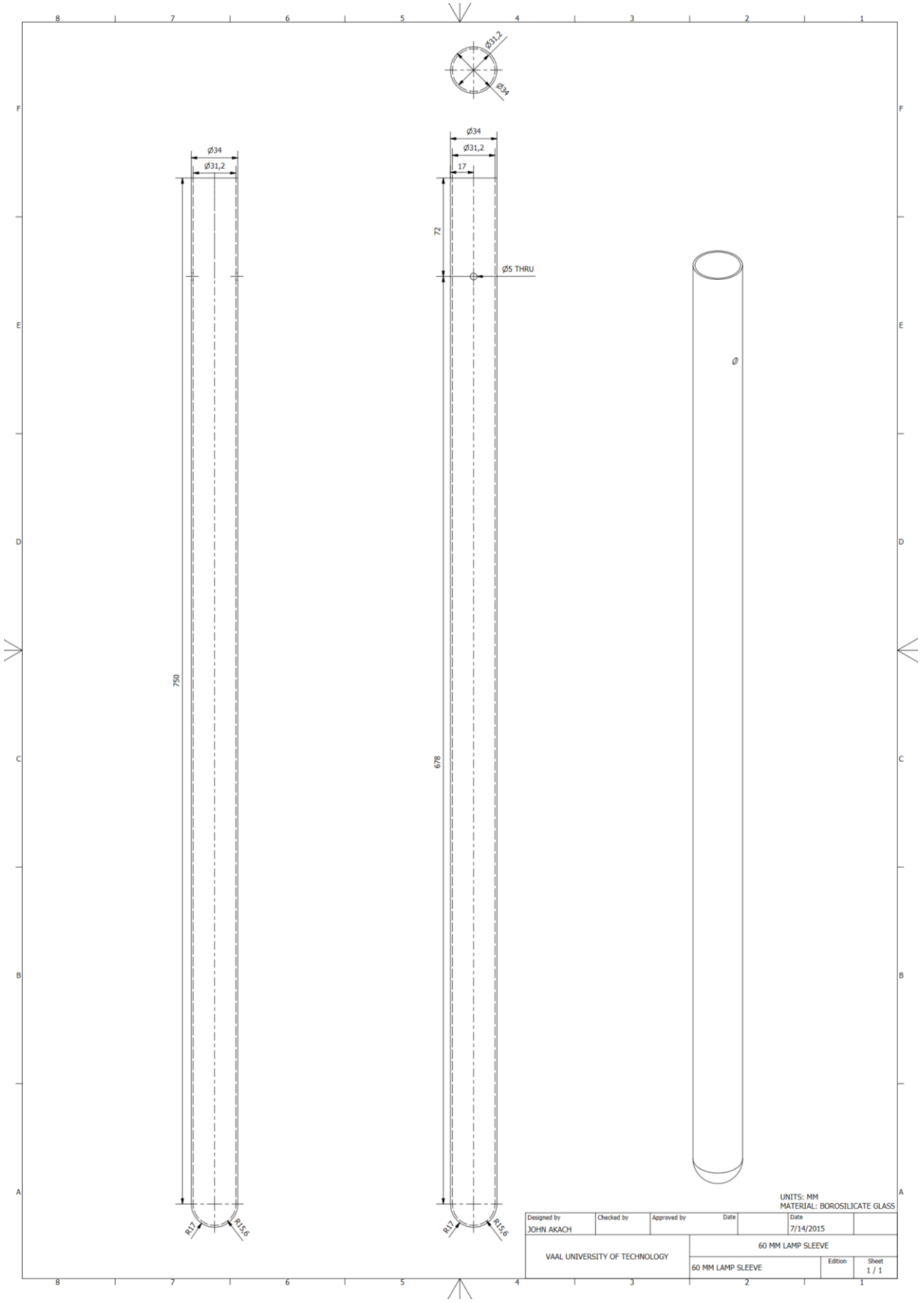

Figure B2: Detailed specifications of the fluidized bed reactor lamp sleeve

Figure B3: Pictures of reactors: (a) tubular solar reactor (b) annular solar reactor (c) UV lamp reactor/hybrid light reactor

Appendix C

Sample Monte Carlo code

```
% Author: John Akach, 2016 - 2020
% Contact: johnakach@gmail.com
% Developed using MATLAB R2015a on Microsoft Windows 10 Home

function [] = loop()
%% PARAMETERS
global catalyst_loading total_packets bubble_radius reactor_geometry
global reactor_length reactor_radius glass_absorbance glass_sleeve_radius
global GHI local_time reactor_tilt solar_azimuth solar_flow_rate

total_packets = 1e7; %total number of photon packets to be tracked
catalyst_loading = 0.4; %catalyst loading [g/L]

reactor_geometry = '65 mm hybrid'; %reactor geometry
geometry_data(); %load the geometry data

UV_flow_rate = 2.159060842e-05; %UV photon molar flow rate [Einsteins/s or moles/s]
GHI = 6.6623E-06; %global horizontal molar flow rate [moles/s]
local_time = '2017-04-29 12:47';
reactor_tilt = degtorad(90); %reactor tilt from the horizontal [rad]
solar_azimuth = degtorad(0); %azimuth angle of sun in the sky [rad]

solar_position(); %load solar position data and solar flow rate

bubble_radius = 6/2000; %average radius of bubbles [m]
gas_height = 59/1000; %gas height [m]

global air_ref_index glass_ref_index water_ref_index
air_ref_index = 1.00029; %refraction index of air
glass_ref_index = 1.473; %refraction index of glass
water_ref_index = 1.332986; %refraction index of water

global sensor_radius
sensor_radius = 6.35/2000; %radius of the radiation sensor [m]

global photon_location photon_direction photon_lost
photon_location = [0 0 0]; %x y z location of the photon [m]
photon_direction = [0 0]; %phi theta direction of the photon [rad]

global ttr vrea_solar vrea_UV
ttr = 0; %total transmitted radiation [uW/cm2]
vrea_solar = 0; %volumetric rate of energy absorption [uW/cm2]
vrea_UV = 0; %volumetric rate of energy absorption [uW/cm2]

global UV_spectrum solar_spectrum Fabs Fscatt Fpze abs_coeff scatt_coeff
wavelength = load('UV_spectra\wavelength.txt');
cumulative_intensity = load('UV_spectra\cumulative_intensity.txt');
UV_spectrum = fit(cumulative_intensity, wavelength,'cubicinterp'); %UV spectrum

wavelength = load('solar_spectra\wavelength.txt');
cumulative_intensity = load('solar_spectra\cumulative_intensity.txt');
solar_spectrum = fit(cumulative_intensity, wavelength,'cubicinterp'); %solar spectrum

wavelength = load('romero\wavelength.txt');
abs_coefficient = load('romero\abs_coeff.txt');
scatt_coefficient = load('romero\scatt_coeff.txt');
Fabs = fit(wavelength,abs_coefficient,'cubicinterp'); %spectral absorption coefficients
Fscatt = fit(wavelength,scatt_coefficient,'cubicinterp'); %spectral scattering coefficients

z = load('tsekov\z.txt');
```

```
cumulative_Pze = load('tsekov\cumulative_Pze.txt');
Fpze = fit(cumulative_Pze,z,'cubicinterp'); %UV lamp axial output

%% GRID DISTRIBUTION
global ttr_coeff lvrea_coeff vrea_coeff liquid_volume photon_source
avogadros_number = 6.022140857e23; %avogadro's number [photons/mole]
total_photons = (UV_flow_rate + solar_flow_rate)*avogadros_number; %total photon flow rate
plancks_constant = 6.62607004e-34; %planck's constant
speed_of_light = 299792458; %speed of light [m/s]
ttr_coeff                                                                                    =
total_photons*plancks_constant*speed_of_light*1e6/(total_packets*pi*sensor_radius*sensor_ra
dius*1e4*1e-9);
vrea_coeff                                                                                   =
total_photons*plancks_constant*speed_of_light/(total_packets*(liquid_volume)*1e-9);
lvrea_coeff = total_photons*plancks_constant*speed_of_light/(total_packets*1e-9);

grid(); %load the storage grid

%% BUBBLE DISTRIBUTION
global bubble_centroid gas_volume_fraction gas_volume
bubble_centroid = [0 0 0];
gas_volume = pi*((reactor_radius(1)^2)-(glass_sleeve_radius(2)^2))*gas_height;
gas_volume_fraction = gas_volume/(gas_volume + liquid_volume);

bubble_distribution(); %load the random bubble centroids
bubble_iteration = 1;

%% MONTE CARLO LOOP
for emitted_packets = 0:1:total_packets
    if emitted_packets > total_packets
        break
    end
    %decide if the emitted photon is a solar or UV photon
    if (UV_flow_rate/(UV_flow_rate + solar_flow_rate)) > rand %emitted photon is a UV photon
        photon_source = 'UV';
        UV_emission(); %emit a photon from the UV surface
    else %emitted photon is a solar photon
        photon_source = 'solar';
        solar_emission(); %emit a photon from the solar surface
    end

    %the photon is on the outer glass sleeve
    %the photon will start travelling in the slurry
    while(photon_lost == false) %while photon has not been lost...
        %check the distance between the photon and boundaries:
        path_length = [1 1 1 1]; %pathlength of photon to the boundaries

        if glass_sleeve_radius(2) > 0 %if reactor has a glass sleeve...
            %photon pathlength to outer glass sleeve
            [path_length(1), location1] = intersect_cylinder(glass_sleeve_radius(2));
        end

        if catalyst_loading > 0 %if catalyst slurry is modelled...
            %photon free pathlength in the slurry
            path_length(2) = (-1/(abs_coeff + scatt_coeff))*log(rand);
        end

        %photon pathlength to the reactor wall
        [path_length(3), location3] = intersect_cylinder(reactor_radius(1));

        if bubble_radius > 0 %if photon-bubble interactions are modelled...
            %photon pathlength to nearest bubble
            path_length(4) = nearest_bubbles(); %calculate distance to nearest bubble
        end

        %the closest boundary to the photon is:
```

```
        [M,I] = min(path_length); %the shortest photon pathlength to boundary
        if M == 1
            photon_lost = true;
        else
            switch I
                case 1 %the photon hits the outer glass sleeve
                    if(glass_absorbance(1) > rand) %if photon absorbed by the glass sleeve...
                        photon_lost = true; %the photon has been lost
                    else %if photon is transmitted with refraction...
                        photon_location = location1;
                        outer_glass_sleeve(); %calculate new trajectory
                    end
                case 2 %the photon is still moving within the slurry
                     %location of photon at the end of the slurry pathlength
                    location2 = photon_location + path_length(2)*direction_cosine;

                     %if the z coordinate is outside the reactor...
                    if (location2(3) < 0) || (location2(3) > (reactor_length))
                        photon_lost = true; %the photon has been lost
                    else
                        photon_location = location2;
                        slurry(); %calculate absorption/new trajectory after scattering
                    end
                case 3 %the photon hits the reactor wall
                    photon_location = location3;
                    inner_reactor_wall(); %calculate the new trajectory
                case 4 %the photon hits a bubble
                    photon_location = photon_location + path_length(4)*direction_cosine;
                    bubble(); %calculate the new trajectory
            end
        end
    end
    if emitted_packets == 1e5*bubble_iteration %calculate another random bubble centroids
        bubble_distribution;
        bubble_iteration = bubble_iteration + 1;
    end
end
end
```